Design of immunosensor for the detection of C-reactive protein using oriented antibody immobilization

A thesis submitted in fulfillment of the requirements for the degree of

DOCTOR OF PHILOSOPHY (PhD)

Of

RHODES UNIVERSITY

By

ADESINA ABIOLA OLANIKE

MARCH 2019

DEDICATION

This thesis is dedicated to the Almighty God

To my late Dad (Chief J.A Akinkugbe J.P) who passed on to glory a few months ago
&

To my beloved husband Mr. S.A Adesina

ACKNOWLEDGEMENTS

I am very grateful to the Almighty God the giver of life for sustaining me throughout my stay in South Africa.

Behind this successful piece of work is a rare illustrious and highly disciplined academician of a versatile intelligibility who supervised the work in person of Dr. Philani Mashazi. Thanks for your relentless effort amidst your tight schedule, you devoted attention to the planning and the completion of my PhD research.

My profound gratitude also goes to Prof. Samson Khene for his advice and encouragement. I would like to thank the F3 and F5 research group, without you guys it would have been a different story. To the entire member of staff of Chemistry department of Rhodes University, I say thank you all.

Special thanks to my wonderful parents Chief & Chief Mrs. J.A Akinkugbe not only bringing me to the world but for giving me the best. I will forever be grateful to God for blessing me with a parent like you. Words cannot express my gratitude to my siblings, for your support and prayers always. May God reward you abundantly.

My sincere gratitude goes to Prof. Oladoja, Dr. Olonisakin of Chemistry Dept AAUA Nigeria for your support and kindness. May the Lord reward and bless you. I cannot but appreciate the Akinbo's family, Kayode, Mrs Adewumi, and RCCG family Grahamstown. It's nice being part of this wonderful set of people.

Many thanks to my employer, Adekunle Ajasin University Akungba Akoko for giving me study leave with pay as well as TETFUND for scholarship.

To the love of my life, my darling husband thanks for being there for me and my lovely children, Adetola, Adetomiwa, and Adetomilola wow!!! You are wonderful indeed.

ABSTRACT

Early diagnosis of cardiovascular diseases (CVDs) has been a major challenge since CVDs are clinically silent. The current methods available for the diagnosis are not sensitive enough at the onset of the disease. Also, the use of sophisticated equipments and experts in the result interpretation has created a lot of barriers to the early diagnosis of CVDs. Biomarkers detection using electrochemical immunoassay offers great advantages in terms of sensitivity, miniaturization and low cost. This can be integrated into portable devices which can be made available in the remote areas for easy assessment of health care services.

The fabrication of piezoelectric and electrochemical immunosensors for the detection of C-reactive protein (a cardiac biomarker) are presented in this thesis. The electrochemical immunosensor investigates the effect of linkers chain length on the analytical performance of the immunosensor. The fabricated immunosensors were based on two simple and sensitive label-free impedimetric assay. Oriented immobilization of anti-CRP monoclonal antibody (mAb) unto gold surface was achieved using carbohydrate specific boronic ester reaction for enhanced capture and specific detection of CRP protein.

Quartz crystal microbalance with dissipation (QCM-D) was employed to establish the immunocomplex formation between the mAb and CRP antigen. This was achieved by forming a self-assembled monolayer (SAM) of 4-mercaptophenylboronic acid (MPBA) onto the quartz crystal surface. The limit of detection (LoD) for the direct and sandwich immunoassay was 5.45 and 3.65 ng mL^{-1}, respectively.

The Au-MPBA-mAb/glucose immunosensor with the shortest chain length of boronic acid was fabricated. The use of SAM of 4-mercaptophenylboronic acid (MPBA) afforded a thio phenylboronic acid functionalized gold surface (Au-MPBA SAM). The anti-CRP-mAb capture antibody was immobilized in an oriented manner onto gold thiophenylboronic acid to yield an Au-MPBA-mAb surface. The non-specific boronic surface was blocked using glucose to yield an Au-MPBA-mAb/glucose. The modified gold surface could detect CRP antigen. The limit of detection (LoD) was found to be 9.82 and 6.23 ng mL^{-1} for the direct and sandwich immunoassay; respectively.

The Au-MBA-APBA-mAb/glucose immunosensor was designed by forming a SAM of 4-mercaptobenzoic acid (MBA) onto gold electrode surface. The terminal -COOH group of the MBA SAM reacted with an amino (NH_2) group the 4-aminophenylboronic acid (APBA) using EDC/NHS coupling. This was followed by the immobilization of the capture antibody and the blocking of non-specific binding sites using glucose. Improved analytical parameters were obtained with LoD for the direct and sandwich immunoassays found to be 2.90 and 1.20 ng mL^{-1}; respectively.

A more stable immunosensor utilizing electrochemical grafting was investigated for the fabrication of Au-PEA-SA-APBA-mAb/glucose. The enhanced stability of the immunosensor was through the electrochemical reduction of 4-aminoethyl benzene diazonium (AEBD) salt. The surface was further derivatized with succinic anhydride to have a carboxylic derivatized surface. Carbodiimide chemistry was used to form a covalent linkage between the APBA amine group and the surface -COOH terminal group to yield an Au-PEA-SA-APBA surface. The immobilization of mAb and glucose resulted in Au-PEA-SA-APBA-mAb/glucose immunosensor.

For the detection and signal enhancement, the magnetic nanoparticles conjugated with anti-CRP polyclonal antibody (pAb) was prepared. The sandwich immunoassay was used to detect CRP by the first capture at Au-PEA-SA-APBA-mAb/glucose. This was followed by signal amplification using magnetic nanoparticles coated with a silica shell and conjugated to pAb (MNP-SiO-APTES-PBA-pAb/glucose). The limit of detection was found to be 560 pg mL^{-1} and much lower than sandwich immunosensor fabricated using SAMS. The signal enhancement, lower detection limits and high sensitivity were obtained due to the nanoparticles for the sandwich immunoassay.

The linear range for all the fabricated immunosensor ranges from 10 – 100 ng mL^{-1}. The sensitivity obtained for Au-MPBA-mAb/glucose, Au-MBA-APBA-mAb/glucose, and Au-PEA-SA-APBA-mAb/glucose were 0.691, 0.885, and 11.08 $k\Omega.ng^{-1}.ml.cm^{-2}$ for the sandwich immunoassay. The piezoelectric immunosensor was regenerated using 0.1 M HCl without affecting the immobilized capture antibody. The real sample analysis was carried out in 10 % serum in a recovery study for all the fabricated immunosensor. The percentage of recovery was very close to 100 %.

TABLE OF CONTENTS

LIST OF ABBREVIATIONS

ACS	Acute Coronary Syndrome
AEBD	2-Aminoethanebenzene diazonium salt
Ag	Silver electrode
AMI	Acute myocardial infarction
ANP	Atrial natriuretic peptide
APA	4-(2-aminoethyl)phenylamine
APBA	4-aminophenylboronic acid
Au	Gold electrode
AuCQC	Gold coated quartz crystal
BHF	British Heart Foundation
BNP	Brain natriuretic peptide
CDC	Centre for Disease Control and Prevention
CDs	Communicable diseases
CHD	Coronary heart disease
CVDs	Cardiovascular diseases
CRP	C-reactive protein
CT	Computed tomography scan
CV	Cyclic Voltammetry
DNP	Dendroaspis natriuretic peptide
DPV	Differential pulse voltammetry
ECG	Electrocardiography
EDX	Energy dispersive X-ray Spectroscopy
EIS	Electrochemical impedance spectroscopy
ESCA	Electron spectroscopy for chemical analysis
Fab	antigen-binding fragment
FTIR	Fourier transform infrared spectroscopy

GA	Glutaric anhydride
HDL-C	High-density lipoprotein cholesterol
H-FABP	Heart fatty acid binding protein
^{1}H NMR	^{1}H Nuclear Magnetic Resonance
ICAM-1	Intercellular adhesion m olecule-1
IL-6	Interleukin-6
IL-1	Interleukin-1β
INJ	Injuries
ISE	Ion-selective electrode
ISFET	Ion-sensitive field effect transistor
LDL-C	Low-density lipoprotein cholesterol
Lp[a]	Lipoprotein(a)
LV	Left ventricular
MBA	4-mercaptobenzoic acid
MCSF	Macrophage-colony stimulating factor
MI	Myocardial infarction
MNPs	Magnetic nanoparticles
MNP-SiOH	Silica-coated magnetic nanoparticles
MNP-SiO-APTES	APTES functionalized magnetic nanoparticles
MNP-SiO-APTES-PBA	Phenylboronic acid functionalized magnetic nanoparticles
MNP-SiO-APTES-PBA-pAb	Antibody conjugated to phenylboronic acid functionalized magnetic nanoparticles
MPBA	4-mercaptophenylboronic acid
MPO	Myeloperoxidase
MRI	Magnetic imaging resonance
NCDs	Non-communicable diseases
PDGF	Platelet-derived growth factor

QCM-D	Quartz crystal microbalance with dissipation
SA	Succinic anhydride
SAA	Serum amyloid A
SAM	Self-assembled monolayer
SEM	Scanning Electron Microscopy
SMC	Smooth muscle cells
SPR	Surface plasmon resonance
TEM	Transmission Electron Microscopy
TNFα	Tissue necrosis factor
VCAM-1	Vascular adhesion molecule 1
WHO	World Health Organization
XRD	X-ray diffraction

LIST OF SYMBOLS

C_{dl}	Double-layer capacitance
CPE	Constant phase element
f	frequency
Hz	Hertz
I	Current
I(t)	sinusodial current
R_{CT}	Charge transfer resistance
Rs or Re	Solution or electrolyte resistance
V(t)	Sinusodial potential
Z	Impedance
Z'	Real component of impedance
Z''	Imaginary component of impedance
Z_w	Warburg impedance
Ω	Ohm

LIST OF FIGURES

Figures in APPENDIX

LIST OF TABLES

LIST OF SCHEMES

Chapter 1:

Introduction and literature review

1.0. Introduction

1.1. The need for cardiovascular diseases (CVDs) diagnosis

Non-communicable diseases (NCDs) are the leading cause of mortality globally. NCDs accounts for about 68% of death, that is 36 million out of the 56 million in 2012, and it was projected that figure would increase to 52 million by 2030 [1]. The low and the middle-income countries are at a major disadvantage because about three-quarter of all the deaths occurring from NCDs occur in these countries. This account for about 28 million deaths from NCDs [1].

The four major types of NCDs are cardiovascular diseases, cancer, chronic respiratory disease, and diabetes. These major classes are responsible for 82% of death arising from NCDs [1]. It was reported globally that about 42% of all the NCDs occurred before the attainment of age 70 in 2012 [1]. The death arising from NCD is about 48% in the low and middle-income countries, and 28% was reported [1] to have occurred in the high-income countries. These diseases are driven by lifestyle changes, the effect of globalization, unhealthy lifestyle, rapid urbanization and ageing population [2]. This change in lifestyle has led to a shift in the dominance of infectious diseases such as pneumonia, diarrhoea, to the high occurrence of non-communicable diseases such as cardiovascular diseases (CVDs) and cancer [3,4].

CVDs are non-communicable diseases which comprise a broad range of diseases affecting the heart and the blood vessels [5]. The two major types of CVDs are further classified into different types as summarized in **Table 1.1** below, that is those involving the blood vessel and those involving the heart.

Table 1.1: Classification of CVDs into different types based on the heart and blood vessel they affect.

Cardiovascular diseases (CVDs)	
Blood vessel	**Heart**
• Coronary artery disease	• Cardiomyopathy
• Peripheral arterial disease	• Hypertensive heart disease
• Cerebrovascular disease	• Heart failure
• Renal artery stenosis	• Cardiac dysrhythmias
	• Congenital heart disease
	• Rheumatic heart disease

The statistics from the World Health Organization (WHO) shows the prevalence of cardiovascular diseases (CVDs) as the leading cause of death globally [6–10]. Therefore, there is a need for surveillance to curb the scourge of CVDs. The alarming trend of deaths occurring due CVDs shows that this is a global threat especially to the low-income/developing countries [11].

Thomas Gaziano in 2005 reported that the death occurring from CVDs at the beginning of the 20th century was less than 10% [12]. Recently, this figure has drastically increased to about 30% with the prevalence of CVDs in developing/middle-income countries [12]. CVDs accounts for one-third of all the global deaths. It was reported that about 17 million people die yearly from CVDs and a substantial increase to 24 million is expected by the year 2030 [13]. The chart showing the global distribution of death and death occurring from CVDs is presented in **Fig. 1.1.**

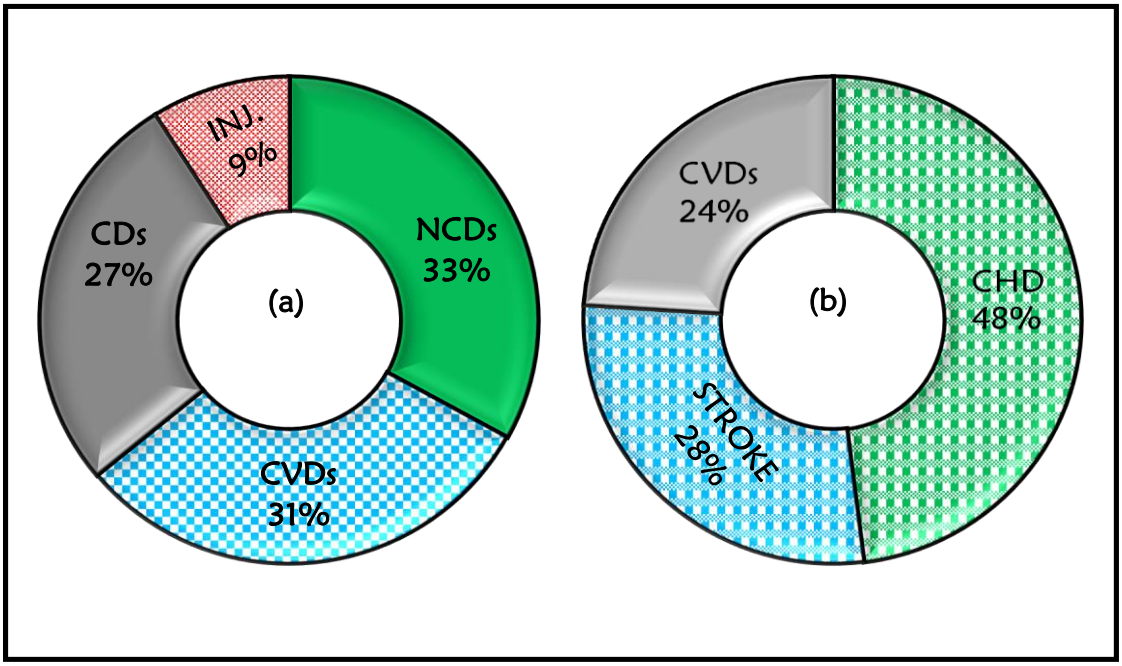

Figure 1.1: Chart showing (a) the global distribution of death and (b) the global distribution of death arising from cardiovascular diseases (CVDs). Adapted from WHO Global Atlas on CVD Prevention and Control, 2011. (**INJ** = Injuries, **CDs** = Communicable diseases, **CHD** = Coronary heart disease, **CVDs** = Cardiovascular diseases and **NCDs** = Non-communicable diseases)

1.2. Risk factors associated with CVDs

Lenfant 2001, reported that the risk factors for CVDs are the same in different populations [14]. The major risk factors associated with CVDs are grouped into two: immutable and mutable risk factors. The immutable factors are non-modifiable risk factors which are non-changing with times, and these include age, gender and family history. The mutable risk factors are modifiable, that is, can be changed with time, and these include unhealthy diet, smoking, physical inactivity, increased inflammatory markers, high blood cholesterol, high blood pressure, and obesity. Other factors like poverty, low educational standard, and social inequalities have been found to be

associated with increased levels of CVDs in low and middle-income countries [15–18]. Estimates have shown that 90 % of CVDs are preventable [19]. Mutable risk factors can be prevented, by changing lifestyle, by promoting non-smoking, non-fatty, low-calorie diet, and increased physical activity. Furthermore, much effort has been put into treating hypertension and diabetics both with lifestyle changes and pharmacologically [20].

1.2.1. Age

Age is a crucial predictor of CVDs, an unavoidable risk factor and is generally considered to be a non-modifiable risk factor [21]. The severity of disease manifestation is brought about as a result of aging [22], and the chances of developing CVD at an older age is high or the prevalence of CVDs increases with age [23]. Elevated risk of health complications and diseases are associated with aging occurring from gradual deterioration in numerous physiological process [24]. The cellular composition of the heart is affected due to complex changes taking place with aging [24]. Therefore, aging has a significant effect on the heart and the arterial system leading to an increase in CVDs including atherosclerosis, hypertension, myocardial infarction and stroke [22].

The consequential effect of aging on the heart and the arterial system could also lead to alteration in treatment response [25]. Also, ageing CVD tissues are characterized by pathological alterations including hypertrophy, altered left ventricular (LV) diastolic function and diminished LV systolic reverse capacity, increased arterial stiffness and impaired endothelial function [22,26]. Statistical data revealed that 82% of people who die of heart disease are 65 years and above. It was also reported that the risk of stroke doubles after 55 years in every decade [27].

1.2.2. Family history of the coronary event

The family history of the coronary event is a non-modifiable risk factor which has been well investigated as an independent risk factor [28,29]. The family history of myocardial infarction (MI) increase the chances of developing coronary heart disease both in men and women. It was reported that 15.1% of cases of MI in men and 16.1 % in women could be linked to family history excluding other known risk factors [30]. The risk associated with patients having siblings that experienced heart problems in the early stage of their life is about 40%. A 75% increase in risk factor is traceable to the paternal history while 60% risk is linked to the maternal history of CVDs [31]. Therefore a positive family history of CVDs poses a greater threat of developing coronary event later in life [32].

1.2.3. Gender-based risk factor

Gender-based risk factors have shown that the risk of men developing heart disease is higher than women before menopause [33]. Hormonal difference was considered to be a major explanation for the gender differences in CVDs risk factor. It was commonly observed that women experience myocardial infarction (MI) approximately ten years after men [34]. The late emergence of CVDs event in women is seen across populations. However, the drastic increase in CVDs occurrence in women after menopause led to the suggestion that estrogen is likely responsible for this benefit in earlier years [33]. The cardioprotective benefit of estrogen has been attributed to favourable changes in lipid profiles (lower low-density lipoprotein cholesterol (LDL-C) and lipoprotein(a) Lp[a] levels and increased high-density cholesterol (HDL-C) level [35,36].

1.2.4. Female-specific risk factors

While sex hormone may explain the difference in cardiovascular risk between women and men, other risk factors that are gender-based must also be involved.

Risk factor such as pregnancy and its complications is a major female-specific risk factor. The inability of the mother to adapt to the vascular challenge occurring from pregnancies has led to different types of complications in pregnant women [37]. These pregnancy-induced complications expose women to the risk of coronary heart disease. Risk factors like, insulin resistance, hyperlipidemia, hypercoagulability, and inflammation are associated with a healthy pregnancy [38].

Other pregnancy-associated diseases capable of increasing the risk of coronary heart disease (CHD) are gestational diabetes and hypertensive disease due to pregnancy. About 2% to 4% of pregnant women are affected by gestational diabetes [39]. Hypertensive disease due to pregnancy includes pregnancy-induced hypertension, pre-eclampsia, and eclampsia. This is common in first pregnancies which affect up to 30% pregnant women [40]. All these female-specific risk factors can pose a threat of future coronary event which is strongly associated with future maternal CVDs.

1.3. Atherosclerosis and CVDs

Great attention has been paid to the significant role of inflammation in the pathogenesis of atherosclerosis [41,42]. Atherosclerosis is the main cause of CVDs and results from the accumulation of fatty deposit called atheroma plaques in the walls of the arteries [43]. The atheromatous plaques consist of cholesterol or macrophages which narrows the arteries [44].

Evidence from research conducted over the years have shown that inflammation is a major contributor to atherogenesis [45]. Inflammation is a biological process arising as a response to stimulus from damaged cells, toxins, irritant, pathogens which is harmful to cell survival [44].

The developmental process involved in the formation of atheromatous plague is referred to as atherogenesis [46–49]. It is the disorder of the arterial wall which begins with the adhesion of monocytes to the endothelial cell surface as shown in **Fig. 1.2.** The monocytes migrate into the sub-endothelial space and differentiation into macrophages [50,51]. The differentiation of monocytes into macrophages (monocytes becomes macrophage) are enhanced by redox signaling induction factor like vascular adhesion molecule 1 (VCAM-1). VCAM-1 which helps in recruiting circulating monocytes into the tissue [52]. This process is also mediated by a macrophage-colony stimulating factor (MCSF) which allows the conversion of monocytes into macrophages [44]. Followed by the ingestion of low-density lipoproteins [LDL] and modified or oxidized LDL by macrophages. Several pathways are involved in the accumulation of the LDL to form foam cell this includes the scavenger pathway [53,54]. MCSF also facilitates the expression of the scavenger receptor which binds to LDL thereby leading to the formation of the foam cells [52]. Vascular smooth muscle cells (SMC) migrate from the media and proliferate into the intima [55]. This migration arises from the platelet-derived growth factor (PDGF) secreted by the macrophage [56]. SMC just like macrophages takes up lipid and transform to foam cell [57–59]. These foam cells together with T lymphocytes form the fatty streak. The fatty streaks swell up as they accumulate lipids, calcium, and debris with a covering of fibrous connective tissue forming the atheromatous plaque.

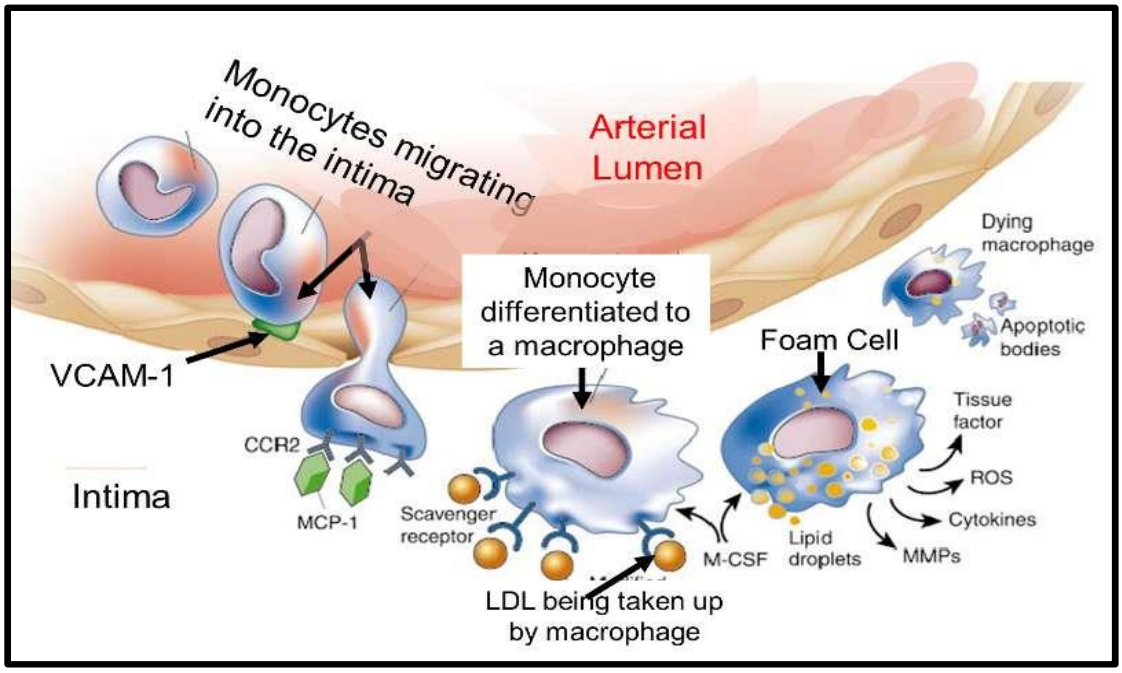

Figure 1.2: Representation showing the role of inflammation in the formation of atherosclerotic plaque.

Adapted from http://www.nature.com/nature/journal/v420/n691/fig tab/nature01323 F1.html

1.4. Coronary heart disease (CHD)

According to the British Heart Foundation (BHF), coronary artery diseases and stroke accounts for the highest form of mortality from CVDs. Coronary heart disease (CHD) also known as ischaemic heart disease results from atherosclerosis. CHD accounts for about half of the deaths occurring from CVDs, while deaths occurring from stroke account for about 28% [60].

Plague deposit resulting from atherosclerosis narrows the coronary arteries thereby causing a decrease in the blood flows into the heart leading to angina **Fig.1.3.** Angina is the main symptoms of CHD. It is a chronic chest pain which has to do with tightness or

feeling of pressure usually at the centre of the chest. The pain can spread to other part of the body including the jaw, arm, and neck [61]. The two types of angina are stable and unstable angina. They are usually stirred up by the event such as cold weather, heavy meal, physical exertion, stress or emotional upset. Similar symptoms characterize both types of angina. Stable angina occurs when there is an increase in physical or emotional activity, and inadequate blood is supplied into the heart, but the pain starts to reduce on resting for a few minutes. However, in unstable angina, these symptoms could be experienced at any time. It is unpredictable, and the symptoms may occur and even persist on resting [62].

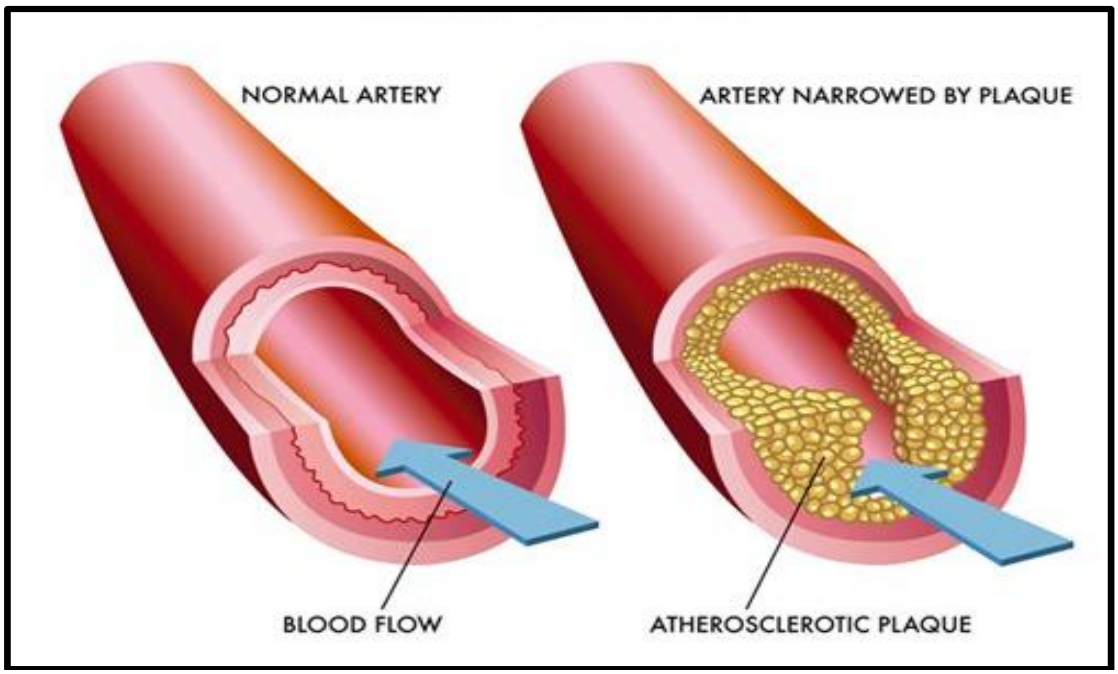

Figure 1.3: Diagram showing a normal artery and the artery narrowed by plaque. Adapted from http://www.hri.org.au/about-heart-disease/what-is-atherosclerosis

1.5. Acute Coronary Syndrome (ACS)

Acute Coronary Syndrome is the name given to a group of conditions which occurs when there is partial or complete obstruction blood supply to the heart muscles such as myocardial infarction (MI) or unstable angina. Damaged blood vessels or ruptured atheromatous plague is usually characterized by a thrombus (blood clot) **Fig. 1.4.** The thrombus can cause a sudden total occlusion of the artery **Fig. 1.4.** If the thrombus is large enough and a coronary blood vessel or the cerebral blood vessel is blocked. This results in a heart disease or stroke depending on the location of the blockage. Complete blockage of blood flow to the heart is referred to as acute myocardial infarction (AMI) commonly called a heart attack. The blockage prevents oxygen and nutrient from getting into the heart muscle cells leading to cell death. This eventually results in myocardial tissue necrosis causes permanent damage to the heart.

Ischaemic stroke arises from the blockage of the arteries to the brain by either atheroma or thrombosis. The ischaemic stroke is the most common form of stroke, and it accounts for 80% while haemorrhagic stroke results from the bleeding in the brain [27,63].

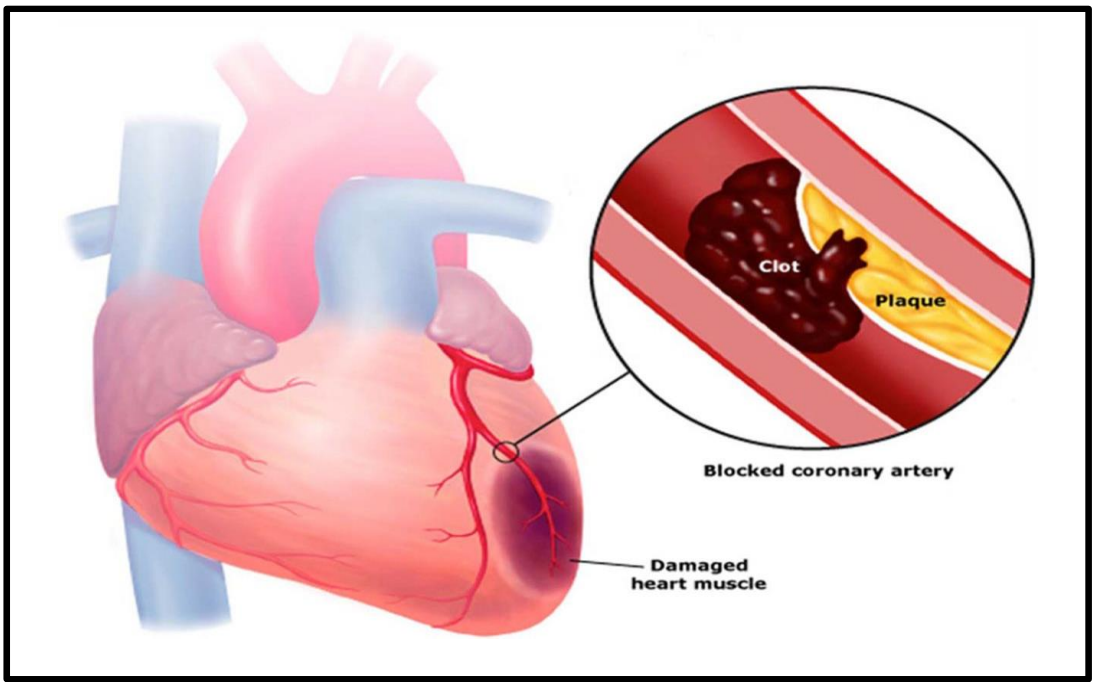

Figure 1.4: Representation showing a ruptured plaque [64].

1.6. Current methods of diagnosing CVD

Early diagnosis of CVDs has been a major challenge because CVDs are clinically silent. The current methods available for the CVDs diagnosis are not sensitive enough to detect at the onset of the disease. Also, the use of sophisticated equipment and expert in the result interpretation has created a lot of barriers towards early diagnosis of CVDs. Most of the currently used equipment are in urban areas (big cities) and not easily accessible to the majority of the populations in low resource settings. There is, therefore, a need to develop a portable easy to use devices that will be available in the remote areas for easy assessment and diagnosis of CVDs. Conventional methods used for the diagnosis of CVDs are discussed below:

1.6.1. Electrocardiography (ECG)

ECG is a non-invasive technique that records electrical signals used in detecting irregularities in the heart rhythms. The changes can be used in monitoring healthy state and irregularities in the diseased state [65]. ECG is not expensive, and it is widely available. Hence it is the most commonly used method for CVD diagnosis. ECG is also an important management tool for guiding therapy [66,67]. However, ECG is not a good diagnostic tool for CVDs, as some patients may show normal or negative diagnostic ECG even in a diseased state. This makes the early diagnosis of CVDs difficult [66–69].

1.6.2. Imaging techniques

Different imaging techniques have been used for the diagnosis and the management of CVDs. Two types of imaging techniques are (i) the invasive, and (ii) non-invasive.

The non-invasive techniques could further be subdivided into two; that is, functional and anatomical imaging [70]. Magnetic imaging resonance (MRI), Computed tomography (CT) scan, and non-invasive angiography are anatomical techniques which give the image of the heart and the coronary tree [70]. The functional techniques include stress echocardiography, and nuclear cardiology. It gives the perfusion image under stress and haemodynamic consequences of coronary artery disease [70].

The major imaging techniques reviewed in this thesis is the Magnetic Resonance Imaging (MRI) and the Computed tomography (CT) scan.

MRI plays a vital role in the diagnosis of CVDs as it provides information on the plaque composition [71]. Patients with high risk are easily identified as MRI also provides

information about the pathological state of the atheromatous plaque and the thickness of the fibrous cap [72,73].

Computed tomography also known as the CT scan is the frequently used technique for CVDs diagnosis. This is achieved by taking multiple X-ray images around a single axis of rotation with the aid of a computer to obtain a cross-sectional view of the body. The heart imaging test can be achieved through cardiac CT, which uses CT technology to visualize the heart anatomy, coronary circulation and blood vessels [74].

1.6.3. Immunoassay techniques

Antibodies are produced by the body's immune system as a response to foreign objects invading the body. The foreign objects such as bacteria, virus are known as pathogens. This is the mechanisms that the biological system (body) gets rid of the foreign object and, is highly specific. Once a bacteria or virus is covered by antibodies it is excreted out of the body. Using the natural phenomenon, researchers have utilized this specificity to design immunoassays. Antibodies have been used as the recognition elements in immunoassays and the development of immunosensor owing to their high affinity, high specificity, versatility and commercial availability [75]. Antibodies obtained from separate cell lines and recognize multiple epitopes (sites) of the antigen are known as polyclonal antibody while those obtained from single cell lines are called monoclonal antibodies and recognize a single epitope.

Antibodies are proteins made up of four polypeptide chains which consist of two identical light chains (L) and heavy (H) chains. The light and the heavy chains are linked by disulfide bond to form a Y-shaped molecule as presented in **Fig. 1.5**. The light and heavy chains contain constant and variable regions. The variable regions are responsible

for the antigen-specific binding (Fab, antigen-binding fragment) [76,77]. The Fab region is located at the tip of the arms of the Y-shaped antibody structure. Interactions between antibody and antigen can occur through multiple non-covalent bonds such as hydrogen bonds, ionic bonds, hydrophobic bond, and van der Waals interactions.

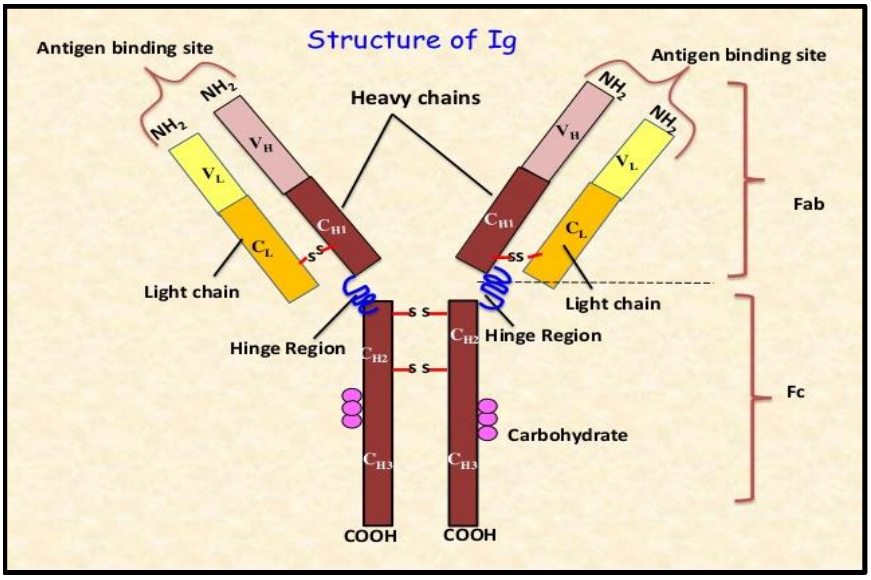

Figure 1.5: The structure of antibody

https://www.slideshare.net/ranajni_09/immunoglobulins-42896475

Immunoassays depend on the specificity of the antibody-antigen interactions. Antibody-antigen interactions are capable of producing both quantitative and qualitative results which have offered significant improvement in sensitivity [78]. Immunoassay is divided into two classes which are the homogenous and heterogeneous methods [79–81]. Homogenous immunoassay involves the biochemical reaction occurring in a solution phase. While in heterogeneous immunoassay involves the immobilization of either antibody or antigen on the surface of the transducer and the reaction takes place at the interface. Immunoassays are further classified based on the method of detection which

depend on factors such as (i) the nature of the target analyte, (ii) analytical sample, (iii) instrument sensitivity, and (iv) application [80–82]. Different immunoassay formats have been employed, but the most commonly used formats are direct, sandwich, indirect and displacement immunoassays. Direct immunoassay is the simplest form of an immunoassay format for the detection of the analyte. It involves the binding of the analyte in solution with the immobilized captured biomolecule. Sandwich immunoassay is a biochemical reaction where an antigen is sandwiched between two antibodies. This is used when the response generated from the interaction between the immobilized/captured antibody and the antigen does not give an adequate or measurable signal. The signal is generated through the binding of the captured antigen with the second antibody (with a signal generator) [83,84]. The detection sensitivity can be improved through the indirect immunoassay format. The target analyte is bound to a specific antibody after immobilization onto the surface. The detection procedure uses a labelled secondary antibody that is specific to the primary antibody. The displacement immunoassay format is used for the detection of small analyte by displacing the captured conjugated analyte on the surface [85,86].

Immunoassays involve the detection of antibodies or antigens, and these are referred to as biological markers (biomarkers).

1.7. Biomarkers

A biomarker is a measurable feature that serves an indicator capable of reflecting the severity or presence of some disease state [87]. Biomarkers could be produced in response to disease or produced by diseased organ (a tumour) [88]. Biomarkers are

needed for early risk stratification and improve patient management to obtain better outcome [89].

The role of the biomarker in screening and risk assessment before diagnosis, early stage and monitoring the progression of the disease is a major advantage in clinical applications [88]. Also their ability to monitor therapy, select therapy or monitor disease reoccurrence has added value to the use of biomarker in medicine [90]. The diagnostic and prognostic biomarkers also provide therapeutic value in medical applications. Biomarkers can be classified into five groups based on their application in different disease stages: (i) antecedent biomarkers, (ii) screening biomarkers, (iii) diagnostic biomarkers, (iv) staging biomarkers, and (v) prognostic biomarkers.

(i) Antecedent biomarkers are capable of evaluating or predicting the risk of developing a particular disease.

(ii) The screening biomarkers are usually employed in the screening of a particular disease.

(iii) Diagnostic biomarkers are types of biomarkers that serve as a diagnostic yardstick for a particular disease.

(iv) Staging biomarkers are used to categorise disease severity.

(v) Prognostic biomarkers are capable of predicting the course of future disease which includes reoccurrence, response to therapy and monitoring the efficacy of therapy [90].

Diagnosis of CVDs through the use of cardiac markers was one of the success stories of the use of biomarkers in medicine. The emergence of diagnostic and prognostic biomarkers identified in the blood are used in predicting CVDs risk which also provides

therapeutic value in medical applications. A cardiac marker is a biological analyte that is detectable in elevated levels in the blood upon the onset or progression of CVD including myocardial damage [91]. It also gives clinical evidence which helps in the early diagnosis of CVDs.

1.7.1. Characteristics of ideal cardiac biomarker

The characteristics of an ideal biomarker is high clinical sensitivity and specificity, ability to remain elevated for a long time, quick release of biomarker into the blood to enable early diagnosis and the ability to be assayed quantitatively, and at an affordable cost [92].

The risk of CVDs has been associated mostly with biomarkers for inflammation and tissue damages [93–95]. **Table 1.2** shows the summary of some biomarkers used for the CVD assessment with their normal and disease level.

However, the use of these biomarkers in disease prognosis pose some disadvantages such as (i) inability to locate the position and the composition of the atherosclerotic of the plaque, (ii) the tendency to rupture and the development of other heart challenges. Nevertheless, the above-mentioned disadvantage cannot be compared to the plethora of advantages offered by the use of a cardiac biomarker for the detection of CVDs.

Table 1.2: Selected biomarkers used for CVD diagnosis

Type of CVD	Biomarkers	Normal level (ng mL^{-1})	Intermediate risk (ng mL^{-1})	Disease level (ng mL^{-1})	[ref]
• Inflammation	Tissue Necrosis Factor (TNFα)	0.0048	-	0.048	[96]
	Myeloperoxidase (MPO)		-	> 350	[97]
• Inflammation • Cardiac risk	Interleukin-6 (IL-6)	0.0040	-	0.138	[96]
	C-reactive protein (CRP)	$< 10^3$	$1 – 3 \times 10^3$	$3 – 15 \times 10^3$	[98]
• Myocardial necrosis	Heart fatty acid binding protein (H-FABP)	-	-	≥ 6.0	[98]
• Acute coronary syndrome • Heart failure • Ventricular overload	N-terminal pro-B-type natriuretic peptide (NT-proBNP)	0.25 – 2.00	-	-	[98]
• Acute myocardial infarction (AMI)	Creatine kinase MB subform (CK-MB)	10	-	-	[98]
	Troponin T	0.050	-	0.10	[95,99]
	Troponin I	0.010	-	0.10	[99,100]
	Myoglobin	70	-	200	[100]
• Cardiac risk	Inteleukin-1β (IL-1)	< 0.070	-	0.120	[101]
	Intercellular adhesion molecule-1 (ICAM-1)	227	-	513	[102]
	Serum amyloid A (SAA)	0.37	-	220	[103]

1.7.2. CRP: an inflammatory and cardiac risk biomarker

C-reactive protein is a well-known biomarker for inflammation which can be used to assess the risk of cardiovascular disease since atherosclerosis is associated with a chronic inflammatory process [104–106]. It is an acute phase reactant secreted in the liver in response to stimulus by inflammatory cytokines, interleukin 6 (IL-6). The concentration increases about 1000 fold in response to injury, inflammation, and tissue damage [107]. CRP has been identified as the most specific biomarker for inflammation that independently predicts the risk of myocardial infarction [108].

The American Heart Association (AHA) and the Centre for Disease Control and Prevention (CDC) reported the evaluation of CRP concentration associated with CVD risk. Individuals with CRP concentration <1 μg mL^{-1}, 1-3 μg mL^{-1}, >3 μg mL^{-1} were associated with low, moderate and high risk of cardiovascular disease [109,110]. Therefore monitoring the concentration of CRP in the body and quantifying the amount present may help in reducing or predicting the risk of cardiovascular diseases and also disease management [110]. The direct role of CRP in the pathogenesis of atherosclerosis has been widely investigated. It has been reported that elevated concentration of CRP is associated with unstable angina [111] and acute myocardial infarction [112]. Pasceri and co-workers [113] recently reported the ability of CRP to induce the expression of ICAM-1, and vascular cell adhesion molecule at a concentration greater than 5μg mL^{-1}. This contributes tremendously to the formation of atherosclerotic plaque. Reports have shown that CRP is not only an inflammatory biomarker but also contribute directly to the development of atherosclerosis [113,114].

1.7.3. Cardiac Troponins

Cardiac troponins T and I are highly specific biomarkers for tissue damage which was recently discovered by Braunwald [115]. Cardiac troponins T and I are the cardiac isoforms of contractile proteins of the myofibril. Although not present in the serum of a healthy individual, they are released between 2-4 hours and remain in the system up 5 to 10 days after the onset of Acute Myocardial Infarction (AMI). Cardiac troponin is highly sensitive and specific biomarkers for cardiac damage, and both are used as a gold standard for acute myocardial infarction diagnosis [116–119]. Cardiac troponins could also arise as a result of cases like renal failure, sepsis and hypervolemia thereby questioning the authenticity of cardiac troponins for the Acute Coronary Syndrome (ACS) [120,121]. Notwithstanding, cardiac troponins are still known to be the most cardiac specific biomarker as they remain abnormal for 5-10 days after the onset of AMI. Therefore, they offer a wide diagnostic window for cardiac damage [122].

1.7.4. Myoglobin

Myoglobin is a non-enzymatic protein that was first used for the diagnosis of myocardial infarction in 1970 [123]. Myoglobin is released into the systems 2 hours after the onset of myocardial infarction (MI). It is highly sensitive, and this feature has made it useful for early screening of MI [124]. The low clinical specificity is the major limitation of myoglobin. This limitation is attributed to the presence of myoglobin in the skeletal muscle cells. The elevation in plasma concentration of myoglobin could also result from renal failure as well as injury in the skeletal muscles thereby reducing the clinical specificity of myoglobin [123].

1.7.5. Creatine Kinase

Creatine Kinase enzyme comprises three isoforms which are found in skeletal muscle (CK-MM), heart muscles (CK-MB), and the brain (CK-BB). Myocardial infarction accounts for over 90% increase in creatine kinase [125]. CK-MB is highly sensitive as the biomarker for acute myocardial infarction among the three isoforms of creatine kinase. CK-MB was formerly used as a gold standard in the diagnosis of Acute Myocardial Infarction (AMI) [125–127]. The major challenge of CK-MB has to do with its clinical specificity as it is also present in the skeletal muscles just like myoglobin. The implication is the concentration of CK-MB could also increase during physical exertion, muscular trauma, convulsions, and other related conditions. Also, the concentration of CK-MB doubles once released into the bloodstreams after the onset of MI within 5-6 hours and reaches a peak in 12-24 hours [128]. It is a diagnostic tool for persistent or re-infarctions [129].

1.7.6. Natriuretic peptides

Natriuretic peptides are cardiac biomarkers that are produced as a result of myocyte stress, and they are secreted in the heart. They are divided into four groups (i) Atrial natriuretic peptide (ANP), brain natriuretic peptide (BNP), C-type natriuretic peptide (CNP) and Dendroaspis natriuretic peptide or D-type natriuretic peptide (DNP) [130]. ANP is synthesized in the atrial myocyte [131]. BNP was initially thought to be a neurotransmitter because it was originally found in the porcine brain [132], hence it was called brain natriuretic peptide. The abundance of BNP was later discovered ten folds in the heart [133,134]. BNP is produced in the cardiac ventricle in response to expansion and pressure overload [135,136]. BNP is a useful diagnostic tool for heart

failure [137]. The C-type natriuretic peptide (CNP) is found primarily in the endothelial cell which is not directly used for CVD diagnosis [138]. D-type natriuretic peptide is a new member of the natriuretic peptide which shows similar properties like other natriuretic peptide family [139].

1.7.7. Myeloperoxidase (MPO)

Myeloperoxidase is a biomarker for inflammation which has a stimulating effect on the formation of foam cells and the atherosclerotic plaque. As an enzyme myeloperoxidase helps in lipid oxidation [140–142]. MPO has been shown to participate in the oxidation of low-density lipoprotein (LDL) which are rapidly engulfed by macrophages thus leading to the formation of foam cells [143,144]. MPO is associated with MSCF which has a role in the formation of atherosclerotic plaque [145].

1.8. Immobilization of capture protein for biosensor applications

The sensitivity and specificity of diagnostic devices based on antibody-antigen relies on the controlled orientation of the capture antibody or antigen. Therefore, the method of immobilization of capture proteins on the solid surface is important. The immobilization of capture protein has been a major challenge in immunosensor fabrication. To enhance the antibody-antigen interaction, the orientation of the capture antibody or antigen must be taken into consideration. Proper orientation enhances the sensitivity and specificity of immunosensor [146,147]. Different methods for antibody immobilization have been reported in the literature which includes physical adsorption [148–154], covalent immobilization [155–157] and bio-affinity immobilization [158]. Physical adsorption of antibody or antigen onto a solid support is the easiest method. It involves a simple method of immobilization, no antibody modification and high level

of immobilization achieved. The drawback of this method includes uncontrollable and random orientation of the immobilized antibody or antigen, weak attachment, [148–154], non-specific protein binding and leaching of the antibody or antigen from the surface [159]. Covalent immobilization by targeting functional groups that do not interfere with the binding is ideal. The functional groups present in proteins are amine, carboxyl, thiol, and carbohydrate moieties and can be targeted for covalent attachment [155–157]. The covalent immobilization of antigen or antibodies requires pre-functionalization of the solid surface. The several reactions used for protein immobilization are discussed below.

1.8.1. Carbodiimide coupling

The carbodiimide activation of the carboxylic acid makes the ester that is susceptible to amine forming amide bond [160]. This is a mild modification and proteins (antibodies and antigens) contain peptide bonds similar to the amide coupling and may not alter the protein structure. The biggest challenge in immunoassays is the orientation of the capture proteins. Therefore, this method allows for either C-terminus (COOH) or an N-terminus (NH_2) coupling. Oriented immobilization via the amine and carboxyl group is presented in **Fig. 1.6.**

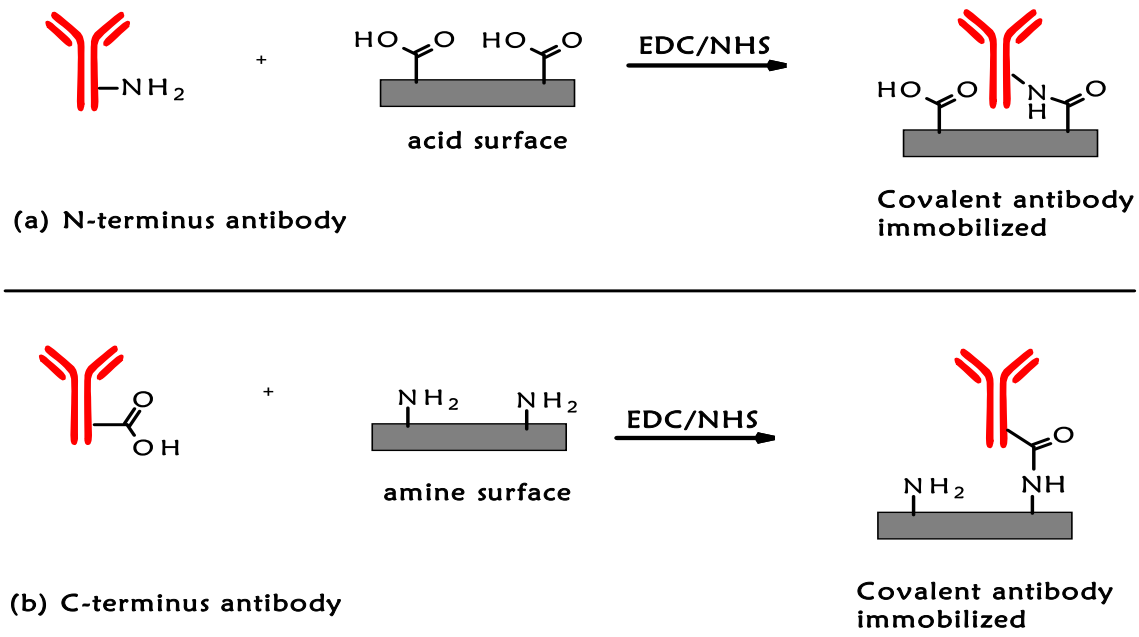

Figure 1.6: Carbodiimide coupling of (a) N-terminus and (b) C- terminus antibody onto a pre-functionalized surface with a complementary functional group.

1.8.2. Self-assembled monolayer immobilization

Disulfide bridge present at the hinge region of the antibodies can be targeted through the use of reducing agents like 2-mercaptoethylamine (2-MEA) or tris (2-carboxyethyl)phosphine (TCEP) leading to the formation of reactive thiols [161,162]. After the reduction of the disulphide, the thiols (-SH) are exposed and can be used for the immobilization of antibodies. The surface can be pre-modified with maleimide functional group to form a thiosuccinimide adduct as shown in **Fig. 1.7.** These methods have been used for the coupling of antibody onto gold nanoparticles before [147].

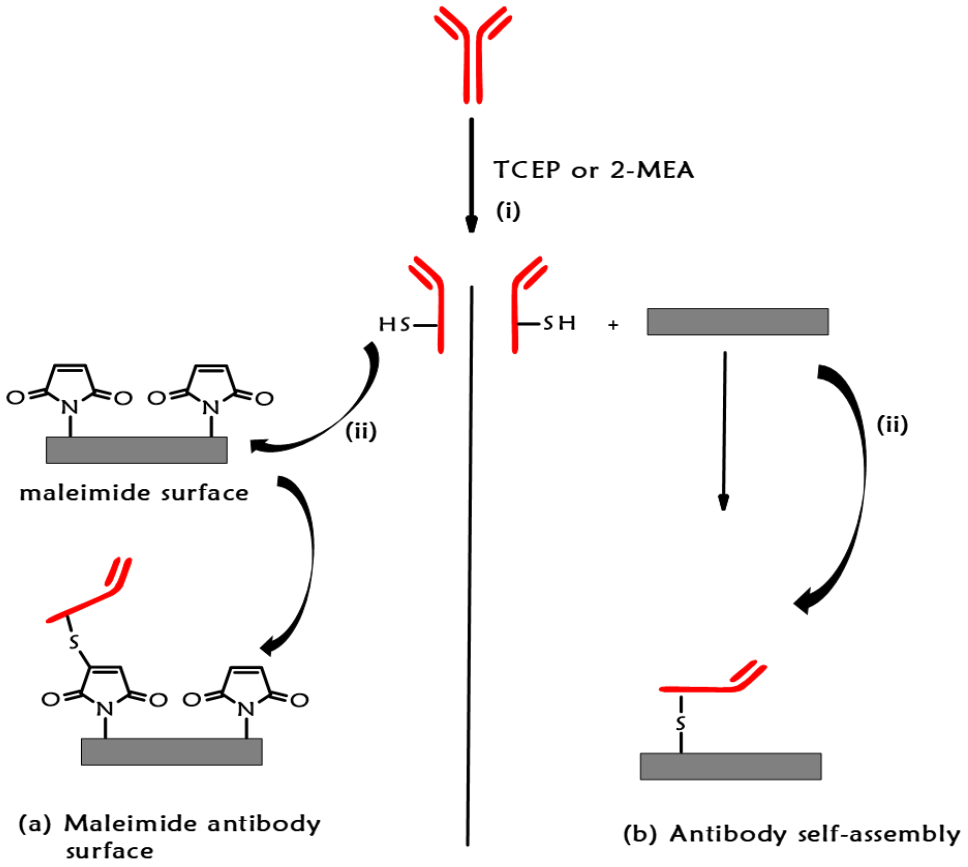

Figure 1.7: Reduction of dithiol antibody functional group (MEA or TCEP) and immobilization of the fragments via (a) thio succinimide adduct and (b) self-assembly.

1.8.3. Bio-affinity immobilization

1.8.3.1. Biotin-Avidin or Biotin-Streptavidin

Biotin or vitamin H is a naturally occurring vitamin found in living cells. Biotin-avidin interaction is one of the most useful affinity interactions for biological techniques. It results in a tight binding of biotin (vitamin H) to the protein avidin (from egg white/albumin) or streptavidin (from bacterium Streptomyces avidinii). The interaction between biotin-avidin is the strongest non-covalent interaction between a protein and ligand with the dissociation constant (Kd $=10^{-15}$ M). Avidin is a tetrameric glycoprotein, and it can bind up to four molecules of biotin. The bond formation is very fast, not

affected by pH, temperature and organic solvent. Streptavidin is a closely related tetrameric protein with similar affinity to biotin [163]. Streptavidin-biotin system is broadly employed for biomolecule labelling, immobilization, purification, and other biotechnology applications [164,165]. Streptavidin-biotin interaction is shown in **Fig. 1.8.**

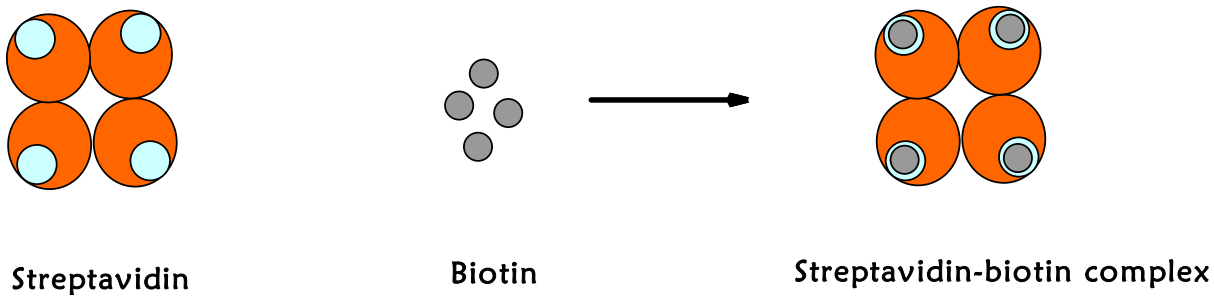

Figure 1.8: Streptavidin-Biotin interaction.

1.8.3.2. Protein A/G mediated antibody conjugation

Protein A and protein G are constituents of the cell wall of bacterial staphylococcal protein A and streptococcal protein G [166]. They are capable of binding or interacting with the Fc portion of the antibodies **Fig. 1.9.** They provide proper orientation of antibody which eventually exposes the antigenic site (Fab) region for antigen capture [167,168]. The immobilization strategy of these proteins does not require any antibody pre-modifications. Some of the benefits of this method include: (i) high degree of sensitivity, (ii) inexpensive, (iii) reduced time required for preparation of functional surfaces, and (iv) the immobilized antibody does not lose specificity and affinity. Protein A and protein G have been employed in oriented immobilization of antibody due to their specific recognition of the Fc portion of the antibody [169,170].

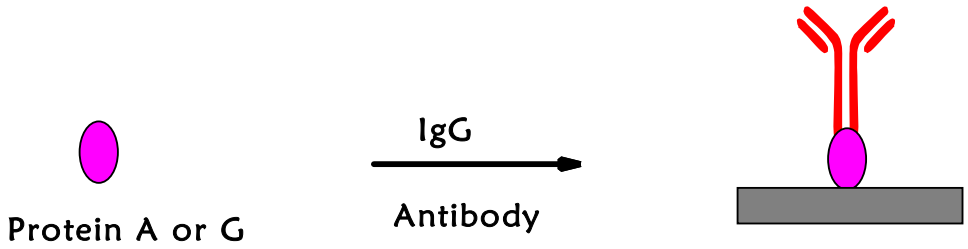

Figure 1.9: Immobilized protein A or G onto solid support through noncovalent affinity interactions with the Fc region of the antibody.

1.8.4. Carbohydrates moieties

Oriented immobilization could be achieved through antibody glycosylation owing to the presence of carbohydrate moieties present at Fc region of the antibody [171,172]. Boronic acid modified surfaces are of great importance in the bio-sensing applications. Boronic acid-mediated glycoprotein coupling have attracted much attention due to the high reactivity between boronic acid and carbohydrate residue found at the Fc region of the antibody. Boronic acid reacts with cis-1,2-diols and 1,3-diols at room temperature to form a stable cyclic ester [173–175]. The boronate ester interactions have been used for several applications including construction of biosensor for saccharides with piezoelectric [176], and Surface plasmon resonance (SPR) [177] transducers, boronate affinity chromatography [178,179], fluorescent [180,181], electrochemical detection [182]. Surface immobilized boronic acid derivatives have been used for the detection of compounds like glycated hemoglobin, galactose, and dopamine [183–186].

Qian et al. in 2018, developed a boronic acid functionalized fibre optic SPR sensor for the detection of Concanavalin A (ConA) [187]. The detection was based on the immobilization of SAM of long and short chain phenylboronic acid (PBA). The long chain boronic acid (3-(11-mercaptoun-decamido)methyl)phenyl)boronic acid denoted

as L-PBA. The L-PBA was obtained from the reaction of 11-Mercaptoundecanoic acid and 3-Aminobenzeneboronic acid. The short chain boronic acid (4-Mercaptophenylboronic acid) denoted as S-PBA. The glycoprotein affinity was investigated using both the L-PBA and S-PBA for the detection of ConA. The probe was also tested for protein-protein interaction by modifying the sensor surface with Ribonuclease B (RNase B) for the detection of ConA. The L-PBA modified sensor showed the highest affinity towards ConA than the S-PBA and RNase B based sensors. The response of both the L-PBA SAM and the S-PBA SAM were stronger than the protein-protein interaction.

Mayang et al., 2017 reported a label-free detection of transferrin (Trf) using SPR sensor modified with 4-Mercaptophenylboronic acid (4-MPBA) [188]. The modification of the SPR sensor was carried out by forming a self-assembled monolayer of 4-MPBA onto the gold surface. The online sensing of transferrin was monitored by the change in the SPR signal. The reversible interaction between the glycosyl group of the transferrin and the 4-MPBA on the sensor chip results in the changes in the refractive index of the SPR.

The detection of galactose-based on affinity boronate ester interaction has been reported by Yang et al., 2016 [189]. The galactose detection was investigated using boronic acid functionalized fluorescent carbon dot. The carbon dot was synthesized via chemical oxidation of galactose with strong acid. The synthesized carbon dot was linked to m-aminophenylboronic acid thereby forming the APBA-Carbon dot fluorescent probe. The APBA-Carbon dot was used for the optical detection of galactose in urine. The fluorescent intensity decreased with increasing galactose concentration. This is as a result of the interaction between the cis-diol molecules in galactose and the boronic acid present in the APBA-Carbon dot.

Yang et al., 2017 reported a novel method for selective enrichment of glycoprotein based on boronic acid [190]. Thiol-yne click reaction was exploited in the synthesis of 4-mercaptophenylboronic acid functionalized silica nanoparticles graphene oxide composite (GO@MPBA). The adsorption capacity of the nanocomposite towards glycoproteins such as ovalbumin (OVA), immunoglobulin (IgG), transferrin (Trf), horseradish peroxidase (HRP) and non-glycoproteins (lysozyme, deoxyribonuclease A, bovine serum albumin, cytochrome C, pepsin and trypsin) were tested. The binding capacity and the selectivity of GO@MPBA were investigated using four different types of glycoproteins and six non-glycoproteins. The binding capacity for all the glycoproteins is very high with OVA having the highest binding capacity of 1288.8 mg g^{-1}. However, the binding capacity of the six non-glycoproteins is less than 50 mg g^{-1}. This showed the boronate affinity for glycoproteins.

The fabrication of 4-aminophenylboronic acid using QCM and SPR sensors for the diagnosis of influenza was reported by Diltemiz et al., 2013 [191]. The 4-aminophenylboronic acid – sialic acid (4-APBA-SA) functionalized QCM and SPR sensors were fabricated via the self-assembled monolayer of 11-mercaptoundecacanoic acid. The APBA and SA immobilization were based on the carbodiimide chemistry using EDC/NHS coupling between the mercaptoundecanoic acid and the boronic acid. The modified sensors were used for the real-time detection of hemagglutinin (HA). Hemagglutinin is a major component of an influenza A virus which has a sialic acid (SA) binding site. The detection method was based on affinity boronate interaction between the boronic acid and the SA which eventually bind to the hemagglutinin.

The electrochemical detection of biotin using aminophenylboronic acid modified screen printed graphite electrode (SPGE) was reported by Ho et al., 2010 [186]. The modified

electrode involved the diazotization of 4-aminobenzoic acid and the functionalization of the carboxyl group on the SPGE. The diazotization was carried out by the in-situ generation of the diazonium salt by $NaNO_2$ and HCl. This was followed by the functionalization of the SPGE with aminophenylboronic acid via amide coupling. The fabricated immunosensor exploited the affinity of boronic acid towards the carbohydrate moiety at the Fc region of the anti-biotin antibody.

Moreno-Guzman et al., 2012 reported the detection of adrenocorticotropin hormone (ACTH) using disposable phenylboronic acid modified electrochemical immunosensor [192]. The fabricated immunosensor was based on the electrografting of 4-aminobenzoic acid via in-situ generation of diazonium salt using $NaNO_2$ and HCl onto a screen-printed carbon electrode. The electrode was further modified with aminophenylboronic acid using carbodiimide chemistry for the immobilization of ACTH antibodies. The oriented immobilization of the ACTH antibodies was achieved through the boronic acid-saccharide bond between the boronic acid and the ACTH antibody. The fabricated immunosensor was a labelled technique that utilizes biotinylated ACTH and alkaline phosphatase labelled streptavidin. The analytical response was measured by differential pulse voltammetry (DPV). The oriented immobilization of antibody via the boronate affinity is shown in **Fig. 1.10.**

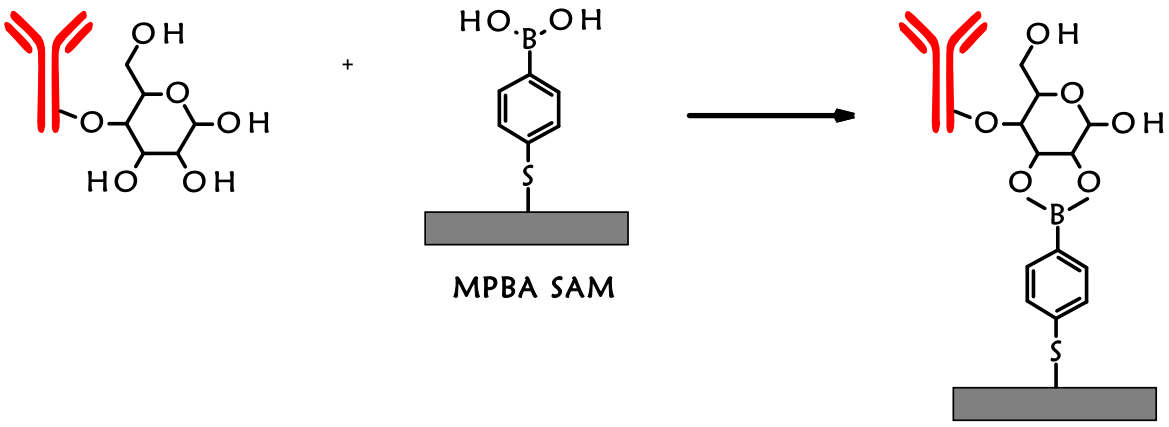

MPBA SAM : Self-assembled monolayer of 4-mercaptophenylboronic acid

Figure 1.10: Oriented immobilization of antibody via affinity boronate interaction through the carbohydrate residue at the Fc region of the antibody.

1.8.5. Oriented antibody immobilization on the performance of immunosensor

Immobilization of biomolecules has been a major challenge in immunosensor fabrication. It is also an important factor to consider in the fabrication of immunosensor. Proper antibody orientation allows the exposure of the antigen binding site for effective binding. It enhances the antibody-antigen immunocomplex formation.

Various studies have clearly shown the importance of proper orientation of capture protein which can lead to excellent performance. Kaiki Tsagimura et al., 2017 reported the use of impedance biosensor for the detection of myoglobin, an acute myocardial infarction (AMI) biomarker. A comparative study on the effect of oriented and random antibody immobilization was carried out. The oriented immobilization of anti-myoglobin immunoglobulin G (anti-myo IgG) was achieved through the attachment of anti-myo IgG to protein G on a self-assembled monolayer (SAM). Random immobilization of anti-myo IgG was prepared by direct covalent attachment to the

SAM surface. This reported that the normalized charge transfer resistance for the oriented sample was three folds higher than the random sample [193].

A comparative study was investigated using the immobilization of IgG on a thiolated protein G layer and 11-mercaptoundecanoic acid (11-MUA). The protein G immobilization was due to the affinity binding with the Fc region of the IgG while the MUA immobilization was obtained via chemical bonding. The immobilization procedure was confirmed using surface plasmon resonance (SPR). The SPR measurement obtained revealed a better immobilization efficiency for the protein G than the 11-MUA [166].

The fabrication of reflectometric interference spectroscopy (RIfS) based biosensor was developed by Choi et al., 2012. The immobilization of anti-CRP was achieved through protein A on a silicon nitride coated silicon substrate (SiN chip). The sensitivity of the RIfS based sensor with protein A was compared with the direct immobilization without protein A. It was found that the sensitivity of the sensor was enhanced as a result of the oriented immobilization achieved through protein A [194].

Moreso, a comparative study was investigated showing the binding signal of random and site-specific biotinylated IgG on streptavidin coated surface. The study was carried out in a sandwich immunoassay format. The binding signal obtained for site specific biotinylated antibody was 2-3 folds higher compared to random orientation [195].

The orientation of immobilized antibody was investigated via three methods namely: random orientation, partial orientation and controlled orientation. Controlled orientation of antibodies was achieved using protein A. The site selective immobilization of the protein A was obtained by conjugating the protein A to an amino

group carrying platform using tyrosinase. A stronger antigen affinity was observed for the orientation-controlled antibodies. The obtained k_d value was 100-fold stronger for the orientation-controlled antibodies than the k_d reported for the randomly and partially oriented antibodies [196].

1.9. Biosensors

Biosensors have become an excellent alternative to conventional analytical techniques owing to their low cost, portability and high sensitivity. A biosensor (an analytical device) which can convert biochemical information into a measurable signal. Biosensors are made up of three major components: (i) bioreceptor, (ii) transducers, and (iii) the detector system. The bioreceptor is a recognition component. It recognises the analyte in a complex sample matrix. A broad range of biological entities such as antibodies, enzymes, cell receptors, nucleic acid (RNA, DNA, and aptamers), tissues and micro-organisms can be used as bio-receptors [197,198]. The transducer aids in the conversion of the biochemical response between the analyte and the bioreceptor into a measurable electrical signal [199]. The examples of transducers that have been studied include electrochemical, optical, piezoelectric (acoustic), thermometric and micromechanical transducers. The analyte is the substance of interest to be detected. For instance, glucose is considered as an analyte in a biosensor fabricated for glucose detection. The detector is the third component of the biosensor. It receives and amplifies the electrical signal from the transducer. Then the amplified signal can be read and properly investigated.

1.9.1. Types of biosensor

Biosensors can be grouped according to their biological element or according to their transduction element. The classification is shown in **Table 1.3.** Biological elements include enzymes, antibodies, biological tissues, microorganisms, and organelles. Classification of biosensor based on transduction element can be classified into three major classes namely: optical, electrochemical and mass based. These three classes are the major transducers used for CVDs biomarkers detection.

Table 1.3: Classification of different types of biosensors based on their transduction method or biological receptor.

Transducer Electrochemical	Optical	Mass-sensitive	Bio-receptors
• Impedimetric	• SPR	• Piezoelectric	• Antibody
• Potentiometric	• Fibre optic	• Magnetoelastic	• Antigen
• Amperometric	• Raman & FTIR	• SAW	• Biomimetic
• Conductimetric	• Other	• QCM	• DNA or RNA
			• Cells
			• Tissues
			• Enzymes
			• Others

Legend: SPR – Surface Plasmon Resonance, QCM – Quartz Crystal Microbalance, SAW – Surface Acoustic Wave.

1.9.2. Optical biosensors

The detection of biochemical analytes using optical technique is a well-established and highly sensitive method in immunosensing. It is made up of a light source, a modulating

agent and a photodetector for processing the optical signal [200,201]. Optical biosensors can be grouped into colourimetric, luminescence, fluorescence, surface plasmon resonance (SPR) and fibre optics. Colourimetric, fluorescence, and luminescence biosensors are the largest groups of optical biosensors. In colourimetric and fluorescence-based detection the analyte of interest or the biorecognition element is labelled with chromogenic or fluorescence tag, such as dyes. In the label-free detection method, the target molecules are not labelled, and they are detected in their native forms. This type of detection is relatively easy and cheap to perform and allows for quantitative/kinetic measurement of molecular interactions by SPR or optical fibre biosensor. Although optical biosensors are highly sensitive, they are bulky, expensive and required dedicated personnel to perform the tests. Colourimetric fluorescence-based optical sensors also require difficult labelling procedures that depend on indirect indicator-based signal generators. Fluorescence labels are used as detection system mostly in the commercial setup [6]. This method is laboratory-based, and the equipment used for their signal readout is bulky and expensive.

SPR based biosensors are unique optical transduction techniques, commercially used for an optical biosensor which allows direct label-free detection [202,203]. SPR uses special electromagnetic waves known as surface plasmon to investigate the changes in the refractive index (RI) at the metal (transducer) surface [204]. SPR can be used to monitor and establish antibody-antigen interactions taking place on the metal surface. The main SPR apparatus is known as the Kretschmann prism arrangement [205,206]. In SPR a thin of metal (usually a 400-500 nm thick gold or silver film) is coated unto which a bio-sensing layer is immobilized as bio-recognition elements (Protein/antibodies, RNA). When an electric light of an appropriate wavelength strikes the dielectric metal surface,

it induces SPR phenomenon at the metal surface. SPR leads to a graded reduction of the intensity of the reflected light [207]. The angle of incidence at which resonance takes place depends on the optical thickness of the layer. SPR based immunosensor have been broadly used for the detection of some cardiac biomarkers as shown in **Table 1.4.**

Table 1.4: SPR based immunosensor for cardiac biomarkers detection

Biomarkers	Linear concentration range (ng mL^{-1})	LoD (ng mL^{-1})	[ref]
Myoglobin	1 - 50	0.9	[208]
CRP	2000 - 5000	-	[209]
	0.1 - 200	25	[210]
	1.2 - 80	1.2	[211]
Cardiac Troponin T	-	100	[212]
	0.03 – 6.5	0.01	[213]
	0.5 – 4.5	-	[214]
Cardiac Troponin I	1 - 50	0.7	[208]
	0 - 160	0.068	[215]
BNP	0.005 - 100	1.5×10^{-5}	[216]

1.9.3. Piezoelectric/acoustic transducer

Quartz crystal microbalance (QCM) is a piezoelectric biosensor also known as an acoustic biosensor. It is a special sensor that has an impedance detector by mass loading. QCM is made up of a thin disk of an AT-cut quartz crystal with a circular metal electrode on both sides. It is a well-known method employed in immunoassay due to its simplicity, ease of use and low cost. QCM and other acoustic devices are used for real-

life monitoring and label-free detection [217]. It is a mass sensitive technique which allows label-free detection of biomolecules. Quartz crystal immunosensor rely on the immobilization of the antibody or antigen at the surface of the quartz crystal. The biomolecule detection is based on the mass of the captured analyte by the recognition element on the quartz crystal resonator surface which is proportional to the frequency [218,219]. QCM allows quantitative measurement for binding affinity and capable of detecting any additional mass on the surface of the quartz crystal.

1.9.4. Electrochemical biosensor

The quantification and the detection of CRP using electrochemical immunoassay is the major alternative to the currently used imaging techniques for the clinical diagnostic of CVDs. This method provides real opportunities to overcome the challenges of traditional ELISAs and other laboratory-based diagnostic techniques [197,220,221]. Electrochemical immunosensors have received much attention in the field of clinical diagnosis owing to its high analytical efficiency, unique advantages of high sensitivity, fast response, portability, low cost, a simple instrument, ease of miniaturization and point-of-care applications [222–224]. Antibodies are the most used biological recognition element used in the electrochemical immunosensors. The detection of CVDs biomarkers using electrochemical immunosensors have been developed for myoglobin [99] and cardiac troponins [225]. The electrochemical immunosensors for CRP detection are presented in **Table 1.5.**

Table 1.5: Analytical characteristics of electrochemical immunosensor for CRP detection reported in the literature

Immunoassay	Linear range (ng mL^{-1})	LoD (ng mL^{-1})	[ref]
Amperometry	0.5 - 200	0.5	[226]
Voltammetry	0.2 - 80	0.04	[227]
Amperometry	up to 100	2.6	[228]
SWASV	0.5 – 200	0.22	[229]
EIS	45 - 5840	30	[230]
Amperometry	0.07 - 1000	0.04	[231]
EIS	0.1 – 20	0.1	[232]
ASV	0.2 – 100	0.05	[233]
EIS	8.5 - 9120	3.5	[234]
EIS	-	11	[235]

Legend: EIS – Electrochemical Impedimetric Spectroscopy, ASV – Anodic Stripping Voltammetry, SWASV – Square Wave Anodic Stripping Voltammetry.

The electrochemical immunoassay can be direct and indirect immunosensors. The changes in property occurring during the formation of antibody-antigen immunocomplex in the direct immunosensor can be measured in real time. The indirect or labelled immunosensors operate by incorporating additional step as a secondary reaction requiring the use of an enzyme label to produce the property to be measured. ELISA is a labelled technique commonly used for monitoring the formation of antibody-antigen immunocomplex. However, label-free detection is of great interest because the required enzyme label in ELISA are difficult and are also quite expensive to produce.

The schematic representation showing the comparison between (a) label and (b) labelled-free detection of an antigen onto an antibody bound surface is shown in **Fig.1.11.**

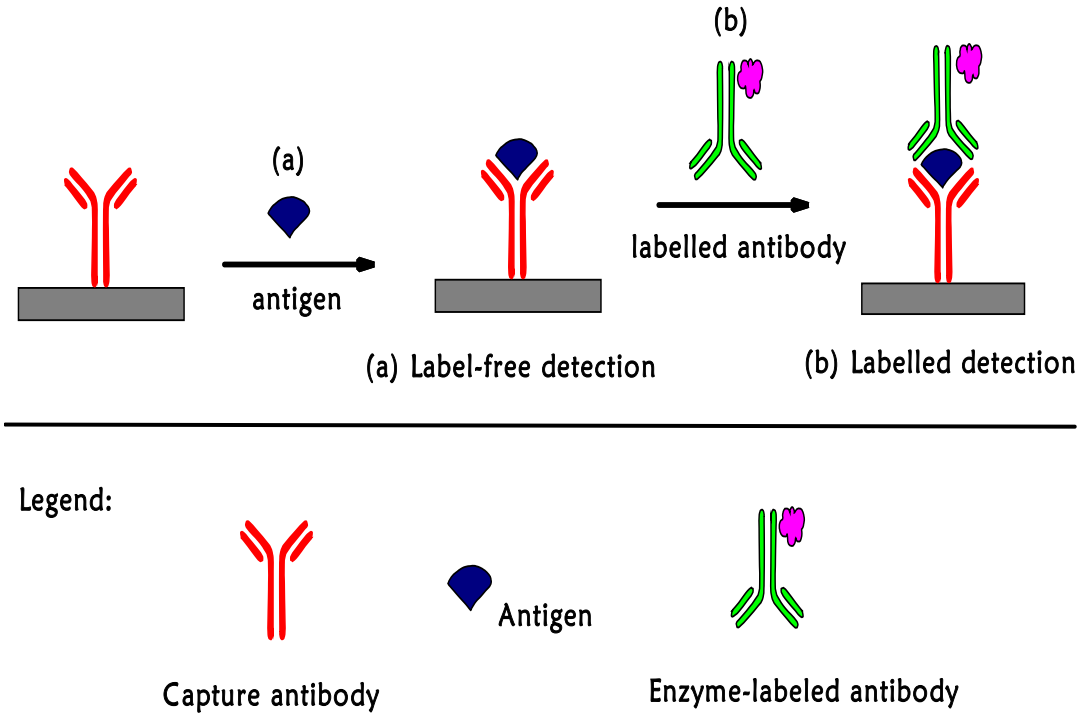

Figure 1.11: Representation of (a) label-free and (b) labelled detection of antigen onto an antibody-bound electrode surface.

Electrochemical biosensors can be classified into three types: potentiometric, amperometric and impedimetric.

1.9.4.1. Amperometry based electrochemical biosensors

In an amperometric measurement, current is monitored, and the potential of the working electrode or the sensor is kept constant. The current is then related to the concentration of the analyte present [236]. Amperometry biosensors are useful in the transduction of biological recognition event caused by an electroactive element at the

sensing surface. The generated current signal can be used to quantify the analyte of interest. It is used to investigate the electron or charge transfers between two electrodes separated by electrolyte [237].

1.9.4.2. Potentiometric based electrochemical biosensors

Potentiometric biosensors are effective quantitative method also referred to as zero current methods. It measures the potential of an electrochemical cell under a constant condition. [238]. Potentiometric sensor permits the determination of ion activity in a wide range of concentration [239]. They are based on ion-selective electrode [ISE] and ion-sensitive field effect transistor [ISFET]. The major output signal could be as a result of accumulated ions at the ion selective membrane. The basic principle of the potentiometric transducer is governed by the Nernst equation [240,241].

1.9.4.3. Impedimetric based electrochemical biosensors

Much attention has been given to impedance based immunosensors. This is attributed to the fact that label-free techniques offer real-time detection [242,243]. This transduction method is highly sensitive and gives a lower detection limit up to nanomolar to the picomolar range [244–246]. Impedance-based electrochemical immunosensor measure the impedance changes at the electrode-electrolyte interface when the target analyte interacts with the bio-recognition biomolecule immobilized onto the electrode surface [247]. Electrochemical impedance spectroscopy (EIS) is a useful tool for sensing the formation of antibody-antigen interaction on the electrode surface. EIS probes the features of the interfacial properties [248]. EIS is a non-destructive and highly informative technique which requires no labelled secondary antibody for a signal generation [249,250]. The results are direct as the affinitive

interactions between the antibody and the antigen can be directly detected using the change in charge transfer resistance (R_{CT}) [251,252].

1.10. Application of nanomaterials in bio-sensing

Due to the huge impact demonstrated by the use of nanomaterials in biosensing application and other related fields. Much attention has been given to their use in designing and improving sensing devices in electrochemical sensors and biosensors [253].

Nanobiosensors is a chemical or physical sensor fabricated using nanomaterials, usually microscopic or submicroscopic in size. Due to their small size (1-100 nm), nanoparticles exhibit unique physical and chemical properties. These unique properties have led to their applications in different areas of biomedical sciences such as sensing application, gene delivery, biomolecules detection and clinical diagnostics [254]. The role of nanoparticles in biosensor applications is for signal amplification. The antibody-antigen immunocomplex formation and detection can be greatly improved if nanoparticles are incorporated within the biosensors resulting in improved sensitivity [255–257]. Various types of nanoparticles such as metal oxide, semiconductors, and nanocomposites have been used in the fabrication of electrochemical sensors and biosensors. The nanoparticles are capable of playing different roles in different sensing systems, especially in electrochemical sensing and biosensor systems [258]. The basic functions of nanoparticles are (i) biomolecules immobilization, (ii) enhancement of electron transfer between electrode surface and protein, (iii) labelling of biomolecules, (iv) playing the role of reactant, and (v) catalysis of electrochemical reaction [253].

The remarkable success achieved by integrating nanomaterials into electrochemical and optical sensing systems as the active element has led to enhanced detection signals in small sample volume [259], stable sensing probes [260,261], miniaturized tools [262], and system for multiplex detection [263]. Nanomaterials have been broadly used both for in-vivo [264] and in-vitro [265] detection. Examples of nanomaterials that have been used for signal amplification are reviewed below.

A sandwich immunosensor for the detection of α-fetoprotein based on HRP-functionalized silica nanoparticles was reported by Liu et al., 2009. The sensitivity was enhanced by reducing the physical adsorption using the silica nanoparticles as a label. The signal amplification was confirmed using electrochemical and chemiluminescence measurement. The detection signal for the electrochemical and chemiluminescence measurement revealed 29.5 and 61-fold better than or the traditional sandwich immunoassay [266].

Won and Sim 2012, designed an antibody-based biosensor using polydiacetylene (PDA) liposomes for the detection of human immunoglobulin E (hIgE). The fluorescent signals were enhanced by conjugating gold nanoparticles with polyclonal antibodies added on a PDA liposomes. About 100-fold increase in sensitivity was obtained due to the gold nanoparticles that was employed in the detection of human immunoglobulin E (hIgE) [267].

Furthermore, the fabrication of electrochemical immunosensor for the detection of CRP was investigated by Buch and Rishpon 2008. The immunosensor was based on multi-walled carbon nanotubes (CNTs) modified screen printed electrode as disposable working electrode. Protein A was used to obtain oriented antibody immobilization.

The CNTs layer increased the sensitivity of the sensor by lowering the detection limit from 10 ng mL^{-1} for the unmodified sensor to 0.5 ng mL^{-1} for the screen-printed electrode modified with carbon nanotubes sensor [226].

1.11. Magnetic nanoparticles (MNPs) in electrochemical immunosensors

Appreciable attention has been given to MNPs and their use in immunosensors. Magnetic nanoparticles possess unique advantages which include (i) cheap and ease of preparation, (ii) biocompatibility, (iii) physical and chemical stability, environmentally safe, and (iv) ease of separation of biological components [268]. Applications of MNPs in biomedical field include molecular detection [269], bio-separation [270,271], drug delivery [272–274], hyperthermia [275,276] and MRI [277,278]. Magnetic nanoparticles are also used for signal amplification of electrochemical sensing (biosensing) applications [258]. The use of nanomaterials allows for signal enhancement resulting in high sensitivity and lower detection limit [279], thus allowing for easy diagnosis especially of disease biomarkers.

The functionalization of magnetic nanoparticles is vital to their performance and applications as it enhances stability and reduces aggregation [280]. Bare magnetic nanoparticles agglomerate easily in an aqueous system and are prone to air oxidation [281]. Bare magnetic nanoparticles also undergo rapid biodegradation when exposed directly to biological systems [282,283]. Hence there is a need for protecting the bare magnetic nanoparticles against oxidation. Methods involved in the protection leads to the formation of a shell around the magnetic nanoparticles thereby having a core-shell that is protected against the environment influence or conditions.

Surface modification with organic shell involves the use of surfactant and polymer [284–286]. The second type of coating has to do with an inorganic component like silica [287,288], carbon, precious metals such as gold [289–291] and silver [292,293]. The common methods used for the coating of magnetic nanoparticles with silica are the sol-gel process and the stober method [294–297]. The coating thickness can be adjusted by changing the concentration of ammonium and the ratio of tetraethoxysilane (TEOS) to water [298]. Magnetic nanoparticles modified with suitable functional groups (silica) allows for superb interactions of MNP with biomolecules of interest and suitable for bio-sensing applications.

Research focus

The development of biosensor detection systems for CRP (a cardiac biomarker) is of great importance due to the rapid progression in the spread of CVDs. To arrest this situation, different methods that can facilitate early detection of this biomarker is needed. Effective method of antibody immobilization is one of the ways to improve the sensitivity and the analytical performance of immunosensor.

Different methods of antibody immobilization have been reported in literature for the detection of CRP. Most of these methods are not affordable and they are not applicable in a low resource setting. This thesis is focused at targeting the oriented antibody immobilization of CRP through affinity boronate ester interaction. Although similar systems have been reported for the detection of several biomarkers. All these systems are labelled techniques which are quite expensive and time consuming. The present study investigates a label free detection method in a sandwich immunoassay using piezoelectric and impedimetric immunosensors for the detection of C-reactive protein.

Aims of this study

The aims and objectives of this project are presented below:

- The fabrication of electrochemical immunosensor for the detection of CRP will be investigated
- Investigation of oriented immobilization of monoclonal antibody using boronate ester interaction
- Effect of chain length of the linker on the fabricated immunosensors will also be investigated
- Synthesis and characterization of phenylboronic acid functionalized magnetic nanoparticles
- Signal enhancement using phenylboronic acid functionalized magnetic nanoparticles will be investigated.

1.12. Surface characterization techniques

Different characterization techniques were used to investigate and also to monitor the reactions taking place on the surface of the electrode. Electrochemical Impedance Spectroscopy (EIS) and Cyclic Voltammetry (CV) are the major electrochemical characterization methods that were used in this thesis. Other methods used for further characterization are Quartz Crystal Microbalance with Dissipation (QCM-D), X-ray Photoelectron Spectroscopy (XPS), and Scanning Electron Microscopy (SEM). All these techniques are useful in investigating the surface chemical properties and confirming the surface modifications.

1.12.1. Electrochemical Impedance Spectroscopy (EIS)

Impedance (Z) is defined as a complex resistance which hinders the flow of alternating current in a complex electrical system. It is obtained by applying sinusoidal potential, V(t), of small amplitude to an electrical circuit and measures the resulting sinusoidal current, I(t), through the circuit. Impedance is similar to resistance because it is the ratio between the applied sinusoidal potential and the measured sinusoidal current, **Equation (1.1)** below shows this relationship

$$Z = \frac{V_{(t)}}{I_{(t)}} \quad \ldots\ldots\ldots (1.1)$$

The sinusoidal potential and currents are represented as a function of time. Electrochemical impedance spectroscopy is a powerful and versatile technique used for extensive investigation of electrochemical systems. It is an effective tool for sensing the formation of antibody-antigen interaction on the electrode surface by probing the

features of the interfacial properties [248,299–302]. The acquired results are carried out over a suitable frequency range which can be related to the physical and chemical properties of electrode materials and its modifiers. The impedance is a vector quantity with magnitude and direction. The magnitude is Z(V/I), and the direction is represented as a phase angle (θ), shown in **Fig. 1.12.** The complex impedance notation is represented in **Equation (1.2).**

$$Z=Z' +jZ'' = Z_{real} + jZ_{imaginary} \quad \text{.....(1.2)}$$

Where Z' and Z'' are the real and the imaginary part of the impedance respectively and j is a complex number.

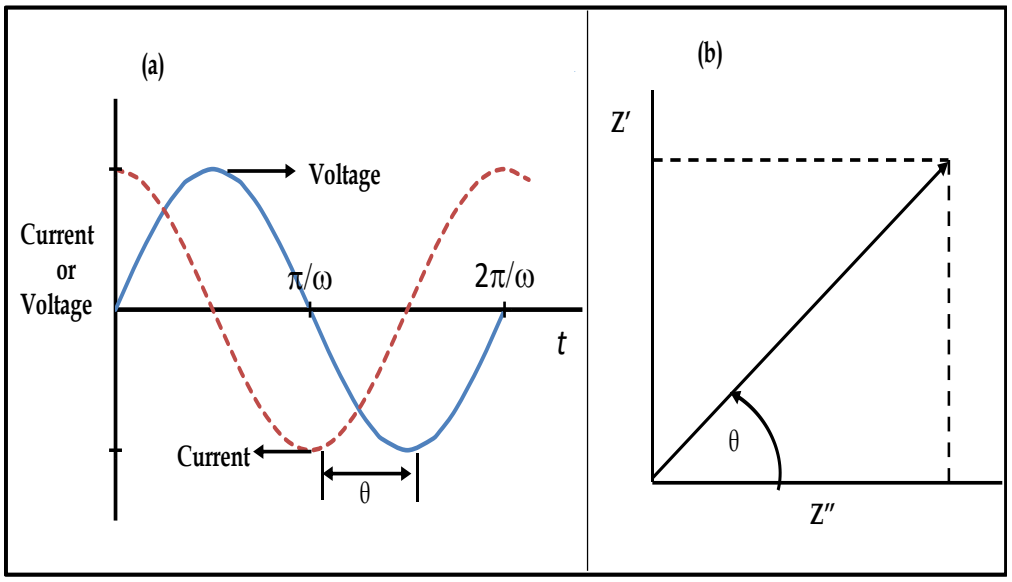

Figure 1.12: (a) Applied sinusoidal voltage and resulting current response and (b) vector representation of real (Z') and the imaginary (Z'') part of the impedance [300,301].

1.12.2. EIS data representation

Nyquist and the Bode plots are the most impedance data representations widely used amongst various graphical representation. The Nyquist plot is a plot of an imaginary

(Z") versus the real (Z') parts of the impedance. **Fig. 1.13(a)** shows a Nyquist plot impedance data representation. A characteristic semi-circle at high-frequency region and a straight line at a low-frequency region corresponds to the kinetic and diffusion process. During the impedance measurements, the absolute impedance is measured at different frequency values as determined by the experiment. However, the Nyquist plot data representation does not account for the frequency where the impedance was measured. Therefore, another data representation that gives additional frequency information at the measured impedance is needed. The Bodes plot gives the frequency information at the measured impedance [301,302]. Bode data representation is a plot of phase angle (θ) and the logarithms of impedance magnitude (log Z) versus logarithms of frequency (log f). Bodes plot are complementary to Nyquist plot and can further be used to confirm the structural differences between the functionalized and the bare surface. The Nyquist plot gives information about the resistance, that is, charge transfer, solution resistance, capacitance, and Warburg impedance while the Bodes plot gives information about the nature of capacitance.

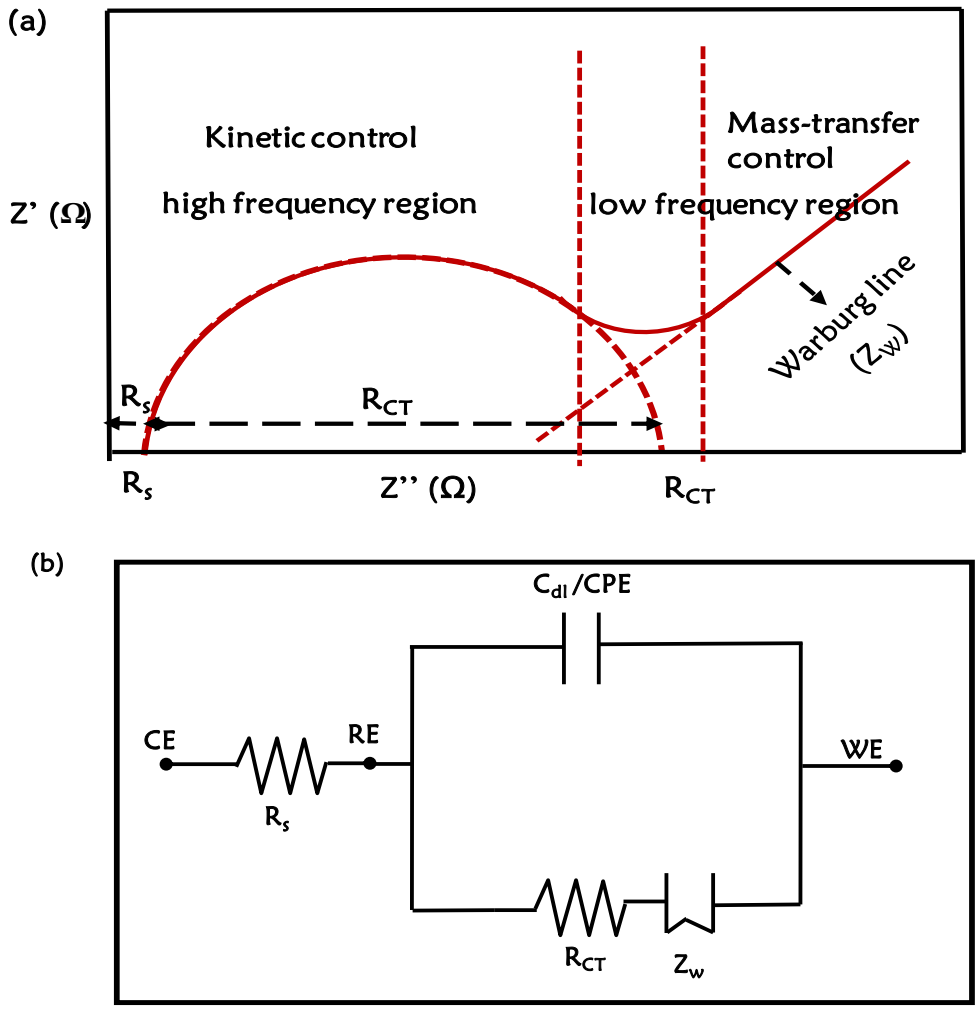

Figure 1.13: Impedance data representation (a) Nyquist plot, and (b) corresponding Randles equivalent circuit. RE: Reference electrode, R_s: Solution or electrolyte resistance, WE: Working electrode, CE: Counter electrode.

The impedance data can be represented and analysed using electrical equivalent circuits. The circuit is made up of simple electrical elements such as resistors (resistance, R) and capacitors (capacitance, C) connected to model the electrochemical process under investigation [300–302]. The resistance within circuit denotes an electrical conductivity of the electrolyte and that of the electrode surface and its modifiers under investigation. The capacitance is either a double layer (C_{dl}) or constant phase element (CPE) arising from excess charge at the electrode-electrolyte interface. In fitting impedance data, the

most widely used electrical circuit is the Randles-Sevcik equivalent circuit presented in **Fig. 1.13(b)** with (a) C_{dl} or (b) CPE capacitance connected.

Solution or electrolyte resistance (R_S) shown by the Randles-Sevcik equivalent circuit are connected in series to the parallel combination of the polarization or charge transfer resistance (R_{CT}) and the double layer capacitance (C_{dl}), **Fig. 1.13(b)** or the constant phase element (CPE). CPE is for the real practical situation, resulting from (i) the nature of the electrode, (ii) material porosity, (iii) dynamic disorder associated with diffusion and (iv) distribution of relaxation times due to heterogeneity occurring at the electrode-electrolyte interface [303]. Another factor to be considered in fitting the impedance data is a situation whereby a transport phenomenon controls the rate of reaction. An additional component that model the diffusion process called the Warburg impedance (Z_w) is introduced. The Warburg impedance influences the conditions of transport or diffusion of electroactive species as shown in **Fig. 1.13(b).** The C_{dl}, R_{CT} (Ω) and Z_w (Ω) represent the reaction occurring on the working electrode (WE) or sensor surface. Rs is the electrolyte resistance between the reference electrode (RE) and the working electrode (WE).

EIS offers several advantages over other characterization techniques, which include: (i) the ability of the system to remain at equilibrium as a result of the use of low-amplitude sinusoidal voltage (about 5 mV), (ii) characterizing interfacial properties in the absence of redox reaction, (iii) acquisition of accurate and repeatable measurements, (iv) high adaptability of this technique to various applications, and (v) rapid acquisition and quantification of data such as ohmic resistance, double layer capacitance, conductivity of the film, as well as charge or electron transfer resistance at the electrolyte-electrode interface and within the film in a single experiment.

1.12.3. XPS: Surface characterization techniques

X-ray photoelectron spectroscopy (XPS) is a highly sensitive and versatile surface characterization technique which gives insight to the type of bond and interaction that exist on a surface [304]. XPS is the most frequently used technique in surface science owing to its wide application [305]. XPS is an electron spectroscopic technique used for the determination of chemical and elemental composition of materials or organic films on metal surfaces [306,307]. The elemental or atomic composition can be evaluated using the XPS survey spectra [308]. The technique is sometimes referred to as electron spectroscopy for chemical analysis (ESCA) and is a well-known method for the analysis of molecular information of organic thin films. XPS is a technique based on a photoelectron effect [306,307] which occurs when the surface is irradiated with X-ray photons. The binding energy of the emitted electron is the characteristics of the atom from which it was ejected and also depend on the chemical environment of the atom. This phenomenon makes the XPS a very sensitive and material analysis technique. The XPS characterization in conjunction with other surface characterization techniques is useful to further confirm surface modifications.

1.12.4. Microscopic surface characterization techniques

1.12.4.1. Scanning electron microscopy (SEM)

Scanning electron microscopy (SEM) is a surface technique that uses a high energy beam of electrons in a raster scan manner to obtain the topographical image and the composition of the sample on the surface. By scanning the surface, the interaction between the electrons (from the electron beam) and the surface occurs, resulting in the deflection of electrons from the sample. The deflected electrons result in a signal that

contains information about the sample topography and composition [309,310]. The electrons are collected by the secondary detector for imaging or backscatter detector for elemental composition. The elemental composition or chemistry of the sample may be obtained with an energy dispersive X-ray spectrometer (EDX) [309,310]. EDX is based on photoelectron effect. It utilizes X-rays that are emitted from the specimen when bombarded by the electron beam to identify the elemental composition of the specimen.

1.12.4.2. Transmission Electron Microscopy (TEM)

TEM is one of the most powerful techniques in material science, which has been broadly used in the characterization of nanomaterials [311]. It can investigate the constitutional features (morphology) of these nanoparticles such as shape, size and particles arrangement, crystallinity and chemical variations at a resolution down to the nanometer scale [312,313]. The operation of TEM is similar to a slide projector. It involves shining a beam of electrons, instead of light, produced from an electron gun. This stream of electrons is focused by a coherent beam that is restricted by a condenser aperture. The beam striking the sample transmits portions of the sample which are focused by the objective lens projected image on the screen. The image presents both dark and light areas. The dark area represents the densely packed section which permits the passage of fewer electrons. On the other hand, the light area is less densely packed section which permit more electron to pass through [314].

1.13. Quartz Crystal Microbalance with Dissipation (QCM-D)

The Quartz Crystal Microbalance (QCM) has been described in the earlier part of this thesis as one of the two mass-sensitive techniques. It is a piezoelectric biosensor which is mass sensitive and allows label free detection of biomolecules. This technique has played a major role in elucidating various aspect of biological materials and their interactions [315]. QCM-D is used in this thesis to establish the immunocomplex formation between anti-CRP antibodies and CRP-antigen. QCM is an ultrasensitive weighing device that measures antibody-antigen reaction in nanograms. It is based on oscillating piezoelectric quartz crystal that resonates at a fundamental frequency with the application of an electrical signal of a specific frequency. Upon protein immobilization the resonance frequency shifts. The major advantage of this technique is the real-time monitoring of adsorbed analyte on the surface of the quartz crystal. Depending on the experiment different materials are used as a surface coating. The surface materials could be platinum coated, gold-coated and these quartz crystals are used as weighing devices (AT-cut crystals). The AT-cut crystals ensure high-temperature stability and pure shear motion when subjected to an electric field. The mechanical resonance (at the applied electric field) is a phenomenon that induces a mechanical strain in a crystal making it oscillate [316]. **Fig. 1.14** shows an illustration for the QCM principle where the thin crystal is sandwiched between a pair of metal electrodes [317–319].

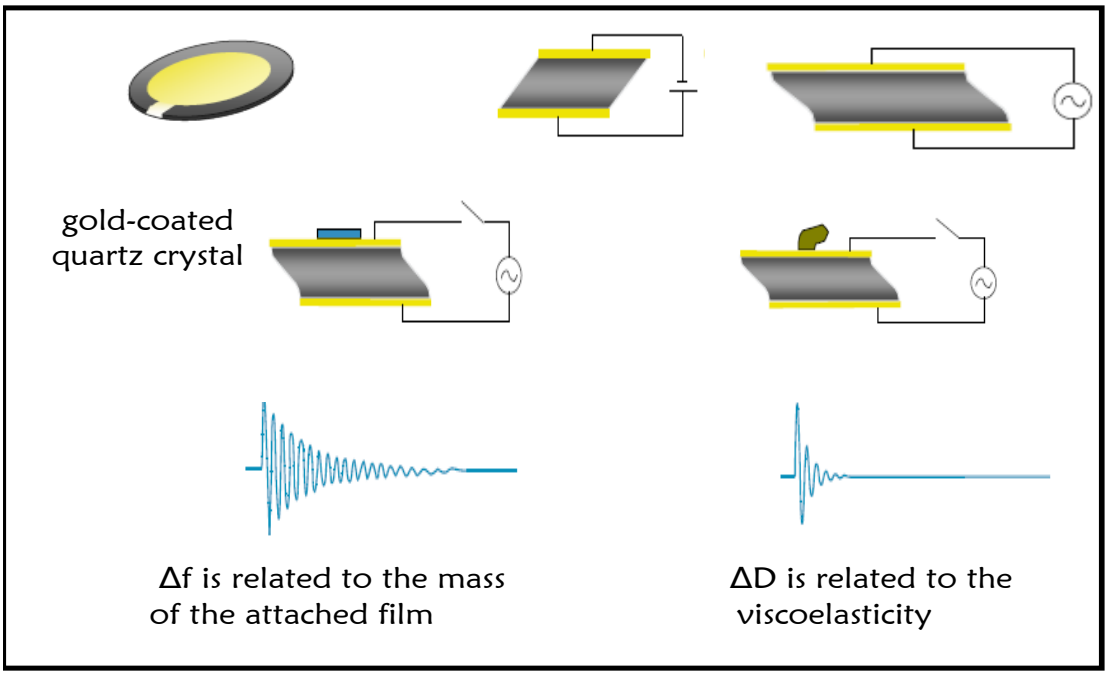

Figure 1.14: Illustration of the QCM-D principle. The Δf (change in frequency) of the oscillating crystal is related to the total oscillating mass, while the ΔD (energy dissipation) is related to the viscoelastic properties of the oscillating mass [320].

The resonating frequency (f_o) of a crystal obtained when the AC voltage is applied, and it corresponds to the frequency of the crystal. This resonance frequency occurs when the thickness of the crystal is an odd integer number (or overtone number) of half-wavelength causing the oscillation to have its antinodes at each electrode interface. The resonance frequency of the crystal is directly proportional to the total mass on the crystal provided that the additional mass (Δm) on the surface results in change of frequency (Δf). The relationship between the frequency and the mass adsorbed was discovered by Sauerbrey and is shown in **Equation (1.3)** [321].

$$\Delta m = -C \frac{\Delta f}{n} \qquad \text{..... (1.3)}$$

where C is the mass sensitivity constant (17.7 ng Hz^{-1} cm^{-2} at an oscillation frequency of 5 MHz or overtone n=1) and n is the overtone number (1, 3, 5, 7, 9…). Sauerbrey **Equation (1.3)** only holds under the following conditions (i) the adsorbed film should be rigid and evenly distributed over the active area of the crystal, and (ii) total mass of the adsorbed film should be small compared to the weight of the crystals. The change in total mass of the crystal (Δm) can be estimated using **Equation (1.3).** The potential use of QCM in liquid or solution phase has increased in a number of applications for QCM in the field of biotechnology [322–328]. For biotechnology applications, other parameters also need to be taken into consideration, and these include (i) non-rigid character of the adsorbed film, and (ii) water molecule trapped between the adsorbed films. These make the analysis difficult as the adsorbed film does not obey Sauerbrey relationship. Therefore, in trying to accommodate these film factors, the technique was upgraded so that it can provide further information such as the change in energy dissipation (ΔD) of the oscillating crystal. In addition to the mass adsorbed the energy dissipation can estimate the viscoelastic properties of the adsorbed layers and the equipment used is called QCM-D. **Figure 1.15** shows the data representation as acquired with the QCM-D, showing both changes in frequency (Δf) and the changes in dissipation (ΔD).

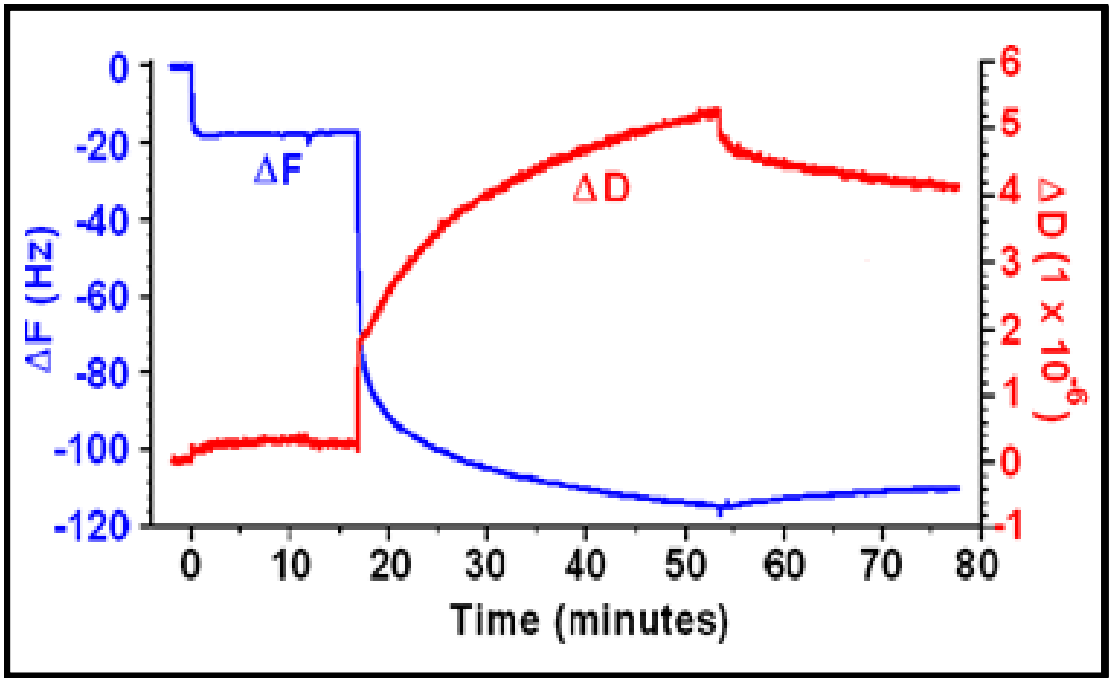

Figure 1.15: Frequency (f) and dissipation (D) shift following the immobilization of biomolecular layer on a gold-coated surface [320].

In this thesis, QCM-D was employed for the real-time monitoring of the reaction occurring at the surface, that is, the mass and structural changes on the quartz crystal surface during the adsorption and the formation of the antibody-antigen immunocomplex. The technique will be useful in estimating the amount, that is, the mass of the adsorbed film, the thickness and the viscoelastic properties of the immobilized molecules.

Summary of the Chapters

The work in this thesis is presented in various chapters:

Chapter 1: Introduction and literature review

This chapter introduces the scourge of Non-communicable diseases (NCDs), cardiovascular diseases (CVDs) as the global leading cause of death, different types of cardiovascular diseases, various methods of CVDs diagnosis, biomarkers for CVDs diagnosis, CRP as a biomarker for inflammation and cardiac damage, different antibody immobilization methods, oriented immobilization of antibody, various sensors and immunosensors, application of magnetic nanoparticles in immunosensors and surface characterization techniques.

Chapter 2: Experimental

This chapter describes the experimental processes and methods employed for the synthesis of magnetic nanoparticles, phenylboronic acid functionalized magnetic nanoparticles, biomolecules, and their immobilization procedure onto the gold electrode surface and gold quartz crystal electrode.

Chapter 3: The design of piezoelectric and electrochemical immunosensor for CRP detection

This chapter investigates the development of piezoelectric and electrochemical immunosensor for CRP detection. The fabrication of the immunosensor was investigated using SAM of 4-Mercaptophenylboronic acid (MPBA) and the immobilization of monoclonal anti-CRP antibody (mAb) to form Au

MPBAmAb/glucose. The characterization of the immunosensor fabrication was achieved. The immunosensor was evaluated for the successful detection of CRP-antigen.

Chapter 4: Impedimetric detection of CRP by coupling of 4-aminophenylboronic onto mercaptobenzoic acid self-assembled monolayer

This chapter investigates the oriented immobilization of anti-CRP monoclonal antibody through the SAMs of 4-mercaptobenzoic acid coupled with boronic acid for the label-free detection of CRP. The surface involved the increased SAM chain length and the effect of that towards the detection of CRP-antigen.

Chapter 5: The development of impedimetric immunosensor using phenylboronic acid functionalized magnetic nanoparticles as a detection nanobioprobe.

This chapter investigates the oriented immobilization of anti-CRP antibody unto succinic anhydride activated phenylethylamine electrografted gold surface via the coupling of 4-aminophenyl boronic acid for CRP detection. The effect of chain length was also investigated. The detection of the CRP-antigen was carried out using antibody conjugated to phenylboronic acid functionalized magnetic nanoparticles as the nanobioprobe.

Conclusion

References

Chapter 6: Appendix

Chapter 2:

Experimental

2.0. Experimental

2.1. Materials and reagents

2.1.1. General

Absolute ethanol (EtOH), iron (III) chloride hexahydrate ($FeCl_3.6H_2O$), 3-aminopropyltriethoxysilane (APTES), N,N-dimethyl formamide (DMF), tetraethoxysilane (TEOS), 28% ammonium hydroxide (NH_4OH), iron (II) chloride tetrahydrate ($FeCl_2.4H_2O$), N-hydroxysuccinimide (NHS), 1-ethyl-3(3-dimethyl aminopropyl)-carbodiimide (EDC), 4- aminophenylboronic acid hydrochloride (APBA), sodium carbonate (Na_2CO_3), glutaric anhydride (GA), sodium bicarbonate ($NaHCO_3$), 4-mercaptobenzoic acid (MBA), ferricyanide ($K_3Fe(CN)_6$), ferrocyanide ($K_4Fe(CN)_6$), potassium chloride (KCl), sodium chloride (NaCl), 4-mercaptophenylboronic acid (MPBA), 4-(2-aminoethyl)phenylamine (APA), succinic anhydride (SA), sodium nitrite ($NaNO_2$), D-glucose, tetrafluoroboric acid (HBF_4), tetrabutylammonium tetrafluoroborate ($TBABF_4$), acetonitrile (ACN), citric acid, 2-N-(morpholino)ethane-sulfonic acid (MES) were purchased from Sigma Aldrich and used as received. Sulphuric acid, hydrogen peroxide (H_2O_2) (30%) were purchased from ACE chemicals (South Africa). Ultrapure water with a resistivity of 18.2 MΩ.cm obtained from Milli-Q water purification system (Millipore Corp, Bedford, USA) was used throughout the experiment.

The phosphate salts were used to prepare phosphate buffer solutions. For electrochemical measurement, the solutions were de-aerated by bubbling argon or nitrogen prior to every experiment, and the electrochemical cell was kept under argon or nitrogen atmosphere. Phosphate buffered saline (PBS, 10 mM) solutions of pH 7.4,

8.0), were prepared using 10 mM KH_2PO_4:K_2HPO_4 and 0.15 M NaCl, the pH adjustments were conducted using 0.10 M of either HCl or NaOH. All chemicals were of analytical grade. The 4-(2-aminoethyl)benzene diazonium tetrafluoroborate (AEBD) used for electrochemical grafting was synthesized according to our previously reported method [329].

2.1.2. Biologicals

Mouse anti-human CRP (MCA5880G, mAb capture antibody), is a monoclonal primary antibody (1° mAb), polyclonal goat anti-human CRP (1707-0189G, pAb detection antibody), native human CRP (1707-2029) were purchased from AbD Serotech. The required concentrations for all biological substances were prepared as per the experimental requirement. All the antibodies studied here are of IgG isotype. New calf serum and glucose purchased from Sigma Aldrich (0.167 μ mol L^{-1}) of the glucose was prepared and used as blocking reagent. For Electrochemical experiments, phosphate buffer saline (PBS) 10 mM KH_2PO_4 and K_2HPO_4 in distilled water pH 7.4 was used. The anti-human CRP monoclonal antibody was used for the fabrication of the electrochemical immunosensors and the detection of CRP antigen. Quartz Crystal Microbalance with Dissipation (QCM-D) was used to establish the formation of antibody-antigen immunocomplex also, to confirm the binding affinity of primary antibody towards the CRP antigen.

2.2. Equipment and methods

2.2.1. General electrochemical methods

All electrochemical measurements were carried out using the AUTOLAB PGSTAT 302N Electrochemical Workstation interfaced to a proline desktop computer equipped with a 1.10 version NOVA. A three-electrode system was used for all the electrochemistry measurement. The electrochemical data was collected using a gold disk electrode as working electrodes (r=0.8 mm) purchased from BASi (USA), platinum wire as counter electrode and silver|silver chloride Ag|AgCl) 3M NaCl solution as reference electrode. Electrochemical Impedance Spectroscopy (EIS) experiments were recorded in the frequency range between 10 kHz to 100 mHz at the half-wave potential ($E_{1/2}$) of 2.0 mM $[Fe(CN)_6]^{3-/4-}$ redox couple for bare gold with an amplitude 5 mV rms sinusoidal modulation.

2.2.2. Microscopic and Spectroscopic equipment and method

2.2.2.1. Energy dispersive X-ray Spectroscopy (EDX)

Energy dispersive X-ray (EDX) analysis spectra were obtained using an X-ray microanalysis system added as a module on the Nova NanoSEM 200.

2.2.2.2. Transmission electron microscopy (TEM)

The images were acquired using JEOL 2100F equipment and the copper grid coated (using drop-dry) with materials to be investigated.

2.2.2.3. X-ray photoelectron spectroscopy (XPS)

Surface composition analysis, for gold-coated crystals modified with SAM and grafted monolayers, was acquired using XPS AXIS Ultra DLD, with Al (monochromatic) anode equipped with a charge neutralizer, supplied by Kratos Analytical. The following parameters were used: the emission was 10 mA, the anode (HT) was 15 kV and the operating pressure below 5 x 10^{-9} torr. A hybrid lens was used and resolution to acquire scans was at 160 eV pass energy in slot mode. The centre used for the scans was 520 eV with a width of 1205 eV, with steps at 1 eV and dwell time at 100 ms as reported before [330]. The high-resolution scans were acquired using 80 eV pass energy in slot mode.

2.2.2.4. X-ray diffraction (XRD)

XRD analysis was performed on a Bruker D8 Discover diffractometer, equipped with a Lynx Eye detector, under Cu-K_α radiation (λ= 1.50405 Å). Data were collected in the range 2θ = 10° to 70°, scanning at 1° min^{-1} with a filter time-constant of 2.5 s per step and a slit width of 6.0 nm. The samples were placed on a zero-background silicon wafer slide. The X-ray diffraction data were treated using the freely-available Eva (evaluation curve fitting) software. Baseline correction was performed on each diffraction pattern by subtracting a spline-fitted to the curved background, and the full-width at half-maximum values used in this study were obtained from the fitted curves.

2.2.3. Quartz crystal microbalance with Dissipation (QCM-D)

QCM-D measurement and frequency change monitoring were performed with the QSense instrument. Mass (frequency) changes on the QSX-301 crystals as reaction carriers were conducted using quartz crystal microbalance with dissipation (QCM-D, QSense, Sweden). The gold coated crystal QSX-301 (Au-CQC, 5 MHz AT-cut) was purchased from QSense, (Sweden).

2.2.4 Other equipments

2.2.4.1. ^{1}H Nuclear Magnetic Resonance (^{1}H NMR)

The proton nuclear magnetic resonance (1H NMR, 400 MHz) spectra were acquired using Bruker AMX NMR spectrometer in either $CDCl_3$ or DMSO-d_6.

2.2.4.2. Fourier transform infrared spectroscopy (FTIR)

Infrared spectra were collected on a Bruker Alpha model FT-IR Spectrometer (4000 - 650 cm^{-1}) or/and Perkin Elmer Spectrum 100 FT-IR Spectrometer (4000 - 400 cm^{-1}) equipped with the diamond – ATR sampler. FT-IR spectra were collected at room temperature 100 scans were taken for each interferogram at 4 cm^{-1} resolution. The spectrum in the air was recorded as the background and automatically subtracted from the sample spectra by the appropriate software (Bruker opus 6.5 software and (Perkin Elmer spectrum one software).

2.2.4.3. Zetasizer Nano series

Zeta potential experiments were measured on a Malvern Zetasizer Nano series, Nano-ZS90.

2.3. Synthesis of magnetic nanoparticles (MNPs)

The magnetic nanoparticles were prepared using previously reported conventional co-precipitation method [331,332] with some modifications. Briefly, iron (III) chloride hexahydrate (4.17 g, 15.42 mmol) and iron (II) chloride tetrahydrate (1.52 g, 7.64 mmol) were dissolved in the degassed Millipore water (80 ml) under argon gas. Ammonium hydroxide (28%, 7.0 ml) was added dropwise. The colour of the mixture turned black from golden yellow. The mixture was stirred at 60 ^{0}C for 3 hours in an argon atmosphere. The magnetic nanoparticles were stabilized by direct addition method using citric acid [333,334]. Citric acid (0.5 g mL^{-1}) was added, and the reaction temperature was raised to 90 $^{\circ}$C. The reaction was made to proceed for 30 mins after the addition of citric acid. The slurry was washed repeatedly with Millipore water, and the particles were magnetically separated from the supernatant and re-dispersed in aqueous solution at least three times. The magnetic nanoparticles were finally dispersed in ethanol, magnetically isolated and dried in vacuum at room temperature. The magnetic nanoparticles are represented as MNPs. IR [(ATR), τ_{max}/cm^{-1}]: 1574 (C=O), 543 (Fe-O).

2.3.1. Silica-coated magnetic nanoparticles (MNP-SiOH)

The bare magnetic nanoparticles (MNPs) were encapsulated with silica for the ease of functionalization. The magnetic nanoparticles (0.26 g) were dispersed in a degassed mixture of absolute ethanol (80 ml) and water (20 ml) followed by ultrasonication of the mixture for 30 minutes. Tetraethoxysilane (0.5 ml) was added to the mixture, and the pH was adjusted to pH 12 using ammonium hydroxide (NH_4OH). The mixture was stirred in an inert argon environment for 12 hours. This was followed by refluxing at

130 ^{0}C for 24 hours. The brown precipitate was separated, washed with distilled water and dried in the vacuum for 24 hours. The silica-coated magnetic nanoparticles are represented as MNP-SiOH IR [(ATR), τ_{max}/cm^{-1}]: 3380 (O-H), 1069 (Si-O-Si), 955 (Si-OH).

2.3.2. APTES functionalized magnetic nanoparticles (MNP-SiO-APTES)

About 0.15 g of the silica-coated nanoparticles and 100 ml of absolute ethanol were ultrasonicated for 30 minutes to form a homogenous colloid suspension. 3-Aminopropyltriethoxysilane (APTES, 0.5 ml) was added to the mixture. The mixture was heated and refluxed in a nitrogen atmosphere at 130 ^{0}C for 7 hours. The precipitate was separated magnetically, and the residue was washed with distilled water and dried in the vacuum for 24 hours. The APTES functionalized magnetic nanoparticles are represented as MNP-SiO-APTES. IR [(ATR), τ_{max}/cm^{-1}]: 3272 (N-H), 1047 (Si-O-Si), 947 (Si-OH).

2.4. Phenylboronic acid functionalized magnetic nanoparticles (MNP-SiO-APTES-PBA)

A novel method was employed for the synthesis of phenylboronic acid functionalized magnetic nanoparticles via two steps. Firstly, 5-(4-boronoanilino)-5-oxo-pentanoic acid (pentanoic acid terminated phenylboronic acid) was synthesized through the reaction of glutaric anhydride and 4-aminophenylboronic acid. The second step involves the amide coupling of the 5-(4-boronoanilino)-5-oxo-pentanoic acid with APTES functionalized magnetic nanoparticles. The procedure is as follows:

2.4.1. Synthesis of 5-(4-boronoanilino)-5-oxo-pentanoic acid

The synthesis of 5-(4-boronoanilino)-5-oxo-pentanoic acid **(3)** was carried out by dissolving 4-aminophenylboronic acid (0.0867 g, 0.50 mmol) in carbonate buffer (5 ml, pH 9.2) and stirred for 30 mins. Glutaric anhydride (0.2853 g, 2.50 mmol) in carbonate buffer (5 ml) was added in drops to the solution. The mixture was stirred continuously for 24 hours at room temperature. 5-(4-Boronoanilino)-5-oxo-pentanoic acid was obtained as white precipitate and was separated and dried at 60 ^{0}C for 24 hours. Yield 56%. IR [(ATR), τ_{max}/cm^{-1}]: 1690 (C=O), 3322 (OH), 1384 (B-O). ^{1}H NMR 400 MHZ (DMSO-d_6, ppm): 12.01 (1H, br s, COOH), 9.92 (1H, s, NH), 7.62 (4H, d, Ar-H), 3.38 (2H, br s, OH) and 2.12 (6H, m, CH_2).

The synthesized 5-(4-boronoanilino)-5-oxo-pentanoic acid **(3)** (20 mg, 0.080 mmol) was dissolved in dry DMF (3ml). Then EDC (10 mg, 0.052 mmol) and NHS (7 mg, 0.060 mmol) were added, and the mixture was stirred for two hours. The APTES functionalized magnetic nanoparticles (MNP-SiO-APTES) (20 mg) dispersed in dry DMF (5 ml) was added to the solution. The resulting solution was stirred for 24 hours and washed several times with absolute ethanol. The residue was magnetically separated and dried under vacuum for 48 hours. The phenylboronic functionalized magnetic nanoparticles are represented as MNP-SiO-APTES-PBA. IR [(ATR), τ_{max}/cm^{-1}]: 1647 (C=O), 1391 (B-O).

2.4.2. Preparation MNP-SiO-APTES-PBA-pAb

The procedure for the preparation of the polyclonal anti-CRP antibody conjugated to phenylboronic acid functionalized magnetic nanoparticles is as follows: The MNP-SiO-APTES-PBA (1 mg) was dispersed in 30 μg mL^{-1} of anti-CRP polyclonal antibody (as a detection antibody). The mixture was shaken at 4^0C for 24 hours. The residue was washed three times with PBS pH 7.4 and was magnetically separated. The brown precipitate was further incubated with glucose (0.167 μ mol L^{-1}) for 3 hours, washed with (PBS, pH 7.4) and was suspended in 1 ml PBS. The antibody functionalized MNP-SiO-APTES-PBA-pAb was stored at 4^0C for further use.

2.5. Electrodes pretreatment and their modification

2.5.1. Electrode pretreatments

Prior to electrode modification, the electrode surfaces were cleaned using reported methods for gold [335,336]. Briefly, the gold disk electrode was first polished using an aqueous slurry of alumina (<10 um) on a SiC-emery paper (type 2400 grit), and then to a mirror finish on a Buehler felt pad with alumina slurries (1, 0.5, 0.03 μm). The electrode was then rinsed with a copious amount of deionized water and then placed in ethanol and subjected to ultrasonic vibration to remove residual alumina particles that might be trapped on the surface. After this mechanical treatment, the gold electrode was chemically treated by etching for about two minutes in a piranha solution {3:1 (v/v) 30 % H_2O_2 and concentrated H_2SO_4}. Then rinsed with copious amounts of distilled water or ultra-pure Milli-Q water followed by ethanol. The chemical treatment with piranha solution serves to remove the organic contaminants on the gold electrode surface. To ascertain the cleanliness of the bare electrode surface, the electrode was

placed in 0.5 M H_2SO_4 and scanning the potential between -0.2 and 1.5 V (versus Ag|AgCl reference) at a scan rate of 100 $mV.s^{-1}$ until reproducible scans were obtained.

2.5.2. Electrode modification: Self-assembly monolayer (SAMs) and electrografting

The modification of electrode was achieved by forming a self-assembled monolayer (SAMs) of 4-mercaptophenylboronic acid MPBA or 4-mercaptobenzoic acid onto a gold surface. The SAMs were represented as Au-MPBA-SAM or Au-MBA-SAM. The SAMs were allowed to form for 24 hours, and the modified electrodes were first rinsed with ethanol and water to remove any physically adsorbed MPBA or MBA compounds. The second method of modification was the electrochemical grafting of AEBD salt in acetonitrile solution containing 0.1 M $TBABF_4$ onto the gold electrode. The fabrication process was fully described in **section 2.6.2.**

2.6. C-reactive protein immunosensor design

The design of immunosensor for the detection of CRP antigen was achieved via the two methods described above. Both methods afforded the oriented immobilization of the capture antibody (anti-CRP monoclonal antibody). The synthesis of the AEBD salt used for the electrografting and the procedure for the covalent attachment of the monoclonal anti-CRP antibody are discussed below.

2.6.1. Synthesis of 4-(2-aminoethyl) benzene diazonium (AEBD) salt

4-2-(Aminoethyl) benzene aniline (15 mmol) was dissolved in tetrafluoroboric acid (HBF_4 40 %, 3 ml) diluted with water (2 ml). The mixture was allowed to cool in an acetone-ice bath for 15 mins under vigorous stirring. The ice solution of sodium nitrite (20 mM, 1 ml) was added dropwise into the aniline solution under stirring. The reaction was left stirring for about 50 mins. The precipitate formed was filtered. The precipitate

was dissolved in acetone (1 ml) and cooled in an acetone-ice bath with the gradual addition of diethyl ether to reprecipitate the AEBD salt as a dark brown solid. The residue was washed with cold diethyl ether, dried under vacuum and kept in the dark at -20 °C. IR [(ATR), τ_{max}/cm^{-1}]: 3269 (N-H), 3111 (C-H), 2286 (N≡N), 1590, 1620, 1498, 1474, 1430, 1198 and 1320 (C-N).

2.6.2. Covalent immobilization of CRP antibody

The attachment of CRP antibody unto gold electrode surface was achieved via three methods. The immobilization of the capture antibody for anti-CRP monoclonal antibody was accomplished by immersing the Au-MPBA SAM electrode into (mAb, 30 μg mL^{-1} pH 7.4) for 24 hours via the boronate ester reaction. The unreacted boronic acid reactive surfaces from the Au-MPBA-mAb was blocked with glucose (0.167 μ mol L^{-1}), and the electrode is represented as Au-MPBA-mAb/glucose.

The second method involved the use of Au-MBA-SAM. The terminal -COOH group of the MBA SAM reacted with the amino functional group of 4-aminophenyl boronic acid (APBA) using amide coupling reaction. The carboxylic acid of the Au-MBA SAM was activated in 0.40 mol L^{-1} of EDC and 0.10 mol L^{-1} of NHS in 10 mmol L^{-1} PBS pH 7.4 solution for two hours. The electrode was further rinsed with water and dried with argon gas. The EDC/NHS activated electrode was then immersed in a pH 7.4 PBS solution containing 25 mmol L^{-1} 4-aminophenyl boronic solution. After 6 hours, the resulting phenylboronic acid electrode, represented as Au-MBA-APBA SAM was rinsed with water and ethanol to remove unreacted 4-aminophenyl boronic acid. The Au-MBA-APBA SAM was further dried under argon atmosphere. The Au-MBA-APBA SAM was immersed into 10 µl mouse anti-human CRP pH 7.4 solution (30 μg mL^{-1}) at 4 °C for 24 hours to give the Au-MBA-APBA-mAb. The antibody-modified gold electrode

was washed with PBS (pH 7.4) to remove the unbound antibodies. The blocking of non-specific adsorption site was accomplished by immersing the Au-MBA-APBA-mAb in D-glucose (0.167 μ mol L^{-1}) in pH 7.4 PBS at room temperature for 2 hours to yield an Au-MBA-APBA-mAb/glucose surface. The Au-MBA-APBA-mAb/glucose electrode was rinsed with pH 7.4 PBS and stored at 4 ^{0}C before use.

The third method was achieved by the electrografting method. Briefly, the gold electrode surface was modified by electrochemical grafting of 1.0 mM AEBD diazonium salt in acetonitrile solution containing 0.1 M $TBABF_4$. The cyclic voltammogram was scanned from +0.4 V to -0.4 V. Three cycles or scan were used for the electrografting, and the phenylethylamine layer was obtained, Au-PEA. The Au-PEA was further reacted with succinic anhydride (5 %) in DMF solution for 4 hours to yield carboxylic acid functionalized gold surface, Au-PEA-SA. The Au-PEA-SA surface was activated using EDC/NHS to yield a reactive amine surface, Au-PEA-SA-EDC/NHS. The Au-PEA-SA-EDC/NHS was used to immobilize 4- aminophenylboronic acid (25 mmol L^{-1}), Au-PEA-SA-APBA. The Au-PEA-SA-APBA surface was used to immobilize the monoclonal anti-CRP antibody (mAb, 30 μg mL^{-1}) via the boronic ester reaction. The boronic ester reaction occurred between the boronic acid functionalized electrode and the glycosylated Fc of the mAb to yield Au-PEA-SA-APBA-mAb. The non-specific binding site was blocked by exposing the Au-PEA-SA- APBA-mAb to pH 7.4 of glucose solution (0.167 μ mol L^{-1}) to yield an immunoelectrode, Au-PEA-SA-APBA-mAb/glucose.

2.6.3. Quartz Crystal Microbalance with Dissipation (QCM-D) measurements

2.6.3.1. QCM-D and SAM functionalization

Prior to QCM-D measurement, the crystals were pretreated by first rinsing in absolute ethanol and dried in nitrogen. The crystals were cleaned using the reported method [322,337,338]. Briefly, the crystals were cleaned by immersing the gold-coated quartz crystal (AuCQC) in the solution of H_2O:H_2O_2:NH_3 in the ratio 5:1:1 and heated to 75 ^{0}C for 5 mins. The AuCQC-MPBA SAM were thoroughly rinsed with water and dried under nitrogen gas and then exposed to (UV-O) for 5 minutes. The crystals were immersed in the solution of 4-mercaptophenylboronic acid (4-MPBA) for 24 hours to form a self-assembled monolayer (SAM) onto a gold plate. The AuCQC-MPBA SAM was further used to follow the immobilization of mouse monoclonal anti-CRP antibody and blocking of non-specific binding by glucose solution. The functionalized gold-coated quartz crystal surfaces were used for QCM-D studies, i.e. AuCQC-MBPA-mAb/glucose.

2.6.3.2. CRP antibody immobilization monitoring with QCM-D

The QCM-D analysis took place under the following parameters: 25 ^{0}C temperature and flow rate of 50 μ mL^{-1}. Following the pretreatment and the functionalization of the AuCQC with 4-mercaptophenylboronic acid SAM electrode represented as AuCQC–MPBA SAM in **Scheme 3.1**, the QCM-D experiment was then commenced. The mouse monoclonal anti-CRP antibody (30 μg mL^{-1}) layer was immobilized onto the 4-mercaptophenylboronic acid functionalized gold surface. The change in frequency (Δf) and energy dissipation (ΔD) was obtained. The blocking of non-specific binding was achieved by using glucose (0.167 μ mol L^{-1}) and this was represented as (AuCQC-MPBA-

mAb/glucose) in **Scheme 3.1.** The interaction of the immobilized CRP antibody with the CRP-antigen was achieved by flowing different concentrations of CRP-antigen solution (10 – 400 ng mL^{-1}) onto an AuCQC-MPBA-mAb/glucose surface represented in the scheme as (AuCQC-MPBA-mAb/glucose-CRP antigen).

2.6.3.3. QCM-D data acquisition, analysis, and fitting

The changes in frequency (Δf) and dissipation (ΔD) were obtained by periodically switching off the driving power of the oscillation of the sensor crystal and by recording the decay of the damped oscillation. The time constant of the decay is inversely proportional to D, and the period of the decaying signal gives f. The noise level of f and D factor with liquid loads are 0.3 Hz and 2 x 10^{-7}, respectively. The Sauerbrey sensitivity of this crystal is 1 Hz C = 17.7 ng.cm^{-2}. The frequency and dissipation responses were recorded using overtones (n=3, 5, 7, 9, and 11). For the analysis, the frequency and dissipation data for 7^{th}, 9^{th}, and 11^{th} overtones or harmonics were used. Data at other overtones are included for the modelling of the effective mass loading, effective thickness and shear viscosity using Kevin-Voigt model [322,337,338]. During the measurements, the crystals were fixed in a flow cell allowing the solution to flow through only one side of the crystal. The flow cell was used to evaluate the analytical response. The biomolecules studied were prepared in 10 mmol L^{-1} phosphate buffer saline (PBS, pH 7.4) solution. Parameters for the Kevin-Voigt model were set to have the viscousity (kg.ms^{-1}) between 0.01 and 100, the shear force (Pa) between 1000 and 1 x 10^{9}, and the film thickness (m) forced between 1 x 10^{-11} and 1 x 10^{-6}. The film density on the gold surface was assumed to be 1100 kg.m^{-3}. From QCM-D frequency and dissipation data, the deposited layer thickness, d, was calculated using Voigt viscoelastic

modelling for a film in liquid and was fitted using Q-Sense software (Q-Tools) with built-in equations. The fitting results can be generated automatically for the user.

List of publications

Section of this thesis that has been submitted and is in preparation for publication in peer review journals.

1. **Adesina, A.O.,** Mashazi, P.N., Direct and indirect impedimetric immunoassays for the detection of C-reactive protein and signal amplification. Biosensor and Bioelectronics (submitted).
2. **Adesina, A.O.,** Adeniyi, O.K., Mashazi, P.N. Design of piezoelectric and electrochemical immunosensor for the detection of C-reactive protein. Talanta (to be submitted).
3. **Adesina, A.O.,** Mashazi, P.N. Electrochemical impedimetric detection of C-reactive protein using phenylboronic acid functionalized magnetic nanoparticles as nanobioprobe. Sensor and Actuators B (to be submitted).
4. **Adesina A.O.,** Adeniyi, O.K., Mashazi, P.N. A review of oriented immobilization of antibodies and enhanced detection of biomarkers for diagnostic applications. Chemical Review (in preparation).

Section of this thesis have been presented at the following scientific conferences and symposiums.

1. **Adesina, A.O.,** Mashazi, P.N. Quartz crystal microbalance biosensor for selective and sensitive detection of C-reactive protein. (The 8th Interdisciplinary Postgraduate Conference (IPGC), Grahamstown, South Africa, 26th to 29th, September 2017; National symposium; Oral presentation).
2. **Mashazi, P.N.** Adesina, A.O., Adeniyi, O.K. Oriented immobilization of antibodies and enhanced detection of biomarkers in the resource-limited settings. (28th Anniversary of World Congress on Biosensors, Biosensor 2018, Miami, Florida, USA, 12th to 15th June 2018; International Conference; Poster Presentation)

Chapter 3:

Piezoelectric and Electrochemical Impedimetric Immunosensor using (Au-MPBA SAM)

3.0. Preamble

The next three chapters investigate the piezoelectric and impedimetric label-free detection of CRP. The differences in each chapter is the method of immobilizing the anti-CRP monoclonal antibody by varying the chain-length of SAMs and electrografted gold surface. The similarity of the chapters is the boronic acid functionality for the oriented attachment of anti-CRP monoclonal antibody.

This chapter describes the investigation and fabrication of a piezoelectric and impedimetric immunosensors for the detection of C-reactive protein. The use of the QCM-D for the real-time capture of recognition element (mAb) and the evaluation of the CRP-antigen detection. The QCM-D allowed us to follow in real time the attachment of anti-CRP monoclonal antibody as capture antibody onto a gold-coated quartz crystal (AuCQC) of a 5 MHz AT-cut piezoelectric crystal. The formation of a self-assembled monolayer (SAM) of 4-mercaptophenylboronic acid was accomplished ex-situ due to the incompatibility of the QCM-D tubing to organic solvents. Two different immunoassay formats (direct and sandwich immunoassay) were used to investigate the immunosensor performance and to establish the formation of the immunocomplex between the anti-CRP monoclonal antibody and the CRP-antigen. In the direct immunoassay format (DIA), the CRP antigen binds directly to the capture antibody (CRP mAb), and the change in frequency and dissipation were recorded. The antibody-antigen interaction generates a signal which can be correlated to the concentration of the analyte in the sample. The same procedure was followed in the sandwich immunoassay (SIA). The last step of the SIA utilizes the capturing of the polyclonal anti-CRP antibody (pAb) after CRP-antigen immunoreaction. Using the polyclonal antibody afforded the detection of CRP antigen with an enhanced signal. The antigen is

sandwiched in between two antibodies, and the signal is generated. However, in ELISAs the second antibody or the detection antibody is labelled with an enzyme or fluorophore. This method was employed in this thesis as the enzyme labelled polyclonal antibody was expensive to fabricate. QCM-D is a label-free technique that does not require any labelled second antibody. The binding of the detection antibody with the immobilized antibody-antigen immunocomplex brings about a shift in the frequency of the quartz crystal which is related to the mass of the adsorbed molecule.

The developed protocol was translated onto a gold electrode for the impedimetric detection of CRP-antigen. Cyclic voltammetry and electrochemical impedance spectroscopy were used to investigate the fabrication steps of the immunosensor and immunochemical reaction between the surface-bound antibody and the antigen. The impedance change due to antibody-antigen interaction at the surface of the immunosensor was utilized for the detection of CRP.

The major challenges of immunosensor in real application is their specificity and selectivity towards the analyte of interest. In this work, the oriented immobilization of anti-CRP monoclonal antibody for the detection of CRP-antigen is investigated. The method of choice involves the use of boronic acid functional group exposed onto the surface of the electrode to target Fc carbohydrate. This method allows for the oriented immobilization of the antibody. **Scheme 3.1** shows the step-by-step immobilization method.

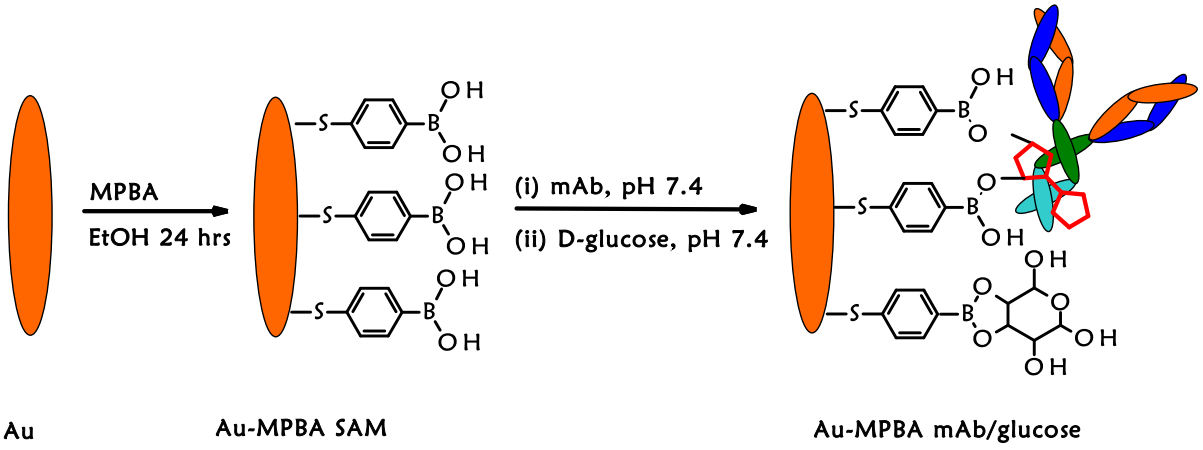

Scheme 3.1: Step-by-step oriented immobilization of monoclonal mouse anti-human CRP antibody (mAb) onto QCM-D sensor chips using affinity boronate ester interaction.

3.1. Piezoelectric immunosensing of CRP-antigen

The MPBA modified crystal was fixed in a flow cell allowing the solution to flow through only one side of the crystal. The flow cell was used to evaluate the analytical response. Firstly, previously degassed buffer solution was passed through a chamber by the peristaltic pump at a flow rate of 50 μl.min^{-1} until a stable baseline was obtained for the buffer. Monoclonal antibody (mouse anti-human CRP, 30 μg mL^{-1}) was flowed into the sensor chamber. The shift in frequency was recorded as a function of time. After this, a running buffer was flowed through the chamber to remove any physically adsorbed antibody. Glucose solution was flowed to block the unreacted boronic acid groups. This was further followed by rinsing with buffer to remove the unreacted glucose. After obtaining a steady state resonant frequency, varied CRP-antigen concentration ranging from 10 - 400 ng mL^{-1} was allowed to flow into the sensor surface, and the frequency shift and dissipation were also recorded. CRP detection polyclonal antibody (goat anti-human 30 μg mL^{-1}) was used for the sandwich

immunoassay. The change in frequency (Δf) was recorded as a function of the antigen concentration. Running buffer was injected to obtain a stable baseline.

3.2. Sensor surface regeneration

The reusability of the sensor chips for real-time analysis was demonstrated through online regeneration of the sensor surface using 100 mmol L^{-1} HCl solution. The efficiency of the regeneration solution was studied by flowing the solution through the surface of the sensor chip breaking the antibody-antigen immunocomplex without causing any deformation to the surface of the capture antibody.

3.3. Results and Discussion

3.4. Immobilization of mAb-CRP

QCM-D was used to validate the biomolecular interaction, specific recognition and real-time monitoring of antibody-antigen reaction. The formation of anti-CRP antibody-CRP-antigen immunocomplex was established after the surface-bound anti-CRP antibody (1° mAb) recognizes CRP antigen in solution. According to Sauerbrey, a linear relationship exists between the observed frequency changes which is proportional to the mass of the captured analyte. The amount of CRP antibody molecule on the surface of the sensor chips can be calculated using **Equation (1.3)** as previously discussed in chapter one (**section 1.13)**. The resonant frequency and dissipation changes during the immobilization of the antibody (mAb) and blocking of the non-specific binding sites and antigen and antibody interactions is shown in **Fig. 3.1.**

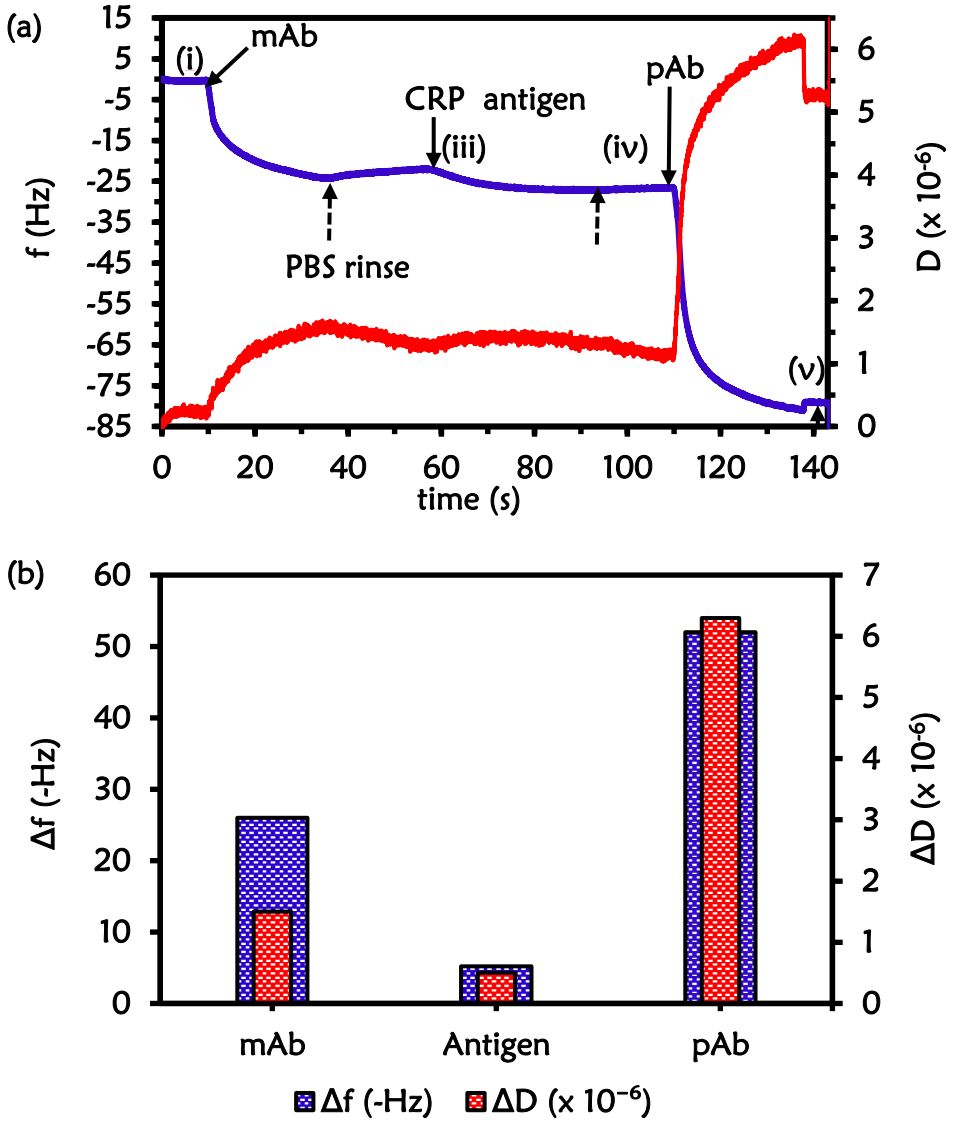

Figure 3.1: (a) QCM-D showing frequency and dissipation changes (i) immobilization of anti-CRP monoclonal antibody, (ii) buffer rinse (black dotted arrow) (iii) CRP-antigen capture (iv) polyclonal antibody exposure, and (v) buffer rinse (b) Corresponding chart showing the frequency and dissipation changes.

Fig. 3.1 shows the response of the QCM-D during the immobilization of anti-CRP monoclonal antibody and its interaction with CRP-antigen on the modified sensor surface. The immobilization of the mouse anti-human CRP antibody resulted in the -26 Hz decrease in the frequency. This confirmed that the anti-CRP antibody was covalently

attached onto the sensor surface. The following Δf and (ΔD, in brackets) values were obtained -26 Hz (1.5 x 10^{-6}), -5.2 Hz (5.0 x 10^{-7}), and -52 Hz (6.3 x 10^{-6}) obtained for monoclonal CRP antibody (mAb, 25 μg mL^{-1}), CRP-antigen and polyclonal anti-CRP antibody (pAb, 30 μg mL^{-1}). The observed frequency shift (-26 Hz) is an indication of the monoclonal anti-CRP antibody attachment to the sensor surface did not significantly change during the PBS rinse. This suggests that most of the anti-CRP antibody is irreversibly bound to the sensor surface. A frequency decrease of approx. ~5.2 Hz was observed upon the immobilization of the 60 ng mL^{-1} CRP-antigen and there was no significant decrease with the PBS rinse. This confirms that the oriented immobilization of the anti-CRP antibody binds the CRP antigen in an irreversible manner. The observed changes were enough to confirm the interaction between the CRP antibody (1° mAb) and the antigen thereby confirming the immunocomplex formation. The changes in frequency caused by the binding of the CRP-antigen with the first antibody was enhanced using sandwich immunoassay. Using the polyclonal antibody afforded the detection of CRP-antigen and signal enhancement. For the sandwich immunoassay, upon the immobilization of the polyclonal antibody. A significant increase was observed in the frequency (-52 Hz). Similar case was reported in a sandwich immunoassay using the mass-amplified second anti-CRP antibody [339]. The polyclonal anti-CRP antibody (pAb) that recognises different epitopes on the captured CRP-antigen and was used for the signal amplification. The low frequency for CRP antigen is attributed to the use of the monoclonal antibody. The high frequency of the polyclonal antibody recognizing CRP antigen is the fact that the polyclonal recognizes multiple epitopes.

3.5. Piezoelectric detection of CRP-antigen

Direct and sandwich immunoassay formats were used to evaluate the immunocomplex formation between the CRP-mAb and the antigen on the QCM-D sensor chips. The QCM-D sensor was exposed to different concentrations of antigen ranging from (10 - 400 ng mL^{-1}). The frequency shift obtained for different antigen concentrations for the direct and sandwich immunoassays is presented in **Fig. 3.2(a) and 3.2(b).** The change in frequency and dissipation (ΔD, in brackets) for the direct immunoassay (antigen capture) gave the values of about -1.54 Hz (0.61 x 10^{-7}) for 10 ng mL^{-1}, -2.9 Hz (0.24 x 10^{-6}) for 25 ng mL^{-1}, -5.24 Hz (0.33 x 10^{-6}) for 50 ng mL^{-1}, -7.7 Hz (0.4 x 10^{-6}) for 75 ng mL^{-1}, -10.2 Hz (0.62 x 10^{-6}) for 100 ng mL^{-1}, -8.8 Hz (0.48x 10^{-6}) for 200 ng mL^{-1} and -8.4 Hz (0.46 x 10^{-6}) for 400 ng mL^{-1}. The frequency change and dissipation for the sandwich immunoassay, polyclonal antibody signal gave -30 Hz (1.85 x 10^{-6}) for 10 ng mL^{-1}, -37.4 Hz (1.88 x 10^{-6}) for 25 ng mL^{-1}, -53 Hz (2.61 x 10^{-6}) for 50 ng mL^{-1}, -68 Hz (3.11 x 10^{-6}) for 75 ng mL^{-1}, -78.4 (3.25 x 10^{-6}) for 100 ng mL^{-1}, -74.2 Hz (3.33 x 10^{-6}) for 200 ng mL^{-1} and 70.1 Hz (3.31 x 10^{-6}) for 400 ng mL^{-1}. The change in frequency increased linearly with an increasing antigen concentration up to 100 ng mL^{-1} for both DIA and SIA immunoassays. A decrease in frequency was observed at higher antigen concentrations (200 and 400 ng mL^{-1}) for the direct and sandwich immunoassays. The decrease in frequency observed at higher concentrations is attributed to the excess amount of CRP-antigen competing for the same binding site. This competition results in the loss of binding efficiency between the immobilized anti-CRP monoclonal antibody and CRP-antigen. The same phenomenon has been reported before for antibody-antigen reaction [340].

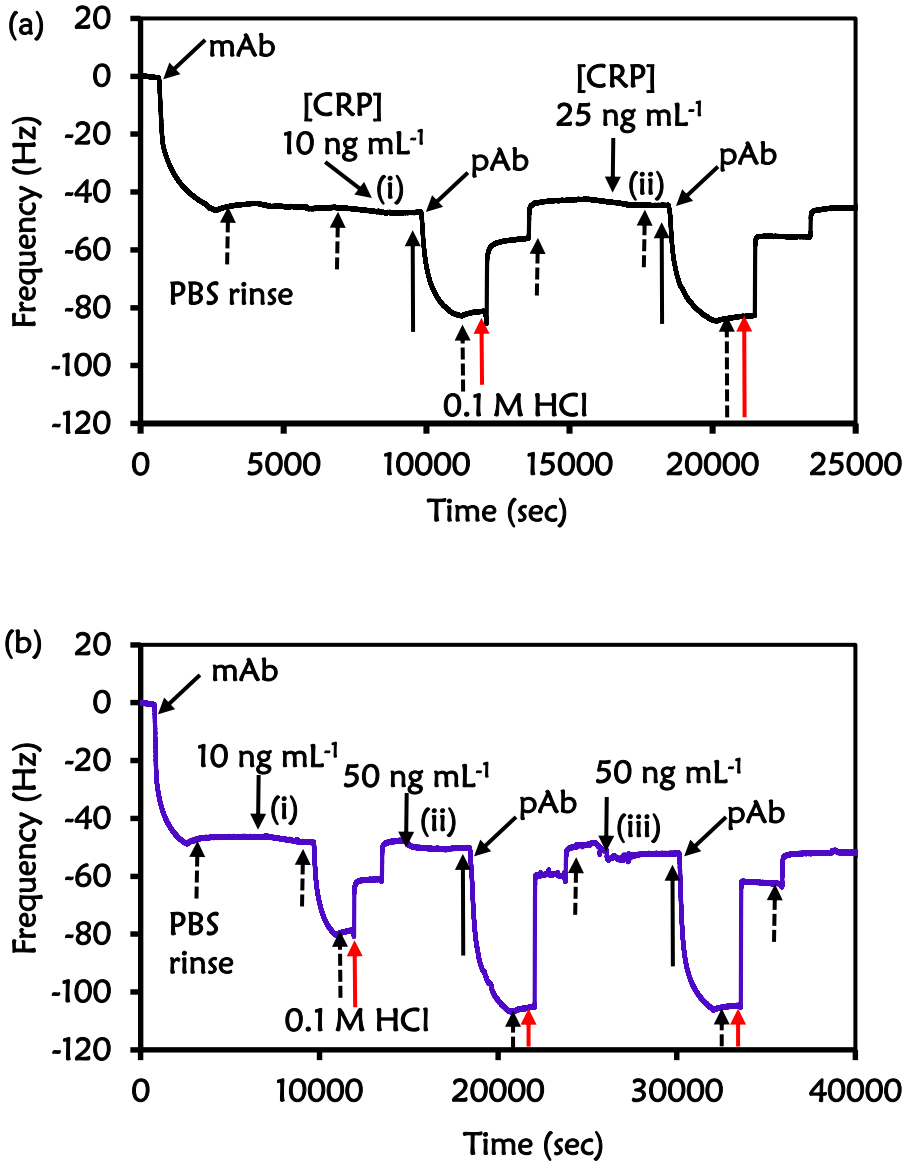

Figure 3.2(a & b): QCM-D sensorgram for different CRP antigen concentrations: (i) 10 ng mL^{-1}, (ii) 25 ng mL^{-1}, and (iii) 50 ng mL^{-1} the red arrows are due to surface regeneration; dotted black arrows indicate buffer rinse, undotted black arrow indicates the amplified signal by pAb.

The bar chart and the calibration curves for DIA and SIA are shown in **Fig. 3.3.** The linear equations for DIA and SIA are **(3.1)** and **(3.2)**, respectively:

DIA: Δf (Hz) = 0.0963 [CRP] + 0.5008 ……. **(3.1)**

SIA: Δf (Hz) = 0.5519 [CRP] + 22.62 ……. **(3.2)**

The regression line coefficient (R^2) for the DIA was 0.999 and for SIA 0.995. The R^2 are close to 1 indicating a very good correlation between the measured signal (Δf) and the CRP concentration. The key parameters for evaluating an analytical method performance are the limit of detection (LoD) and limit of quantification (LoQ). The LoD, and the LoQ were calculated using the IUPAC methods of 3 x SD/m and 10 SD/m respectively. Where m is the slope of the calibration curve and SD is the standard deviation of the blank measurement without the presence of the analyte. The LoD and LoQ were calculated to be 5.72 and 19.09 ng mL^{-1} for the DIA, 3.84 and 12.81 ng mL^{-1} was obtained for the SIA.

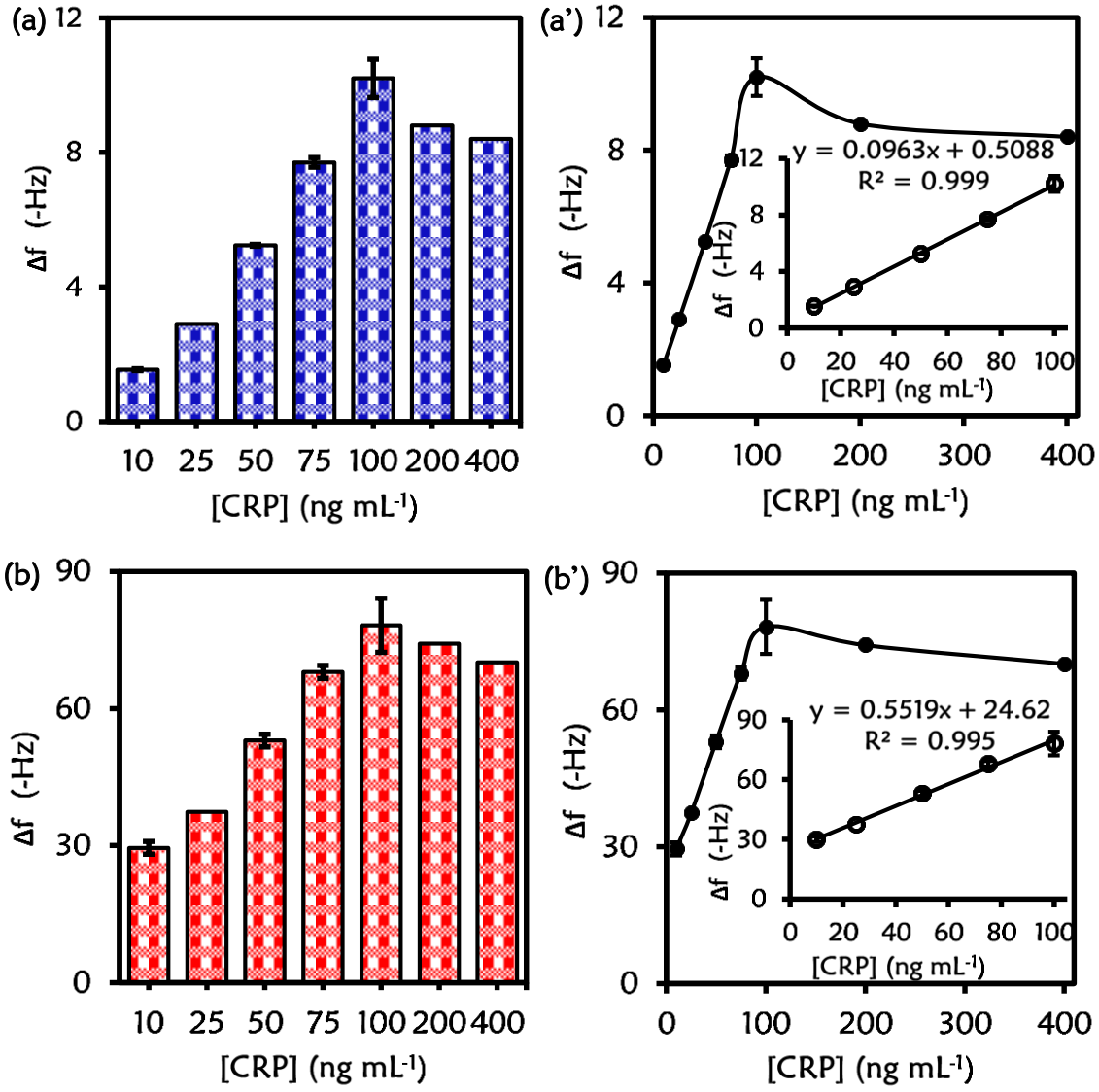

Figure 3.3: Bar chart showing the QCM-D, response (Δf) and the corresponding calibration curve for CRP concentration ranging from 10 – 400 ng mL^{-1} for (a) direct and (b) sandwich immunoassay.

Table 3.1 shows the mass uptake for different CRP-antigen concentrations ranging from 10 – 400 ng mL^{-1} for the DIA and SIA immunoassays. The amount of mass attached was obtained using the Kelvin-Voigt model and Sauerbrey model (brackets), and the following values were obtained in $ng.cm^{-2}$. For the DIA, 40.00 (27.25) for 10 ng mL^{-1}, 80.00 (51.33) for 25 ng mL^{-1}, 110.00 (92.97) for 50 ng mL^{-1}, 255.00 (136.30) for 75 ng mL^{-1}, 350 (180.54) for 100 ng mL^{-1}, 300.00 (155.80) for 200 ng mL^{-1} and 270.00 (148.68) for 400 ng mL^{-1}. The mass attached for the SIA found was 740.00 (525.00) for 10 ng mL^{-1}, 940.00 (662.00) for 25 ng mL^{-1}, 1080.00 (938.1) for 50 ng mL^{-1}, 1370.00 (1203.60) for 75 ng mL^{-1}, 1510.00 (1384.14) for 100 ng mL^{-1}, 1470 (1313.34) for 200 ng mL^{-1} and 1440.00 (1240.77) for 400 ng mL^{-1}. The amount of mass attached increased with increase in the concentration of the CRP-antigen. At higher concentration of the CRP-antigen (>100 ng mL^{-1}), a decrease in the mass uptake was observed. This could be attributed to the saturation of the electrode surface at higher antigen concentration. The same trend has been reported in the literature [232]. The estimated values obtained for the mass uptake for the DIA and SIA were higher for the Kelvin-Voigt fitting model compare to Sauerbrey's model. The reason for the difference in mass was attributed to the fact that Sauerbrey assumes a rigid mass attached to the crystal surface. However, the Kelvin-Voigt mass takes into account the viscoelastic properties of the adsorbed materials. Hence, the Kelvin-Voigt model for mass estimation is more realistic. The Sauerbrey mass calculations underestimate the mass and does not account for the mass of water molecules trapped within the film.

The film thickness (nm) was also calculated using the Sauerbrey and Kelvin-Voigt model at different CRP concentrations (10 – 400 ng mL^{-1}) for the DIA and the SIA, the Sauerbrey values in the bracket. The film thickness for the DIA were found to be 0.11 (0.07) for

10 ng mL^{-1}, 0.20 (0.12) for 25 ng mL^{-1}, 1.10 (0.30) for 50 ng mL^{-1}, 1.24 (0.79) for 75 ng mL^{-1}, 4.30 (1.96) for 100 ng mL^{-1}, 3.00 (1.62) for 200 ng mL^{-1} and 2.60 (1.34) for 400 $ng.ml^{-1}$. For the SIA the film thickness was estimated to be 7.50 (5.60) for 10 ng mL^{-1}, 8.00 (6.93) for 25 ng mL^{-1}, 10.00 (7.92) for 50 ng mL^{-1}, 13.58 (11.98) for 75 ng mL^{-1}, 15.10, (14.36) for 100 ng mL^{-1}, 14.80 (13.62) for 200 ng mL^{-1} and 14.50 (13.21) for 400 ng mL^{-1}. An increase in film thickness was observed with the antigen concentrations immobilized onto the surface of the quartz crystal up to 100 ng mL^{-1}. The estimated film thickness values for the Kelvin-Voigt model was higher at different antigen concentrations than the values obtained from Sauerbrey's model. The higher values obtained for the Kelvin-Voigt was attributed to the fact Kelvin-Voigt account for the viscoelastic parameters of the adsorbed materials.

The Kelvin-Voigt model was used to calculate the viscosity of the CRP-antigen at different concentrations shown in **Table 3.1**. The viscosity was calculated for the DIA to be 5.9×10^{-5} for 10 ng mL^{-1}, 7.9×10^{-5} for 25 ng mL^{-1}, 8.6×10^{-5} for 50 ng mL^{-1}, 1.7×10^{-4} for 75 ng mL^{-1}, 2.9×10^{-4} for 100 ng mL^{-1}, 1.8×10^{-4} for 200 ng mL^{-1} and 1.3×10^{-4} for 400 ng mL^{-1}. For SIA the viscosity was estimated to be 6.2×10^{-4} for 10 ng mL^{-1}, 9.1×10^{-4} for 25 ng mL^{-1}, 1.03×10^{-3} for 50 ng mL^{-1}, 1.5×10^{-3} for 75 ng mL^{-1}, 2.5×10^{-3} for 100 ng mL^{-1}, 2.0×10^{-3} for 200 ng mL^{-1} and 1.7×10^{-3} for 400 ng mL^{-1}. The viscosity of the CRP-antigen increases with increase in antigen concentration for both the direct and sandwich immunoassays. At higher antigen concentration (>100 ng mL^{-1}) the viscosity tends to reduce. This observation was similar to the result obtained for mass uptake.

Table 3.1: Kelvin-Voigt and Sauerbrey parameters obtained from Q-tools modelling software for different [CRP] using Au-MPBA-mAb/glucose. [pAb] = 30 μg mL^{-1}.

	Kelvin-Voigt			Sauerbrey	
Immobilized layer	Viscosity (kg.ms^{-1})	Mass/area (ng.cm^{-2})	Thickness (nm)	Mass/area (ng.cm^{-2})	Thickness (nm)
CRP (10 ng mL^{-1})	0.000059	40.00	0.11	27.25	0.07
Δf_7= -1.54 Hz					
ΔD_7= 0.61x10^{-7}					
pAb	0.00062	740.00	7.50	525.00	5.60
Δf_7= -30 Hz					
ΔD_7 = 1.85x10^{-6}					
CRP (25 ng mL^{-1})	0.000079	80.00	0.20	51.33	0.12
Δf_7= -2.9 Hz					
ΔD_7= 0.24x10^{-6}					
pAb	0.00091	940.00	8.00	662.00	6.93
Δf_7= -37.4 Hz					
ΔD_7 = 1.88x10^{-6}					
CRP (50 ng mL^{-1})	0.000086	110.00	1.10	92.75	0.30
Δf_9= -5.24 Hz					
ΔD_9= 0.33x10^{-6}					
pAb	0.00103	1080.00	10.00	938.10	7.92
Δf_9= -53 Hz					
ΔD_9 = 2.61x10^{-6}					
CRP (75 ng mL^{-1})	0.00017	255.00	1.24	136.30	0.79
Δf_9= -7.7 Hz					
ΔD_9= 0.4x10^{-6}					
pAb	0.0015	1370.00	13.58	1203.60	11.98
Δf_9= -68 Hz					
ΔD_9 = 3.11x10^{-6}					
CRP (100 ng mL^{-1})	0.00029	350.00	4.30	180.54	1.96
Δf_9= -10.2 Hz					
ΔD_9= 0.62x10^{-6}					
pAb	0.0025	1510.00	15.10	1384.14	14.36
Δf_9= -78.2 Hz					
ΔD_9 = 3.25x10^{-6}					
CRP (200 ng mL^{-1})	0.00018	300.00	3.00	155.80	1.62
Δf_7= -8.8 Hz					
ΔD_7= 0.48x10^{-6}					
pAb	0.002	1470.00	14.80	1313.34	13.62
Δf_7= -74.2 Hz					
ΔD_7 = 3.33x10^{-6}					
CRP (400 ng mL^{-1})	0.00013	270.00	2.60	148.68	1.34
Δf_7= -8.40 Hz					
ΔD_7= 0.46x10^{-6}					
pAb	0.0017	1440.00	14.50	1240.77	13.21
Δf_7= -70.1 Hz					
ΔD_7 = 3.31x10^{-6}					

3.6. Online regeneration of the Au-MPBA-mAb/glucose sensor

Reusability and regeneration of used crystals is an essential factor to be considered in immunoassay development [341]. Several methods have been used for sensor regeneration. Hu et al., [342] reported the use of 8 $mol.L^{-1}$ urea, 0.2 $mol.L^{-1}$ ethanolamine, 0.1 $mol.L^{-1}$ phosphate saline-citrate buffer solution for antigen desorption. It was found that these dissociating agents were not able to desorb the antigen completely. At the same time, these methods involve relatively aggressive chemicals that could partly desorb the bound antibody thereby reducing the lifetime and reusability of the immunosensor [342]. Park et al. 2004 [317],and Chen et al. 2007 [318] have reported the use of 0.1 M NaOH solution and surfactant for immunocomplex dissociation [319]. In the present study, the regeneration of the immunosensor was tested by using 0.1 M HCl to desorb the bound antigen without affecting the covalently attached antibody. The surface regeneration is shown in **Appendix Fig. S6.1(a)** and this confirms the stability of the immobilized antibody onto the electrode surface. The regenerated surface was evaluated by immobilizing a new antigen layer, and the crystal could be reused up to 5 times without much difference in the sensitivity of the immunosensor. The regeneration of the QCM-D immunosensor was achieved by flowing the dissociating solution through the sensor surface to break the immunocomplex formation between the antibody and the antigen. Finally, PBS solution was flowed through the sensor surface until the recovery of the original baseline was achieved. Then the immunosensor was made ready for the subsequent run.

Figure 3.4 shows the regeneration of the base-line of Au-MPBA-mAb/glucose sensor a multiple time without loss of signal with the RSD of 3.14 %. The regenerated surface

was highly stable. The detection was also accomplished at the regenerated surface. The immobilized antibody did not leach off of the surface, this attests to the covalent and the oriented immobilization of the monoclonal anti-CRP antibody. The result in this work shows excellent stability of the immobilized capture antibody, reusable immunoelectrode, stable signal for the concentration measured, reproducible amount of surface-bound capture antibody and reproducible signal for the CRP antigen detection. In addition to the above, we have obtained the oriented antibody immobilization by targeting the Fc carbohydrate moiety of the antibody thus exposing the antigen binding site. The SIA exhibited an enhanced signal without labelling the polyclonal antibody.

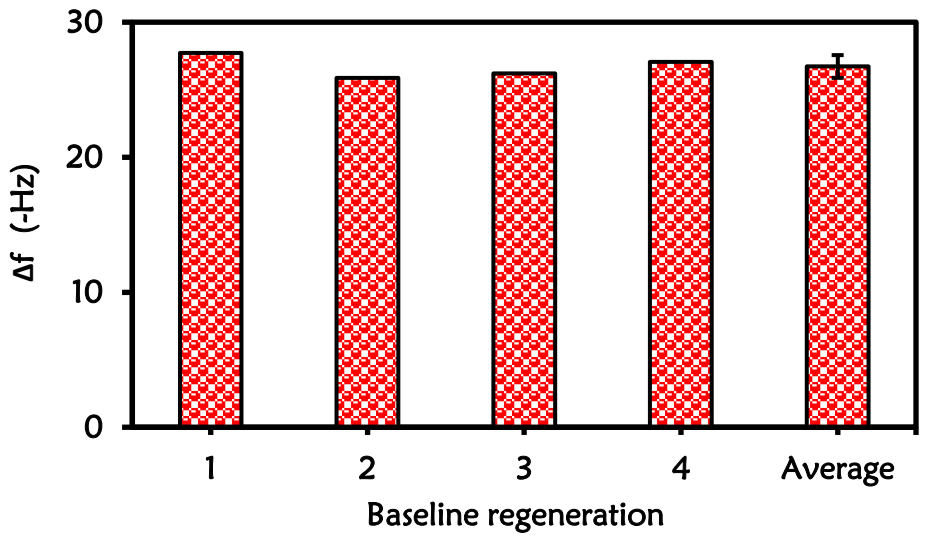

Figure 3.4: Baseline regeneration of the Au-MPBA-mAb/glucose immunosensor.

3.7. Stability of the immobilized monoclonal anti-CRP antibody

The fabricated immunosensor was very stable due to the covalent attachment of the antibody onto the sensor surface. The immobilization of the anti-CRP monoclonal antibody onto the sensor surface was tested on the quartz crystal with the RSD of 1.96% thereby confirming the stability of the immobilized antibody.

The stability study was carried out with the piezoelectric immunosensor. Stability data was extrapolated from the frequency obtained from the QCM-D sensogram after the immobilization of anti-CRP mAb, and the RSD was calculated.

The piezoelectric immunosensor showed a stable baseline even after the surface regeneration with 100 mM HCl. The regeneration solution was able to break the antibody-antigen immunocomplex formation without causing any deformation to the surface bound capture antibody. Furthermore, a stable signal was obtained for the concentration measured, reproducible amount of surface-bound capture antibody and reproducible signal for the CRP antigen detection. The reproducibility of the immunosensor is also a function of the stability of the surface-bound antibody even

after the surface was regenerated.

3.8. Reproducibility of the immunosensor

The reproducibility of the immunosensor was tested using four different concentrations of the CRP-antigen as shown in **Fig 3.5(a) and (b)**. The concentrations are (10, 50, 75, and 100 ng mL^{-1}) of the CRP-antigen. The relative standard deviations (RSD) were calculated both for the DIA in **Fig 3.5(a)** and SIA in **Fig 3.5(b)**. The good RSD values ranging from 0.54 to 5.54 for DIA and 2.08 to 7.59 for SIA were an indication of the

good reproducibility of the fabricated immunosensors. The response of the developed immunosensor was reproducible and stable. The RSD values are presented in **Table 3.2.**

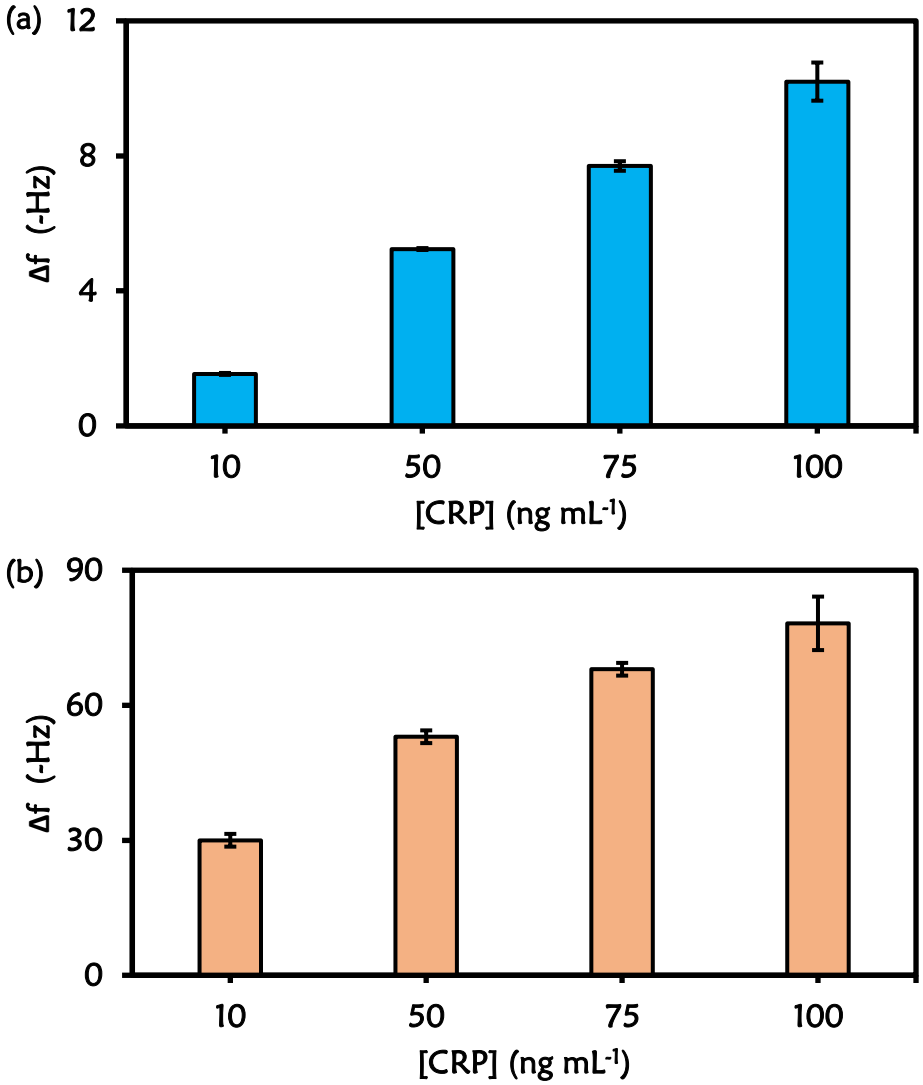

Figure 3.5: Bar chart showing the reproducibility of the immunosensor for (a) DIA and (b) SIA at varying [CRP].

Table 3.2: Table showing the RSD for the reproducibility of the immunosensor for the DIA and SIA.

Concentrations (ng mL^{-1})	DIA (RSD %)	SIA (RSD %)
10	1.83	4.71
50	0.54	2.67
75	1.84	2.08
100	5.54	7.59

3.9. Electrochemical impedimetric immunosensor for C-reactive protein detection

3.9.1. Fabrication of Au-MPBA-mAb/glucose

The design of the CRP-antigen sensing gold surface was modified following the step-by-step procedure shown in **Scheme 3.1** and as described in the experimental section above. The gold surface used was the gold disk electrode (BASi) with 0.8 mm radius was used. The method for the immobilization of monoclonal anti-CRP antibody (mAb) in **Scheme 3.1** was followed. This afforded the oriented immobilization of the monoclonal mouse anti-human CRP antibody (mAb) via site-specific glycosylation reaction. The unreacted 1,2-diol reactive surfaces from the Au-MPBA SAM was blocked with glucose. After the fabrication steps, the immunosensors is represented as Au-MPBA-mAb/glucose. The step-by-step modification of gold surfaces was followed using electrochemistry.

3.9.2. Assay procedure for detection of CRP using Au-MPBA-mAb/glucose

The analytical performance of the Au-MPBA-mAb/glucose immunosensor, was evaluated in 20 μl of CRP antigen with concentrations ranging from 10 to 400 ng mL^{-1} detection in PBS (pH 7.4). The antibody-modified electrode surface was incubated in

the CRP-antigen solution at room temperature. The electrode was rinsed with PBS (pH 7.4) to remove the physically adsorbed antigen. For the direct immunoassay (DIA) the electrode was immersed in 2.0 mM $K_3/K_4Fe(CN)_6$, and the CV and EIS were recorded. For the sandwich immunoassay (SIA), the electrode was further incubated with 20 μl of 30 μg mL^{-1} polyclonal anti-CRP antibody. The electrode was further washed with PBS to remove physisorbed polyclonal anti-CRP antibody. The CV and EIS measurements in 2.0 mM $K_3/K_4Fe(CN)_6$ were measured. All measurements were performed in triplicates. The change in total charge transfer resistance (R_{CT}) for each concentration was calculated from **Equation (3.3).**

$$\Delta R_{CT} = R_{CT(Ab-Ag)} - R_{CT(Ab)} \quad \text{---------- (3.3)}$$

where A_b is the charge transfer resistance of the Au-MPBA-mAb/glucose and $R_{CT(Ab-Ag)}$ is the value of the Au-MPBA-mAb/glucose after the immunoreaction with the CRP antigen for the DIA and with polyclonal anti-CRP antibody for the SIA.

3.10. Electrochemical characterization of Au-MPBA-mAb/glucose immunosensor

Cyclic voltammetry (CV) and electrochemical impedance spectroscopy (EIS) were used to confirm the modification steps of the design of the Au-MPBA-mAb/glucose immunosensor. The inhibition of the electron transfer properties of the bare gold surface upon modification in the presence of the redox probe was used as a measure of surface functionalization. **Figure 3.6** shows (a) CV and (b) EIS of (i) bare Au, (ii) Au-MPBA SAM, and (iii) Au-MPBA-mAb/glucose in (1:1) 2 mM $K_3Fe(CN)_6$:$K_4Fe(CN)_6$ solution containing 0.1 M KCl. The cyclic voltammograms of the bare electrode in **Fig. 3.6(a)(i)** exhibited a reversible redox couple due to $[Fe(CN)_6]^{3-/4-}$ with peak-to-peak separation of (ΔE) of 80.3 ±7.7 mV. The Au-MPBA SAM in **Fig. 3.6(a)(ii)** shows a slight

increase in the peak to peak separation (ΔE = 86 mV). A further increase in peak-to-peak separation (ΔE = 104 mV) was observed with the Au-MPBA-mAb/glucose electrode which is an indication of the blocking behaviour due to the immobilized mAb antibody and blocking of non-specific sites using glucose **Fig. 3.6(a)(iii).**

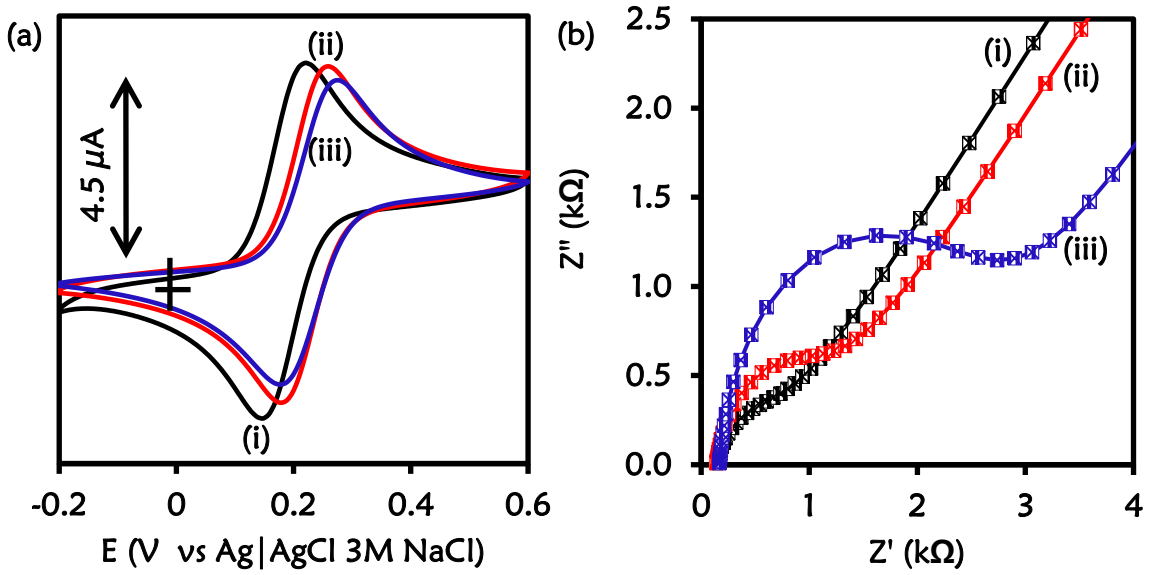

Figure 3.6: (a) CV and (b) EIS of (i) bare Au, (ii) Au-MPBA SAM and (iii) Au-MPBA-mAb/glucose in (1:1) 2 mM $K_3/K_4Fe(CN)_6$ solution containing 0.1 M KCl.

The electrochemical impedance spectroscopy (EIS) was used to monitor and confirm the immobilization of monoclonal anti-CRP antibody (mAb) as this is a more sensitive technique than the cyclic voltammetry. The bare gold electrode exhibited a small semicircle at a high-frequency region with a charge transfer resistance (R_{CT}) value of 0.602±0.097 kΩ in **Fig. 3.6(b)(i).** A slight increase in the charge transfer resistance (1.08 kΩ) was observed after the formation of Au-MPBA SAM in **Fig. 3.6(b)(ii).** Upon the immobilization of the mAb and the blocking of non-specific binding site with glucose, Au-MPBA-mAb/glucose modified electrode, in **Fig. 3.6(b)(iii),** the R_{CT} increased

from 1.08 kΩ to 2.44 kΩ. The increase in R_{CT} is due to the insulating properties of the immobilized monoclonal antibody (mAb) and the glucose. This results in a slow rate of electron transfer properties of the gold electrode and increases the charge transfer resistance. The EIS and CV results confirm the successful modification of the electrode surface. It was interesting to see the electrochemical changes as the surface of the gold electrode was modified. This confirmed the immobilization of gold surface via self-assembled monolayer and the glycosylation of mAb as was observed with QCM-D studies above. The EIS was more sensitive as an electrochemical characterization technique, the CV showed changes, but these were invisible to the naked eyes. The ΔE values were Au (80.3 mV), Au-MPBA SAM (86 mV) and Au-MPBA-mAb/glucose (104 mV). The difference in ΔE is 6 mV between Au and Au-MPBA SAM and 18 mV between Au-MPBA SAM and Au-MPBA-mAb/glucose. The impedance also shows the difference of 0.478 kΩ between Au and Au-MPBA SAM and 1.36 kΩ between Au-MPBA SAM and Au-MPBA-mAb/glucose. The CV and EIS confirmed the modification and oriented immobilization of MPBA to form Au-MPBA SAM and Au-MPBA-mAb/glucose. The modified gold surface was employed in the detection of CRP-antigen.

3.11. Impedimetric detection of CRP-antigen

The inhibition of immunocomplex formation between the anti-CRP monoclonal antibody and CRP antigen was studied using $[Fe(CN)_6]^{3-}$ redox probe. The Au-MPBA-mAb/glucose electrode was used for the detection of different concentrations of CRP-antigen from (10 - 400 ng mL^{-1}) using a direct and sandwich immunoassay formats as previously studied for QCM-D. The EIS signal (R_{CT}) was used to monitor the change in total charge transfer resistance (ΔR_{CT}) of the Au-MPBA-mAb/glucose electrode. The R_{CT}

(charge transfer resistance) was measured by fitting the raw impedance data (Nyquist plot) using an equivalent circuit. The Randles-Sevcik equivalent circuit shown in **Fig. 1.13(b)** was used. The fitted data was optimised until the % error was less than 5% and acceptable. This was very important as it allowed for precise and comparative signal analysis. **Figure. 3.7** shows the Nyquist plots (a) and (b) with their corresponding linear graphs of ΔR_{CT} against CRP-antigen concentrations (a') and (b') for the (a) direct and (b) sandwich immunoassays. For the direct immunoassay, the fabricated anti-CRP mAb/glucose immunosensor was exposed to the CRP-antigen, and the impedance was measured. The increase in the (R_{CT}) was observed with increasing CRP-antigen concentrations. The change in total charge transfer resistance for each CRP-antigen concentration was calculated using **Equation (3.3).** A linear increase of the ΔR_{CT} was observed with increasing antigen concentration from 10 – 100 ng mL^{-1} and a regression equation was ΔR_{CT} = 0.0088 [CRP-antigen] – 0.0536 and R^2 0.9982 (n=3), shown in **Fig. 3.7(a')**. However, at higher CRP-antigen concentrations (> 100 ng mL^{-1}) a decrease in the R_{CT} value was observed in **Fig. 3.8(a) and (b)** for the (a) direct and (b) sandwich immunoassays. This observation is attributed to the fact that all the available antigen binding sites on the surface of the immunosensor were saturated due to an excess amount of CRP-antigen competing for the same binding site. This competition leads to the partial binding of the CRP-antigen which washes off during rinsing. This phenomenon has been observed before [340] for immunosensors based on antibody-antigen affinity detection. The competition at high antigen concentration reduced the binding efficiency between the immobilized anti-CRP mAb and the CRP antigen. A similar trend was observed with the QCM-D studies. The sandwich immunoassay using polyclonal anti-CRP antibody (pAb) that recognises different epitopes on the captured

CRP-antigen was used for signal amplification. Two steps were involved in the sandwich immunoassay; firstly the capture of the CRP-antigen, and the immunoreaction with pAb after rinsing, and the impedance measurement was recorded.

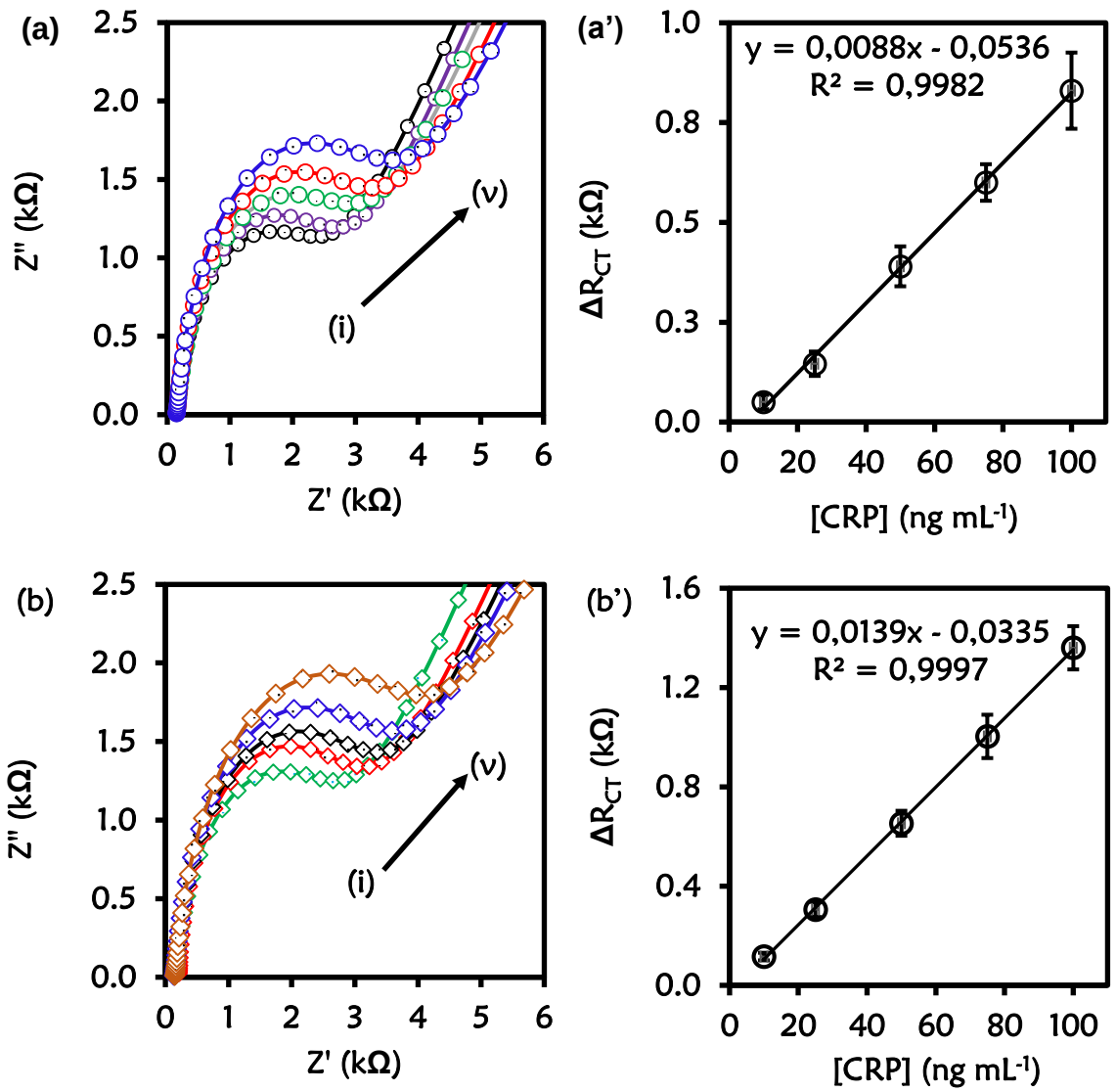

Figure 3.7: (a) and (b) Nyquist plots and (a') and (b') the corresponding calibration curves at varied CRP-antigen concentrations (i) 10 ng mL^{-1} (ii) 25 ng mL^{-1} (iii) 50 ng mL^{-1} (iv) 75 ng mL^{-1} (v) 100 ng mL^{-1} for the (a) direct assay (b) sandwich immunoassays.

The Nyquist plot for the detection of CRP-antigen concentrations (10 – 100 ng mL^{-1}) for the sandwich immunoassay is shown in **Fig. 3.7(b).** The concentration of the polyclonal

antibody was kept constant (30 μg mL^{-1}). The increase in the diameter of the semicircle (R_{CT}) with increasing concentration of CRP-antigen confirms the immunocomplex formation between the mAb and the CRP-antigen and lastly with the pAb. The ΔR_{CT} of the sandwich immunoassay was higher than that of the direct immunoassay. The observed increase R_{CT} was attributed to the formation of mAb/CRP-antigen/pAb immunocomplex due to the bulky and the insulating properties of the pAb. The calibration curve is shown in **Fig. 3.7(b')** for the change in total charge transfer resistance according to **Equation (3.3, above).** The regression line of ΔR_{CT} = 0.0139 [CRP-antigen] – 0.0335 with R^2 0.9997 (n = 3) was obtained for the sandwich immunoassay. The sensitivity of the direct immunoassay was 0.438 kΩ.ng^{-1}.ml.cm^{-2} and 0.691 kΩ.ng^{-1}.ml.cm^{-2} for the sandwich immunoassay. The observed increase in the sensitivity of the sandwich immunoassay was attributed to the enhanced signal generated by the pAb as observed in **Fig. 3.7(b').** The limit of detection (LoD) and the limit of quantification (LoQ) are the key analytical parameters for evaluating the developed method and the performance of the immunosensor. The LoD and LoQ were calculated using the IUPAC method of 3 x SD/m and 10 x SD/m; respectively. Where m is the slope of the calibration curve and SD is the standard deviation of the blank measurement without the presence of the CRP-antigen (as an analyte). The LoD and LoQ values were found to be 9.75 and 32.51 ng mL^{-1} for the direct immunoassay and 6.23 and 20.77 ng mL^{-1} for the sandwich immunoassay.

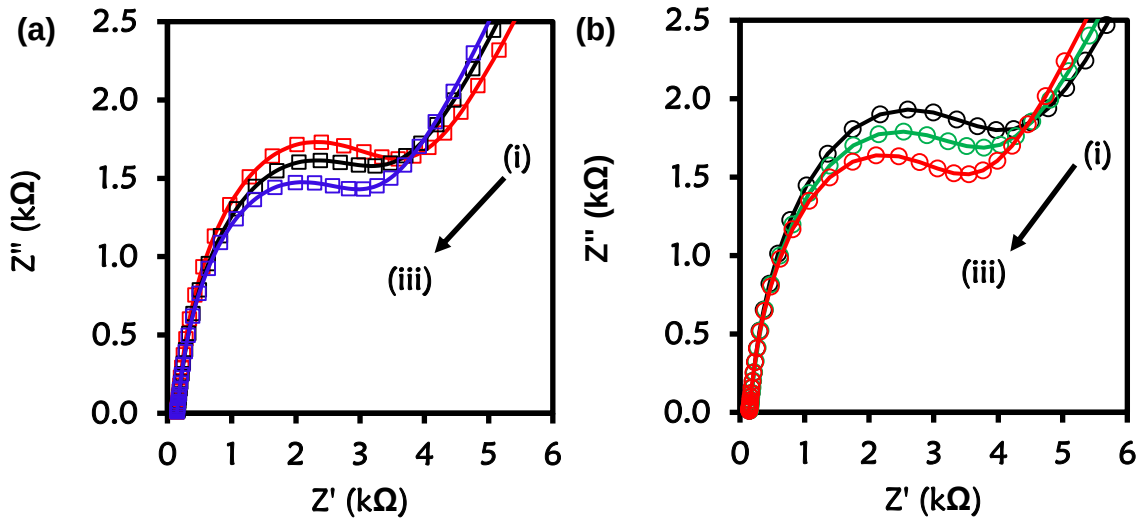

Figure 3.8: Nyquist plots showing a decrease in charge transfer resistance (ΔR_{CT}) at higher concentrations (i) 100 ng.ml^{-1} (ii) 200 ng mL^{-1} and (iii) 400 ng mL^{-1} for (a) direct (b) sandwich immunoassays

3.12. Comparison of piezoelectric versus impedimetric immunosensors

The sandwich immunoassay (SIA) for the piezoelectric and impedimetric immunosensors showed a better analytical performance in terms of LoD, LoQ, and sensitivity. The sensitivity of the immunoassays was calculated from the slope of the regression equation for the piezoelectric and the impedimetric immunosensors. The sensitivity of the piezoelectric immunosensor increased from 0.063 (DIA) to 0.358 Hz.ml.ng^{-1} for the SIA. The sensitivity of the impedimetric immunosensor was found to be 0.438 kΩ.ng^{-1}.ml.cm^{-2} for the DIA and 0.691 kΩ.ng^{-1}.ml.cm^{-2} for the SIA. The analytical parameters for the piezoelectric immunosensor for the direct immunoassay were calculated to be 5.72 ng mL^{-1} (LoD). For the sandwich immunoassay, the enhanced analytical parameter gave an LoD of 3.84 ng mL^{-1}. The LoD of the impedimetric immunosensor was found to be 9.75 ng mL^{-1} (DIA) and 6.23 ng mL^{-1} (SIA). The higher

sensitivity of the sandwich immunoassay was attributed to the signal generated by the anti-CRP polyclonal antibody by recognizing different epitopes on the CRP-antigen. From the observed result shown in **Table 3.3**, the piezoelectric immunosensor gave a better LoD than the impedimetric immunosensor. This could be attributed to the larger surface area of the quartz crystal (1.54 cm^2) used in the piezoelectric immunosensor compare with the surface area of the gold electrode (0.0201 cm^2). The larger surface area of the quartz crystal allowed a greater amount of the immobilized antibody onto the sensor surface. However, the impedimetric immunosensor showed better sensitivity than the piezoelectric immunosensor.

Furthermore, the performance of the piezoelectric and impedimetric immunosensors was compared with some of the CRP immunosensors reported in the literature as presented in **Table 3.3.** The piezoelectric immunosensor developed by Ogi et al., in 2011 [339] shows better LoD than the immunosensor developed in this work. The detection limit was 0.1 ng mL^{-1}. The lower detection limit could be attributed to the conjugation of the detection antibody with biotin-streptavidin for improved sensitivity. However, this method is a labelled technique which also requires an additional reagent, and it is quite expensive compared with the label-free method in our proposed work.

The fabricated piezoelectric immunosensor in this work offers a lower LoD (3.84 ng mL^{-1}) than the piezoelectric immunosensor reported by Fuchiwaki et al., in 2014 [343]. The LoD was found to be 50 ng mL^{-1}. The lower detection limit achieved in this study could be attributed to the oriented immobilization of the immobilized (mAb) anti-CRP antibody.

Furthermore, the piezoelectric immunosensor developed by Gan et al., [344] has a lower detection limit (5.0 pg mL^{-1}) than the present work as shown in **Table 3.3.** The lower LoD value could be as a result of the horseradish peroxidase (HRP)-doped magnetic core-shell Fe_3O_4@SiO_2@Au nanostructures used as labels for an enhanced signal. However, this system is quite expensive due to the use of HRP compare with the label-free method adopted in our current study. However, the LoD of immunosensor developed in this study falls within the diagnostic range of CRP. As earlier mentioned, the clinical reference range of CRP assay are ≤ 1 μg mL^{-1} (low risk), 1-3 μg mL^{-1} (medium risk) and ≥ 3 μg mL^{-1} (high risk).

Also, the impedimetric immunosensor developed in this work shows a better LoD (6.23 ng mL^{-1}) than the fabricated immunosensor reported by Gupta et al., [235] as shown in **Table 3.3.** A label-free method for the detection of CRP using a carbon nanofiber-based biosensor was developed with an LoD of 11 ng mL^{-1}. The lower detection limit achieved by this present study could be attributed to the oriented immobilization of the captured antibody. The oriented immobilization allows for better CRP-antigen capture thereby increasing the sensitivity and specificity of the immunosensor.

Moreover, Puri et al., reported a label-free electrochemical impedance immunosensor for the detection of CRP on a gold electrode modified with aliphatic SAMs, such as mercaptoundecanoic acid (MUA) and mercaptopropionic acid (MPA) [230]. Carbodiimide chemistry was used for the covalent immobilization of the anti-CRP antibodies onto the gold electrode. The LoD was 30 ng mL^{-1}. The proposed immunosensor in this study shows a lower detection limit of 6.23 ng mL^{-1}.

Table 3.3: Comparison of analytical performance of CRP immunosensors.

Immunoassay	Linear range (ng mL^{-1})	LoD (ng mL^{-1})	References
Piezoelectric	0.1 - 100	0.1	[339]
Piezoelectric	50 - 1000	50	[343]
Piezoelectric	0.01 - 200	0.005	[344]
Amperometry	0.5 - 200	0.5	[226]
SWASV	0.5 – 200	0.22	[229]
EIS	45 - 5840	30	[230]
EIS	0.1 – 20	0.1	[232]
ASV	0.2 – 100	0.05	[233]
EIS	8.5 - 9120	3.5	[234]
Fluorescence	1.56 – 400	0.46	[345]
EIS	-	11	[235]
Piezoelectric	10 - 100	3.84	This work
Impedimetric	10 - 100	6.23	This work

3.13. Serum analysis

The evaluation of the analytical performance of Au-MPBA-mAb/glucose immunosensor to mimic real-life application was carried out in 10% new calf serum. The recovery study was carried out using two concentrations of the CRP-antigen (50 and 100 ng mL^{-1} was spiked in the serum. The recovery test was an indication of the good analytical performance of the Au-MPBA-mAb/glucose immunosensor. The amount recovered for the two concentrations were very close to 100% (88.54 - 94.34 %) and are shown in **Table 3.4.**

Table 3.4: Table showing the recovery results obtained Au-MPBA-mAb/glucose immunosensor in serum samples.

Sample no	Spiked (ng mL^{-1})	Found (ng mL^{-1})	Recovery (%)
1	50 (DIA)	50.40	90.96
2	50 (SIA)	49.60	88.54
3	100 (DIA)	100.40	94.34
4	100 (SIA)	100.20	94.27

3.14. Conclusions

The design of Quartz Crystal Microbalance with Dissipation (QCM-D) and impedimetric immunosensor for the detection of CRP antigen was investigated in this chapter. The developed method was based on the formation of a self-assembled monolayer of MPBA onto the gold-coated quartz crystal for QCM-D and gold electrode for electrochemical impedance spectroscopy. The two immunosensors were tested for CRP-antigen detection using direct and sandwich immunoassay formats. The polyclonal anti-CRP antibody was used for the signal generator in the sandwich immunoassay. The use of pAb in the sandwich immunoassay allowed higher sensitivity of the immunosensor. The piezoelectric immunosensor was highly stable, and reproducible. The surface of the immunosensor could be regenerated using 100 mM HCl without loss of selectivity and specificity of the immunosensor. Also, the immobilized antibody was not affected by the regeneration solution, and a stable baseline was achieved with the RSD 3.14%. The strong interaction between MPBA SAM and the capture antibody confirms the oriented immobilization of the antibody onto the electrode surface via the boronate ester interaction.

The fabricated immunosensors are suitable for label-free detection of human CRP antigen in clinical applications. The method used was reproducible with RSD 1.96 % for the immobilization of the monoclonal anti-human CRP antibody.

The real-life application was carried out in 10% serum and recovery study for the percentage recovery. It was observed that approximately 100% recovery was obtained. The two immunosensors showed promising towards label-free detection of human-CRP antigen. The simple method of the fabrication of the immunosensor makes it an excellent alternative for clinical applications where human CRP antigen is an analyte of interest.

Chapter 4:

Electrochemical impedimetric immunosensor using (Au-MBA-APBA-mAb/glucose)

4.0. Preamble

The fabricated immunosensor in this chapter was based on the formation of a self-assembled monolayer (SAMs) of 4-mercaptobenzoic acid onto a gold electrode surface. The attachment of 4-aminophenylboronic acid (APBA) unto the gold electrode surface for antibody capture was achieved through carbodiimide chemistry. The full fabrication procedure was presented in **section 2.6.2.** To improve the analytical performance of the mercaptophenyl boronic acid modified electrode reported in the previous chapter. The effect chain length of the linker through the introduction of a spacer for enhanced analytical performance was investigated in this chapter. The introduction of a spacer will allow a better interaction of the anti-CRP monoclonal antibody with the boronic acid thereby increase the sensitivity of the immunosensor [187].

Self-assembled monolayer (SAMs) are widely used for biomolecules attachment onto the gold surface [346,347]. Different head-groups are available for immobilization of biomolecules. Carboxylic acid (COOH) terminated SAMs are extensively used and preferred in bio-sensing applications. The preference of COOH functional groups is their ability to react with the amine group (NH_2) that are present in protein or peptide to form a stable amide bond [348]. However, a covalent amide bond can only be achieved if the surface bearing the carboxylic acid is activated via EDC/NHS coupling. The activation entails the formation of a reactive N-hydroxylsuccimidyl (NHS) ester by reacting the carboxylic acid with carbodiimide and NHS. Two steps are involved in the surface activation. Firstly, the reaction between the acid and the carbodiimide to form O-acylurea, followed by a reaction between O-acylurea and NHS to yield the activated NHS ester [349]. The immobilization of anti-CRP monoclonal antibody using COOH terminated SAMs has been previously reported in the literature [107,232]. COOH

terminated surfaces could also be used for the attachment of NH_2 terminated linker before protein immobilization [186].

This chapter investigates the covalent attachment of COOH terminated SAMs of 4-mercaptobenzoic acid with 4-aminophenylboronic acid for the immobilization of anti-CRP mAb. The method chosen for the immobilization of the anti-CRP monoclonal antibody in the thesis was targeted towards the oriented antibody immobilization. This was achieved through the affinity boronate interaction between carbohydrate moiety present at the Fc region of the mAb and the 4-aminophenylboronic acid. As previously reported in the literature phenylboronic acid modified electrode can be used to achieve oriented immobilization of antibody [186,191,192]. The covalent attachment of the APBA unto the electrode surface was confirmed using electrochemistry and XPS.

4.1. Assay procedure for the detection of CRP using Au-MBA-APBA-mAb/glucose

The analytical performance of the Au-MBA-APBA-mAb/glucose immunosensor was evaluated following the same analytical procedure reported in **section 3.9.2.** for Au-MPBA-mAb/glucose.

4.2. Results and Discussion

4.2.1. Surface modification using APBA and biomolecules

The design of the CRP-antigen sensing gold surface was modified following the step-by-step procedure shown in **Scheme 4.1** and as described in the experimental section above. The method followed was chosen to allow for oriented immobilization of the monoclonal mouse anti-human CRP antibody (mAb) via site-specific glycosylation reaction. The unreacted boronic acid reactive surfaces from the Au-MBA-APBA-mAb

was blocked with glucose. After the fabrication steps, the immunosensor is represented as Au-MBA-APBA-mAb/glucose. The step-by-step modification of gold surfaces was followed using electrochemistry and X-ray photoelectron spectroscopy (XPS).

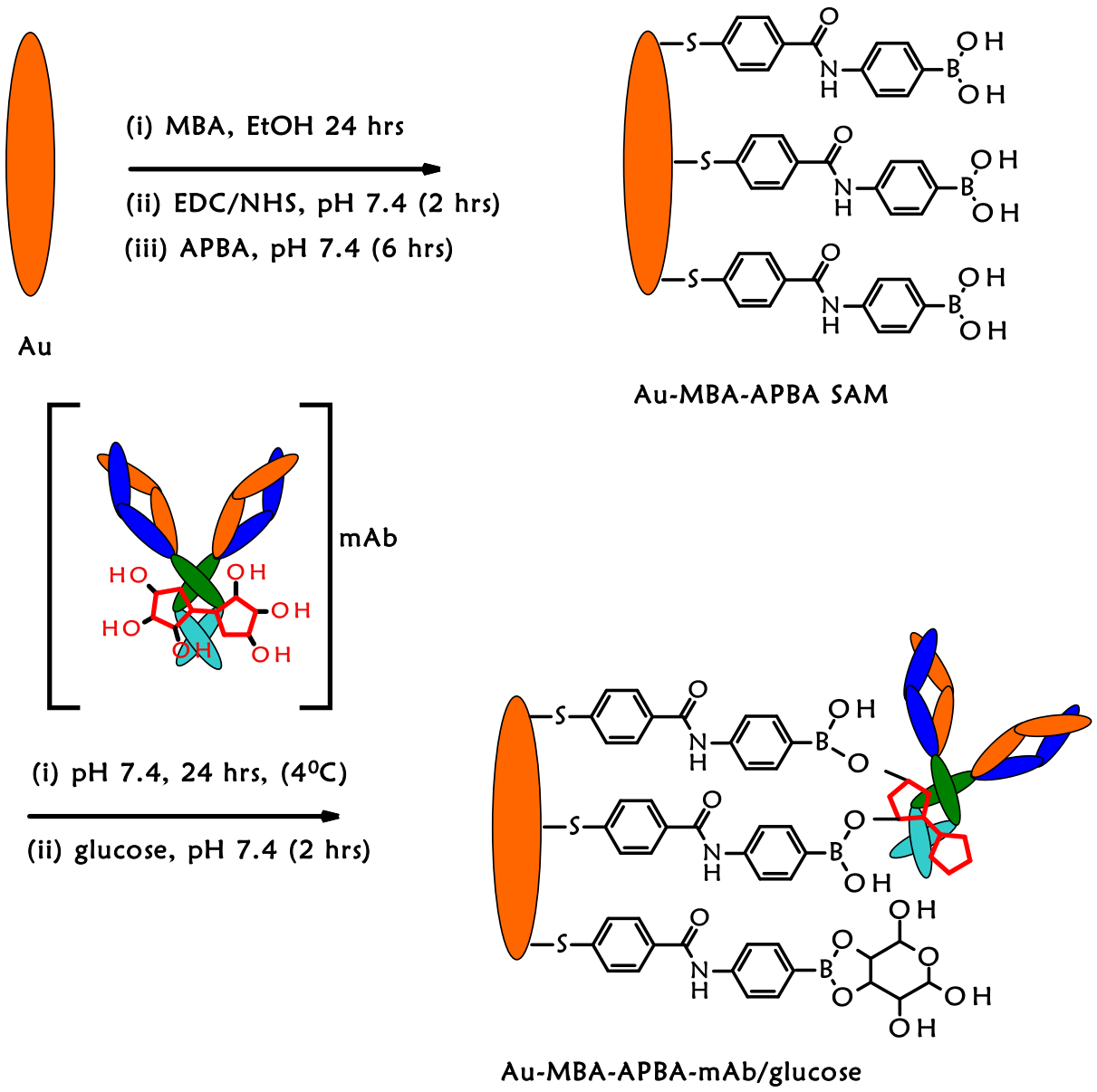

Scheme 4.1: Step-by-step modification of gold surface to form MBA-APBA SAM and the immobilization of monoclonal anti-human CRP antibody.

4.2.2. Electrochemical characterization of the electrode modification

Cyclic voltammetry (CV) and electrochemical impedance spectroscopy (EIS) were used to confirm the modification steps of the fabrication of the Au-MBA-APBA-mAb/glucose immunosensor. The inhibition of electron transfer properties of the bare gold surface upon modification in the presence of the redox probe ($[Fe(CN)_6]^{3-/4-}$) was used as a measure of surface functionalization. **Fig. 4.1** shows (a) CV and (b) EIS of (i) bare Au, (ii) Au-MBA-APBA-SAM, and (iii) Au-MBA-APBA-mAb/glucose in (1:1) 2 mM $K_3Fe(CN)_6$:$K_4Fe(CN)_6$ solution containing 0.1 M KCl. The cyclic voltammograms of the bare Au electrode **Fig 4.1(a)(i),** exhibited a reversible redox couple due to $[Fe(CN)_6]^{3-/4-}$ with a peak to peak separation (ΔE) of 80.3 ± 7.7 mV. For the Au-MBA SAM in **Appendix Fig. S6.2(a)(i)** an increase in ΔE from 80.3 mV to 247 mV was observed and due to electrostatic repulsion between the negatively charged carboxyl group and the negatively charged ($[Fe(CN)_6]^{3-/4-}$). A drastic decrease in ΔE from 247 mV to 100 mV was observed when amide coupling between Au-MBA SAM and 4-aminophenylboronic acid occurred, Au-MBA-APBA SAM in **Fig. 4.1(a)(ii).** The decrease in peak-to-peak separation at the Au-MBA-APBA SAM was due to the coupling of 4-aminophenylboronic acid and neutralization of the COO- functional group of the Au-MBA SAM. The deprotonation of COO- at Au-MBA SAM is due to high pH conditions (pH 7.4) of the redox probing species, $[Fe(CN)_6]^{3-/4-}$. The pKa of the carboxylic acid functional group of Au-MBA SAM is 5.8. Upon amide coupling of the phenylboronic acid, the neutral monolayer resulted due to the fact that the pKa of the boronic acid (OH) functional group is 8.83. At the Au-MBA-APBA-mAb/glucose in **Fig. 4.1(a)(iii),** further inhibition of the redox probe from the solution was observed. This was due to the blocking behaviour and the insulating properties of the Au-MBA-APBA-

mAb/glucose. For the Au-MBA-APBA-mAb/glucose electrode, an increase in ΔE from 100 mV to 220 mV occurred. A drastic decrease in peak currents in the cyclic voltammogram was observed with the increase in ΔE. This observation was as a result of the insulating feature of the mAb. This confirms the successful immobilization of the mAb and the blocking of non-specific binding sites by glucose.

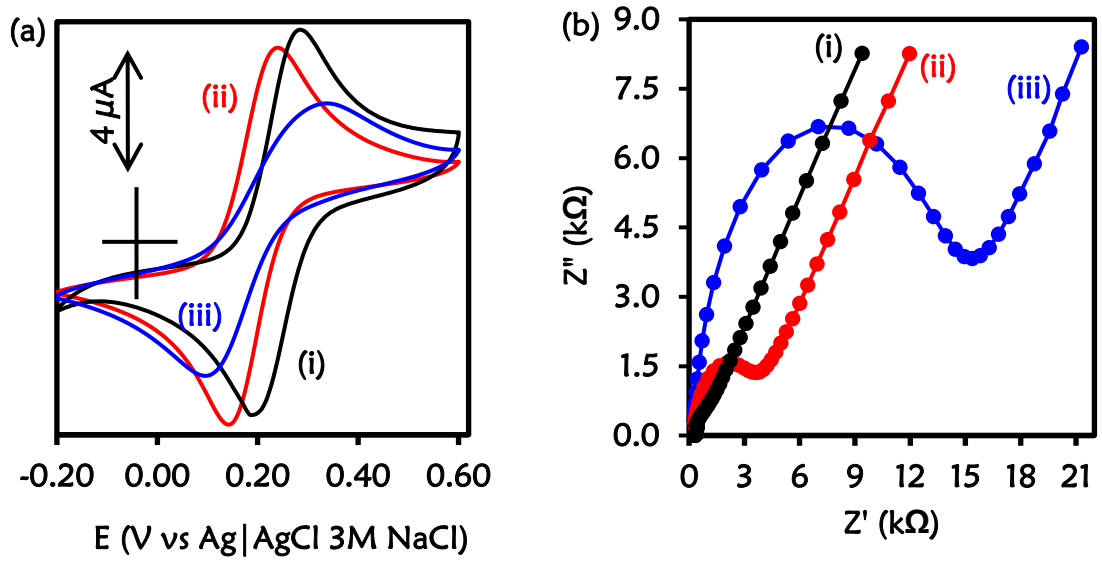

Figure 4.1: (a) Cyclic voltammograms and (b) Nyquist plot of (i) bare Au, (ii) Au-MBA-APBA SAM and (iii) Au-MBA-APBA-mAb/glucose in (1:1) 2 mM $K_3Fe(CN)_6$:$K_4Fe(CN)_6$ solution containing 0.1 M KCl.

The electrochemical impedance spectroscopy (EIS) was used to monitor and confirm the immobilization of monoclonal anti-CRP antibody (mAb). The bare gold electrode exhibited a small semicircle at high frequency with a charge transfer resistance (R_{CT}) value of 0.602 ±0.097 kΩ, in **Fig. 4.1(b)(i).** An increase in R_{CT} to 12.0 kΩ was obtained after the formation of the MBA SAM on the Au-electrode (Au-MBA SAM) **Appendix Fig. S6.2(b)(i)**. The increase in R_{CT} observed was an indication of the electrostatic

repulsion between the negatively charged carboxyl (COO-) groups of the Au-MBA SAM and the negatively charged $[Fe(CN)_6]^{3-/4-}$ ions. This reduced the ability of the $[Fe(CN)_6]^{3-/4-}$ ions to reach the underlying gold electrode surface and has been previously reported before [192]. Upon the coupling of aminophenylboronic acid (Au-MBA-APBA SAM) **Fig. 4.1(b)(ii)** a drastic decrease in R_{CT} from 12.0 kΩ to 2.84 kΩ was observed. This could be attributed to the neutralization of the negative charge carboxylic group upon reaction with the amino group of the aminophenylboronic acid. An increase in R_{CT} from 2.84 kΩ to 12.8 kΩ was observed after the immobilization of the mAb and the blocking of the non-specific binding site with glucose, Au-MBA-APBA-mAb/glucose modified electrode, in Fig. 4.1(b)(iii). The increase in R_{CT} was due to the insulating properties of the immobilized monoclonal antibody and the glucose. This results in a slow rate of electron transfer properties of the gold electrode and increase in the charge transfer resistance. The EIS and CV results confirm the successful modification of the electrode surface. Additional characterization of the gold electrode surface modification was carried out using a surface sensitive and quantitative X-ray photoelectron spectroscopy (XPS) technique.

4.3. XPS characterization of the immunosensor fabrication

X-ray photoelectron spectroscopy (XPS) is a highly sensitive, versatile and quantitative surface characterization technique that gives insight into the type of bonding and interactions after surface modifications [304]. The elemental and the atomic composition can be evaluated using the XPS survey spectra thus giving this technique the quantitative analytical capability [308]. To ascertain the successful fabrication of the immunosensor, different modification stages of the fabricated immunosensor were characterized using XPS. **Fig. 4.2**, shows the survey spectra of (a) bare Au, (b) 4-

mercaptobenzoic acid modified surface (Au-MBA SAM), (c) 4- aminophenyl boronic acid modified electrode (Au-MBA-APBA SAM), and (d) monoclonal anti-CRP antibody and glucose modified electrode (Au-MBA-APBA-mAb/glucose). The survey spectrum of the bare Au revealed the presence of peaks majorly due to gold (Au 4f, Au 4p, and Au 4d), and other elements such as chromium (Cr), silver (Ag), oxygen (O1s) and carbon (C1s) peaks. The presence of carbon and oxygen peaks could be due to the washing of the bare Au surface using ethanol and air dried before measurement. The presence of silver and chromium peak is attributed to the surface coating of the gold-coated quartz crystal to obtain a smooth gold thin layer with the chromium underlayer and conducting silver. The atomic percentage (at %) of carbon and oxygen were found to be 45.2 % and 12.2 % respectively for the bare electrode **Fig. 4.2(a).** Upon formation of the self-assembled monolayer of MBA **Fig. 4.2(b),** a significant increase in both for carbon (from 45.2 to 60.4 %) and oxygen (12.2 to 18.9 %) was observed. The observed increase in both carbon and the oxygen for the MBA SAM accounts for the successful formation of the self-assembled monolayer. Furthermore, the silver composition decreased from 5.7 % to 1.7 %. This is attributed to the addition of the SAM layer on the electrode surface causing a reduction of the silver signal. The covalent immobilization of 4-aminophenyl boronic acid onto Au-MBA SAM (**Fig. 4.2c,** Au-MBA-APBA SAM) resulted in the appearance of nitrogen (N 1s) peak. The (N 1s) peak is attributed to amide (-CONH-) moiety that formed during the amide coupling of 4-aminophenylboronic acid to the EDC/NHS activated COOH terminated surface of the Au-MBA-SAM. The presence of boron (B 1s) element was also seen at the APBA modified electrode which is an indication of the successful coupling of the APBA onto the gold surface. A significant increase in the intensity of the (N 1s) peak was observed

upon boronate ester formation of the Au-MBA-APBA SAM with the Fc carbohydrates of the anti-CRP monoclonal antibody to yield an Au-MBA-APBA-mAb surface, **Fig. 4.2(d).** The boronate ester reactions allow for the oriented immobilization of the antibody exposing the antigen binding site. The increase in (N 1s) intensity at Au-MBA-APBA-mAb is attributed to the immobilization of the antibody containing numerous peptide bonds.

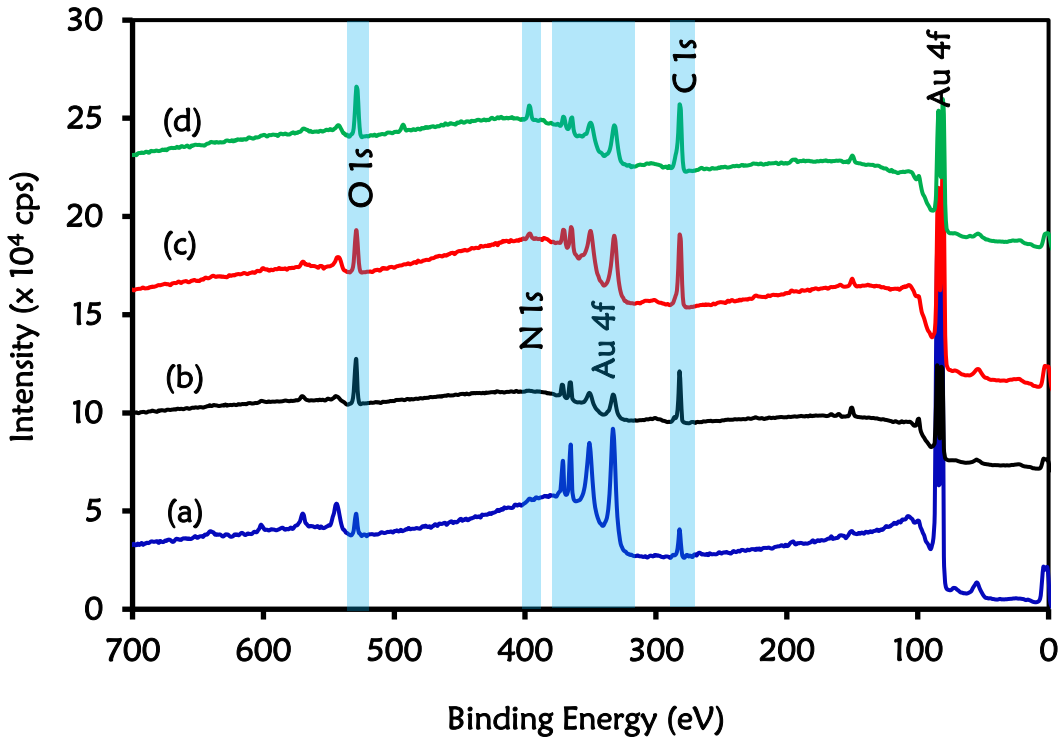

Figure 4.2: The survey spectra of (a) bare Au, (b) Au-MBA SAM, (c) Au-MBA-APBA SAM and (d) Au-MBA-APBA-mAb/glucose

Figure 4.3 shows the high-resolution C 1s of (a) Au-MBA-SAM, (b) Au-MBA-APBA SAM and (c) Au-MBA-APBA-mAb/glucose and O 1s of (a') Au-MBA-SAM, (b') Au-MBA-APBA SAM and (c') Au-MBA-APBA-mAb/glucose. The deconvoluted C 1s high-resolution spectra showed the chemical environment of carbon present on the gold surface and according to the material used for the modification. For Au-MBA-SAM in **Fig. 4.3(a),** four components were observed at 284.6 eV, 285.7 eV, 286.7 eV and 288.8 eV. The components observed at 284.6 eV and 285.7 eV (binding energy) are assigned to C-C, C=C, and C-H [350,351]. The component at 286.7 eV is assigned to C-O, C-S [352]. The component at 288.9 eV is due to carboxyl carbon (O-C=O) [353,354]. The C 1s high resolution of the Au-MBA-APBA SAM surface in **Fig. 4.3(b)** shows three components at 284.6 eV, 286.7 eV and 288.3 eV and their assignments are similar to the Au-MBA SAM except for the component at 288.3 eV is assigned to N-C=O (amide bond) [355]. The C 1s spectrum of Au-MBA-APBA-mAb/glucose surface was deconvoluted, and four components were synthesized in **Fig. 4.3(c)** at 284.6 eV, 286.4 eV, 288.0 eV and 292.4 eV. The component with at 284.6 eV is assigned as the above. The component at 286.4 eV corresponds to C-O, C-S and C-N carbons of the protein backbone [356]. The third component at 288.0 eV is assigned to the carboxyl (O-C=O) and peptide carbon (N-C=O) [357] also due to various amide bonds on the backbone of the antibody. The last component seen at 292.4 eV is the shake-up which is associated with carbon in the aromatic ring [358]. The high resolution of O 1s for (a') Au-MBA-SAM, (b') Au-MBA-APBA SAM and (c') Au-MBA-APBA-mAb/glucose surfaces is also presented in **Fig. 4.3.**

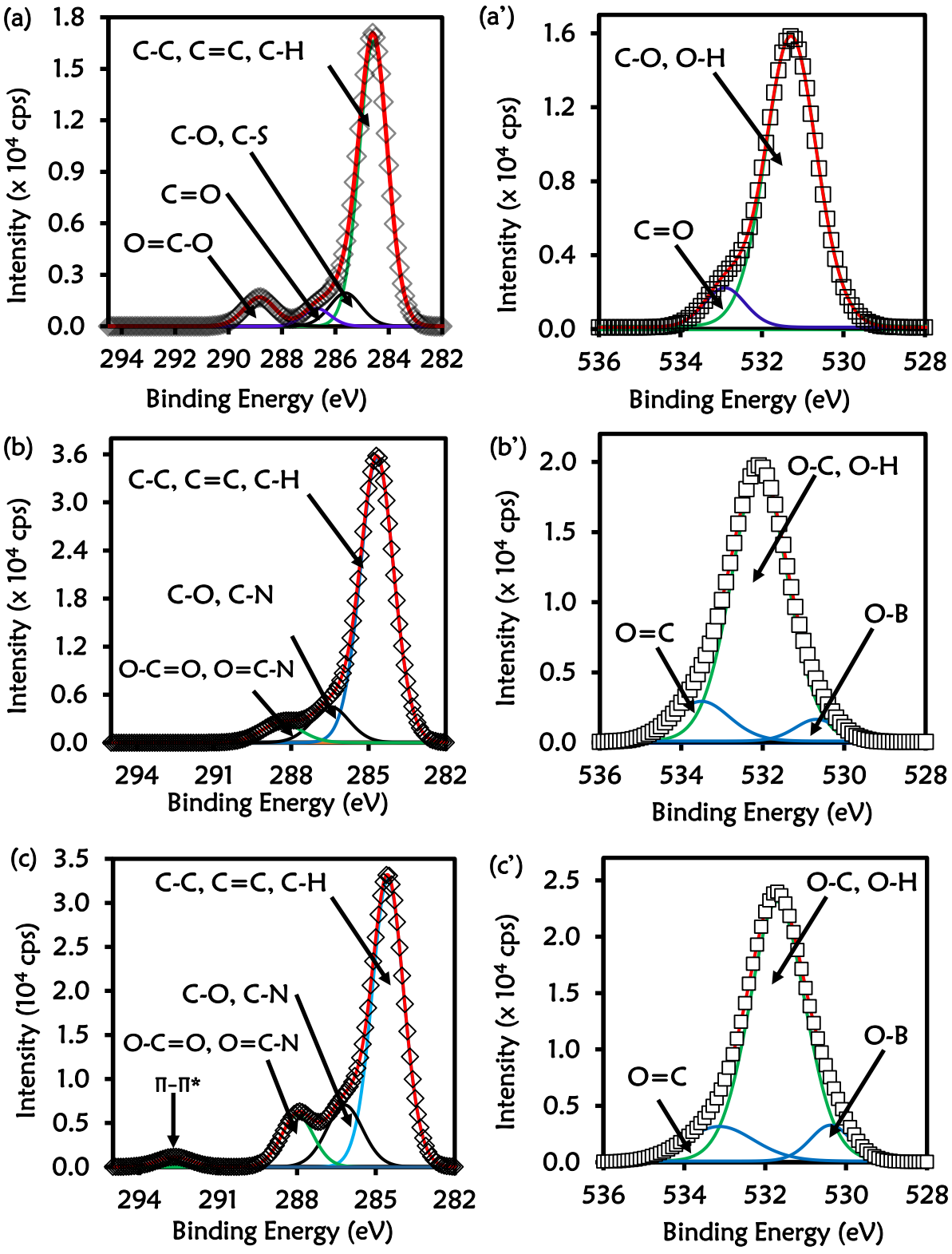

Figure 4.3: High-resolution spectra of C 1s (a) Au-MBA-SAM, (b) Au-MBA-APBA SAM and (c) Au-MBA-APBA-m Ab/glucose and O 1s (a') Au-MBA-SAM, (b') Au-MBA-APBA SAM and (c') Au-MBA-APBA-mAb/glucose.

The deconvolution of the O 1s Au-MBA-SAM **Fig. 4.3(a')**, was fitted into two components. The component at 531.3 eV is assigned to the O-C and O-H of the mercaptobenzoic acid (Au-MBA-SAM). The second component at 533.2 eV is due to carbonyl oxygen (C=O) of the carboxyl group [359]. The deconvolution of the O 1s spectrum in **Fig. 4.3(b')** and **4.3(c')** for Au-MBA-APBA SAM and Au-MBA-APBA-mAb/glucose both fitted into three components. The components were observed at binding energies at 530.6 eV, 532.0 eV and 533.4 eV for Au-MBA-APBA SAM and corresponding to O-B, (O-C, O-H) and O=C respectively. For the Au-MBA-APBA-mAb/glucose, the binding energies were at 530.9 eV, 531.8 eV and 533.1 eV, corresponding to O-B, (O-C, O-H) and O=C respectively from the MBA-APBA-mAb/glucose. The binding energies at, 532.0 eV and 531.8 eV can be assigned to (O-C, and O-H). The component centred at approximately 530.6 eV and 530.9 eV is assigned to B-O bond due to boron atom [360]. The components at approximately 533.4 eV and 533.1 eV is attributed to the carbonyl oxygen (C=O) present in COOH and amide (HNCO) functional group. The presence of the observed carbon and oxygen species with their chemical environments confirmed the immobilization of MBA, MBA-APBA, and MBA-APBA-mAb/glucose. There was also an increase in the intensity after each immobilization signifying the attachment of the various materials.

Figure 4.4 shows the high-resolution N 1s for (a) Au-MBA-APBA SAM and (b) Au-MBA-APBA-mAb/glucose surfaces and (c) the boron (B 1s) for Au-MBA-APBA SAM. The high resolution of N 1s for Au-MBA-APBA SAM and Au-MBA-APBA-mAb/glucose in **Fig. 4.4(a)** and **Fig. 4.4(b)** shows a single component at 400.2 eV and 400.3 eV, respectively attributed to the amide (CONH) bond [361,362]. Two major and distinct components were observed from the high-resolution spectrum of B 1s in **Fig. 4.4(c)** and were centred at 183.9 eV and 190.5 eV. These components are indicative of the presence of the boron element with two chemical environments. The component at 183.9 eV is assigned to B-C bond while the other component at 190.5 eV was assigned to B-O bond [363]. The presence of boron and nitrogen peaks on the Au-MBA-APBA SAM confirms the successful amide coupling of APBA onto an Au-MBA SAM. However, the disappearance of the boron element was observed with the Au-MBA-APBA-mAb/glucose electrode and due to the bulky mAb and glucose boronate ester formation. This observation could further be attributed to the size of the mAb and confirms the successful immobilization of the antibody onto the MBA-APBA functionalized gold surface. The quantitative analysis results are summarized in **Table 4.1.**

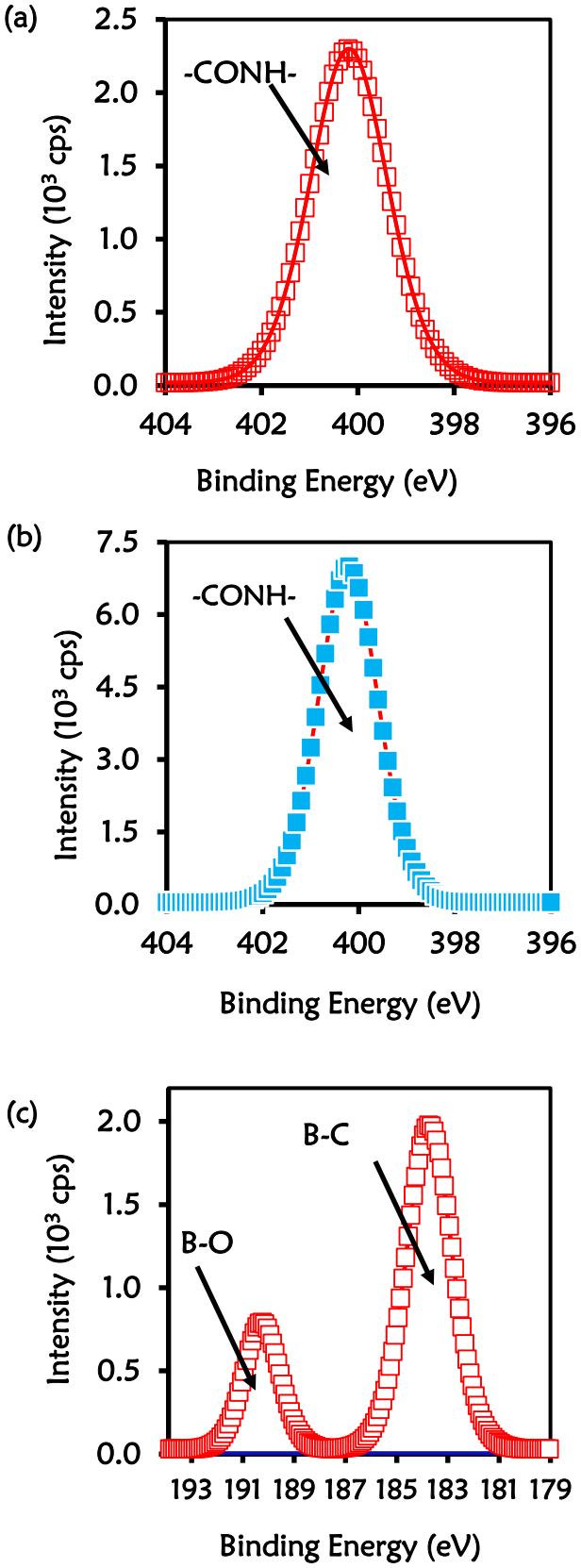

Figure 4.4: High-resolution spectra of N 1s for (a) Au-MBA-APBA SAM and (b) Au-MBA-APBA-mAb/glucose and (c) the high-resolution spectrum B 1s of Au-MBA-APBA SAM.

Table 4.1 shows the elemental composition of the different modification stages of the fabricated immunosensor. The changes in percentage (%) composition and the appearance of some elements at different stage of the modified surface confirms the successful fabrication of the immunosensor. The percentage proportion of different elements present in different environments for the Au-MBA-SAM, Au-MBA-APBA SAM and Au Au-MBA-APBA-mAb/glucose presented in **Table 4.1.**

The carbon peak seen at 288.3 eV for the Au-MBA-APBA-SAM assigned to the amide bond has a percentage composition of 6.83 %. An increase in the percentage composition of the carbon due to amide was located at 288 eV for Au-MBA-APBA-mAb/glucose was observed. The % composition was found to be 12.54 % almost twice the value obtained for the Au-MBA-APBA-SAM. This observation is attributed to the presence of carbon atoms present in the antibody molecules. Also, there is an increase in the % composition of the carbon peak situated at 286.7 (C-O, C-S) for Au-MBA SAM, C-O, C-S, and C-N for both Au-MBA-APBA-SAM, Au-MBA-APBA-mAb/glucose. The composition was found to be 4.75 % Au-MBA SAM, 11.51 % for Au-MBA-APBA-SAM, and 16.93 % for Au-MBA-APBA-mAb/glucose. This observation could be attributed to the additional carbon atoms from the APBA also, to the numerous carbon atoms present in the mAb. This also confirms the successful attachment of the mAb onto the electrode surface. The elemental composition of boron (Au-MBA-APBA SAM) was found to be 76.8% for the B-C and 23.2% for the B-O.

Table 4.1: summary of the component positions, component percentage and their assignments for different stages of the fabricated immunosensor

Surfaces	Atoms	Component positions (eV)	Assignments	Component percent (%)
Au-MBA-SAM	C 1s	284.6, 285.7	C-C, C=C, C-H	76.4, 10.2
		286.7	C-O, C,S	4.8
		288.9	O-C=O	8.7
	O 1s	531.2	C-O, O-H	87.8
		532.8	C-OH	12.2
Au-MBA-APBA	C 1s	284.6	C-C, C=C, C-H	81.7
		286.7	C-O, C-S, C-N	11.5
		288.3	O-C=O N-C=O	6.8
	O 1s	530.6	O-C, OH	82.9
		532.0	B-O	4.9
		533.4	O-C=O, N-C=O	12.2
	N 1s	400.2	N-C=O	100.0
	B 1s	184.4	B-C	76.8
		190.7	B-O	23.2
Au-MBA-APBA-mAb/glucose	C 1s	284.6	C-C, C=C, C-H	67.9
		286.3	C-O, C-S, C-N	16.9
		288.0	N-C=O, O-C=O	12.5
		292.4	π-π^*	2.6
	O 1s	530.5	O-C, OH	81.9
		531.8	B-O	7.5
		533.1	O-C=O, N-C=O	10.6
	N 1s	400.3	N-C=O	100.0

4.4. Impedimetric detection of CRP-antigen

The Au-MBA-APBA-mAb/glucose immunosensor was used to detect CRP-antigen at different concentrations ranging from 10 to 400 ng mL^{-1} using direct and sandwich immunoassay formats. The relative standard deviation (% RSD) for the direct and sandwich immunoassay at different CRP-antigen concentrations are shown in **Appendix (Table S6.1).** **Fig. 4.5** shows the Nyquist plots (a) and (b) with their corresponding linear graphs of ΔR_{CT} against CRP-antigen concentrations (a') and (b') for the (a) direct and (b) sandwich immunoassays. For the direct immunoassay, the fabricated anti-CRP mAb/glucose immunosensor was exposed to the CRP-antigen, and the impedance spectroscopy was measured. The increase in the charge transfer resistance (R_{CT}) was observed with increasing CRP-antigen concentrations. The change in total charge transfer resistance ΔR_{CT} for each CRP-antigen concentration was calculated using **Equation (3.3).** The ΔR_{CT} increased linearly with increasing antigen concentration from 10 – 100 ng mL^{-1} and a regression equation was ΔR_{CT} = 0.0117 [CRP-antigen] – 0.0301 and R^2= 0.998 (n =3) shown in **Fig. 4.5(a').** However, at higher antigen concentration, a decrease in the R_{CT} value was observed between 200 - 400 ng mL^{-1} in **Appendix Fig. S 6.3**. The decrease in R_{CT} at high CRP antigen concentration was as observed above and in the literature [340]. The sandwich immunoassay using a polyclonal antibody that recognizes different epitopes on the captured CRP-antigen was used for the signal amplification. The SIA is as discussed above.

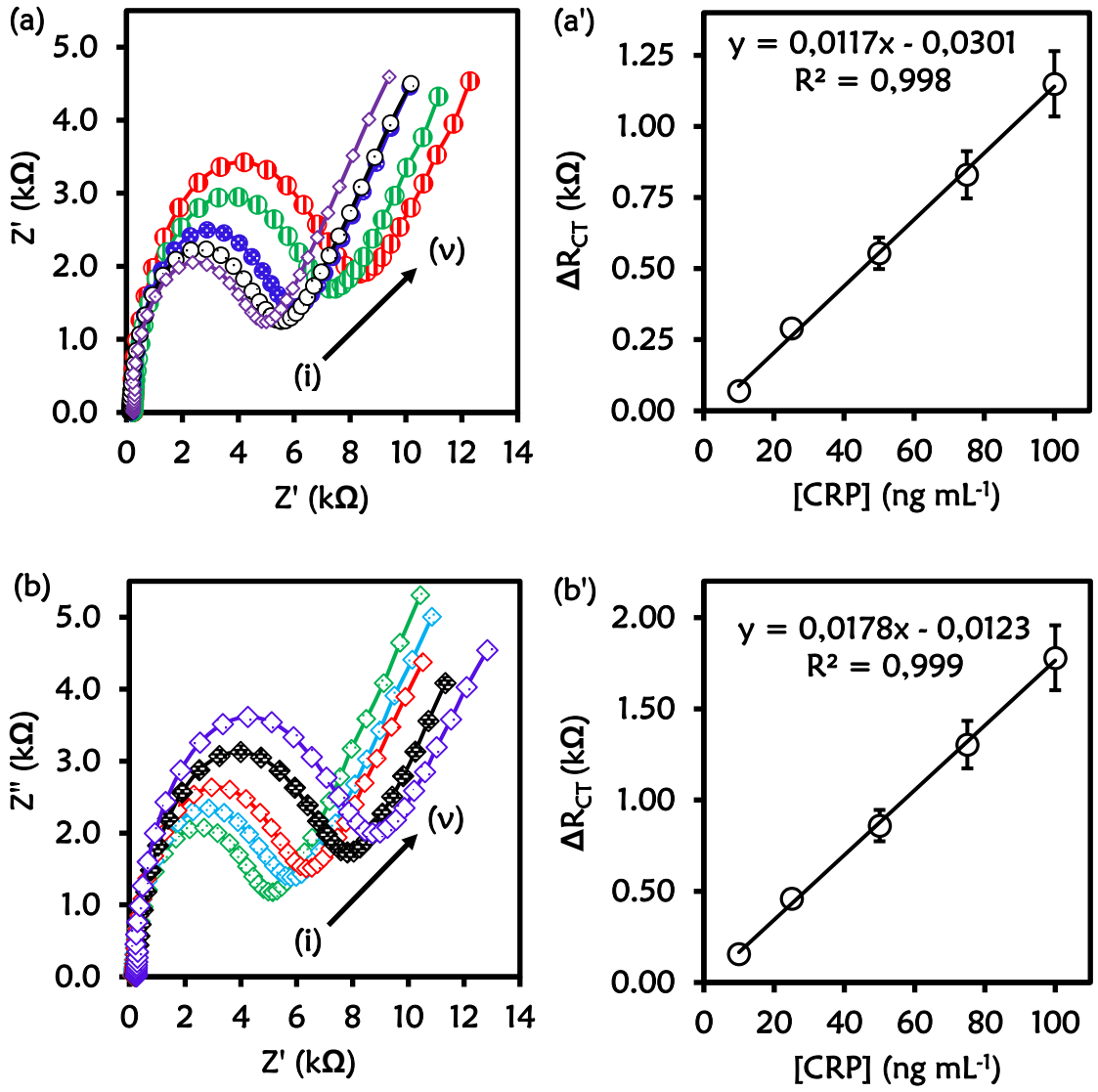

Figure 4.5: (a) and (b) Nyquist plots and (a') and (b') the corresponding callibration curves at varied CRP-antigen concentrations (i) 10 ng.ml^{-1} (ii) 25 ng mL^{-1} (iii) 50 ng mL^{-1} (iv) 75 ng.ml^{-1} and (v) 100 ng mL^{-1} for the (a) direct and (b) sandwich immunoassays. (n = 3, SD ≤ 9.0 %).

Figure 4.5(b) shows the Nyquist plots for the indirect detection of different concentrations of CRP-antigen (10 - 100 ng mL^{-1}) for the sandwich immunoassay. The pAb was kept constant at 30 μg mL^{-1}. The increase in the semicircle R_{CT} with the increasing concentration of CRP-antigen confirms that binding occurs between the mAb and CRP-antigen and lastly the pAb. The mAb-glucose/CRP-antigen/pAb immunocomplex formed and even further passivated the electrode surface due to the bulky pAb and insulating properties. The observed increase in R_{CT} was even high than that of a direct CRP-antigen immunoassay. The calibration curve is shown in **Fig. 4.5(b')** for the change in total charge transfer resistance according to **Equation (3.3).** The regression line of ΔR_{CT} = 0.0178 [CRP-antigen] – 0.0123 with R^2 = 0.999 (n =3) was obtained for sandwich immunoassay. The sensitivity of the direct immunoassay was 0.585 $k\Omega.ng^{-1}.ml.cm^{-2}$ and increased for the sandwich immunoassay 0.885 $k\Omega.ng^{-1}.ml.cm^{-2}$. The increase in the sensitivity of the sandwich immunoassay was attributed to the enhancement in the signal generated by the pAb as observed in **Fig. 4.5(b').** The key analytical parameters for evaluating the developed method and the performance are the limit of detection (LoD) and limit of quantification (LoQ). The LoD and LoQ were calculated as previously described. The LoD and LoQ for the direct immunoassay were calculated to be 2.90 and 9.66 ng mL^{-1}; respectively and the sandwich immunoassay the LoD was 1.20 and LoQ was 3.97 ng mL^{-1}. The lower LoD and LoQ for the sandwich immunoassay were attributed to the high sensitivity and the signal amplification. The fabricated immunosensor is highly sensitive and shows lower LoDs and LoQs. The enhanced detection and better analytical properties of the designed immunosensor is further attributed to the oriented immobilization of the capture monoclonal anti-CRP antibody (mAb). This method of immobilizing mAb via Fc specific

region boronate ester allows for the CRP-antigen site to be exposed to the analyte (CRP-antigen). Lower LoDs 2.90 ng mL^{-1} and 1.20 ng mL^{-1} and LoQs 9.66 ng mL^{-1} and 3.97 ng mL^{-1} for direct and sandwich immunoassays are respectively reported for the detection of human CRP-antigen. As previously shown in **Table 3.3** the analytical performance of the immunosensor reported in this chapter is better than the fabricated immunosensor in chapter three. The enhanced analytical performance exhibited in terms of LoD, LoQ and the sensitivity could be attributed to the effect of chain length of the linker [364]. A similar case has been reported in the literature with short chain and long chain phenylboronic acid (PBA) modified surface. It was found that the long chain phenylboronic acid modified surface gave a better LoD than the short chain PBA. The explanation for this was based on the fact that the antibody is a big macromolecule that needs enough space for interaction. The short chain PBA could not offer enough space for antibody interaction unlike, the long chain PBA which could offer enough space for the antibody interaction with boronic acid [187].

The LoD of the impedimetric immunosensor decreased from 6.23 ng mL^{-1} for the (SIA) in the previously fabricated (Au-MPBA-mAb/glucose) immunosensor to 1.20 ng mL^{-1} for the Au-MBA-APBA-mAb/glucose immunosensor. The higher sensitivity values obtained for both DIA and SIA of the Au-MBA-APBA-mAb/glucose electrode could be attributed to the effect of chain length of the linker compare with the Au-MPBA-mAb/glucose immunosensor. The sensitivity of the Au-MPBA-mAb/glucose was 0.691 $k\Omega.ng^{-1}.ml.cm^{-2}$ and 0.885 $k\Omega.ng^{-1}.ml.cm^{-2}$ for the Au-MBA-APBA-mAb/glucose for the SIA. The performance of the immunosensor was compared with some of the immunosensor previously reported in the literature as shown in **Table 3.3.** The obtained result (LoD) was better than some of those previously reported **in Table 3.3.** The LoD (1.20 ng mL^{-}

^{1}) of the fabricated immunosensor was better than the impedimetric immunosensor reported by Gupta et al. (LoD, 11 ng mL^{-1}) [235], Puri et al. (LoD, 30 ng mL^{-1}) [230] and Rajesh et al. (3.5 ng mL^{-1}) [234]. The lower LoD could be attributed to the oriented immobilization strategy employed in this work. However, the developed immunosensors reported by Chen et al. [232], Zhou et al. [229], and Lv et al. [345] gave a better LoD than the one reported in this chapter (**Table 3.3)**. The lower limit of detection reported by Zhou et al. [229], and Lv et al. [345] could be attributed to the incorporation of quantum dot labelled detection probe. The fluorescence labelled technique requires additional time and quite expensive than the label-free method in this work. Hence the developed immunosensor provides a simple low-cost technique for the detection of CRP-antigen.

4.5. Specificity and the reproducibility of the immunosensor

To assess the specificity of the immunosensor, a control experiment was carried out with the direct interaction of the anti-CRP mAb modified gold electrode with the polyclonal anti-CRP antibody (pAb). The R_{CT} is for the CRP-antigen was found to be 5.46 kΩ, and after exposure to pAb, the R_{CT} changed to 5.48 kΩ showing no change in R_{CT}. This shows that the increased in total charge-transfer resistance (ΔR_{CT}) between anti-CRP antibody (mAb) and CRP-antigen in **Fig. 4.5** is due to the formation of an immunocomplex. The reproducibility of the immunosensor was investigated since it is a crucial factor to be considered in real life application. Three different immunosensors were prepared independently at the same experimental condition and tested for the same concentration of CRP-antigen. The relative standard deviation of (% RSD) for the immunosensor was 5.84 % for the direct immunoassay and 4.23 % for the sandwich immunoassay for the tested 50 ng mL^{-1} CRP-antigen concentration.

4.6. Analysis in serum sample

The accuracy of the proposed immunosensor for the detection of CRP-antigen was investigated in serum sample through a recovery experiment. The recovery test was carried out in 10% new calf serum. Two different CRP-antigen concentrations (25 and 50 ng mL^{-1}) were used for the recovery experiment. The percentage obtained from the recovery test was between 91.18 – 96.47%. The amount recovered was very close to 100%. This shows that the fabricated immunosensor can be applied in clinical applications for the analysis of CRP-antigen.

Table 4.2: Spike and recovery results obtained from the fabricated CRP immunosensor in serum samples

Sample no	Spiked (ng mL^{-1})	Found (ng mL^{-1})	Recovery (%)
1	25 (DIA)	27.30	95.87
2	25 (SIA)	26.50	96.47
3	50 (DIA)	49.90	94.94
4	50 (SIA)	49.00	91.18

4.7. Conclusion

This work demonstrated the fabrication of electrochemical impedimetric immunosensor for the detection of C-reactive protein antigen. The electrochemical characterization and X-ray photoelectron spectroscopy was used to confirm the formation of self-assembled monolayers of mercaptobenzoic acid and coupling of aminophenylboronic acid via an amide bond. The increase in the intensity of C 1s, O 1s, and N 1s confirmed the immobilization and coupling (via an amide bond and boronate ester) of various materials studied. An excellent sensitivity of the immunosensor was obtained to be 0.585 $k\Omega.ng^{-1}.ml.cm^{-2}$ for the direct immunoassay. A better sensitivity was obtained for the sandwich immunoassay to be 0.885 $k\Omega.ng^{-1}.ml.cm^{-2}$ and almost double that of the direct immunoassay. The excellent sensitivity was ascribed to the linker for the oriented immobilization via boronate ester targeting an Fc region of the capture anti-CRP monoclonal antibody. The analytical parameters for the immunosensor for direct immunoassay were calculated to be 2.90 ng mL^{-1} for LoD and 9.66 ng mL^{-1} for LoQ. For the sandwich immunoassay, the enhanced analytical parameters were 1.20 ng mL^{-1} for the LoD and 3.97 ng mL^{-1} for the LoQ. The immunosensor showed good reproducibility with %RSD of 5.84% for the direct immunoassay and 4.23% for sandwich immunoassay. The fabricated immunosensor showed promising results towards the label-free detection of C-reactive protein in clinical applications.

Chapter 5:

Electrochemical Impedimetric Immunosensor using Electrografting method

5.0. Preamble

Nanomaterials modified with different probes on the surface offers a great advantage for diagnostic applications [365]. Magnetic nanoparticles (MNPs) have attracted international research attention in various applications including the fabrication of immunosensors. Their unique properties which include high surface-to-volume ratio, biocompatibility, signal amplification and their ability to bind antibodies onto their surfaces via their functional groups [366,367].

From the previous chapters, self-assembled monolayer (SAMs) has been used for the electrode modification and then antibody immobilization. In this chapter a more stable method that utilizes electrochemical grafting of aryl diazonium salt will be investigated. Electrochemical grafting is a simple and versatile method which enables the stability of the grafted organic layer on many conductive [368–371] and semiconducting surface [372]. The reduction of diazonium salt unto carbon surfaces was first demonstrated by Pinson and co-workers to yield a very stable functional layer [368]. Since then, surface modification using diazonium salt has been broadly used due to their excellent method to covalently attach molecules to carbon, Si and metal surfaces [373]. The strong covalent bond form between the aryl diazonium salts and the gold surface enhances the stability of the electrografted surface compared to SAMs [374–377].

Self-assembled monolayers (SAMs) of thiolated molecules on gold have been widely used because of the strong affinity between the thiol (SH) groups and the gold surface [378,379]. SAMs have found widespread applications, but still associated with some drawbacks: the surface modification is time-consuming (24 hrs to obtain a closed-packed monolayer), the stability of SAM platform can be affected on exposure to UV

irradiation [377], electrical potentials [380], and high temperatures [381,382]. Electrochemical grafting addresses some of these drawbacks [375] and offers several advantages in terms of stability, speed, and simplicity [381,383]. Electrografting of aryl diazonium proceeds via the electrochemical reduction and generation of aryl radical which attaches onto the surface and form surface carbon bond. The surface can be metal (M-C bond) [384,385], and carbon (C-C bond) [386,387]. The work recently studied have shown that the diazonium forms on a gold surface have received much attention [369,388,389], and their use in sensor fabrication [375]. Hence the method being explored in this thesis.

The immunosensor was fabricated using the electrochemical reduction of 4-aminoethyl benzene diazonium (AEBD) salt. The surface was further derivatized with succinic anhydride to have a carboxylic derivatized surface. Carbodiimide chemistry was used to form a covalent linkage between the amine group on the APBA and the -COOH terminal group from the succinylated surface. Oriented immobilization of the capture antibody (monoclonal mouse anti-human CRP) onto the electrode surface was achieved via affinity boronate ester interaction. Afterwards, a highly sensitive immunoprobe (anti-CRP phenylboronic acid functionalized magnetic nanoparticles) for the detection of CRP biomarker was introduced. The immunoprobe was achieved by first synthesizing the phenylboronic acid functionalized magnetic nanoparticles. The pAb (detection antibody) was conjugated to the synthesized nanoparticles to obtain a novel highly sensitive immunoprobe for the detection of CRP-antigen.

The effect of linker's chain length and immunoprobe signal enhancement was studied. SIA immunoassay was used for the detection of CRP-antigen in this chapter because

results from the two previous chapters establish the fact that the SIA gave the best analytical response.

The synthesis of the phenylboronic acid functionalized magnetic nanoparticles was achieved by first synthesising the pentanoic acid terminated phenylboronic acid compound **(3).** This compound was then conjugated to APTES functionalized magnetic nanoparticles.

5.1. Synthesis and characterization of pentanoic acid terminated phenylboronic acid (3)

The synthesis of **(3)** was carried out by the reaction of 4-aminophenylboronic acid **(1)** with glutaric anhydride **(2)** in carbonate buffer pH 9.2 to obtain **(3).** Compound **(3)** was further conjugated to APTES functionalized magnetic nanoparticles (MNP-SiO-APTES) using carbodiimide chemistry to yield the phenylboronic acid functionalized magnetic nanoparticles (MNP-SiO-APTES-PBA), **Scheme 5.1**

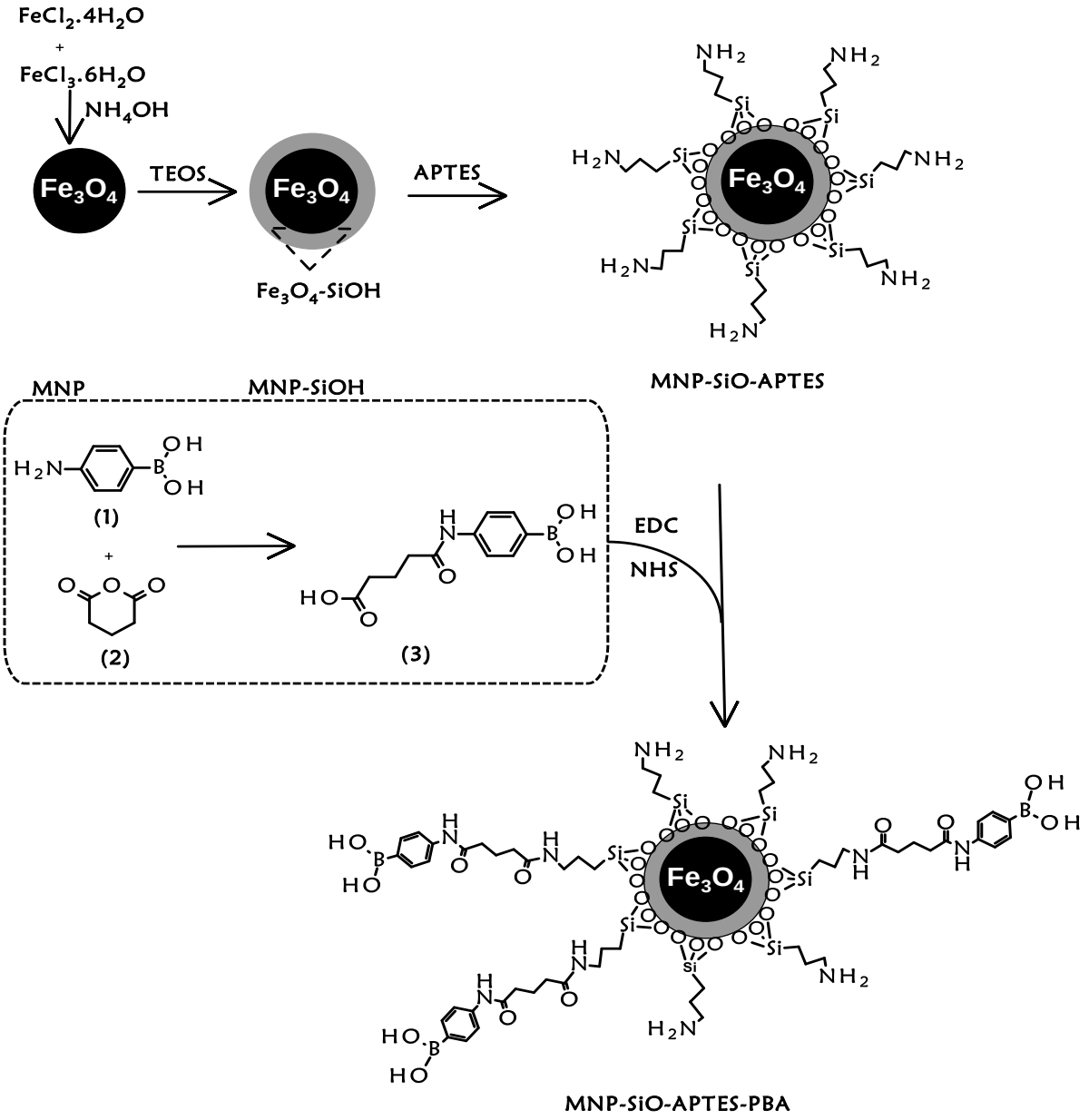

Scheme 5.1: Reaction pathway for the synthesis of MNP-SiO-APTES-PBA

5.1.1. FTIR result

The FTIR spectrum of 4-aminophenylboronic **(1)** in **Fig. 5.1(a)** shows an OH peak at 3312 cm^{-1} and the NH_2 peak at 3516 cm^{-1}. The peak at 2897 cm^{-1} corresponds to aromatic C-H. The B-O vibrational mode was observed at 1381 cm^{-1}. The FTIR spectrum of glutaric anhydride **(2)** in **Fig. 5.1(b)** exhibit the carbonyl peak (C=O) at 1792 and 1746 cm^{-1}. The FTIR spectrum of pentanoic acid terminated phenylboronic acid **(3) Fig. 5.1(c)** revealed an OH peak at 3322 cm^{-1} due to the carboxylic acid functional group. The peaks between 3198 - 2625 cm^{-1} were assigned to the stretching vibration of aromatic C-H. The observed shift of the C=O peak from 1792 cm^{-1} for glutaric anhydride to 1690 cm^{-1} for compound **(3)**. The formation of the pentanoic acid terminated phenylboronic acid was as a result of the opening of the glutaric anhydride ring. The observed spectra changes are indications of the formation of compound **(3).** The formation of compound **(3)** was further confirmed by the disappearance of the NH_2 peak at 3516 cm^{-1} from the 4-aminophenylboronic acid. The peak at 1384 cm^{-1} was assigned to B-O vibrational mode was retained. Also, a slight shift was observed (3 cm^{-1}) from 1381 cm^{-1} before and 1384 cm^{-1} after the formation of compound **(3).**

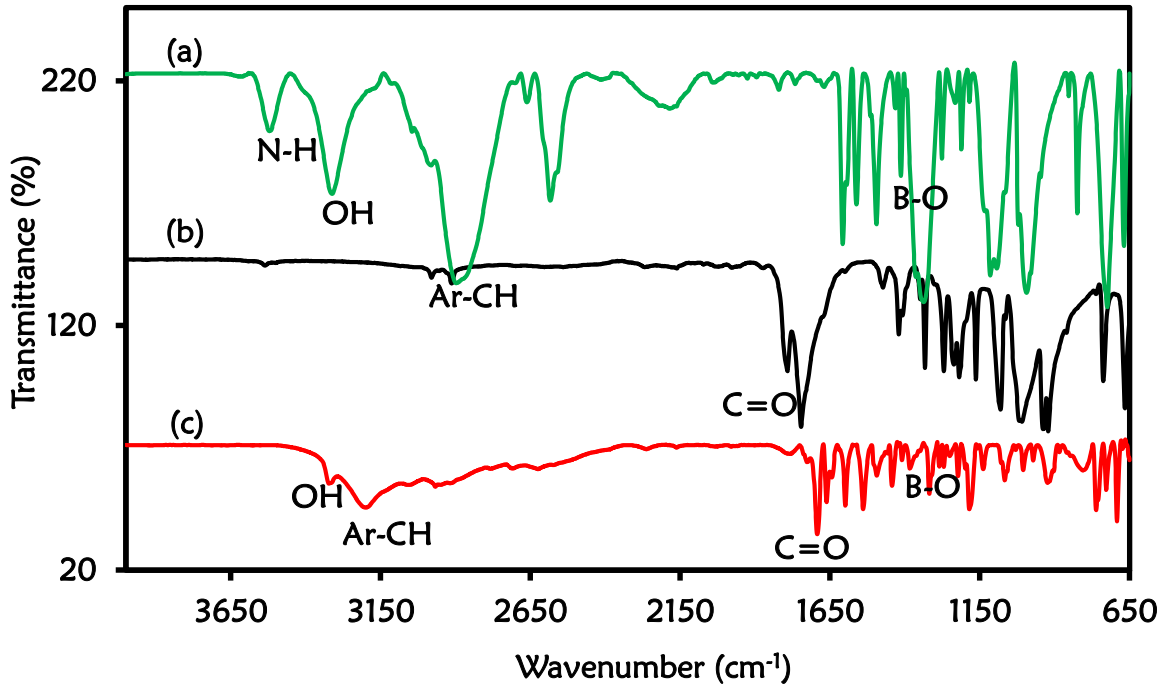

Figure 5.1: FTIR (a) 4-aminophenylboronic acid (b) glutaric anhydride (c) 5-(4-boronoanilino)-5-oxopentanoic acid **(3).**

5.1.2. ^{1}H NMR characterization of (3)

The ^{1}H NMR spectrum of compound **(3)** is shown in **Appendix Fig. S6.5.** Spectrum revealed the purity of compound **(3)** and the expected proton after integrating the peaks confirms the successful synthesis. The ^{1}H NMR spectrum of 4-aminophenylboronic acid **Appendix Fig. S6.6(a)** revealed the splitting of 4 protons in the aromatic region between 7.28 - 7.33 ppm and 7.85 - 7.87 ppm. The 2 protons were observed between 7.28 - 7.33 ppm while the other 2 protons were seen around 7.85 - 7.87 ppm. The splitting could result from the fact that the four aromatic protons are in a different environment. Two protons were close to boron element, and the remaining two were seen around NH_2. **Appendix Fig. S6.6(b)** shows the ^{1}H NMR spectrum of glutaric anhydride. The six protons of the methylene groups (CH_2) were observed at 1.86 - 1.90

ppm and 2.70 - 2.72 ppm. From the structure of the glutaric anhydride, one of the methylene group next to the carbonyl carbon will see the two neighbouring protons of the CH_2 and will show triplet splitting. The triplet peak is presented as one peak because they are symmetric and in the same chemical environment. The CH_2 peak in the middle will see two of the neighbour's CH_2, and the peak is presented as multiplet around 1.86 - 1.90 ppm. ^{1}H NMR spectrum of compound **(3)** provided the characteristics chemical shift for the expected structure. The OH of the carboxylic acid was observed with a broad peak around 12.01 ppm. The NH peak was seen around 9.92 ppm. Four aromatic protons were observed between 7.55 - 7.88 ppm. Six protons were observed for the CH_2 group between 1.71 - 2.35 ppm. The OH group attached to the boron was seen around 3.38 ppm presenting a singlet peak because they are in the same chemical environment. The integration and the assignments confirm the successful synthesis of compound **(3).**

5.2. Characterization of synthesized and modified magnetic nanoparticles

The method in **Scheme 5.1** was followed for the synthesis of magnetic nanoparticles by the co-precipitation of ferric and ferrous salts ($FeCl_3$ and $FeCl_2$) in aqueous solution. Citric acid was used to stabilize the magnetic nanoparticles through direct addition method. The addition of citric acid acts as a dispersing agent during the co-precipitation process, this enhances the stability of the nanoparticles and prevent nanoparticles agglomeration. The citric acid stabilized magnetic nanoparticles (MNPs) were encapsulated in silica using TEOS through Stober method [390]. The formation of silica coating around the surface of the MNPs helps to prevent aggregation and improve stability. It also provides a scaffold for the attachment of different functional groups [391,392]. The silica-coated magnetic nanoparticles (MNP-SiOH) were further

functionalized with APTES to give an amine functionalized magnetic nanoparticles (MNP-SiO-APTES). APTES is a common amino silane coupling agent used for surface modification.

5.2.1. FTIR results for the synthesized magnetic nanoparticles

The FTIR spectra of the MNPs and the MNP-SiOH are shown in Appendix **Fig. S6.7(a) and (b).** The absorption band around 543 cm^{-1} Appendix **Fig. S6.7(a)** is ascribed to the Fe-O stretching vibrational mode of the MNPs. The peak at 1576 is assigned to C=O vibration from the citric acid. This is an indication of the binding of the citric acid to the surface of the MNPs [393]. The coating of the MNPs with silica was verified with the FTIR spectrum of the silica-coated magnetic nanoparticles Appendix **Fig. S6.7(b).** The MNP-SiOH shows a broad OH peak at 3380 cm^{-1}, additional peaks at 1069 cm^{-1} and 947 cm^{-1} indicate the absorption band of siloxanes (Si-O-Si) and silanol (Si-OH) groups, respectively [392,394]. This confirms the successful coating of the magnetic nanoparticles with silica.

Figure 5.2(a) shows the FTIR spectrum of compound **(3),** which was synthesized in **Scheme 5.1** and discussed above. **Figure 5.2(b)** shows the spectrum of MNP-SiO-APTES, exhibiting the two peaks at 3277 cm^{-1} and 1620 cm^{-1} corresponding to N-H stretching vibration and NH_2 stretching [395]. Compound **(3)** was conjugated onto MNP-SiO-APTES to form phenylboronic acid functionalized magnetic nanoparticles (MNP-SiO-APTES-PBA) via the EDC/NHS coupling. The C=O bond of the amide group in **Fig. 5.2(c)** was observed at 1647 cm^{-1} [396]. Also, the absorption peak at 1391 cm^{-1} was ascribed to the stretching vibration of (B-O) [397]. The broad OH bond also confirms

the successful conjugation of compound **(3)** onto MNP-SiO-APTES to form MNP-SiO-APTES-PBA.

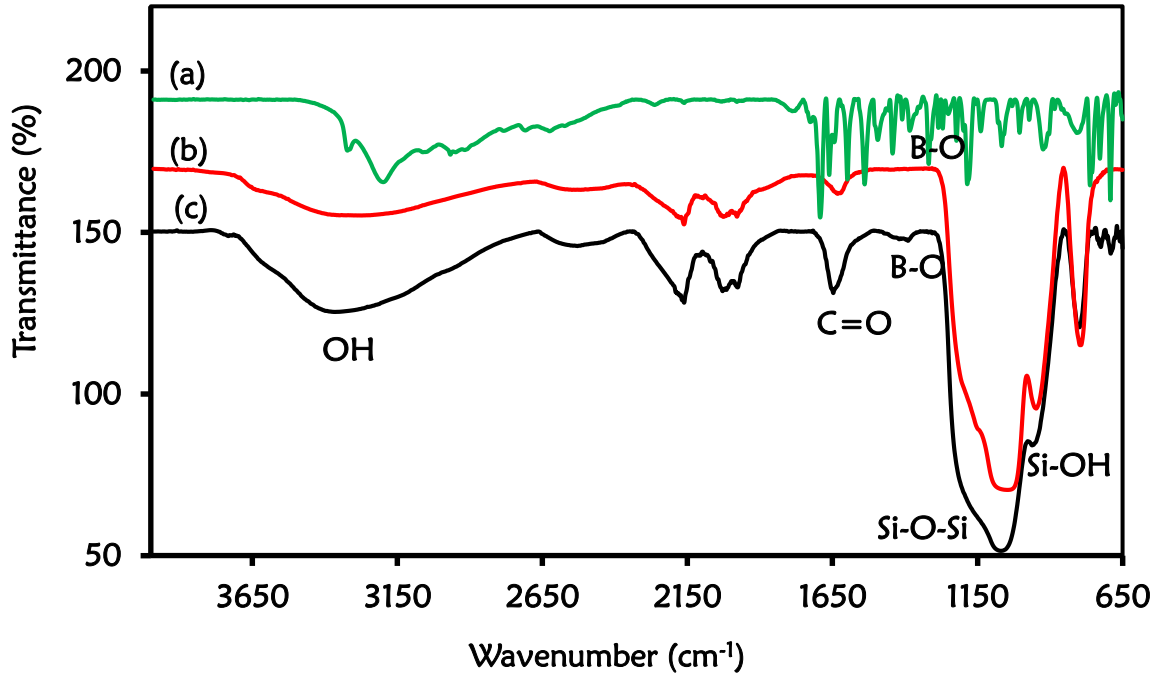

Figure 5.2: FTIR (a) 5-(4-boronoanilino)-5-oxopentanoic acid (b) MNP-SiO-APTES, and (c) MNP-SiO-APTES-PBA.

5.2.2. XRD patterns of the magnetite nanoparticles

Figure 5.3 shows XRD diffractograms of (a) MNPs, (b) MNP-SiOH, (c) MNP-SiO-APTES, and (d) MNP-SiO-APTES-PBA. The diffraction peaks at 2θ equal to 30.6°, 35.9°, 43.6°, 54.1°, 57.6°, and 63.2° were observed indicative of a cubic spinel structure of the magnetite. The XRD diffractograms in **Fig. 5.3(a)** clearly revealed the formation of the MNPs. The diffraction peaks show the characteristic of magnetite which were indexed for the following Miller Indices (220), (311), (400), (422), (511) and (440) [398,399]. Similar peaks were also obtained for the functionalized magnetic nanoparticles showing that the MNPs was stable. The crystalline phase of MNPs during silica coating and

subsequent functionalization remain intact. The functionalized magnetic nanoparticles still retain their magnetic properties when exposed to magnetic field. Similar diffractograms were obtained for the MNP-SiOH in **Fig. 5.3(b),** MNP-SiO-APTES in **Fig. 5.3(c)**, and MNP-SiO-APTES-PBA in **Fig. 5.3(d).** The diffraction peaks decreased in intensity after coating and functionalization due to the silica shell formation.

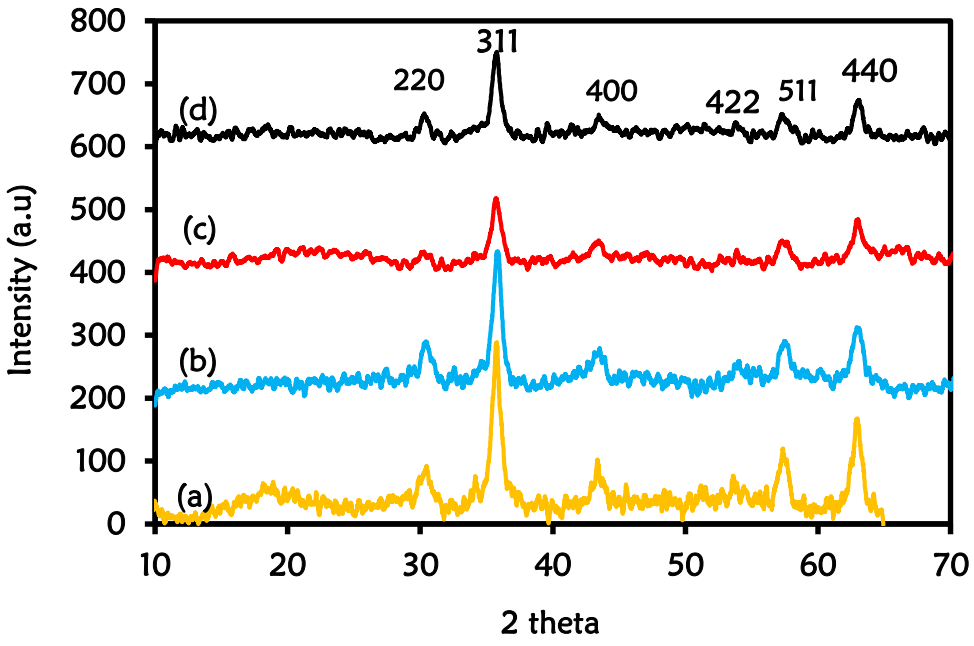

Figure 5.3: XRD diffractograms nanoparticles of (a) MNPs (b) MNP-SiOH (c) MNP-SiO-APTES, and (d) MNP-SiO-APTES-PBA.

5.2.3. Transmission electron microscopy (TEM)

Figure 5.4 shows the TEM micrographs of (a) MNPs (b) MNP-SiOH (c) MNP-SiO-APTES, and (d) MNP-SiO-APTES-PBA. TEM images of the nanoparticles revealed the morphology of the magnetic nanoparticles at different modification stages. The magnetic nanoparticles were spherical in shape. The size distribution of the nanoparticles was shown in histograms with their average diameter. **Fig. 5.4(a)** shows

the TEM image of the magnetic nanoparticles with an average diameter of 11 ± 1.76 nm. The size distribution of the magnetic nanoparticles ranges from 9 to 14 nm with the majority of the nanoparticles between 10 and 12 nm having the highest distribution. The image of the silica-coated magnetic nanoparticles in **Fig. 5.4(b)** showed an increase in nanoparticle size from 10 to 23 nm. This is attributed to the formation of the silica shell around the core of the magnetic nanoparticles. This confirms the coating of the magnetic nanoparticles with the silica. The size distribution was observed between 20 and 26 nm, and the highest distribution was seen around 22 and 24 nm. The average diameter was found to be 23 ± 1.4 nm. The diameter of the APTES functionalized magnetic nanoparticles **Fig. 5.4(c)** was 25 ± 1.2 nm. MNP-SiO-APTES-PBA is shown in **Fig. 5.4(d)** with an average size of 28 ± 1.2 nm. The size distribution ranges from 25 – 31 nm with the highest distribution between 27 – 29 nm. The successive increase in the particle size diameter after each modification is an indication of the successful functionalization of the magnetic nanoparticles.

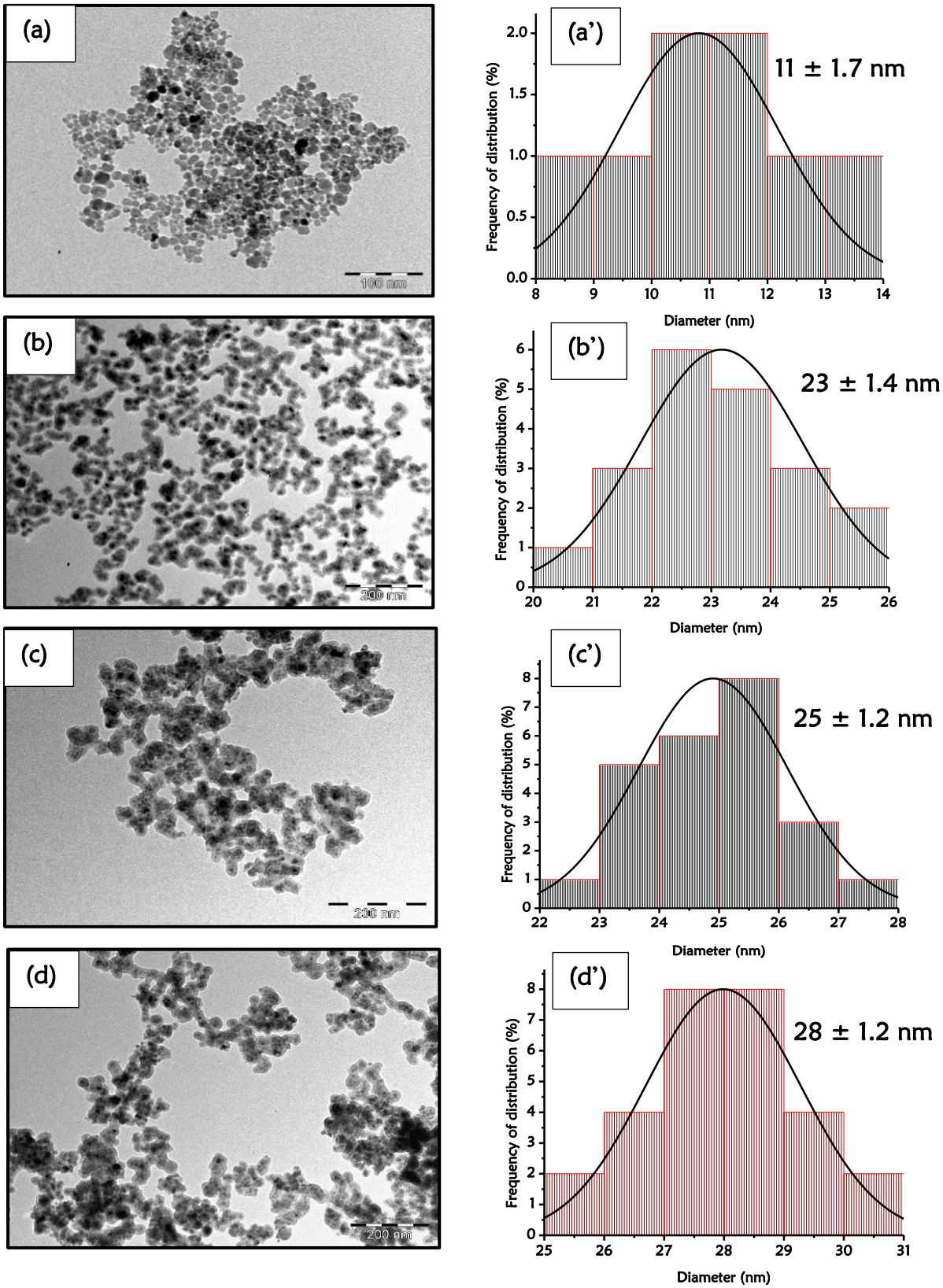

Figure 5.4: TEM images of (a) MNPs (b) MNP-SiOH (c) MNP-SiO-APTES, and (d) MNP-SiO-APTES-PBA and their corresponding histogram showing the size distribution.

5.2.4. Energy dispersive X-ray spectroscopy (EDS)

The EDS spectra in **Fig. 5.5** shows the elemental compositions that are present in (a) MNPs (b) MNP-SiOH, (c) MNP-SiO-APTES, and (d) MNP-SiO-APTES-PBA. The result confirms the presence of the expected elements which are iron and oxygen for the MNPs, in **Fig. 5.5(a)**. The chlorine peak observed in the spectrum **Fig. 5.5(a)** is from the metal salts ($FeCl_3$ and $FeCl_2$) used for the synthesis of the magnetic nanoparticles (MNPs). The formation of silica shell using tetraethoxysilane resulted in the appearance of silica and an increase in oxygen peak, **Fig. 5.5(b).** The iron still remain intact. The chlorine disappeared. The presence of silica peak confirms the successful coating of nanoparticles with silica. Also, the result showed a decrease in the iron peak which could be attributed to the formation of a thin layer of silica shell around the magnetic nanoparticles. An increase in the oxygen peak could be from TEOS. **Figure 5.5(c)** represents the APTES functionalized magnetic nanoparticles, carbon was observed and minute or very small nitrogen peak due to the aminoethyl moiety. A slight reduction was observed in the intensity of the iron peak. The presence of boron element in **Fig. 5.5(d)** (MNP-SiO-APTES-PBA) revealed the successful conjugation of the magnetic nanoparticles to pentanoic acid terminated phenylboronic acid. The presence of silica peak throughout the measurements is an indication that the silica coating is not affected by subsequent functionalization. The magnetic nanoparticles is a magnetic core surrounded by the silica shell.

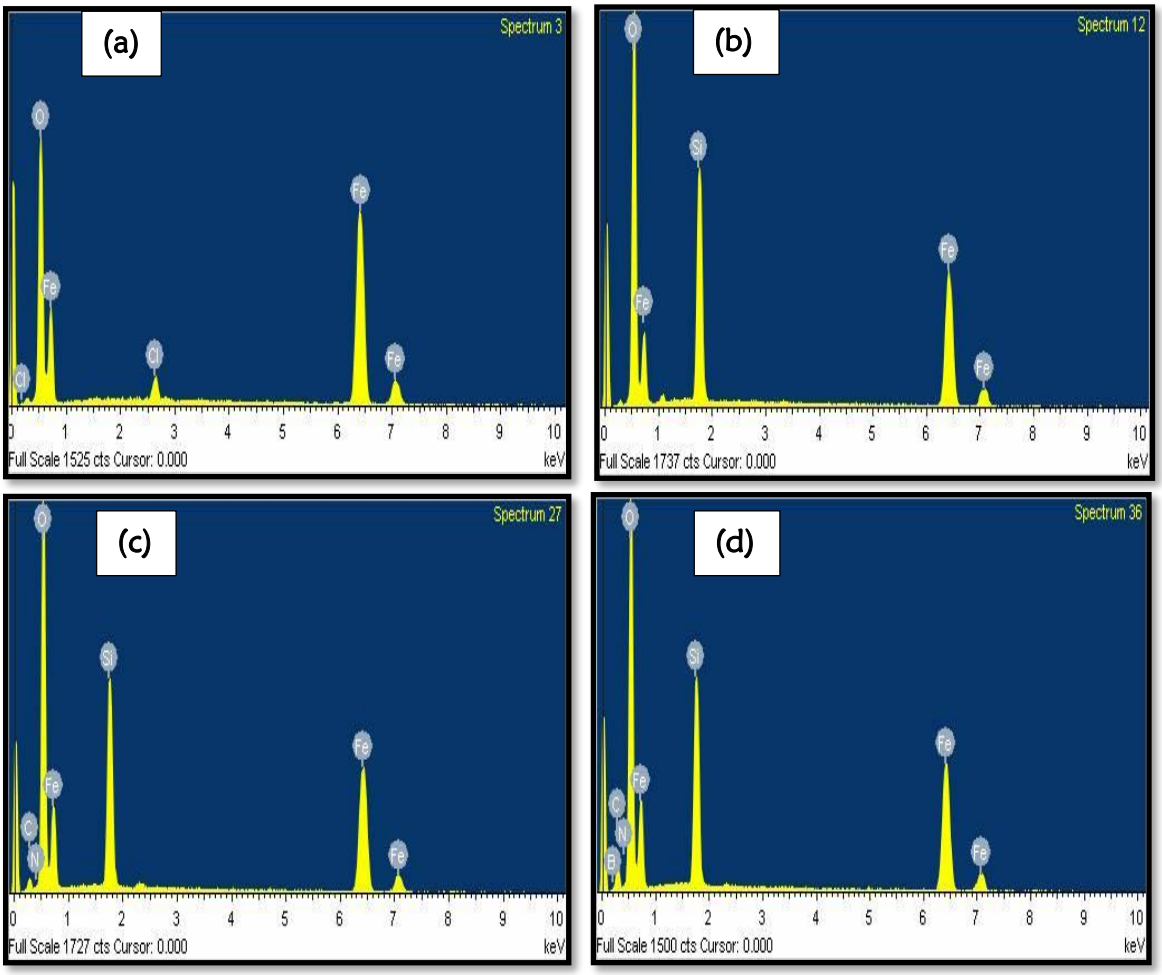

Figure 5.5: EDS images of (a) MNPs (b) MNP-SiOH (c) MNP-SiO-APTES, and (d) MNP-SiO-APTES-PBA.

The percentage composition of the element is presented in **Table 5.1.** A decrease in iron composition was observed from 63.80 % for MNPs to 29.45 % for MNP-SiO-APTES and to 21.94 % for MNP-SiO-APTES-PBA. This was accompanied by the emergence of silica from the shell at MNP-SiOH (20.11 %), 18.54 % at the MNP-SiO-APTES, and 16.49 % at MNP-SiO-APTES-PBA. The emergence of Nitrogen at the MNP-SiO-APTES (1.95%) and an increase in MNP-SiO-APTES-PBA (3.75 %) confirmed the functionalization. Boron (6.62 %) confirmed the functionalization with PBA.

Table 5.1: EDS result showing percentage composition of the element in the nanoparticles

Nanoparticles	Weight (%) composition element						
	Fe K	Cl K	O K	Si K	N K	C K	B K
MNPs	63.8	2.20	34.0	-	-	-	
MNP-SiOH	29.5	-	50.4	20.1	-	-	
MNP-SiO-APTES	26.2	-	49.8	18.5	1.9	3.6	
MNP-SiO-APTES-PBA	21.9		46.2	16.5	3.8	5.0	6.6

5.2.5. Zeta potential measurement characterization of MNPs

The zeta potential of the aqueous solutions of the citric acid stabilized magnetic nanoparticles (MNPs), and the functionalized magnetic nanoparticles were measured. This study was conducted in order to verify the surface charge thus confirming, the successful surface modification. The zeta potential was measured as a function of solution pH. **Figure 5.6** shows the zeta potential graphs of various nanoparticles measured at varying pH conditions (a) MNPs (b) MNP-SiOH (c) MNP-SiO-APTES, and (d) MNP-SiO-APTES-PBA. **Figure 5.6(a)** shows the zeta potential measurement for the bare MNPs. The magnetic nanoparticles showed a negatively charge surface from pH 2 – 12, and this is attributed to the presence of negative charged citric acid on the surface of the nanoparticles. The zeta potential was more negative as the pH increased. The higher the zeta potential, that is > +30 mV or > -30 mV, the more stable the nanoparticles. The MNPs exhibited zeta potential >-30 mV after pH 4. The zeta potential of the MNP-SiOH is shown in **Fig. 5.6(b).** The zeta potential of the MNP-SiOH exhibited a pH-dependent zeta potential values and stability at pH > 4 with high

> 30 mV zeta potential. The higher the pH, the more negative the zeta potential value. This is an indication of the presence of negative charges at the surface of the nanoparticles due to the OH group from the silica shell.

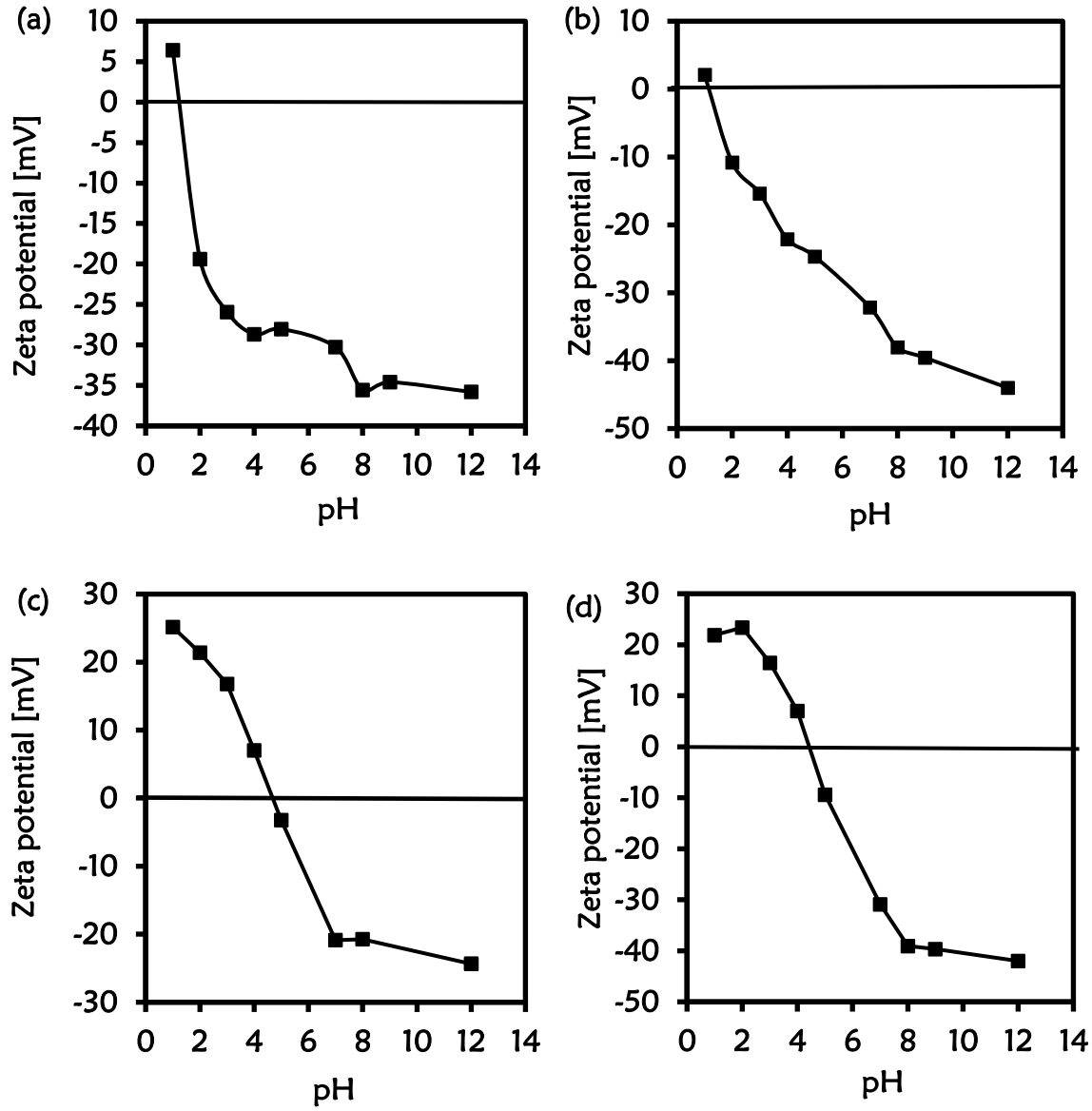

Figure 5.6: Zeta potential of (a) MNPs (b) MNP-SiOH (c) MNP-SiO-APTES, and (d) MNP-SiO-APTES-PBA.

The APTES functionalized magnetic nanoparticles (MNP-SiO-APTES) Fig. 5.6(c), showed a positive potential between pH 1 – 4. The change in zeta potential could be attributed to the presence of positive charges (NH_3^+) on the surface of the nanoparticles. This confirmed the successful modification of the magnetic nanoparticles with APTES. The zeta potential of MNP-SiO-APTES-PBA is presented in **Fig. 5.6(d).** Positive zeta potential values were observed with the phenylboronic acid functionalized magnetic nanoparticles at pH < 4. Similar to the zeta potential values obtained with the APTES functionalized magnetic nanoparticles. However, at higher pH > 5 the MNP-SiO-APTES-PBA showed negative zeta potential values. The stability of the MNP-SiO-APTES-PBA was favoured at high pH > 6 as the charge was less than -30 mV. This observation also confirms the successful functionalization of the phenylboronic acid modified magnetic nanoparticles.

The other information that can be obtained from the plot of zeta potential with pH is the isoelectric point (IEP). IEP is the pH at which zeta potential of the nanoparticles is at 0 mV. The IEP of the citric acid stabilized MNPs was observed at pH 1.1 which was lower than the IEP of pure magnetic nanoparticles reported in the literature. The observed shift to the negative potential is attributed to the presence of carboxylate group on the MNPs which was obtained from the citric acid used to stabilize the MNP [400]. A similar trend was observed with the silica-coated magnetic nanoparticles. However, after the modification with APTES, the IEP of the APTES functionalized magnetic nanoparticles (MNP-SiO-APTES) shifted to a higher pH value (4.7) that is towards the positive potential. This is attributed to the positive charge present at the surface of the APTES functionalized MNPs. The observed changes is an indication of the successful modification of the APTES functionalized MNPs.

5.2.6. XPS characterization

XPS analysis was used to confirm the synthesis of the citric acid stabilized MNPs and the different modification stages of the magnetic nanoparticles. Also, the conjugation of the polyclonal anti-CRP antibody unto MNP-SiO-APTES-PBA was ascertained with the XPS. **Figure 5.7** shows the survey spectra of (a) MNPs, (b) MNP-SiO-APTES, and (c) MNP-SiO-APTES-PBA. The XPS survey spectrum of the MNPs is shown in **Fig. 5.7(a),** and the peaks observed showed the presence of Fe, C, and O. The observed peaks were at 54 eV, 88 eV, 283 eV, 531 eV, 711 eV, and 722 eV were at the binding energies of Fe 3p, Fe 3s, C 1s, O 1s, Fe $2p^{3,}$ and Fe $2p^{1}$ respectively. The atomic percentage (at %) of Fe, C, and O were obtained to be 31.3 %, 30.2 %, and 38.5 %. The presence of carbon in the MNPs is attributed to the citric acid used to stabilize the MNP. Furthermore, the presence of silica coating on the MNP was confirmed from the survey scan in **Fig. 5.7(b)** with the appearance of two new peaks at 100 eV and 151 eV. These two peaks were assigned to the binding energies of Si 2p (100 eV) and Si 2s (151 eV). The disappearance of the Fe peaks (Fe 3p, Fe 3s, Fe 2p, and the Fe Auger peaks) in the MNP-SiO-APTES was observed **Fig. 5.7(b).** This observation could be attributed to the formation of a silica shell around the MNPs. The % of the carbon composition in MNP-SiO-APTES increased from 30.2 to 71.7 %. The high increase in the carbon content is attributed to the presence of carbon from the APTES. A reduction in the oxygen composition of the MNP-SiO-APTES was observed from 38.5 (MNP) to 20.5 %. The higher % composition obtained for the MNPs is attributed to the oxygen present in the citric acid. At MNP-SIO-APTES-PBA in **Fig. 5.7(c)** the emergence of boron element was observed. This was a confirmation of the successful conjugation of pentanoic acid terminated phenylboronic acid forming MNP-SIO-APTES-PBA. The presence of N 1s also confirms

the successful formation of the amide linkage between the EDC/NHS activated COOH terminated end of compound **(3)** and MNP-SiO-APTES. The % composition for C, N, B, and O were found to be 33.8 %, 5.6 %, 6.88 %, and 33.9 %.

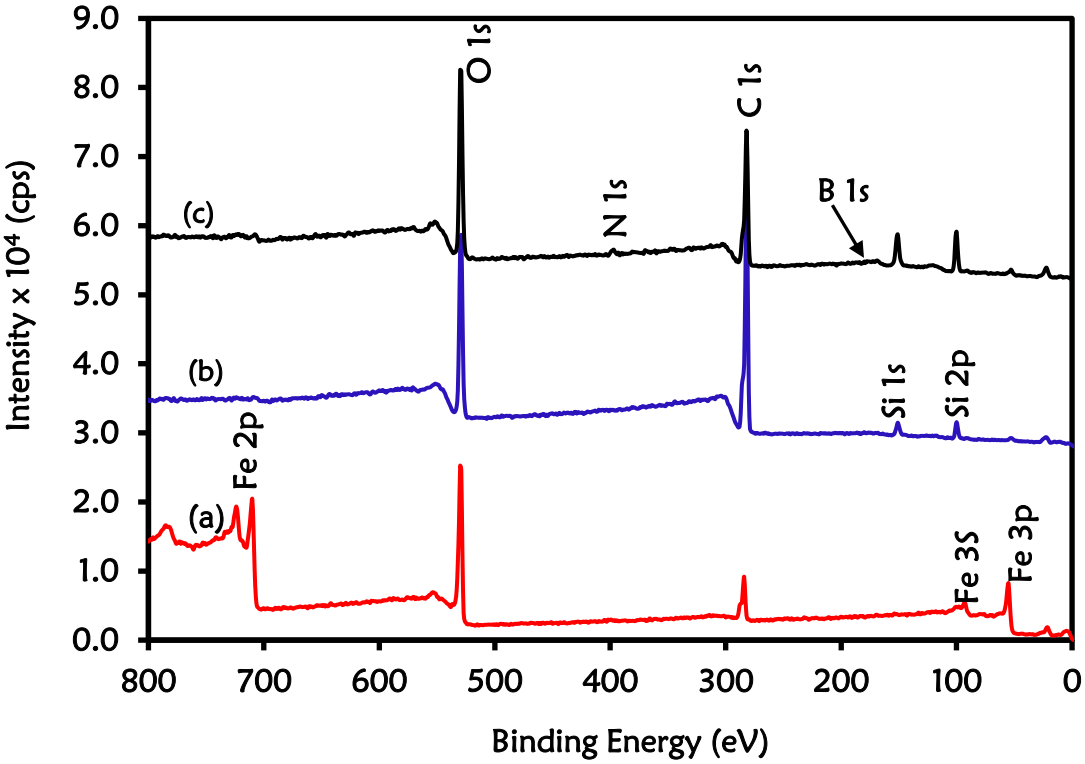

Figure 5.7: XPS survey spectra of (a) MNPs (b) MNP-SiO-APTES, and (c) MNP-SiO-APTES-PBA.

The high-resolution spectrum of Fe 2p of the MNP is shown in **Appendix Fig. S6.8**. The MNPs consist of two oxidation states, Fe^{2+} and Fe^{3+}. Fe^{2+} is octahedrally coordinated, and the Fe^{3+} are distributed over both octahedral and tetrahedral sites. Also, the partially filled 3d levels result in a complex d-d multiplet splitting [401,402] which contribute to the peak structure. The high-resolution spectrum of the Fe 2p shows two broad peaks at binding energy 709.6 eV for Fe $2p_{3/2}$ and 724.6 eV for Fe $2p_{1/2}$. The spin-orbit coupling (ΔE) between the two peaks was calculated to be 15.0 eV. The Fe 2p spectrum consists of three major peaks and satellite peaks in the $2p_{3/2}$ region having

a repeated pattern which is considered to be half of the intensity of the $2p_{1/2}$. The lowest binding energy peak at 709.9 eV is assigned to Fe^{2+} with a corresponding satellite at 716.0 eV. The Fe^{3+} octahedral species is associated with the binding energy of 711.1 eV. The binding energy value for the Fe^{3+} tetrahedral species is found to be 713.6 eV. These values correspond to some of the values reported in the literature [403–406].

Figure 5.8 shows the C 1s high resolution spectra for (a) MNPs, (b) MNP-SiO-APTES, and (c) MNP-SiO-APTES-PBA. The deconvoluted C 1s spectrum shows the presence of carbon components in a different chemical environment with the reference carbon at 285.0 eV. The citric acid stabilized magnetic nanoparticles (MNPs) **Fig. 5.8(a)** was deconvoluted into three components at 285.0 eV, 286.9 eV, and 288.9 eV. The most intense component seen at 285.0 eV is assigned to C-C, and C-H bonding [407]. The second component centred at 286.9 eV is associated with C-O bonding which corresponds to the monodentate bond of the carboxylate from the citric acid. The last component with the highest binding energy at 288.9 eV is attributed to the O-C=O bond which indicates the bidentate bond of the carboxylate from the citric acid [408]. The C 1s spectrum for the MNP-SiO-APTES in **Fig. 5.8(b)** was deconvoluted into four components centred at 285.0 eV, 286.3 eV, 287.8 eV and 288.8 eV. The peak at 285.0 eV is common to all the various stages of the modification and was given the same assignment as above. The peak at 286.3 eV is assigned to C-O due to residual citric acid. The small peak at 287.8 eV is attributed to the amino-linked carbon atom (C-N) [409]. This confirms the successful functionalization of the MNP with APTES. The last peak at 288.8 eV is attributed to (O-C=O) from residual citric acid [410].

The C 1s spectrum for MNP-SiO-APTES-PBA is shown in **Fig 5.8(c),** and four distinct peaks at 285.0 eV, 286.4 eV, 287.1 eV, and 288.5 eV were observed. The components

at 285 eV and 286.4 eV are given a similar assignment as above. The peak at 287.1 eV corresponds to C-N. The last peak at 288.5 eV is attributed to the amide (N-C=O) and (O-C=O) bonds resulting from the pentanoic acid terminated phenylboronic acid, and the APTES functionalized magnetic nanoparticles. The high-resolution of O 1s for (a') MNPs (b') MNP-Si-O-APTES, and (c') MNP-SiO-APTES-PBA is also shown in **Fig. 5.8.**

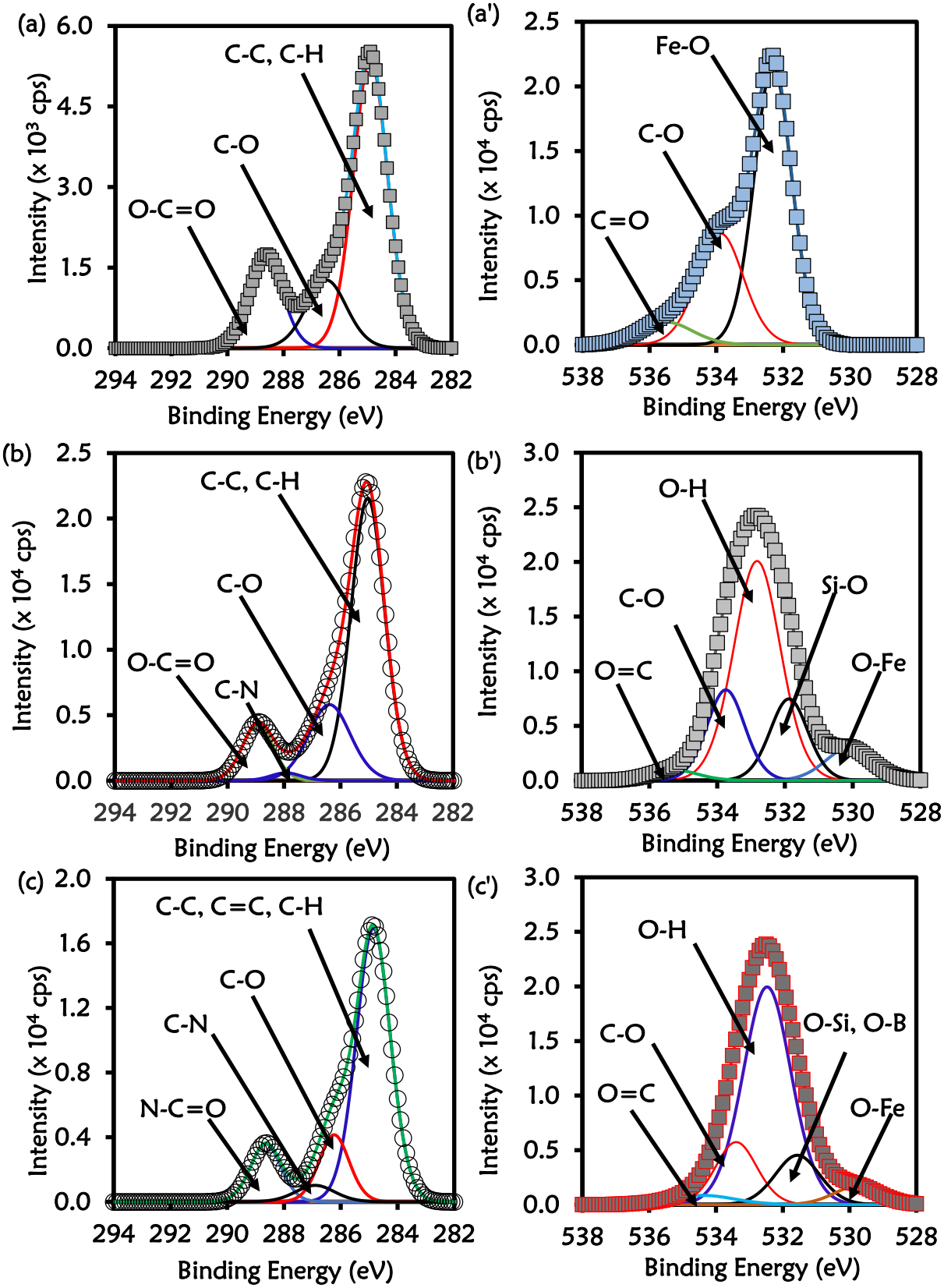

Figure 5.8: The high-resolution spectra of C 1s (a) MNPs (b) MNP-SiO-APTES, and (c) MNP-SiO-APTES-PBA and O 1s (a') MNPs (b') MNP-SiO-APTES, and (c') MNP-SiO-APTES-PBA.

Figure 5.8 shows the high resolution of O 1s for (a') MNPs (b') MNP-Si-O-APTES, and (c') MNP-SiO-APTES-PBA. The O 1s spectrum of the MNPs in **Fig. 5.8(a')** exhibited three components at 530.0 eV, 531.5 eV and 533.2 eV respectively. The peak at 530.0 eV was assigned to Fe-O from the MNPs. The second peak centred at 531.5 eV was attributed to C-O which corresponds to monodentate carboxylate oxygen atoms. The last component at 533.2 eV is assigned to oxygen atoms in the bidentate bond (C=O) at the MNP surface and to the carboxylate from the free citric acid molecule.

The high-resolution spectrum of O 1s of MNP-SiO-APTES is shown in **Fig. 5.8(b')** with five oxygen peaks seen at 530.1 eV, 531.8 eV, 532.8 eV, 533.7 eV, and 535.2 eV. The peak at 530.1 eV is assigned to O-Fe [411]. The peak at 531.8 eV is attributed to Si-O [412]. The peak centred at 532.8 eV is assigned to O-H. The peak at 533.7 eV is attributed to C-O. The last component with the highest binding energy at 535.2 eV is attributed C=O.

Figure 5.8(c') shows the O 1s spectrum of MNP-SIO-APTES-PBA presenting five components at binding energies 529.7 eV, 531.5 eV, 532.4 eV, 533.4 eV, and 534.3 eV. The peak at 529.7 is assigned to the O-Fe [411]. The peak at 531.5 eV is attributed to O-Si, and O-B bond [187]. The component at 532.4 eV is attributed to O-H. The component centred at 533.4 eV is attributed to C-O. The last component at 534.3 eV is assigned to C=O bond.

Figure 5.9 shows the high-resolution N 1s for (a) MNP-SiO-APTES, (b) MNP-SiO-APTES-PBA, and (c) boron (B 1s) for MNP-SiO-APTES-PBA. The MNP-SiO-APTES in **Fig. 5.9(a)** shows two peaks at 399.8 eV and 402.0 eV. The standard binding energy for free amino group (N-H) is expected to be seen in the region 399.0 – 401.0 eV. Therefore, the peak at 399.8 eV is assigned to the ($-NH_2$) while 402.0 eV is attributed to the C-N of the amine group. This shows the presence of the NH_2 group which is an evidence of the successful functionalization of the MNP with APTES.

The formation of the amide bond between the MNP-SiO-APTES and the pentanoic acid terminated phenylboronic acid **Fig. 5.9(b)** in MNP-SiO-APTES-PBA was confirmed with the N1s peak at 400.1 eV for N-H and N-C at 401.6 eV. A slight shift in binding energy was observed from N-H of APTES and N-H of amide. The similar shift was also observed for N-C of APTES and N-C of amide. The high-resolution spectrum of B 1s is presented in **Fig. 5.9(c).** Four components were obtained after the deconvolution of the spectrum; the peaks were centred at 188.3 eV, 190.2 eV, 195.4 eV, and 197.2 eV. The components are assigned to B-C, and B-O. The obtained spectrum shows the presence of boron element in different chemical environments. This observation also confirms the successful synthesis of MNP-SiO-APTES-PBA. The summary of the component positions, component percentage and their assignments for different stages of MNPs functionalization is shown in **Table 5.1.**

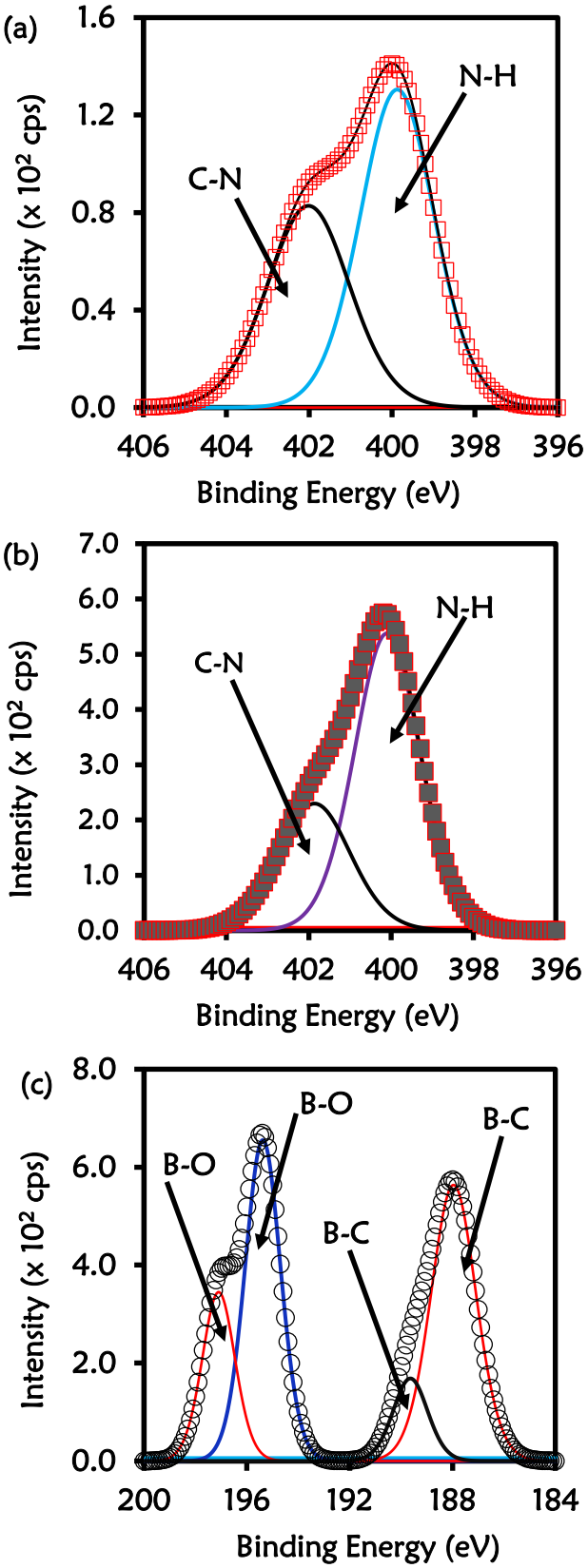

Figure 5.9: The high-resolution spectra of N 1s (a) MNP-SiO-APTES (b) MNP-SiO-APTES-PBA, and (c) the high-resolution spectrum B 1s of MNP-SiO-APTES-PBA.

Table 5.1: summary of the component positions, component percentage and their assignments for different stages of MNPs functionalization

Surfaces	Atoms	Component positions (eV)	Assignments	Component percent (%)
MNPs	C 1s	285.0	C-C, C-H	63.0
		286.9	C-O	17.5
		288.9	O-C=O	19.5
	O 1s	530.0	Fe-O	62.2
		531.0	C-O	30.6
		533.0	C=O	7.2
MNP-SiO-APTES	C 1s	285.0	C-C, C-H	64.9
		286.3	C-O	21.7
		287.9	C-N	1.6
		288.8	C=O	11.8
	O 1s	530.1	O-Fe	8.1
		531.8	Si-O	16.5
		532.8	O-H	54.6
		533.7	C-O	18.3
		535.2	C=O	2.6
	Si 2p	100.8	Si-O	1.9
		103.6	Si-O-Si	96.5
		105.6	Si-C	1.6
	N 1s	399.8	N-H	58.6
		402.0	N-C	41.5
MNP-SiO-APTES-PBA	C 1s	285.0	C-C, C=C, C-H	67.8
		286.4	C-O	14.7
		287.1	C-N	4.7
		288.5	O-C=O,N-C=O	12.8
	O 1s	529.7	O-Fe	5.0
		531.5	O-Si, O-B	13.2
		532.3	O-H	62.8
		533.4	C-O	15.5
		534.3	C=O	3.6
	Si 2p	102.0	Si-O	77.2
		103.2	Si-C	13.3
		104.3	Si-O-Fe	9.5
	B 1s	188.3, 190.2	B-C	38.6, 8.9
		195.4, 197.2	B-O	35.5, 17.2
	N 1s	400.1	N-H	68.0
		401.6	C-N	32.0

5.2.7. Conjugation of anti-CRP antibody to magnetic nanoparticles

The conjugation of anti-CRP antibody to MNP-SiO-APTES-PBA was achieved through the affinity boronate interaction by targeting the carbohydrate moiety present at the Fc region of the anti-CRP antibody. The bioconjugation is shown in **Scheme 5.2.**

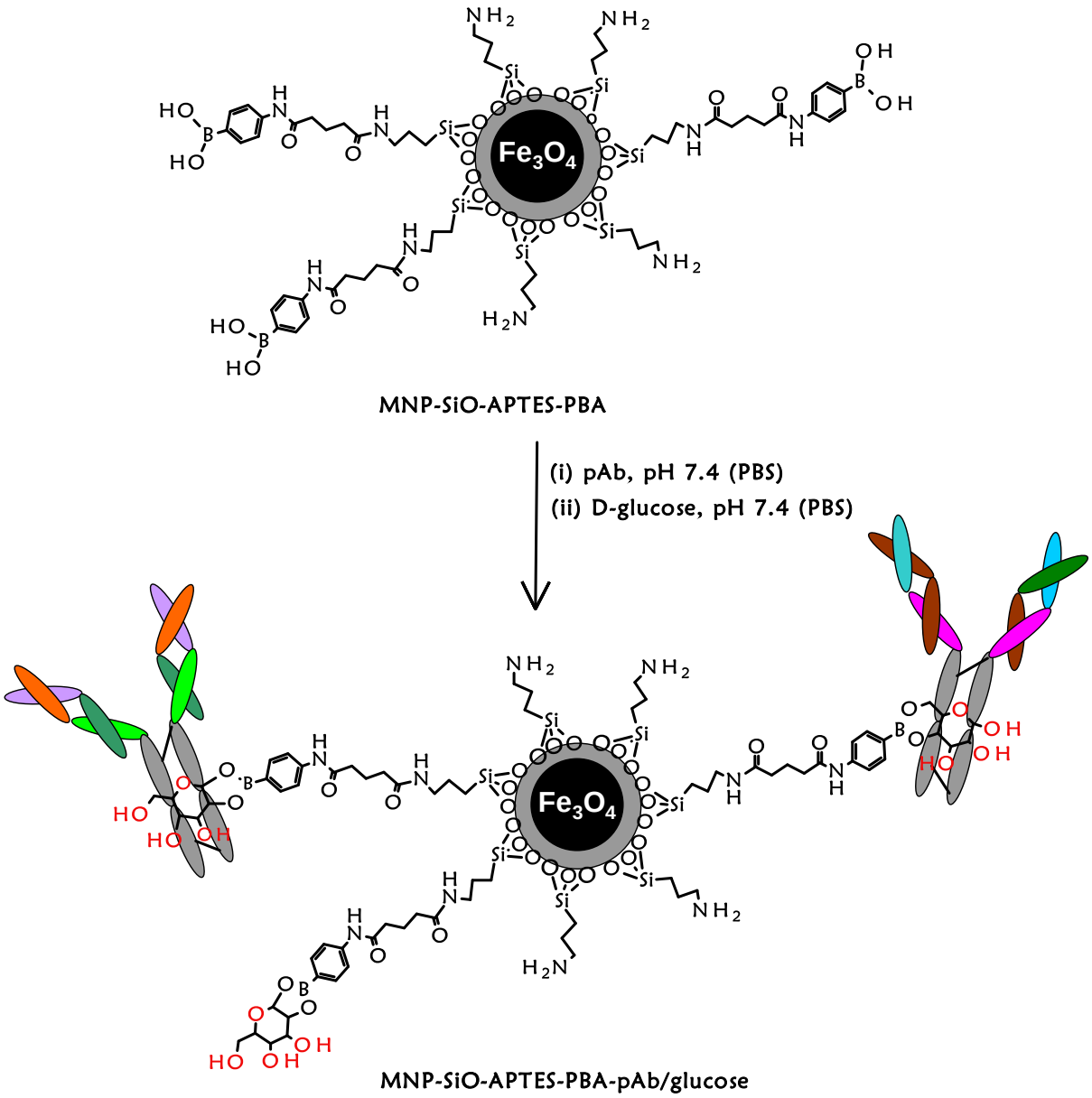

Scheme 5.2: Bioconjugation of anti-CRP polyclonal antibody (pAb) onto MNP-SiO-APTES-PBA, (MNP-SiO-APTES-PBA-pAb).

The conjugation of the anti-CRP antibody was confirmed using the Bradford assay.

Bradford assay (a quantitative colourimetric assay for protein estimation) was used for the quantification of the protein present after the conjugation procedure. To quantify the anti-CRP antibody amount on MNP-SiO-APTES-PBA-pAb after the conjugation procedure, the nanoparticles were separated by a magnet, and the supernatant was used for protein determination. Bovine Serum Albumin (BSA) standard was prepared, and the supernatant obtained from anti-CRP antibody conjugated to MNP-SiO-APTES-PBA samples were also prepared and were made to react with Bradford reagent at room temperature for 30 mins. The UV absorbance measurement was obtained. The absorbance of the supernatant was measured at 595 nm, which correspond to the remaining protein after bioconjugation. The protein amount on the sample was calculated by subtracting the determined concentration in the supernatant from the initial concentration of the antibody solution. The conjugation efficiency was calculated using **Equation (5.1).**

$$\text{Conjugation efficiency} = \frac{[pAb]_o - [pAb]_f}{[pAb]_o} \times 100 \quad \ldots\ldots\ldots\ldots \textbf{(5.1)}$$

where $[pAb]_o$ and $[pAb]_f$ represent the initial and the final concentrations of the polyclonal anti-CRP antibody (pAb). The conjugation efficiency of the nanoparticles was found to be 62.38 %.

5.2.8. XPS characterization of MNP-SiO-APTES-PBA-pAb

Figure 5.10 shows the survey spectrum of the MNP-SiO-APTES-PBA-pAb. An increase in the carbon composition was seen from 33.8 % (MNP-SiO-APTES-PBA) to 51.4 % (MNP-SiO-APTES-PBA-pAb). This observation could be as a result of the carbon atoms present at the backbone of the protein. The % composition of O and N were 29.3 % and 3.29 %. There was a peak observed at the binding energy 1071 eV and the Na 1s. The Na 1s auger peak was also seen at 495 eV, and this was accompanied by a peak at 199 eV assigned to Cl 2p, and the Cl 2s peak at 268 eV. The presence of sodium and chlorine peaks are due to these ions trapped from the buffer. The presence of silica peaks at 100 eV and 151 eV confirms the presence of silica coating throughout the different stages of the functionalized magnetic nanoparticles.

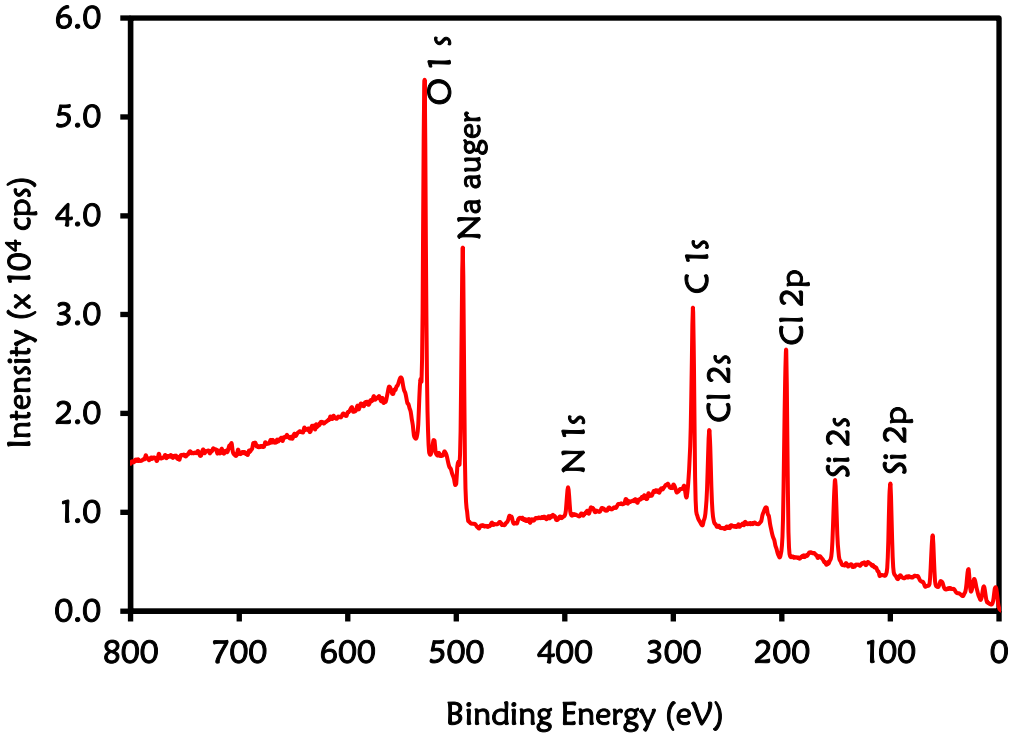

Figure 5.10: Survey spectrum of anti-CRP polyclonal antibody conjugated to phenylboronic acid functionalized magnetic nanoparticles (MNP-SiO-APTES-PBA-pAb).

Figure 5.11 shows the high-resolution spectra of C 1s, O 1s, and N 1s of MNP-SIO-APTES-PBA-pAb. The C 1s of the MNP-SiO-APTES-PBA-pAb is presented in **Fig. 5.11(a)** showing seven peaks located at 285.0 eV, 286.0 eV, 287.1 eV, 288.2 eV, 289.8 eV, 291.1 eV and 293.3 eV. The peak at 286.0 eV is assigned to C-O, and C-N carbon of the protein backbone. The peak at 287.1 eV is due to the amide bond (N-C=O) of peptide carbon. The high intensity of the peak is attributed to the presence of various amide bonds at the backbone of the antibody. This is an indication of the successful attachment of the antibody onto the MNP-SiO-APTES-PBA via the boronate ester reaction. The peak located at 288.2 eV is assigned to C=O. The component centred at 289.8 eV is assigned to O-C=O. The last two components at 291.1 eV and 293.3 eV are associated with shake-up peaks which are attributed with carbon in the aromatic ring [413–415].

Figure 5.11(b) shows the O 1s spectrum for MNP-SiO-APTES-PBA-pAb and it was deconvoluted into six components at 529.9 eV, 531.0 eV, 532.5 eV, 534.3 eV, 536.2 eV and 537.6 eV. Their assignments are similar to MNP-SiO-APTES-PBA except for the last two components at 536.2 eV and 537.6 eV. The component at 536.2 eV, and 537.6 eV are attributed to C=O from an amide and carbonyl bond.

The N 1s spectrum of MNP-SiO-APTES-PBA-pAb in **Fig. 5.11(c)** shows a higher intensity compare with MNP-SiO-APTES and MNP-SiO-APTES-PBA as discussed above. This could be attributed to the presence of numerous peptide bonds in the antibody. This confirms successful conjugation of the anti-CRP polyclonal antibody to the phenylboronic acid functionalized magnetic nanoparticles. The N 1s peak was also seen at 400.1 eV which shows the presence of N-H of amide bond in the MNP-SiO-APTES-PAB-pAb and the second peak at 401.9 eV is due to C-N of peptide bond. The summary of the component positions, %, and their assignments is presented in **Table 5.2.**

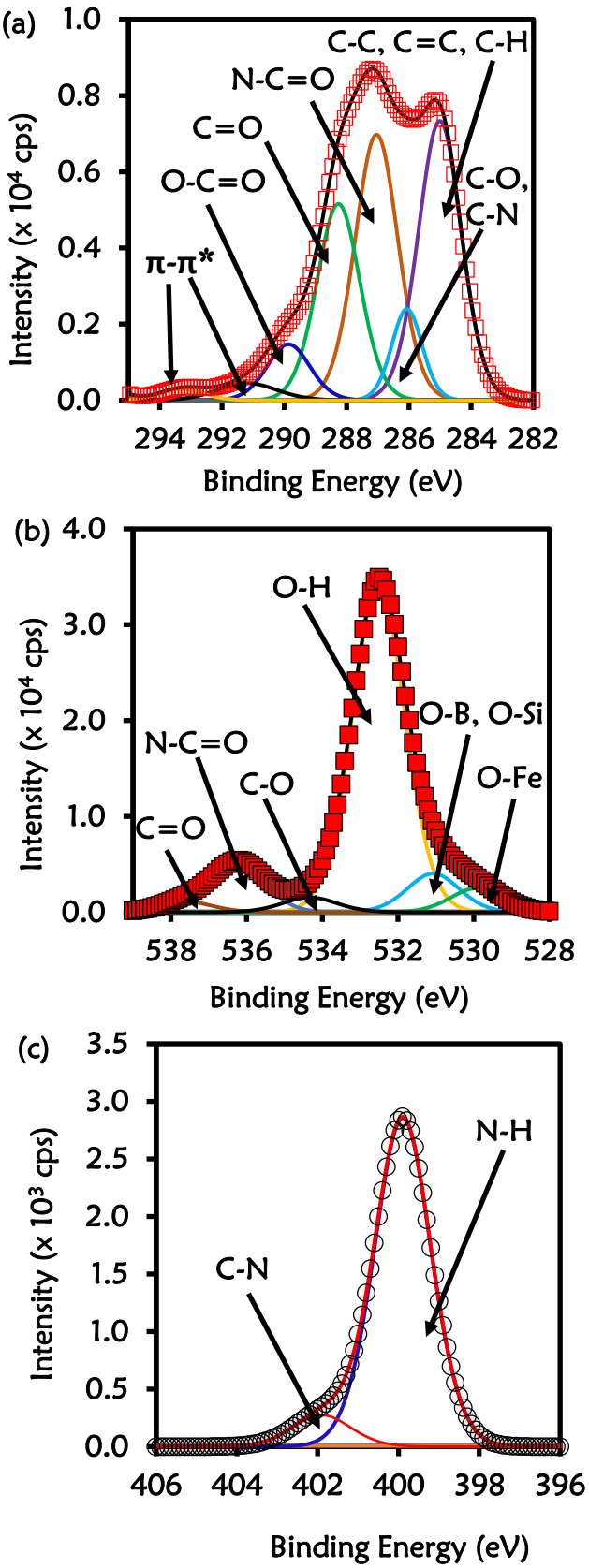

Figure 5.11: The high-resolution spectra of (a) C 1s (b) O 1s, and (c) N 1s of MNP-SiO-APTES-PBA-pAb.

Table 5.2: Summary of the component positions, component percentage and their assignments for MNP-SiO-APTES-PBA-pAb

Surface	Atoms	Component positions (eV)	Assignments	Component percent (%)
MNP-SiO-APTES-PBA-pAb	C 1s	285.0	C-C, C=C, C-H	30.4
		286.4	C-O, C-N	7.1
		287.1	CONH	29.0
		288.2	C=O	21.5
		289.8	O-C=O	6.1
		291.1, 293.3	π-π*	2.6, 1.3
	O 1s	529.9	O-Fe	5.1
		531.0	O-B, O-Si	8.3
		532.5	O-H	70.4
		534.3	C-O	3.3
		536.2	N-C=O	10.6
		537.6	C=O	2.2
	Si 2p	103.6	Si-OH	81.7
		104.5	Si-O-Si	14.2
		102.2	Si-O-Fe	4.0
	N 1s	400.1	N-H	93.2
		401.9	N-C	6.8

5.3. Fabrication of immunosensor, Au-PEA-SA-APBA-mAb/glucose (Scheme 5.3)

The step-by-step fabrication of Au-PEA-SA-APBA-mAb/glucose immunosensor was followed as shown in **Scheme 5.3,** described in the experimental section. The first steps involve the electrochemical reduction of AEBD salt yielded the formation of phenylethylamine (PEA) on the gold electrode, Au-PEA. Secondly, the surface was derivatized with succinic anhydride (SA) to form the carboxylic surface, Au-PEA-SA. Lastly, the covalent attachment of the 4-aminophenylboronic (APBA), Au-PEA-SA-APBA was achieved by carbodiimide chemistry. The oriented immobilization of the mAb was accomplished by exposing the Au-PEA-SA-APBA onto a solution of mAb and blocking of non-specific binding site with glucose to yield Au-PEA-SA-APBA-mAb/glucose.

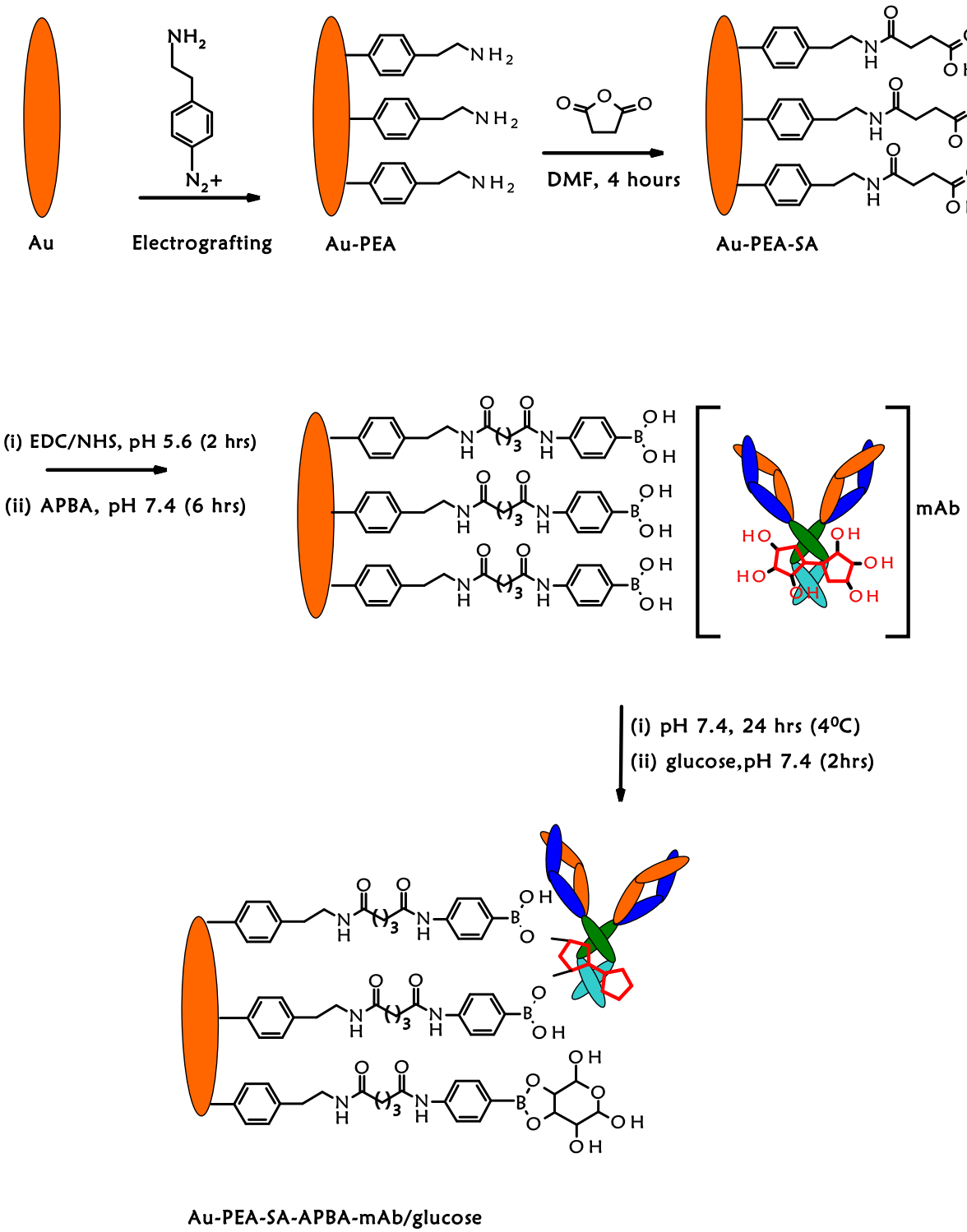

Scheme 5.3: Step-by-step by modification of gold surface and the immobilization of monoclonal anti-human CRP antibody.

Figure 5.12. shows the cyclic voltammograms for the electrografting of AEBD salt onto the Au electrode. The electrochemical grafting on the gold electrode was performed by cyclic voltammetry. Three cycles between 0.4 to -0.4 V at a scan rate of 100 mVs^{-1} were used. The cyclic voltammogram was characterized by the first cycle exhibiting a well-defined and irreversible reduction peak at 0.19 V, **Fig. 5.12(i).** The observed peak corresponds to the electroreduction of the diazonium (AEBD) salt through one electron transfer mechanism which eventually led to the loss of nitrogen. The loss of nitrogen (N_2) results in the formation of a highly reactive radical (2-aminoethylphenyl radical). The radical then attack the surface, thereby forming a stable covalent bond between the aryl group and the gold electrode [416,417]**.** The disappearance of the reduction peak was observed with the second and the third scan **Fig. 5.12(ii) and (iii)**. This behaviour could be attributed to complete blockage of the gold electrode surface by the PEA layer after the first scan thereby preventing the formation of the PEA radicals in solution during the subsequent scan. The observed behaviour is similar to what has been previously reported in the literature and consistent with the grafting of diazonium salt on a gold electrode [368–371,418]**.**

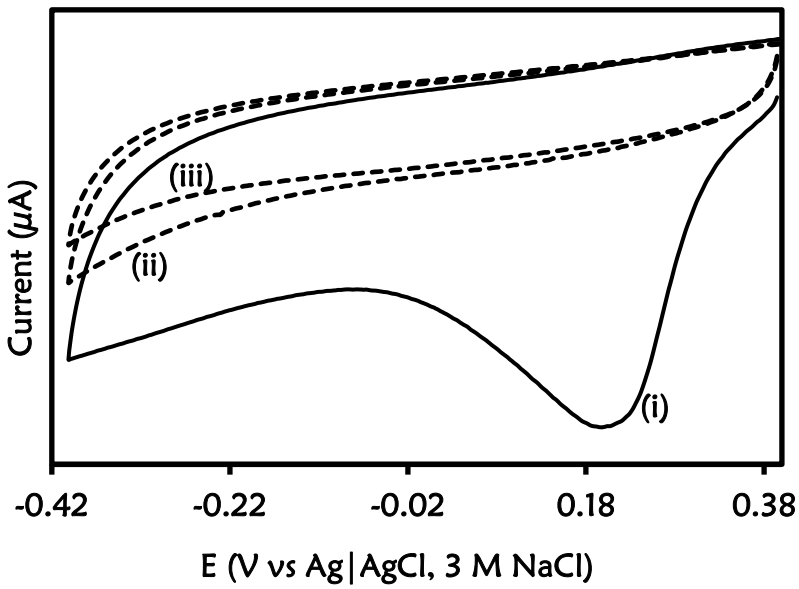

Figure 5.12: Cyclic Voltammograms for the electrochemical grafting 1 mM AEBD salt in Acetonitrile (ACN) solution containing 0.1 M $TBABF_4$ unto gold electrode at a scan rate of 100 mVs^{-1}

Three scans were enough to achieve a covered surface as the electrode surface was passivated with PEA during the first cycle. The amino group on the PEA surface was derivatized using succinic anhydride to form a carboxylic terminated surface. EDC/NHS coupling was used to link the NH_2 group on the 4-aminophenylboronic acid to form a stable amide bond. Similar cases have been reported in the literature for the conversion of the amino-terminated group to carboxyl group by reacting the surface with succinic anhydride [419,420]. Kim in 2012, reported the fabrication of immunosensor through the formation of SAMs of APTES on a silicon wafer for protein immobilization [421]. This was achieved by converting the amino group on the APTES to carboxyl surface using succinic anhydride. Then NHS ester was introduced by reacting the carboxyl group

on the succinylated APTES to form amide linkage for protein immobilization. The conversion of APTES functionalized magnetic nanoparticles to COOH terminal surface using succinic anhydride was also reported by Osifeko et al. 2016 [422]. The electrode was further modified with the monoclonal anti-CRP antibody (mAb) as previously discussed in the experimental section **(section 2.6.2).** The non-specific binding sites were blocked with glucose to yield Au-PEA-SA-APBA-mAb/glucose. The oriented immobilization of the mAb onto the electrode surface was achieved through the affinity boronate ester interaction studied and discussed above. As presented in chapter four, the XPS result confirms the oriented immobilization of the mAb onto the electrode surface.

5.4. Electrochemical characterization of Au-PEA-SA-APBA-mAb/glucose

5.4.1. Cyclic Voltammetry

Cyclic voltammetry (CV) and electrochemical impedance spectroscopy (EIS) were used to confirm the different modification steps of the fabricated Au-PEA-SA-APBA-mAb/glucose immunosensor. The inhibition of electron transfer properties of the bare gold surface upon modification in the presence of redox probe $[Fe(CN)_6]^{3-/4-}$ was used as a measure of surface functionalization. **Figure 5.13** shows (a) CV and (b) EIS of (i) bare Au, (ii) Au-PEA-SA (iii) Au-PEA-APBA (iv) Au-PEA-APBA-mAb/glucose in (1:1) 2 mM $k_3Fe(CN)_6$:$k_4Fe(CN)_6$ solution containing 0.1 M KCl. The cyclic voltammograms of the bare electrode, in **Fig. 5.13(a)(i)** exhibited a reversible redox couple due to $[Fe(CN)_6]^{3-/4-}$ with peak-peak separation of (ΔE) of 80.3 ± 7.7 mV. After the electrochemical grafting with the PEA, **Appendix Fig. S6.9(a)(i)** a decrease in the peak to peak separation to (ΔE = 75 mV) was observed. This is attributed to the conducting nature of the PEA monolayer which enhances the transfer of electron between the $[Fe(CN)_6]^{3-/4-}$ redox probe and the gold electrode surface. The observed conducting behaviour of the PEA modified electrode towards the redox probe is attributed to the electrostatic attraction between the $-NH_3^+$ and the negatively charged $[Fe(CN)_6]^{3-/4-}$ [423]. The succinic anhydride derivatized surface in **Fig. 5.13(a)(ii)** showed a blocking behaviour towards the ferricyanide redox probe with ΔE = 330 mV. The increase in ΔE is attributed to the electrostatic repulsion between the negatively charged carboxyl group and the negatively $[Fe(CN)_6]^{3-/4-}$. The observed behaviour has been previously reported in the literature [424,425]. A drastic decrease from 330 mV to 88 mV was observed after the amide coupling reaction between Au-PEA-SA and 4-aminophenylboronic acid, Au-PEA-SA-APBA in **Fig. 5.13(a)(iii).** The decrease in ΔE to

88 mV at Au-PEA-SA-APBA was due to the coupling of 4-aminophenylboronic acid and the neutralization of the COO- functional group of the Au-PEA-SA electrode [192]. For the monoclonal anti-CRP antibody (mAb) modified electrode **Appendix Fig. S6.9(a)(ii)** an increase in peak to peak separation from 88 mV to 144 mV was observed, and this is attributed to the insulating properties of the mAb. The blocking behaviour inhibits the transfer of electron between the electrode surface and the redox probe. At the Au-PEA-SA-APBA-mAb/glucose in **Fig. 5.13(a)(iv)** a further inhibition of the redox probe from the solution electrolyte due to the blocking behaviour and the insulating properties of the mAb and the glucose was seen. The Au-PEA-SA-APBA-mAb/glucose electrode shows an increase in peak-to-peak separation from 144 mV to 240 mV. A drastic decrease in peak currents in the cyclic voltammograms was observed together with the increase in ΔE. This confirms the successful immobilization of the mAb and the blocking of non-specific binding sites by glucose.

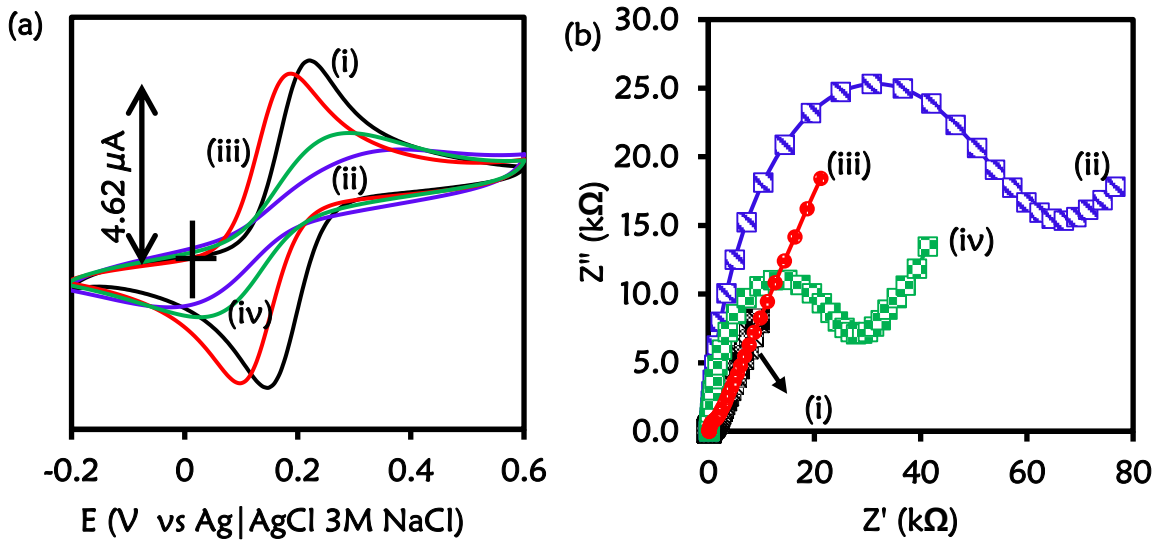

Figure 5.13 (a) CV and (b) EIS of (i) bare Au (ii) Au-PEA-SA (iii) Au-PEA-APBA (iv) Au-PEA-APBA-mAb/glucose in (1:1) 2 mM $k_3Fe(CN)_6$:$k_4Fe(CN)_6$ solution containing 0.1 M KCl.

5.4.2. Electrochemical impedance spectroscopy

The Electrochemical impedance spectroscopy (EIS) was further used to monitor and confirm the immobilization of monoclonal anti-CRP antibody (mAb) as this is more sensitive and versatile technique than cyclic voltammetry. The bare electrode **Fig. 5.13(b)(i)** exhibits a small semicircle at high frequency with a charge transfer resistance of 0.602 ± 0.097 kΩ. A charge transfer resistance similar to that of bare Au electrode was observed in **Appendix Fig. 6.9(b)(i)** with the Au-PEA modified electrode 0.622 kΩ. The R_{CT} of the Au-PEA monolayer remained almost similar to bare Au even after grafting. This confirms the conducting nature of the PEA monolayer. An increase in R_{CT} was observed with the succinic anhydride derivatized surface to 55.3 kΩ, **Fig. 5.13(b)(ii).** The increase in the R_{CT} was attributed to the electrostatic repulsion of the negatively charged carboxyl groups of the Au-PEA-SA and the negative redox probe. This reduced the ability of the ferricyanide probe to access the electrode surface. A drastic decrease in R_{CT} from 55.3 kΩ to 1.25 kΩ was observed at the Au-PEA-SA-APBA electrode **Fig. 5.12(b)(iii).** This observation was as a result of the neutralization of the negative charge carboxylic group upon reaction with the amino group of the aminophenylboronic acid. Upon modification with anti-CRP monoclonal antibody **Appendix Fig. S6.9(b)(ii)** the charge transfer resistance increased from 1.25 kΩ to 14.7 kΩ. The observed increase in the R_{CT} is attributed to the insulating properties of the monoclonal antibody. Upon the immobilization of mAb and the blocking of the non-specific binding site with glucose, Au-PEA-SA-APBA-mAb/glucose electrode in **Fig. 5.13(b)(iv)** an increase in the R_{CT} (from 14.7 to 24.5 kΩ) was observed. This shows the blocking behaviour of the mAb/glucose film. The observed increase in R_{CT} arises from the slow rate of electron transfer of the gold electrode and an increase in the charge

transfer resistance. This is attributed to the insulating properties of the mAb and the glucose. The EIS and the CV results confirm the successful modification of the electrode.

5.5. Optimization of immunosensor parameters

In this study, some important parameters that determine the analytical performance of the immunosensor were optimized. These parameters include: The concentration of the immobilized antibody that enhances the formation of an antibody-antigen immunocomplex, the concentration of the blocking agent and the concentration of the APBA was optimized. These are shown in **Appendix Fig. S6.10(a-c).**

5.6. Impedimetric detection of CRP using Au-PEA-SA-APBA-mAb/glucose

The analytical performance of the Au-PEA-SA-APBA-mAb/glucose immunosensor, 20 μl of CRP antigen concentrations ranging from 10 to 400 ng mL^{-1} in PBS (pH 7.4) was applied to the electrode surface and incubated for 1 hour at room temperature. Afterwards, the electrode was further incubated with 20 μl CRP polyclonal antibody conjugated to phenylboronic functionalized magnetic nanoparticles (MNP-SiO-APTES-PBA-pAb/glucose). All measurements were performed in triplicates. The change in total charge transfer resistance (ΔR_{CT}) for each concentration was calculated from **Equation (5.2).**

$$\Delta R_{CT} = R_{CT(Ab-Ag)} - R_{CTAb} \qquad \ldots\ldots\ldots \quad \textbf{(5.2)}$$

Where $R_{CT(Ab)}$ is the charge transfer resistance of the Au-PEA-SA-APBA-mAb/glucose before the CRP antigen immunoreaction and $R_{CT(Ab-Ag)}$ is the value of the Au-PEA-SA-APBA-mAb/glucose after an immunoreaction with the CRP-antigen, and MNP-SiO-

APTES-PBA-pAb/glucose. The detection of CRP antigen using the MNP-SiO-APTES-PBA-pAb as nanobioprobe is shown in **Scheme 5.4**.

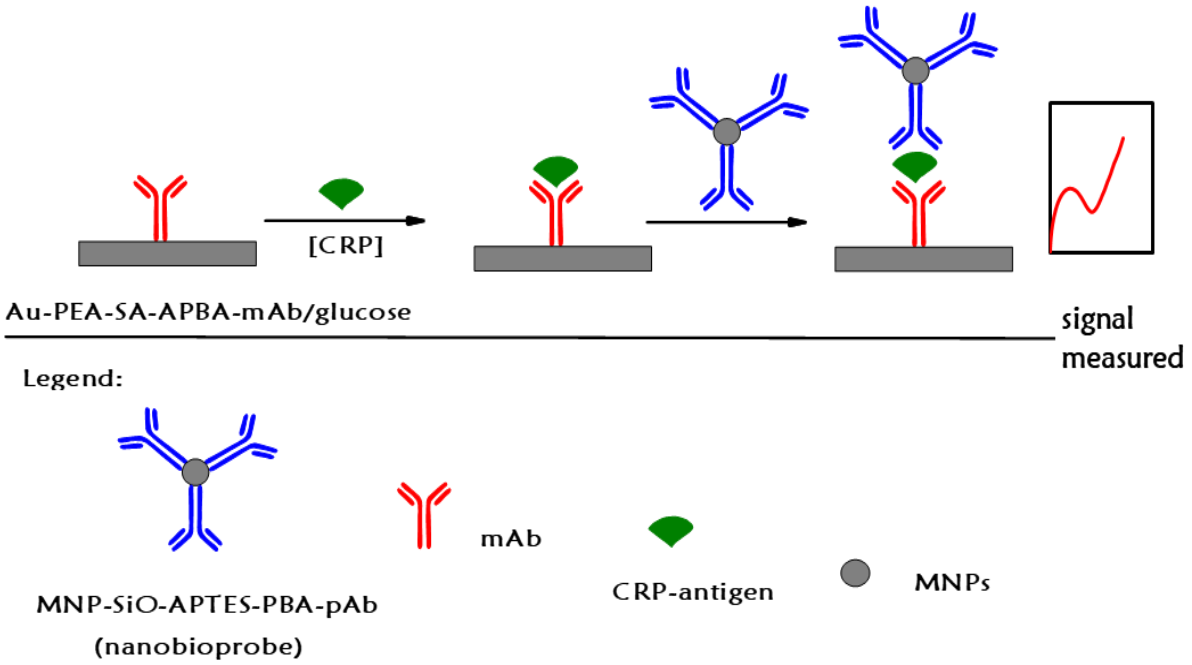

Scheme 5.4: CRP antigen detection using MNP-SiO-APTES-PBA-pAb as nanobioprobe.

Figure 5.14 shows (a) Nyquist plot, and (b) corresponding calibration curve for CRP antigen concentrations ranging from 10 – 100 ng mL^{-1}. In **Fig. 5.14(a),** the increase in charge transfer resistance (R_{CT}) was observed with increasing CRP-antigen concentrations. The change in total charge transfer resistance ΔR_{CT} for each CRP-antigen concentration was calculated using **Equation (5.1)**. The ΔR_{CT} increased linearly with increasing antigen concentration from 10 – 100 ng mL^{-1} and a regression equation was ΔR_{CT} = 0.2228 [CRP-antigen] + 1.0537 and R^2 = 0.9998 (n=3). The immunocomplex

formation of mAb-CRP/CRP-antigen/MNP-SiO-APTES-PBA-pAb/glucose passivates the electrode surface, and this is attributed to its bulkiness and insulating nature. The signal generated by the detection probe led to an increase in charge transfer resistance. The saturation of electrode surface occurs at [CRP] > 100 ng mL^{-1} **(Appendix Fig. S6.11)**. The key parameters for evaluating an analytical method performance are the limit of detection and limit of quantification (LoD and LoQ), and their calculation have been discussed in chapter 3. The LoD and LoQ were calculated to be 0.56 and 1.88 ng mL^{-1}. The sensitivity of the fabricated immunosensor was found to be 11.084 $k\Omega.ng^{-1}.ml.cm^{-2}$. The higher sensitivity of the immunosensor could be attributed to the enhanced signal generated by the nanoparticles. The fabricated immunosensor is highly sensitive and with a lower detection limit compared to some other methods used for the detection of CRP antigen.

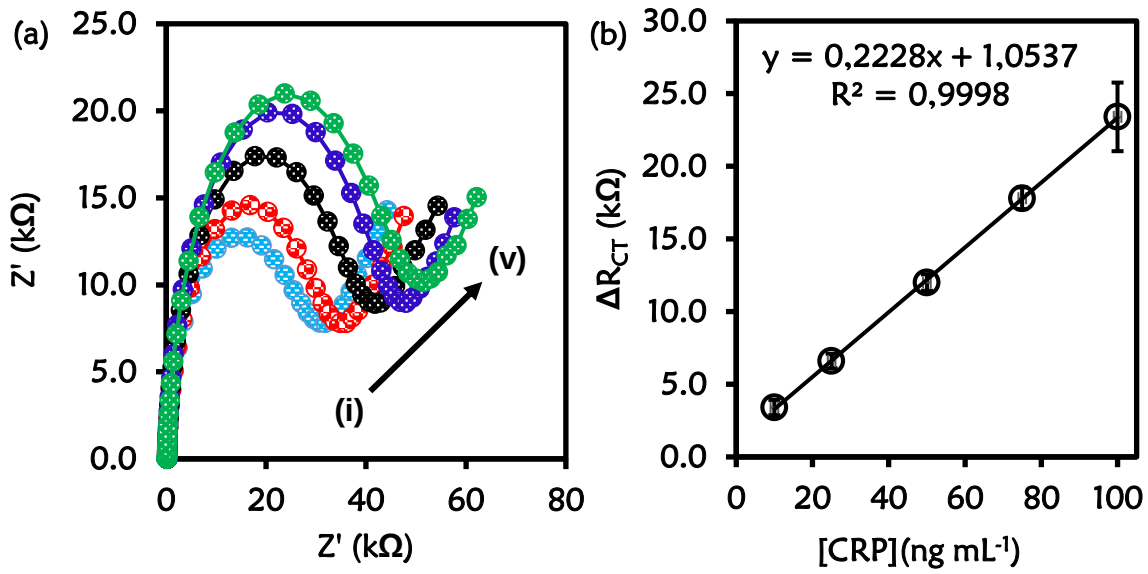

Figure 5.14: (a) Nyquist plot showing different antigen concentrations at (i) 10 ng mL^{-1} (ii) 25 ng mL^{-1} (iii) 50 ng mL^{-1} (iv)75 ng mL^{-1} (v) 100 ng mL^{-1} (b) Calibration curve

Table 5.3 shows the LoD, LoQ and the sensitivity of Au-MPBA-mAb/glucose, Au-MBA-APBA-mAb/glucose, and Au-PEA-SA-APBA-mAb/glucose immunosensors. The fabricated immunosensor (Au-PEA-SA-APBA-mAb/glucose) in this chapter was better than the fabricated immunosensors in chapters three and four. The enhanced analytical performance exhibited by this immunosensor could be attributed to the effect of chain length of the linker [426] and the incorporation of nanoparticles. The fabricated immunosensor has a longer chain length than the previously fabricated immunosensor in chapter three and four. The sensitivity of the fabricated immunosensors were found to be 11.084, 0.885, and 0.691 $k\Omega.ng^{-1}.ml.cm^{-2}$ for Au-PEA-SA-APBA-mAb/glucose, Au-MBA-APBA-mAb/glucose and Au-MPBA-mAb/glucose surfaces. The sensitivity increases with increase in the chain length of the linker, also the high sensitivity of the Au-PEA-SA-APBA-mAb/glucose could be attributed to the effect of the nanoparticles. The effect of the linker was also seen with the values obtained for the LoD of the immunosensor as shown in **Table 5.3.** The LoD (SIA) were 6.23, 1.20 and 0.56 ng mL^{-1} for Au-MPBA-mAb/glucose, Au-MBA-APBA-mAb/glucose and Au-PEA-SA-APBA-mAb/glucose.

Table 5.3: Analytical response of the fabricated immunosensor for C-reactive protein detection using DIA and SIA

	Detection method	Assay type	Linear range	R^2	LoD	LoQ	Sensitivity
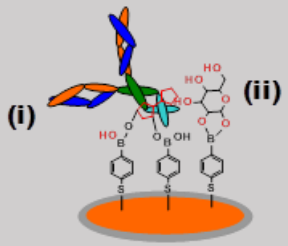	QCM-D	DIA	10 – 100	0.999	5.72	19.09	0.063 Hz.ml.ng^{-1}
		SIA	10 – 100	0.995	3.84	12.81	0.388 Hz.ml.ng^{-1}
	Impedance	DIA	10 – 100	0.998	9.75	32.55	0.438 kΩ.ng^{-1}.ml.cm^{-2}
		SIA	10 – 100	0.999	6.23	20.77	0.691 kΩ.ng^{-1}.ml.cm^{-2}
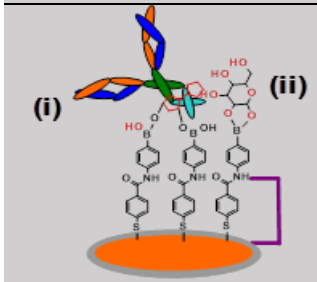	Impedance	DIA	10 – 100	0.998	2.90	9.66	0.585 kΩ.ng^{-1}.ml. cm^{-2}
		SIA	10 – 100	0.999	1.20	3.97	0.885 kΩ.ng^{-1}.ml. cm^{-2}
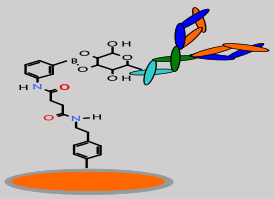	Impedance	SIA	10 – 100	0.999	0.56	1.88	11.08 kΩ.ng^{-1}.ml.cm^{-2}

Furthermore, the analytical response of Au-PEA-SA-APBA-mAb/glucose immunosensor was compared the previously reported immunosensors in **Table 3.3.** The immunosensor reported in this chapter shows a better an LoD value than most of the electrochemical immunosensor presented in **Table 3.3.** as previously discussed in chapter 4. The detection limit obtained in this work (0.56 ng mL^{-1}) was very close to the developed immunosensor reported by Lv et al (0.46 ng mL^{-1}) [345] and Buch et al (0.50 ng mL^{-1}) [226].

5.7. Stability and reproducibility of the immunosensor

The stability of the immunosensor was investigated by storing it at 4°C for three weeks, and there was no significant change in charge transfer resistance ΔR_{CT} of the immunosensor. The immunosensor retained 97.14 % of its initial response after storing for 2 weeks confirming good stability and reproducibility of the immunosensor. The reproducibility of the fabricated immunosensor was evaluated using two different concentrations of CRP-antigen (50, 75 ng mL^{-1}) and the RSD was found to be 4.68 % and 4.22 %.

5.8. The analysis in serum sample (mimicking real sample analysis)

The analysis in serum sample was carried out by spiking with four different concentrations of the CRP-antigen (10, 25, 50 and 100 ng mL^{-1}). The result is shown in **Table 5.4.** The recovery values are close to 100 % (84.36 – 98.70 %) which confirms the good analytical performance of the immunosensor. The recovery test was carried out in 10% serum.

Table 5.4: Spike and recovery results obtained from the fabricated CRP immunosensor in serum samples

Sample no	Spiked (ng mL^{-1})	Found (ng mL^{-1})	Recovery (%)
1	10	10.53	98.70
2	25	24.90	84.36
3	50	49.10	87.98
4	100	100.30	91.56

5.9. Conclusion

In this study, a sandwich immunoassay was designed for the detection of CRP antigen. CRP polyclonal antibody was conjugated to phenylboronic acid functionalized magnetic nanoparticles as the detection probe which enhances the sensitivity of the immunosensor. Antibody-antigen immunocomplex formation was established from the impedimetric response showing the affinitive binding between the CRP antibody and the CRP-antigen. The Au-PEA-SA-APBA-mAb/glucose electrode showed a linear range (10 - 100 ng mL^{-1}) with a detection limit (LoD) of 0.56 ng mL^{-1}. The LoQ was found to be 1.88 ng mL^{-1}. The fabricated immunosensor was sensitive, selective towards the detection of CRP antigen and would be useful for early detection of cardiovascular disease. The proposed immunosensor showed excellent analytical performance for CRP antigen detection. Hence the present fabricated immunosensor provides a desirable alternative to the existing methods due to high simplicity sensitivity and inexpensive instrumentation.

The recovery test in serum was analysed and the value recovered were close to 100% (84.36 – 98.70%) which is an indication that the fabricated immunosensor can be used in real analysis.

CONCLUSIONS

General conclusions

This work investigates the oriented immobilization of anti-CRP monoclonal antibody onto boronic acid functionalized gold surface for the detection of C-reactive protein. The oriented immobilization was achieved by targeting the carbohydrate moiety present at the Fc region of the monoclonal antibody through affinity boronate ester interaction. Initially, two label-free methods were investigated, that is piezoelectric (QCM-D) and impedimetric (EIS) methods.

Quartz crystal microbalance with dissipation (QCM-D) immunosensor was fabricated to establish the immunocomplex formation between the anti-CRP monoclonal antibody and the CRP-antigen. The QCM-D immunosensor was further used for the detection of C-reactive protein. The analytical performance of the immunosensor showed that the mass sensitive analysis yielded linear range between 10 – 100 ng mL^{-1}, with LoD 5.72 and 3.84 ng mL^{-1} for direct and sandwich immunoassay. The LoQ was also investigated, 19.09 and 12.81 $ng.ml^{-1}$ were obtained for direct and sandwich immunoassays respectively. The sandwich immunoassay gave excellent analytical parameters with sensitivity of 0.388 Hz ml. ng^{-1} compared to 0.063 Hz.ml. ng^{-1} for direct immunoassay. Regeneration of the immunosurface was obtained following an online method by treating the surface with 0.10 M HCl. The surface could be regenerated without losing the capture properties of the mAb towards CRP antigen.

Three different impedimetric immunosensors (Au-MPBA-mAb/glucose, Au-MBA-APBA-mAb/glucose and Au-PEA-SA-APBA-mAb/glucose) were fabricated and reported in this thesis for the detection of C-reactive protein. Two of the fabricated immunosensors

(Au-MPBA-mAb/glucose and Au-MBA-APBA-mAb/glucose were achieved through the formation of a self-assembled monolayer onto gold electrode. The third immunosensor (Au-PEA-SA-APBA-mAb/glucose) was achieved through the electrografting of AEBD salt onto gold electrode

- The Au-MPBA-mAb/glucose immunosensor was investigated, and the analytical performance showed the LoD of 9.75 for the direct immunoassay and 6.23 for the sandwich immunoassay. The LoQ for the direct and sandwich immunoassay were found to be 32.55 ng mL^{-1} and 20.77 ng mL^{-1}. The sensitivity value obtained for the sandwich immunoassay increased from 0.438 for the DIA to 0.691 $k\Omega.ng^{-1}.ml.cm^{-2}$.

- The Au-MBA-APBA-mAb/glucose showed a better analytical performance than the Au-MPBA-mAb/glucose. The LoD and the LoQ for the direct and sandwich immunoassay were found to be 2.90 and 9.66 ng mL^{-1} for the direct immunoassay and 1.20 and 3.97 ng mL^{-1} for the sandwich immunoassay. The sensitivity was calculated to be 0.585 $k\Omega.ng^{-1}.ml.cm^{-2}$ for DIA and 0.885 $k\Omega.ng^{-1}.ml.cm^{-2}$ for the SIA. This excellent analytical performance observed with this immunosensor could be attributed to the increased chain length of the linker. This also enhance the sensitivity of the Au-MBA-APBA-mAb/glucose immunosensor.

- Au-PEA-SA-APBA-mAb/glucose immunosensor showed a better analytical performance than the other two immunosensor fabricated. The enhanced

analytical performance was attributed to the use of nanoparticles. The incorporation of nanoparticles yielded a lower detection limit and LoQ for the immunosensor. The LoD was found to be 0.56 ng mL^{-1} with the LoQ value of 1.88 ng mL^{-1}. The sensitivity was found to be 11.08 $k\Omega.ng^{-1}.ml.cm^{-2}$. The sensitivity was higher than the sensitivity of the Au-MPBA-mAb/glucose and Au-MBA-APBA-mAb/glucose. This could be attributed to the effect of the nanoparticles and the increased chain length of the linker.

This study revealed that the covalent immobilization of anti-CRP monoclonal antibody as the sensing platform was achieved. The modified surface were characterized using electrochemical and spectroscopic method. Quartz crystal microbalance with dissipation was also used for the immunological reaction between the anti-CRP monoclonal antibody and the CRP-antigen.

The detection was carried out using direct (DIA) and sandwich (SIA) immunoassay formats. The results revealed higher LoD, LoQ and the sensitivity for the sandwich immunoassay. The higher sensitivity of the sandwich immunoassay was attributed to the fact that the polyclonal anti-CRP antibody (pAb) recognizes the different epitopes on the captured CRP-antigen which tends to amplify the signal.

The effect of chain length on the sensitivity of the immunosensor was studied. The incorporation of nanoparticles for signal enhancement was also investigated. The result revealed a higher sensitivity for the fabricated immunosensor with the longest chain length (Au-PEA-SA-APBA-mAb/glucose). The effect of the nanoparticles on the Au-PEA-

SA-APBA-mAb/glucose immunosensor also increased the sensitivity of the immunosensor.

The real analysis of the fabricated immunosensors were carried out in 10% serum, in a recovery test. The recovery close to 100% was achieved for all the immunosensors.

Future outlook

There are various ways which future research could help to improve the analytical performance of the fabricated CRP immunosensor, these include:

- The evaluation of the performance of the developed immunosensor using another cardiac marker.
- The simultaneous detection of cardiac marker in a multiplex way would go a long way to help the doctors in the early and accurate diagnosis of CVDs.
- The analytical performance of the immunosensor would need to be tested in real patient sample suffering from CVDs.

References

[1] World Health Organization, Attaining Nine Glob. Noncommunicable Dis. Targets; a Shar. Responsib. (2014) 298.

[2] M.E. Kruk, G. Nigenda, F.M. Knaul, Am. J. Public Health 105 (2015) 431–437.

[3] X. Cao, Lancet 385 (2015) e5–e6.

[4] T.J. Bollyky, T. Templin, M. Cohen, J.L. Dieleman, Health Aff. 36 (2017) 1866–1875.

[5] R. Townsend N, Williams J, Bhatnagar P, Wickramasinghe K, M, Cardiovascular Disease Statistics, 2014, 2014.

[6] Z. Altintas, W.M. Fakanya, I.E. Tothill, Talanta 128 (2014) 177–186.

[7] R. Ross, New Engl. J. Med. 1999, 340115-126 340 (1999) 115–126.

[8] World Health Organization, The World Health Report 2002 - Reducing Risks, Promoting Healthy life1. World Health Organisation. The World Health Report 2002 - Reducing Risks, Promoting Healthy Life. Geneva: WHO. 2002., 2002.

[9] C.J. Murray, A. Lopez, in: Glob. Burd. Dis., 1996, pp. 1–51.

[10] C.D. Mathers, A. Lopez, C. Stein, D.M. Fat, C. Rao, M. Inoue, K. Shibuya, N. Tomijima, World Health (2003) 1–117.

[11] World Health Organization, Glob. Status Rep. Non-Communicable Dis. 2010 (2011) 9–31.

[12] T.A. Gaziano, Circulation 112 (2005) 3547–3553.

[13] WHO, Geneva Wold Heal. Organ. (2003) 204.

[14] C. Lenfant, Bull. World Health Organ. 79 (2001) 980–982; discussion 983.

[15] L. Allen, J. Williams, N. Townsend, B. Mikkelsen, N. Roberts, C. Foster, K. Wickramasinghe, Lancet 388 (2016) S17.

[16] Y. Seedat, Cardiovasc. J. AFRICA Cardiovasc J Afr 18 (2007) 316–320.

[17] E.S. Lee, R. Vedanthan, P. Jeemon, J.H. Kamano, P. Kudesia, V. Rajan, M. Engelgau, A.E. Moran, PLoS One 11 (2016).

[18] K. Yeates, L. Lohfeld, J. Sleeth, F. Morales, Y. Rajkotia, O. Ogedegbe, Can. J. Cardiol. 31 (2015) 1081–1093.

[19] H.C. McGill, C.A. McMahan, S.S. Gidding, Circulation 117 (2008) 1216–1227.

[20] L. Wilhelmsen, in: Int. Encycl. Public Heal., 2016, pp. 438–447.

[21] M. Mohammadnezhad, T. Mangum, W. May, J. Jeffrey Lucas, S. Ailson, World J. Cardiovasc. Surg. 6 (2016) 153–170.

[22] E.G. Lakatta, D. Levy, Circulation 107 (2003) 139–146.

[23] J. Tuomilehto, Atheroscler. Suppl. 5 (2004) 9–17.

[24] B.J. North, D.A. Sinclair, Circ. Res. 110 (2012) 1097–1108.

[25] A. Moore, A.A. Mangoni, D. Lyons, S.H.D. Jackson, J Clin Pharmacol 56 (2003) 254–260.

[26] E.G. Lakatta, D. Levy, Circulation 107 (2003) 139–146.

[27] D.G. Beevers, J. Hum. Hypertens. 19 (2005) 505–505.

[28] J.M. Bachmann, B.L. Willis, C.R. Ayers, A. Khera, J.D. Berry, Circulation 125 (2012) 3092–3098.

[29] D.M. Lloyd-Jones, B.H. Nam, R.B. D'Agostino, D. Levy, J.M. Murabito, T.J. Wang, P.W.F. Wilson, C.J. O'Donnell, J. Am. Med. Assoc. 291 (2004) 2204–2211.

[30] M.B. Andresdottir, G. Sigurdsson, H. Sigvaldason, V. Gudnason, Eur. Heart J. 23 (2002) 1655–1663.

[31] M.R. Kolber, C. Scrimshaw, Can. Fam. Physician 60 (2014) 1016.

[32] L. Valerio, R.J. Peters, A.H. Zwinderman, S.J. Pinto-Sietsma, J. Am. Heart Assoc. 5 (2016) 1–10.

[33] G. L. Wells, Curr. Vasc. Pharmacol. 14 (2016) 452–457.

[34] S.S. Anand, S. Islam, A. Rosengren, M.G. Franzosi, K. Steyn, A.H. Yusufali, M. Keltai, R. Diaz, S. Rangarajan, S. Yusuf, Eur. Heart J. 29 (2008) 932–940.

[35] M.A. Espeland, S.M. Marcovina, V. Miller, P.D. Wood, C. Wasilauskas, R. Sherwin, H. Schrott, T.L. Bush, Circulation 97 (1998) 979–986.

[36] The Writing Group for the PEPI Trial, JAMA 273 (1995) 199–208.

[37] N. Sattar, I. a Greer, BMJ 325 (2002) 157–160.

[38] L. Bellamy, J.P. Casas, A.D. Hingorani, D.J. Williams, Br. Med. J. 335 (2007) 974–977.

[39] H. King, Diabetes Care 21 Suppl 2 (1998) B9–B13.

[40] B.J. Wilson, M.S. Watson, G.J. Prescott, S. Sunderland, D.M. Campbell, P. Hannaford, W.C.S. Smith, Br. Med. J. 326 (2003) 845–849.

[41] M.S. Ellulu, I. Patimah, H. Khaza'ai, A. Rahmat, Y. Abed, F. Ali, Inflammopharmacology 24 (2016) 1–10.

[42] D.R. Greaves, S. Gordon, in: Trends Immunol., 2001, pp. 180–181.

[43] J. Gander, X. Sui, L.J. Hazlett, B. Cai, J.R. Hébert, S.N. Blair, Prev. Chronic Dis. 11 (2014) 140045.

[44] L.. Boamponsem, A.G, Boamponsem, Library (Lond). 2 (2011) 194–207.

[45] N.T. Mulvihill, J.B. Foley, Heart 87 (2002) 201–204.

[46] J. Herrmann, L.O. Lerman, D. Mukhopadhyay, C. Napoli, A. Lerman, Arterioscler. Thromb. Vasc. Biol. 26 (2006) 1948–1957.

[47] R. Ross, L. Agius, Diabetologia 35 (1992).

[48] L. Badimon, V. Llorente-Cortés, in: Encycl. Endocr. Dis., 2004, pp. 278–287.

[49] R.A. Brown, E. Shantsila, C. Varma, G.Y.H. Lip, Am. J. Med. 130 (2017) 268–282.

[50] K. Ley, Y.I. Miller, C.C. Hedrick, Arterioscler. Thromb. Vasc. Biol. 31 (2011) 1506–1516.

[51] Y. V. Bobryshev, E.A. Ivanova, D.A. Chistiakov, N.G. Nikiforov, A.N. Orekhov, Biomed Res. Int. 2016 (2016) 1–13.

[52] P. Libby, Nature 420 (2002) 868–874.

[53] D. Steinberg, S. Parthasarathy, T.E. Carew, J.C. Khoo, J.L. Witztum, N. Engl. J. Med. 320 (1989) 915–924.

[54] H.N. Ginsberg, Diabetes Care 14 (1991) 839–855.

[55] S. Allahverdian, P.S. Pannu, G.A. Francis, Cardiovasc. Res. 95 (2012) 165–172.

[56] P. Libby, P.M. Ridker, A. Maseri, Circulation 105 (2002) 1135–1143.

[57] M. Mietus-Snyder, M.S. Gowri, R.E. Pitas, J. Biol. Chem. 275 (2000) 17661–17670.

[58] H.Y. Choi, M. Rahmani, B.W. Wong, S. Allahverdian, B.M. McManus, J.G. Pickering, T. Chan, G.A. Francis, Circulation 119 (2009) 3223–3231.

[59] J.X. Rong, M. Shapiro, E. Trogan, E.A. Fisher, Proc. Natl. Acad. Sci. 100 (2003) 13531–13536.

[60] S. Allender, V. Peto, P. Scarborough, A. Kaur, M. Rayner, Br. Hear. Found. Heal. Promot. Res. Gr. (2008) 1–220.

[61] R.A. Kloner, B. Chaitman, J. Cardiovasc. Pharmacol. Ther. 22 (2017) 199–209.

[62] J.L. Anderson, C.D. Adams, E.M. Antman, C.R. Bridges, R.M. Califf, D.E. Casey, W.E. Chavey, F.M. Fesmire, J.S. Hochman, T.N. Levin, A.M. Lincoff, E.D. Peterson, P. Theroux, N.K. Wenger, R.S. Wright, S.C. Smith, A.K. Jacobs, C.D. Adams, J.L. Anderson, E.M. Antman, J.L. Halperin, S.A. Hunt, H.M. Krumholz, F.G. Kushner, B.W. Lytle, R. Nishimura, J.P. Ornato, R.L. Page, B. Riegel, J. Am. Coll. Cardiol. 50 (2007) 652–726.

[63] J.M. Torpy, F.E. Gorbacheva, G.M. Natiazhkina, B.J. Mink, Feldsher I Akusherka 303 (2010) 2312.

[64] E.T. Carreras, J.L. Mega, Circulation 129 (2014) e506–e508.

[65] C.S. Breathnach, W. Westphal, PACE - Pacing Clin. Electrophysiol. 29 (2006) 422–424.

[66] S. Yusuf, M. Pearson, H. Sterry, S. Parish, D. Ramsdale, P. Rossi, P. Sleight, Eur. Heart J. 5 (1984) 690–696.

[67] S.G. Foy, I.C.S. Kennedy, H. Ikram, C.J.S. Low, T.M. Shirlaw, I.G. Crozier, Aust. N. Z. J. Med. 21 (1991) 335–337.

[68] P. Stubbs, P.O. Collinson, Clin. Chim. Acta 311 (2001) 57–61.

[69] G.J. Kost, N.K. Tran, Cardiol. Clin. 23 (2005) 467–490.

[70] J.D. Schuijf, L.J. Shaw, W. Wijns, H.J. Lamb, D. Poldermans, A. De Roos, E.E. Van Der Wall, J.J. Bax, Heart 91 (2005) 1110–1117.

[71] I.M. Adame, P.J.H. De Koning, B.P.F. Lelieveldt, B.A. Wasserman, J.H.C. Reiber, R.J. Van Der Geest, Stroke 37 (2006) 2162–2164.

[72] J.D. Anderson, C.M. Kramer, Expert Rev. Cardiovasc. Ther. 5 (2007) 69–80.

[73] R.P. Choudhury, V. Fuster, J.J. Badimon, E.A. Fisher, Z.A. Fayad, Arterioscler. Thromb. Vasc. Biol. 22 (2002) 1065–1074.

[74] J. Cai, T.S. Hatsukami, M.S. Ferguson, W.S. Kerwin, T. Saam, B. Chu, N. Takaya, N.L. Polissar, C. Yuan, Circulation 112 (2005) 3437–3444.

[75] F. Ricci, G. Volpe, L. Micheli, G. Palleschi, Anal. Chim. Acta 605 (2007) 111–129.

[76] A. Makaraviciute, A. Ramanaviciene, Biosens. Bioelectron. 50 (2013) 460–471.

[77] N.G. Welch, J.A. Scoble, B.W. Muir, P.J. Pigram, Biointerphases 12 (2017) 02D301-1-02D301-13.

[78] R. Ekins, F. Chu, J. Int. Fed. Clin. Chem. 9 (1997) 100–109.

[79] M.A. Cooper, Nat. Rev. Drug Discov. 1 (2002) 515–528.

[80] P.B. Luppa, L.J. Sokoll, D.W. Chan, Clin. Chim. Acta 314 (2001) 1–26.

[81] C.A. Marquette, L.J. Blum, Biosens. Bioelectron. 21 (2006) 1424–1433.

[82] E. Mallat, D. Barceló, C. Barzen, G. Gauglitz, R. Abuknesha, TrAC - Trends Anal. Chem. 20 (2001) 124–132.

[83] A.H. Severs, R.B.M. Schasfoort, M.H.L. Salden, Biosens. Bioelectron. 8 (1993) 185–189.

[84] J. Wei, Y. Mu, D. Song, X. Fang, X. Liu, L. Bu, H. Zhang, G. Zhang, J. Ding, W. Wang, Q. Jin, G. Luo, Anal. Biochem. 321 (2003) 209–216.

[85] V.I. Chegel, Y.M. Shirshov, E. V. Piletskaya, S.A. Piletsky, Sensors Actuators, B Chem. 48 (1998) 456–460.

[86] P.T. Charles, J.G. Rangasammy, G.P. Anderson, T.C. Romanoski, A.W. Kusterbeck, Anal. Chim. Acta 525 (2004) 199–204.

[87] X.-H. Chen, S. Huang, D. Kerr, IARC Sci. Publ. 163 (2011) 303–322.

[88] M. Kumar, S.K. Sarin, Curr. Trends Sci. 15 (2010) 403–417.

[89] H. Ohigashi, G. Haraguchi, S. Yoshikawa, T. Sasaki, S. Kimura, H. Inagaki, H. Hachiya, K. Hirao, M. Isobe, Int. Heart J. 51 (2010) 416–420.

[90] A.J. Atkinson, W.A. Colburn, V.G. DeGruttola, D.L. DeMets, G.J. Downing, D.F. Hoth, J.A. Oates, C.C. Peck, R.T. Schooley, B.A. Spilker, J. Woodcock, S.L. Zeger, Clin. Pharmacol. Ther. 69 (2001) 89–95.

[91] H.M.E. Azzazy, R.H. Christenson, Clin. Biochem. 35 (2002) 13–27.

[92] M. Panteghini, Eur. Heart J. 25 (2004) 1187–1196.

[93] F.S. Apple, Clin. Chim. Acta 380 (2007) 1–3.

[94] A.S. Jaffe, L. Babuin, F.S. Apple, J. Am. Coll. Cardiol. 48 (2006) 1–11.

[95] B. Mcdonnell, S. Hearty, P. Leonard, R.O.' Kennedy, Clin. Biochem. 42 (2009) 549–561.

[96] G.P. Manukyan, K.A. Ghazaryan, Z.A. Ktsoyan, M. V. Tatyan, Z.A. Khachatryan, G.S. Hakobyan, V.A. Mkrtchyan, D. Kelly, A. Coutts, R.I. Aminov, Clin. Biochem. 41 (2008) 920–922.

[97] B. McDonnell, S. Hearty, W.J.J. Finlay, R. O'Kennedy, Anal. Biochem. 410 (2011) 1–6.

[98] A. Qureshi, Y. Gurbuz, J.H. Niazi, Sensors Actuators, B Chem. 171–172 (2012) 62–76.

[99] M.I. Mohammed, M.P.Y. Desmulliez, Lab Chip 11 (2011) 569–595.

[100] P.K. Nigam, Indian J. Clin. Biochem. 22 (2007) 10–17.

[101] T.A. Pearson, G.A. Mensah, R.W. Alexander, J.L. Anderson, R.O. Cannon, M. Criqui, Y.Y. Fadl, S.P. Fortmann, Y. Hong, G.L. Myers, N. Rifai, S.C. Smith, K. Taubert, R.P. Tracy, F. Vinicor, Circulation 107 (2003) 499–511.

[102] W.E. Secor, M.G. Dos Reis, E.A.G. Ramos, E.P. Matos, E.A.G. Reis, T.M.A. Do Carmo, D.A. Harn, Infect. Immun. 62 (1994) 2695–2701.

[103] J. Wilkins, J.R. Gallimore, G.A. Tennent, P.N. Hawkins, P.C. Limburg, M.H. Van Rijswijk, E.G. Moore, M.B. Pepys, Clin. Chem. 40 (1994) 1284–1290.

[104] EHN, (2008) 1–113.

[105] S.P. Mazer, L.E. Rabbani, J. Thromb. Thrombolysis 17 (2004) 95–105.

[106] M.H.F. Meyer, M. Hartmann, H.-J. Krause, G. Blankenstein, B. Mueller-Chorus, J. Oster, P. Miethe, M. Keusgen, Biosens. Bioelectron. 22 (2007) 973–979.

[107] A. Quershi, Y. Gurbuz, W.P. Kang, J.L. Davidson, Biosens. Bioelectron. 25 (2009) 877–882.

[108] J.-J. Li, C.-H. Fang, Med. Hypotheses 62 (2004) 499–506.

[109] Y.-N. Yang, H.-I. Lin, J.-H. Wang, S.-C. Shiesh, G.-B. Lee, Biosens. Bioelectron. 24 (2009) 3091–3096.

[110] J.D. McBride, M.A. Cooper, J. Nanobiotechnology 6 (2008) 1–8.

[111] B.C. Berk, W.S. Weintraub, R.W. Alexander, Am. J. Cardiol. 65 (1990) 168–172.

[112] F.C. de Beer, C.R. Hind, K.M. Fox, R.M. Allan, A. Maseri, M.B. Pepys, Heart 47 (1982) 239–243.

[113] V. Pasceri, J.T. Willerson, E.T. Yeh, Circulation 102 (2000) 2165–2168.

[114] E.T.H. Yeh, H.V. Anderson, V. Pasceri, J.T. Willerson, Circulation 104 (2001) 974–975.

[115] E. Braunwald, N. Engl. J. Med. 358 (2008) 2148–2159.

[116] L. Babuin, A.S. Jaffe, CMAJ 173 (2005) 1191–1202.

[117] E. Magnus Ohman, Clin. Chem. 63 (2017) 429–430.

[118] S. Hasić, E. Kiseljaković, R. Jadrić, J. Radovanović, M. Winterhalter-Jadrić, Bosn. J. Basic Med. Sci. 3 (2003) 41–44.

[119] S. Mythili, N. Malathi, Biomed. Reports 3 (2015) 743–748.

[120] R. Alcalai, D. Planer, A. Culhaoglu, A. Osman, A. Pollak, C. Lotan, Arch. Intern. Med. 167 (2007) 276–281.

[121] A. Jeremias, C.M. Gibson, Ann. Intern. Med. 142 (2005) 786–791.

[122] J.T. Martins, D.J. Li, L.B. Baskin, I. Jialal, J.H. Keffer, Am. J. Clin. Pathol. 106 (1996) 705–708.

[123] A.B. Storrow, W.B. Gibler, in: Clin. Chim. Acta, 1999, pp. 187–196.

[124] G.X. Brogan, S. Friedman, C. McCuskey, D.S. Cooling, L. Berrutti, H.C. Thode, J.L. Bock, Ann. Emerg. Med. 24 (1994) 665–671.

[125] R.H. Christenson, H.M.E. Azzazy, in: Clin. Chem., 1998, pp. 1855–1864.

[126] F.S. Apple, Clin. Chim. Acta 380 (2007) 1–3.

[127] C.I. Bhagat, P. Langton, M. Lewer, S. Ching, J.P. Beilby, Ann. Clin. Biochem. 34 (1997) 511–516.

[128] R.G. Males, J. Stephenson, P. Harris, Crit. Care Nurs. Q. 24 (2001) 54–61.

[129] M. Panteghini, C. Cuccia, Clin. Cardiol. 21 (1998) 394–398.

[130] K. Pandit, S. Ghosh, P. Mukhopadhyay, S. Chowdhury, Indian J. Endocrinol. Metab. 15 (2011) 345–353.

[131] D.G. Gardner, C.F. Deschepper, W.F. Ganong, S. Hane, J. Fiddes, J.D. Baxter, J. Lewicki, Proc. Nat. Acad. Sci. USA 83 (1986) 6697–6701.

[132] T. Sudoh, K. Kangawa, N. Minamino, H. Matsuo, Nature 332 (1988) 78–81.

[133] M. Mukoyama, K. Nakao, Y. Saito, Y. Ogawa, K. Hosoda, S.I. Suga, G. Shirakami, M. Jougasaki, H. Imura, Lancet 335 (1990) 801–802.

[134] Y. Saito, K. Nakao, H. Itoh, T. Yamada, M. Mukoyama, H. Arai, K. Hosoda, G. Shirakami, S. ichi Suga, N. Minamino, K. Kangawa, H. Matsuo, H. Imura, Biochem. Biophys. Res. Commun. 158 (1989) 360–368.

[135] T. Tsutamoto, A. Wada, K. Maeda, T. Hisanaga, Y. Maeda, D. Fukai, M. Ohnishi, Y. Sugimoto, M. Kinoshita, Circulation 96 (1997) 509–516.

[136] H.H. Chen, J.C. Burnett, Curr. Cardiol. Rep. 2 (2000) 198–205.

[137] J. Koglin, S. Pehlivanli, M. Schwaiblmair, M. Vogeser, P. Cremer, W. VonScheidt, J. Am. Coll. Cardiol. 38 (2001) 1934–1941.

[138] Y. Iwanaga, S. Miyazaki, Circ J 74 (2010) 1274–1282.

[139] S.A. Park, T.G. Kim, M.K. Han, K.C. Ha, S.Z. Kim, Y.G. Kwak, Exp. Mol. Med. 44 (2012) 363–368.

[140] W. Hochholzer, D.A. Morrow, R.P. Giugliano, Am. Heart J. 160 (2010) 583–594.

[141] S.J. Nicholls, S.L. Hazen, in: Jpn. J. Infect. Dis., 2004, pp. S21-22.

[142] N. Teng, G.J. Maghzal, J. Talib, I. Rashid, A.K. Lau, R. Stocker, Redox Rep. 22 (2017) 51–73.

[143] R. Stocker, A. Huang, E. Jeranian, J.Y. Hou, T.T. Wu, S.R. Thomas, J.F. Keaney, Arterioscler. Thromb. Vasc. Biol. 24 (2004) 2028–2033.

[144] A. Prasad, S. Tsimikas, Curr. Atheroscler. Rep. 10 (2008) 309–317.

[145] S. Sugiyama, Y. Okada, G.K. Sukhova, R. Virmani, J.W. Heinecke, P. Libby, Am. J. Pathol. 158 (2001) 879–891.

[146] B. Prieto-Simon, M. Campas, J.-L. Marty, Protein Pept. Lett. 15 (2008) 757–763.

[147] A.A. Karyakin, G. V. Presnova, M.Y. Rubtsova, A.M. Egorov, Anal. Chem. 72 (2000) 3805–3811.

[148] W. Kusnezow, J.D. Hoheisel, J. Mol. Recognit. 16 (2003) 165–176.

[149] J. Buijs, W. Norde, J.W.T. Lichtenbelt, Langmuir 12 (1996) 1605–1613.

[150] V. Hlady, J. Buijs, Curr. Opin. Biotechnol. 7 (1996) 72–77.

[151] M.E. Wiseman, C.W. Frank, Langmuir 28 (2012) 1765–1774.

[152] J.E. Butler, L. Ni, W.R. Brown, K.S. Joshi, J. Chang, B. Rosenberg, E.W. Voss, Mol. Immunol. 30 (1993) 1165–1175.

[153] J.E. Butler, Methods 22 (2000) 4–23.

[154] J.E. Butler, L. Ni, R. Nessler, K.S. Joshi, M. Suter, B. Rosenberg, J. Chang, W.R. Brown, L.A. Cantarero, J. Immunol. Methods 150 (1992) 77–90.

[155] S. V. Rao, K.W. Anderson, L.G. Bachas, Mikrochim. Acta 128 (1998) 127–143.

[156] M. Wilchek, T. Miron, J. Biochem. Biophys. Methods 55 (2003) 67–70.

[157] Y. Liu, J. Yu, Microchim. Acta 183 (2016) 1–19.

[158] F. Rusmini, Z. Zhong, J. Feijen, Biomacromolecules 8 (2007) 1775–1789.

[159] C. Viguier, C. Crean, R. O'Kennedy, in: ANTIBODIES Appl. NEW Dev., 2012, pp. 184–208.

[160] J.M. Goddard, J.H. Hotchkiss, Prog. Polym. Sci. 32 (2007) 698–725.

[161] H. Sharma, R. Mutharasan, Anal. Chem. 85 (2013) 2472–2477.

[162] A.K. Trilling, J. Beekwilder, H. Zuilhof, Analyst 138 (2013) 1619–1627.

[163] T. Matsumoto, S. Sawamoto, T. Sakamoto, T. Tanaka, H. Fukuda, A. Kondo, J. Biotechnol. 152 (2011) 37–42.

[164] T. Matsumoto, T. Tanaka, A. Kondo, Langmuir 28 (2012) 3553–3557.

[165] Y. Mori, R. Wakabayashi, M. Goto, N. Kamiya, Org. Biomol. Chem. 11 (2013) 914–922.

[166] M.B. Young, B.K. Oh, W. Lee, H.L. Won, J.W. Choi, Biosens. Bioelectron. 21 (2005) 103–110.

[167] R. Danczyk, B. Krieder, A. North, T. Webster, H. HogenEsch, A. Rundell, Biotechnol. Bioeng. 84 (2003) 215–223.

[168] E.J. Franco, H. Hofstetter, O. Hofstetter, J. Sep. Sci. 29 (2006) 1458–1469.

[169] H. Kim, D.Y. Kang, H.J. Goh, B.K. Oh, R.P. Singh, S.M. Oh, J.W. Choi, Ultramicroscopy 108 (2008) 1152–1156.

[170] J.W. Choi, Y.K. Kim, B.K. Oh, Ultramicroscopy 108 (2008) 1396–1400.

[171] A.K. Adak, B.Y. Li, L. De Huang, T.W. Lin, T.C. Chang, K.C. Hwang, C.C. Lin, ACS Appl. Mater. Interfaces 6 (2014) 10452–10460.

[172] S. Kumar, J. Aaron, K. Sokolov, Nat. Protoc. 3 (2008) 314–320.

[173] S. Wang, J. Ye, X. Li, Z. Liu, Anal. Chem. 88 (2016) 5088–5096.

[174] J.A. Peters, Coord. Chem. Rev. 268 (2014) 1–22.

[175] W.L.A. Brooks, B.S. Sumerlin, Chem. Rev. 116 (2016) 1375–1397.

[176] O.W. Lau, B. Shao, M.T.W. Lee, Anal. Chim. Acta 403 (2000) 49–56.

[177] A. Kugimiya, T. Takeuchi, in: Biosens. Bioelectron., 2001, pp. 1059–1062.

[178] D. Bongartz, A. Hesse, J. Chromatogr. B Biomed. Sci. Appl. 673 (1995) 223–230.

[179] T. Koyama, K.I. Terauchi, J. Chromatogr. B Biomed. Appl. 679 (1996) 31–40.

[180] K. Aslan, J. Zhang, J.R. Lakowicz, C.D. Geddes, J. Fluoresc. 14 (2004) 391–400.

[181] K. Kataoka, I. Hisamitsu, N. Sayama, T. Okano, Y. Sakurai, J. Biochem. 117 (1995) 1145–1147.

[182] M. Nicolas, B. Fahre, J. Simonet, Electrochim. Acta 46 (2001) 1179–1190.

[183] R. Wannapob, P. Kanatharana, W. Limbut, A. Numnuam, P. Asawatreratanakul, C. Thammakhet, P. Thavarungkul, Biosens. Bioelectron. 26 (2010) 357–364.

[184] J. Přibyl, P. Skládal, in: Biosens. Bioelectron., 2006, pp. 1952–1959.

[185] R. Freeman, L. Bahshi, T. Finder, R. Gill, I. Willner, Chem. Commun. (2009) 764–766.

[186] J. an A. Ho, W.L. Hsu, W.C. Liao, J.K. Chiu, M.L. Chen, H.C. Chang, C.C. Li, Biosens. Bioelectron. 26 (2010) 1021–1027.

[187] S. Qian, Y. Zhang, H. Yuan, W. Ji, Y. Liu, J. Zhao, M. Han, W. Peng, Sensors Actuators, B Chem. 260 (2018) 976–982.

[188] Y. Mayang, X. He, L. Chen, Y. Zhang, Microchim. Acta 184 (2017) 2749–2757.

[189] J. Yang, X. He, L. Chen, Y. Zhang, Anal. Methods 8 (2016) 8345–8351.

[190] J. yang, X. He, L. Chen, Y. Zhang, J. Chromatogr. A 1513 (2017) 118–125.

[191] S.E. Diltemiz, A. Ersöz, D. Hür, R. Keçili, R. Say, Mater. Sci. Eng. C 33 (2013) 824–830.

[192] M. Moreno-Guzmán, I. Ojeda, R. Villalonga, A. González-Cortés, P. Yáñez-Sedeño, J.M. Pingarrón, Biosens. Bioelectron. 35 (2012) 82–86.

[193] D.T. and M.I. kaiki Tsugimura, Hitoshi Ohnuki, Haiyun Wu, Hideaki Endo, J. Phys. (2017) 1–9.

[194] H.C. Woo, Y. Sakata, Y. Kurihara, T. Ooya, T. Takeuchi, Anal. Chim. Acta 728 (2012) 64–68.

[195] D.A. Links, Analyst 136 (2011) 1412–1419.

[196] N. Tajima, M. Takai, K. Ishihara, Anal. Chem. 83 (2011) 1969–1976.

[197] I.E. Tothill, Semin. Cell Dev. Biol. 20 (2009) 55–62.

[198] M. AzizollahiAliabadi, A. Azizzadeh, M. Nourbakhsh, R. Kazemi-Darsanaki, G. Raeisi, J. Biol. Today's World 2 (2015).

[199] B. Bohunicky, S.A. Mousa, Nanotechnol. Sci. Appl. 4 (2011) 1–10.

[200] S.M. Borisov, O.S. Wolfbeis, Chem. Rev. 108 (2008) 423–461.

[201] F.S. Ligler, Anal.Chem. 81 (2009) 519–526.

[202] R.B.M. Schasfoort, F. Abali, I. Stojanovic, G. Vidarsson, L.W.M.M. Terstappen, Biosensors 8 (2018) 1–11.

[203] S. Mohseni, T.T. Moghadam, B. Dabirmanesh, S. Jabbari, K. Khajeh, Biosens. Bioelectron. 81 (2016) 510–516.

[204] Y. Tang, X. Zeng, J. Liang, J. Chem. Educ. 87 (2010) 742–746.

[205] B. Lee, T. Chung, Springer Ser. Surf. Sci. 56 (2015) 335–354.

[206] S. Patskovsky, A. V. Kabashin, M. Meunier, J.H.T. Luong, J. Opt. Soc. Am. A 20 (2007) 1644–1650.

[207] P. Englebienne, A. Van Hoonacker, M. Verhas, Spectroscopy 17 (2003) 255–273.

[208] J.F. Masson, T.M. Battaglia, P. Khairallah, S. Beaudoin, K.S. Booksh, Anal. Chem. 79 (2007) 612–619.

[209] M.H.F. Meyer, M. Hartmann, M. Keusgen, Biosens. Bioelectron. 21 (2006) 1987–1990.

[210] J.P. J. Jose, M.Park, Biosens. Bioelectron. 25 (2010) 1225–1228.

[211] S.K. Vashist, E.M. Schneider, J.H.T. Luong, Analyst 140 (2015) 4445–4452.

[212] J.T. Liu, C.J. Chen, T. Ikoma, T. Yoshioka, J.S. Cross, S.J. Chang, J.Z. Tsai, J. Tanaka, Anal. Chim. Acta 703 (2011) 80–86.

[213] R.F. Dutra, L.T. Kubota, Clin. Chim. Acta 376 (2007) 114–120.

[214] R.F. Dutra, R.K. Mendes, V. Lins da Silva, L.T. Kubota, J. Pharm. Biomed. Anal. 43 (2007) 1744–1750.

[215] Y.C. Kwon, M.G. Kim, E.M. Kim, Y.B. Shin, S.K. Lee, S.D. Lee, M.J. Cho, H.S. Ro, Biotechnol. Lett. 33 (2011) 921–927.

[216] R. Kurita, Y. Yokota, Y. Sato, F. Mizutani, O. Niwa, Anal. Chem. 78 (2006) 5525–5531.

[217] X. Chen, Y. Liu, J. Huang, W. Liu, J. Huang, Y. Zhang, W. Fu, Front. Lab. Med. 1 (2017) 82–85.

[218] C. Steinem, Methods 305 (2005) 47–64.

[219] Ö. Ertekin, S. Öztürk, Z.Z. Öztürk, Sensors (Switzerland) 16 (2016) 1–12.

[220] M.K.A. Kadir, I.E. Tothill, Toxins (Basel). 2 (2010) 382–398.

[221] F. Salam, I.E. Tothill, Biosens. Bioelectron. 24 (2009) 2630–2636.

[222] M. Mazloum-Ardakani, L. Hosseinzadeh, A. Khoshroo, H. Naeimi, M. Moradian, Electroanalysis 26 (2014) 275–284.

[223] J. Wang, R. Yuan, Y. Chai, S. Cao, S. Guan, P. Fu, L. Min, Biochem. Eng. J. 51 (2010) 95–101.

[224] B. Zhang, D. Tang, B. Liu, H. Chen, Y. Cui, G. Chen, Biosens. Bioelectron. 28 (2011) 174–180.

[225] E. V. Suprun, A.L. Shilovskaya, A. V. Lisitsa, T. V. Bulko, V. V. Shumyantseva, A.I. Archakov, Electroanalysis 23 (2011) 1051–1057.

[226] M. Buch, J. Rishpon, Electroanalysis 20 (2008) 2592–2594.

[227] X. Zhang, R. Hu, K. Zhang, R. Bai, D. Li, Y. Yang, Anal. Methods 8 (2016) 6202–6207.

[228] W.M. Fakanya, I.E. Tothill, Biosensors 4 (2014) 340–357.

[229] F. Zhou, M. Lu, W. Wang, Z.P. Bian, J.R. Zhang, J.J. Zhu, Clin. Chem. 56 (2010) 1701–1707.

[230] N. Puri, V.K. Tanwar, V. Sharma, T. Ahuja, A.M. Biradar, Rajesh, Int. J. Integr. Biol. 9 (2010) 1–5.

[231] B. Esteban-Fernández De Ávila, V. Escamilla-Gómez, S. Campuzano, M. Pedrero, J.P. Salvador, M.P. Marco, J.M. Pingarrón, Sensors Actuators, B Chem. 188 (2013) 212–220.

[232] X. Chen, Y. Wang, J. Zhou, W. Yan, X. Li, J.-J. Zhu, Anal.Chem. 80 (2008) 2133–2140.

[233] C. Kokkinos, M. Prodromidis, A. Economou, P. Petrou, S. Kakabakos, Anal. Chim. Acta 886 (2015) 29–36.

[234] Rajesh, V. Sharma, V.K. Tanwar, A.M. Biradar, Sens. Lett. 8 (2010) 362–369.

[235] R.K. Gupta, A. Periyakaruppan, M. Meyyappan, J.E. Koehne, Biosens. Bioelectron. 59 (2014) 112–119.

[236] M. Pohanka, P. Skládal, J. Appl. Biomed. (2008) 57–64.

[237] J.L. Hammond, N. Formisano, P. Estrela, S. Carrara, J. Tkac, Essays Biochem. 60 (2016) 69–80.

[238] Z.P. Aguilar, in: Nanomater. Med. Appl., 2013, pp. 127–179.

[239] R. Koncki, Anal. Chim. Acta 599 (2007) 7–15.

[240] R. Moos, K. Sahner, M. Fleischer, U. Guth, N. Barsan, U. Weimar, Sensors 9 (2009) 4323–4365.

[241] E. Bakker, E. Pretsch, TrAC - Trends Anal. Chem. 24 (2005) 199–207.

[242] H. Zheng, X. Ma, L. Chen, Z. Lin, L. Guo, B. Qiu, G. Chen, Anal. Methods 5 (2013) 5005–5009.

[243] M.I. Prodromidis, Electrochim. Acta 55 (2010) 4227–4233.

[244] L. Yang, Y. Li, G.F. Erf, Anal. Chem. 76 (2004) 1107–1113.

[245] H. Chen, J.H. Jiang, Y. Huang, T. Deng, J.S. Li, G.L. Shen, R.Q. Yu, Sensors Actuators, B Chem. 117 (2006) 211–218.

[246] A.C. Barton, F. Davis, S.P.J. Higson, Anal. Chem. 80 (2008) 9411–9416.

[247] L. Wang, X. Wang, X. Chen, J. Liu, S. Liu, C. Zhao, Bioelectrochemistry 88 (2012) 30–35.

[248] S. Vogt, Q. Su, C. Gutiérrez-Sánchez, G. Nöll, Anal. Chem. 88 (2016) 4383–4390.

[249] A. Chowdhury, P. Singh, T.K. Bera, D. Ghoshal, B. Chakraborty, J. Food Meas. Charact. 11 (2017) 1–11.

[250] T. Repo, D.H. Paine, Taylor A.G.*, Seed Sci. Res. 12 (2002) 17–29.

[251] A. Bogomolova, E. Komarova, K. Reber, T. Gerasimov, O. Yavuz, S. Bhatt, M. Aldissi, Anal. Chem. 81 (2009) 3944–3949.

[252] M.C. Rodriguez, A.-N. Kawde, J. Wang, Chem. Commun. (2005) 4267–4269.

[253] X. Luo, A. Morrin, A.J. Killard, M.R. Smyth, Electroanalysis 18 (2006) 319–326.

[254] P. Pandey, M. Datta, B.D. Malhotra, Anal. Lett. 41 (2008) 159–209.

[255] Y.Y. Xu, C. Bian, S. Chen, S. Xia, Anal. Chim. Acta 561 (2006) 48–54.

[256] B. Qu, X. Chu, G. Shen, R. Yu, Talanta 76 (2008) 785–790.

[257] M. Hnaiein, W.M. Hassen, A. Abdelghani, C. Fournier-Wirth, J. Coste, F. Bessueille, D. Leonard, N. Jaffrezic-Renault, Electrochem. Commun. 10 (2008) 1152–1154.

[258] E. Katz, I. Willner, J. Wang, Electroanalysis 16 (2004) 19–44.

[259] C. Fenzl, T. Hirsch, A.J. Baeumner, TrAC - Trends Anal. Chem. 79 (2016) 306–316.

[260] Y. Seok Kim, N.H. Ahmad Raston, M. Bock Gu, Biosens. Bioelectron. 76 (2016) 2–19.

[261] M.L. Yola, V.K. Gupta, N. Atar, Mater. Sci. Eng. C 61 (2016) 368–375.

[262] T. Lakshmipriya, U. Hashim, S.C.B. Gopinath, N. Azizah, Microsyst. Technol. 22 (2016) 2389–2395.

[263] J. Li, Z. Zhu, B. Zhu, Y. Ma, B. Lin, R. Liu, Y. Song, H. Lin, S. Tu, C. Yang, Anal. Chem. 88 (2016) 7828–7836.

[264] B.R. Smith, S.S. Gambhir, Chem. Rev. 117 (2017) 901–986.

[265] S. Zhang, J. Cai, L. Wu, L. Wu, Zhongguo Yi Liao Qi Xie Za Zhi 38 (2014) 118–121.

[266] Y. Wu, C. Chen, S. Liu, Anal. Chem. 81 (2009) 1600–1607.

[267] Sang Ho Won and Sang Jun Sim, Analyst 137 (2012) 1241–1246.

[268] J.B. Haun, T.J. Yoon, H. Lee, R. Weissleder, Wiley Interdiscip. Rev. Nanomedicine Nanobiotechnology 2 (2010) 291–304.

[269] J.B. Haun, T.J. Yoon, H. Lee, R. Weissleder, Methods Mol. Biol. 726 (2011) 33–49.

[270] D.-W. Lee, H. Fatima, K.-S. Kim, J. Nanosci. Nanotechnol. 18 (2018) 1414–1418.

[271] H. Fatima, K.S. Kim, Korean J. Chem. Eng. 34 (2017) 589–599.

[272] K. El-Boubbou, D. Azar, A. Bekdash, R.J. Abi-Habib, J. Biomed. Nanotechnol. 13 (2017) 500–512.

[273] Wahajuddin, S. Arora, Int. J. Nanomedicine 7 (2012) 3445–3471.

[274] F. Xiong, S. Huang, N. Gu, Drug Dev. Ind. Pharm. 44 (2018) 697–706.

[275] P. Guardia, R. Di Corato, L. Lartigue, C. Wilhelm, A. Espinosa, M. Garcia-Hernandez, F. Gazeau, L. Manna, T. Pellegrino, ACS Nano 6 (2012) 3080–3091.

[276] I. Hilger, Int. J. Hyperth. 29 (2013) 828–834.

[277] C. Rümenapp, B. Gleich, A. Haase, Pharm. Res. 29 (2012) 1165–1179.

[278] A.J. McGrath, C. Dolan, S. Cheong, D.A.J. Herman, B. Naysmith, F. Zong, P. Galvosas, K.J. Farrand, I.F. Hermans, M. Brimble, D.E. Williams, J. Jin, R.D. Tilley, J. Magn. Magn. Mater. 439 (2017) 251–258.

[279] M. Holzinger, A. Le Goff, S. Cosnier, Front. Chem. 2 (2014) 1–10.

[280] L. Zhang, R. He, H.C. Gu, Appl. Surf. Sci. 253 (2006) 2611–2617.

[281] D. Maity, D.C. Agrawal, J. Magn. Magn. Mater. 308 (2007) 46–55.

[282] S. Santra, R. Tapec, N. Theodoropoulou, J. Dobson, A. Hebard, W. Tan, Langmuir 17 (2001) 2900–2906.

[283] H.H. Yang, S.Q. Zhang, X.L. Chen, Z.X. Zhuang, J.G. Xu, X.R. Wang, Anal. Chem. 76 (2004) 1316–1321.

[284] L.E. Euliss, S.G. Grancharov, S. O'Brien, T.J. Deming, G.D. Stucky, C.B. Murray, G.A. Held, Nano Lett. 3 (2003) 1489–1493.

[285] X. Liu, Y. Guan, Z. Ma, H. Liu, Langmuir 20 (2004) 10278–10282.

[286] R. Hong, N.O. Fischer, T. Emrick, V.M. Rotello, Chem. Mater. 17 (2005) 4617–4621.

[287] Y. Kobayashi, M. Horie, M. Konno, B. Rodríguez-González, L.M. Liz-Marzán, J. Phys. Chem. B 107 (2003) 7420–7425.

[288] R. Fu, X. Jin, J. Liang, W. Zheng, J. Zhuang, W. Yang, J. Mater. Chem. 21 (2011) 15352–15356.

[289] Q. Liu, Z. Xu, J.A. Finch, R. Egerton, Chem. Mater. 10 (1998) 3936–3940.

[290] J. Lin, W. Zhou, A. Kumbhar, J. Wiemann, J. Fang, E.E. Carpenter, C.J. O'Connor, J. Solid State Chem. 159 (2001) 26–31.

[291] M. Chen, S. Yamamuro, D. Farrell, S.A. Majetich, in: J. Appl. Phys., 2003, pp. 7551–7553.

[292] M. Knobel, K.R. Pirota, M.E.F. Brollo, D. Muraca, R. López-Ruiz, S.J.A. Figueroa, Sci. Rep. 4 (2014) 1–6.

[293] M. Mahmoudi, V. Serpooshan, ACS Nano 6 (2012) 2656–2664.

[294] C.J. Lee, Y.L. Tsai, H.T. Lee, H.C. Liao, Y.C. Tsai, P.I. Cheng, Int. J. Nanotechnol. 10 (2013) 916–927.

[295] J. Lewandowska, M. Staszewska, M. Kepczynski, M. Szuwarzyński, A. Łatkiewicz, Z. Olejniczak, M. Nowakowska, J. Sol-Gel Sci. Technol. 64 (2012) 67–77.

[296] E. Ghasemi, M. Ghahari, Int. J. Nanosci. Nanotechnol 11 (2015) 133–137.

[297] R. V. Ferreira, I.L.S. Pereira, L.C.D. Cavalcante, L.F. Gamarra, S.M. Carneiro, E. Amaro, J.D. Fabris, R.Z. Domingues, A.L. Andrade, Hyperfine Interact. 195 (2009) 265–274.

[298] H.M. Joshi, M. De, F. Richter, J. He, P. V. Prasad, V.P. Dravid, J. Nanoparticle Res. 15 (2013) 1–8.

[299] C.M.A. Brett, A.M. Oliveira Brett, Electrochemistry: Principles, Methods, and Applications, 1993.

[300] A.J. Bard, L.R. Faulkner, J. Leddy, C.G. Zoski, Electrochemical Methods: Fundamentals and Applications, 1980.

[301] P.R. Bard, Allen J; Stratmann, Martin; Unwin, Encycl. Electrochem. (2003) 81–104.

[302] P. Westbroek, G. Priniotakis, P. Kiekens, Analytical Electrochemistry in Textiles, 2005.

[303] E. Barsoukov, J.R. Macdonald, Impedance Spectroscopy, 2005.

[304] E. Korin, N. Froumin, S. Cohen, ACS Biomater. Sci. Eng. 3 (2017) 882–889.

[305] S.L. McArthur, G. Mishra, C.D. Easton, in: Surf. Anal. Tech. Biol., 2014, pp. 9–36.

[306] H. Bluhm, in: Situ Charact. Thin Film Growth, 2011, pp. 75–98.

[307] M. Aziz, A.F. Ismail, in: Membr. Charact., 2017, pp. 81–93.

[308] A.M. Etorki, F.M.N. Massoudi, M.M. Abuein, Adv. Sci. Lett. 17 (2012) 87–100.

[309] J.I. Goldstein, D.E. Newbury, P. Echlin, D.C. Joy, C.E. Lyman, E. Lifshin, L. Sawyer, J.R. Michael, Scanning Electron Microscopy and X-Ray Microanalysis, 2003.

[310] S. Cengiz, A.C. Karaca, I. Çakir, H.B. Üner, A. Sevindik, Forensic Sci. Int. 141 (2004) 33–37.

[311] R. Wang, J. Tao, K. Du, Y. Wang, B. Ge, F. Li, W. Liu, L. Wu, H. Liu, Y. Zhang, Y. Yao, X. Duan, in: Springer Tracts Mod. Phys., 2018, pp. 69–203.

[312] M.A. Asadabad, M.J. Eskandari, Synth. React. Inorganic, Met. Nano-Metal Chem. 45 (2015) 323–326.

[313] C.S.S.R. Kumar, Transmission Electron Microscopy Characterization of Nanomaterials, 2014.

[314] E. Le Bourhis, G. Patriarche, Micron 38 (2007) 377–389.

[315] M.C. Dixon, J. Biomol. Tech. 19 (2008) 151–158.

[316] E.B. Porcelli, V.S. Filho, J. Power Energy Eng. 6 (2018) 33–50.

[317] I.S. Park, D.K. Kim, N. Adanyi, M. Varadi, N. Kim, Biosens. Bioelectron. 19 (2004) 667–674.

[318] K.S. Chen, S.C. Chen, H.R. Lin, T.R. Yan, C.C. Tseng, Mater. Sci. Eng. C 27 (2007) 716–724.

[319] A.B. Mattos, T.A. Freitas, V.L. Silva, R.F. Dutra, Sensors Actuators, B Chem. 161 (2012) 439–446.

[320] A. Jaiswal, S. Smoukov, M. Poggi, B. Grzybowski, NSTI-Nanotech 1 (2008) 855–858.

[321] G. Sauerbrey, Zeitschrift Fuer Phys. 155 (1959) 206–222.

[322] F. Höök, B. Kasemo, T. Nylander, C. Fant, K. Sott, H. Elwing, Anal. Chem. 73 (2001) 5796–5804.

[323] R. Saber, S. Mutlu, E. Pişkin, Biosens. Bioelectron. 17 (2002) 727–734.

[324] C.A. Keller, B. Kasemo, Biophys. J. 75 (1998) 1397–1402.

[325] M. Liebau, A. Hildebrand, R.H.H. Neubert, Eur. Biophys. J. 30 (2001) 42–52.

[326] L. Tedeschi, L. Citti, C. Domenici, Biosens. Bioelectron. 20 (2005) 2376–2385.

[327] F. Höök, M. Rodahl, P. Brezezinski, B. Kasemo, Langmuir 14 (1998) 729–734.

[328] E.J. Calvo, R. Etchenique, L. Pietrasanta, A. Wolosiuk, C. Danilowicz, Anal. Chem. 73 (2001) 1161–1168.

[329] P. Mashazi, S. Vilakazi, T. Nyokong, Talanta 115 (2013) 694–701.

[330] A. Fashina, E. Antunes, T. Nyokong, Polyhedron 53 (2013) 278–285.

[331] Z.Y. Ma, X.Q. Liu, Y.P. Guan, H.Z. Liu, Colloids Surfaces A Physicochem. Eng. Asp. 275 (2006) 87–91.

[332] X. Liu, Z. Ma, J. Xing, H. Liu, J. Magn. Magn. Mater. 270 (2004) 1–6.

[333] E. Cheraghipour, S. Javadpour, A.R. Mehdizadeh, J. Biomed. Sci. Eng. 5 (2012) 715–719.

[334] S. Nigam, K.C. Barick, D. Bahadur, J. Magn. Magn. Mater. 323 (2011) 237–243.

[335] C. Li, X. Chen, N. Wang, B. Zhang, RSC Adv. 7 (2017) 21666–21670.

[336] D.L. Pilloud, X. Chen, P.L. Dutton, C.C. Moser, J. Phys. Chem. B 104 (2000) 2868–2877.

[337] R. Fogel, P. Mashazi, T. Nyokong, J. Limson, Biosens. Bioelectron. 23 (2007) 95–101.

[338] F. Höök, A. Ray, B. Nordén, B. Kasemo, Langmuir 17 (2001) 8305–8312.

[339] H. Ogi, T. Yanagida, M. Hirao, M. Nishiyama, Biosens. Bioelectron. 26 (2011) 4819–4822.

[340] T. Songjaroen, R.M. Feeny, M.M. Mensack, W. Laiwattanapaisal, C.S. Henry, Sens. Bio-Sensing Res. 8 (2016) 14–19.

[341] Y. Zhang, H. Wang, B. Yan, Y. Zhang, J. Li, G. Shen, R. Yu, J. Immunol. Methods 332 (2008) 103–111.

[342] J. Hu, L. Liu, B. Danielsson, X. Zhou, L. Wang, Anal. Chim. Acta 423 (2000) 215–219.

[343] Y. Fuchiwaki, M. Tanaka, Y. Makita, T. Ooie, Sensors (Switzerland) 14 (2014) 20468–20479.

[344] N. Gan, L. Wang, H. Zhou, T. Li, W. Sang, F. Hu, Y. Cao, Int. J. Electrochem. Sci. 7 (2012) 11564–11577.

[345] Y. Lv, R. Wu, K. Feng, J. Li, Q. Mao, H. Yuan, H. Shen, X. Chai, L.S. Li, J. Nanobiotechnology 15 (2017) 35.

[346] Y. Arima, H. Iwata, J. Mater. Chem. 17 (2007) 4079–4087.

[347] E. Briand, M. Salmain, C. Compère, C.M. Pradier, Colloids Surfaces B Biointerfaces 53 (2006) 215–224.

[348] J.K. Lee, Y.G. Kim, Y.S. Chi, W.S. Yun, I.S. Choi, J. Phys. Chem. B 108 (2004) 7665–7673.

[349] S. Sam, L. Touahir, J. Salvador Andresa, P. Allongue, J.N. Chazalviel, A.C. Gouget-Laemmel, C.H. De Villeneuve, A. Moraillon, F. Ozanam, N. Gabouze, S. Djebbar, Langmuir 26 (2010) 809–814.

[350] C. Gruian, E. Vanea, S. Simon, V. Simon, Biochim. Biophys. Acta - Proteins Proteomics 1824 (2012) 873–881.

[351] J. V. Maya Girón, R. V. Vico, B. Maggio, E. Zelaya, A. Rubert, G. Benítez, P. Carro, R.C. Salvarezza, M.E. Vela, Environ. Sci. Nano 3 (2016) 462–472.

[352] D. Barriet, C.M. Yam, O.E. Shmakova, A.C. Jamison, T.R. Lee, Langmuir 23 (2007) 8866–8875.

[353] B. Fabre, F. Hauquier, Langmuir 33 (2017) 8693–8699.

[354] G. Liu, M. Qi, Y. Zhang, C. Cao, E.M. Goldys, Anal. Chim. Acta 909 (2016) 1–8.

[355] S.Y. Song, H.C. Yoon, Sensors Actuators, B Chem. 140 (2009) 233–239.

[356] G. Iucci, G. Polzonetti, G. Infante, L. Rossi, Surf. Interface Anal. 36 (2004) 724–728.

[357] A. Lebugle, A. Rovira, M. Rabaud, C. Rey, J. Mater. Sci. Mater. Med. 7 (1996) 223–226.

[358] K. Dave, K.H. Park, M. Dhayal, RSC Adv. 5 (2015) 107348–107354.

[359] F. Caprioli, A. Martinelli, V. Di Castro, F. Decker, J. Electroanal. Chem. 693 (2013) 86–94.

[360] D.M. Kim, J.M. Moon, W.C. Lee, J.H. Yoon, C.S. Choi, Y.B. Shim, Biosens. Bioelectron. 91 (2017) 276–283.

[361] C.M. Costello, J.U. Kreft, C.M. Thomas, D.M. Hammes, P. Bao, S.D. Evans, P.M. Mendes, Soft Matter 8 (2012) 9147–9155.

[362] S. Eissa, M. Zourob, Microchim. Acta 184 (2017) 2281–2289.

[363] J. Yang, X. He, L. Chen, Y. Zhang, Anal. Methods 8 (2016) 8345–8351.

[364] E. González-Fernández, M. Staderini, N. Avlonitis, A.F. Murray, A.R. Mount, M. Bradley, Sensors Actuators, B Chem. 255 (2018) 3040–3046.

[365] N.L. Rosi, C.A. Mirkin, Chem. Rev. 105 (2005) 1547–1562.

[366] Y. Zhuo, P.X. Yuan, R. Yuan, Y.Q. Chai, C.L. Hong, Biomaterials 30 (2009) 2284–2290.

[367] C. Liu, Q. Jia, C. Yang, R. Qiao, L. Jing, L. Wang, C. Xu, M. Gao, Anal. Chem. 83 (2011) 6778–6784.

[368] M. Delamar, R. Hitmi, J. Pinson, J. Savéant, J. Am. Chem. Soc. 114 (1992) 5883–5884.

[369] M.C. Bernard, A. Chaussé, E. Cabet-Deliry, M.M. Chehimi, J. Pinson, F. Podvorica, C. Vautrin-Ul, Chem. Mater. 15 (2003) 3450–3462.

[370] O. Ghodbane, G. Chamoulaud, D. Bélanger, Electrochem. Commun. 6 (2004) 254–258.

[371] P.A. Brooksby, A.J. Downard, J. Phys. Chem. B 109 (2005) 8791–8798.

[372] C.H. de Villeneuve, J. Pinson, M.C. Bernard, P. Allongue, J. Phys. Chem. B 101 (1997) 2415–2420.

[373] A. Ricci, C. Bonazzola, E.J. Calvo, Phys. Chem. Chem. Phys. 8 (2006) 4297–4299.

[374] G. Liu, T. Böcking, J.J. Gooding, J. Electroanal. Chem. 600 (2007) 335–344.

[375] J.J. Gooding, Electroanalysis 20 (2008) 573–582.

[376] A.L. Gui, G. Liu, M. Chockalingam, G.L. Saux, J.B. Harper, J.J. Gooding, Electroanalysis 22 (2010) 1283–1289.

[377] D.M. Shewchuk, M.T. McDermott, Langmuir 25 (2009) 4556–4563.

[378] K.A. Peterlinz, R.M. Georgiadis, T.M. Herne, M.J. Tarlov, J. Am. Chem. Soc. 119 (1997) 3401–3402.

[379] P.R.B. De Oliveira Marques, A. Lermo, S. Campoy, H. Yamanaka, J. Barbé, S. Alegret, M.I. Pividori, Anal. Chem. 81 (2009) 1332–1339.

[380] M.R. Lockett, L.M. Smith, Langmuir 25 (2009) 3340–3343.

[381] L. Civit, A. Fragoso, C.K. O'Sullivan, Electrochem. Commun. 12 (2010) 1045–1048.

[382] W.R. Everett, T.L. Welch, L. Reed, I. Fritsch-Faules, Anal. Chem. 67 (1995) 292–298.

[383] M. Torréns, M. Ortiz, A.P.F. Turner, V. Beni, C.K. O'Sullivan, Electrochem. Commun. 53 (2015) 6–10.

[384] A. Chaussé, M.M. Chehimi, N. Karsi, J. Pinson, F. Podvorica, C. Vautrin-Ul, Chem. Mater. 14 (2002) 392–400.

[385] K. Boukerma, M.M. Chehimi, J. Pinson, C. Blomfield, Langmuir 19 (2003) 6333–6335.

[386] T. Menanteau, E. Levillain, T. Breton, Chem. Mater. 25 (2013) 2905–2909.

[387] S. Baranton, D. Bélanger, J. Phys. Chem. B 109 (2005) 24401–24410.

[388] G. Liu, T. Böcking, J.J. Gooding, J. Electroanal. Chem. 600 (2007) 335–344.

[389] A. Laforgue, T. Addou, D. Bélanger, Langmuir 21 (2005) 6855–6865.

[390] R.G. Digigow, J.F. Dechézelles, H. Dietsch, I. Geissbühler, D. Vanhecke, C. Geers, A.M. Hirt, B. Rothen-Rutishauser, A. Petri-Fink, J. Magn. Magn. Mater. 362 (2014) 72–79.

[391] L. Nalbandian, E. Patrikiadou, V. Zaspalis, A. Patrikidou, E. Hatzidaki, C. N. Papandreou, Curr. Nanosci. 12 (2016) 455–468.

[392] a L. Andrade, D.M. Souza, M.C. Pereira, J.D. Fabris, R.Z. Domingues, U. Federal, D.M. Gerais, B. Horizonte, Nano 55 (2009) 420–424.

[393] M. Răcuciu, D.E. Creangă, A. Airinei, Eur. Phys. J. E 21 (2006) 117–121.

[394] A.P. Herrera, C. Barrera, C. Rinaldi, J. Mater. Chem. 18 (2008) 3650–3654.

[395] B. Feng, R.Y. Hong, L.S. Wang, L. Guo, H.Z. Li, J. Ding, Y. Zheng, D.G. Wei, Colloids Surfaces A Physicochem. Eng. Asp. 328 (2008) 52–59.

[396] N. Follain, S. Montanari, I. Jeacomine, S. Gambarelli, M.R. Vignon, Carbohydr. Polym. 74 (2008) 333–343.

[397] T. Cheng, H. Li, Y. Ma, X. Liu, H. Zhang, Anal. Bioanal. Chem. 407 (2015) 3525–3529.

[398] C. Hui, C. Shen, T. Yang, L. Bao, J. Tian, H. Ding, C. Li, H.J. Gao, J. Phys. Chem. C 112 (2008) 11336–11339.

[399] T. Yang, C. Shen, Z. Li, H. Zhang, C. Xiao, S. Chen, Z. Xu, D. Shi, J. Li, H. Gao, J. Phys. Chem. B 109 (2005) 23233–23236.

[400] T. Lü, D. Qi, D. Zhang, S. Lin, Y. Mao, H. Zhao, J. Alloys Compd. 769 (2018) 858–865.

[401] L.W.M. Lau, A.R. Gerson, B.P. Payne, R.S.C. Smart, M.C. Biesinger, A.P. Grosvenor, Appl. Surf. Sci. 257 (2010) 2717–2730.

[402] R.P. Gupta, S.K. Sen, Phys. Rev. B 10 (1975) 71–77.

[403] N.A. Eltouny, P.A. Ariya, Ind. Eng. Chem. Res. 51 (2012) 12787–12795.

[404] T. Fan, D. Pan, H. Zhang, Ind. Eng. Chem. Res. 50 (2011) 9009–9018.

[405] S. Poulin, R. França, L. Moreau-Bélanger, E. Sacher, J. Phys. Chem. C 114 (2010) 10711–10718.

[406] T. Yamashita, P. Hayes, Appl. Surf. Sci. 254 (2008) 2441–2449.

[407] W.Z. Shen, S. Cetinel, K. Sharma, E.R. Borujeny, C. Montemagno, J. Nanoparticle Res. 19 (2017) 1–12.

[408] C. Vasilescu, M. Latikka, K.D. Knudsen, V.M. Garamus, V. Socoliuc, R. Turcu, E. Tombácz, D. Susan-Resiga, R.H.A. Ras, L. Vékás, Soft Matter 14 (2018) 6648–6666.

[409] G. Dharanivasan, T. Rajamuthuramalingam, D. Michael Immanuel Jesse, N. Rajendiran, K. Kathiravan, Appl. Nanosci. 5 (2015) 39–50.

[410] D. Wilson, M.A. Langell, Appl. Surf. Sci. 303 (2014) 6–13.

[411] Y. Li, H. Chen, J. Wu, Q. He, Y. Li, W. Yang, Y. Zhou, Appl. Surf. Sci. 447 (2018) 393–400.

[412] B.K. Sodipo, A.A. Aziz, Beilstein J. Nanotechnol. 5 (2014) 1472–1476.

[413] S. Fleutot, J.C. Dupin, G. Renaudin, H. Martinez, Phys. Chem. Chem. Phys. 13 (2011) 17564–17578.

[414] G. Rajender, P.K. Giri, J. Mater. Chem. C 4 (2016) 10852–10865.

[415] W. Xie, K.M. Ng, L.T. Weng, C.M. Chan, RSC Adv. 6 (2016) 80649–80654.

[416] A. Radi, X. Mu, V. Lates, J. Marty, 24 (2009) 1888–1892.

[417] A. Mesnage, X. Lefèvre, P. Jégou, G. Deniau, S. Palacin, Langmuir 28 (2012) 11767–11778.

[418] Philani Nkosinathi Mashazi, Ph.D Thesis (2011) 1–274.

[419] M.S. Murib, W.S. Yeap, Y. Eurlings, B. Van Grinsven, H.G. Boyen, B. Conings, L. Michiels, M. Ameloot, R. Carleer, J. Warmer, P. Kaul, K. Haenen, M.J. Schöning, W. De Ceuninck, P. Wagner, Sensors Actuators, B Chem. 230 (2016) 260–271.

[420] J. Kim, J. Cho, P.M. Seidler, N.E. Kurland, V.K. Yadavalli, Langmuir 26 (2010) 2599–2608.

[421] J. Kim, Spectroscopy (2012) 9–11.

[422] O.L. Osifeko, I. Uddin, P.N. Mashazi, T. Nyokong, New J. Chem. 40 (2016) 2710–2721.

[423] P. Mashazi, P. Tetyana, S. Vilakazi, T. Nyokong, Biosens. Bioelectron. 49 (2013) 32–38.

[424] Z. Taleat, A. Ravalli, M. Mazloum-Ardakani, G. Marrazza, Electroanalysis 25 (2013) 269–277.

[425] O. Hosu, M. Tertiș, G. Melinte, B. Feier, R. Săndulescu, C. Cristea, Electrochem. Commun. 80 (2017) 39–43.

[426] Y. Yuan, J. Zhang, M. Yin, C. Liu, Adv. Biomater. (2014) 1–8.

6.0. APPENDIX

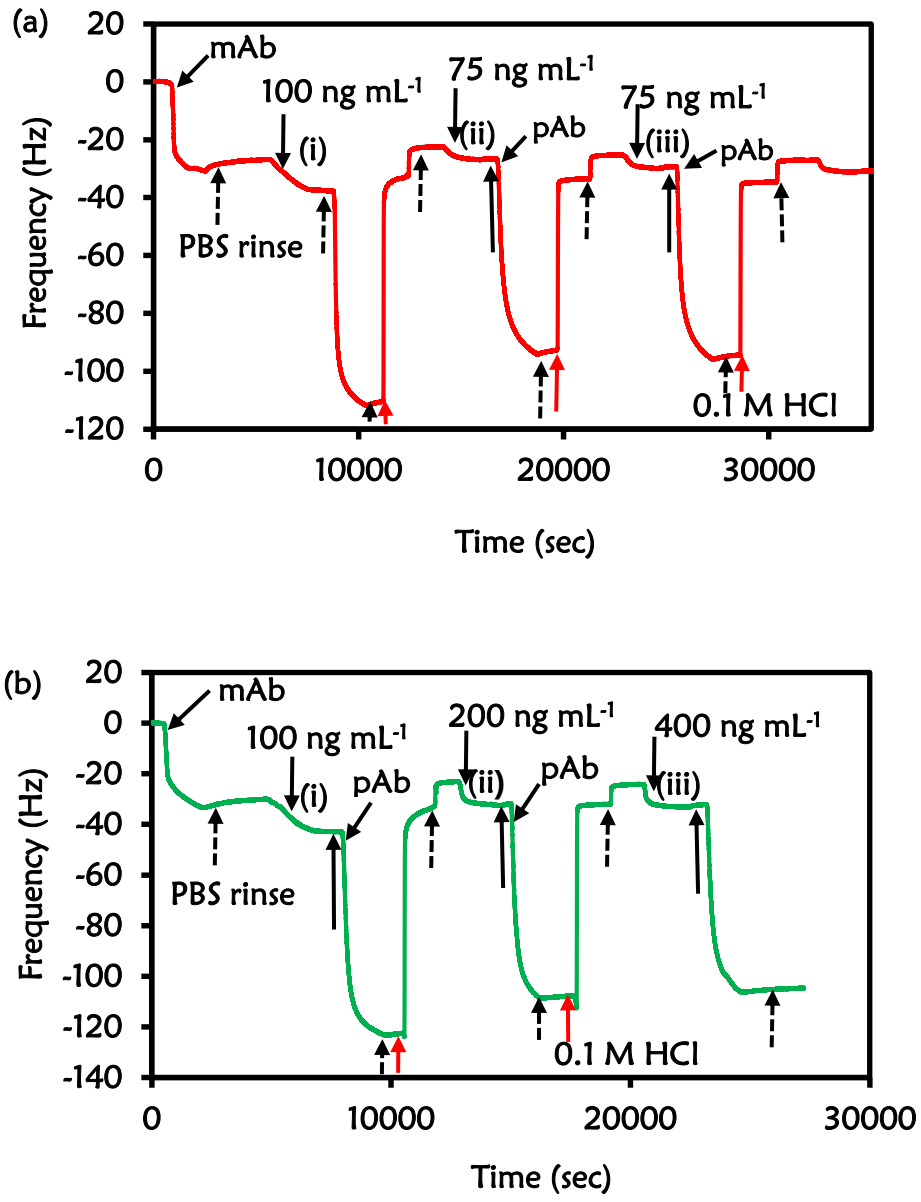

Figure S6.1(a & b): QCM-D sensorgram for different CRP antigen concentrations: (i) 75 ng mL^{-1}, (ii) 100 ng mL^{-1}, (iii) 200 ng mL^{-1} and, (iv) 400 ng mL^{-1} the red arrows are due to surface regeneration; dotted black arrows indicate buffer rinse, undotted black arrow indicates the amplified signal by pAb.

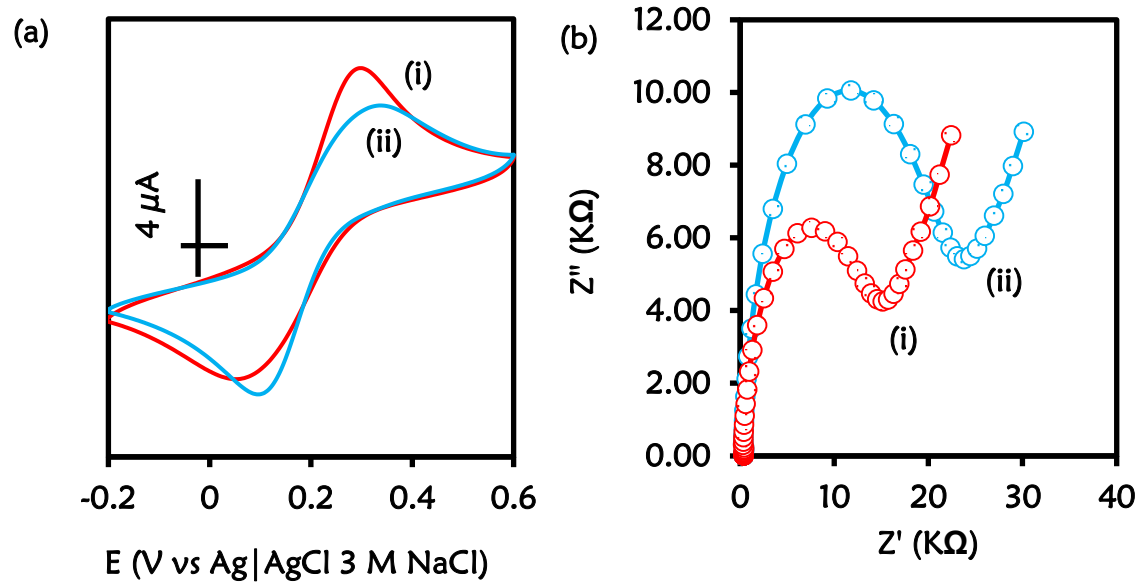

Figure S6.2: (a) CV and (b) EIS of (i) Au-MBA SAM and (ii) Au-MBA-APBA-mAb in (1:1) 2 mM $K_3Fe(CN)_6$:$K_4Fe(CN)_6$ solution containing 0.1 M KCl.

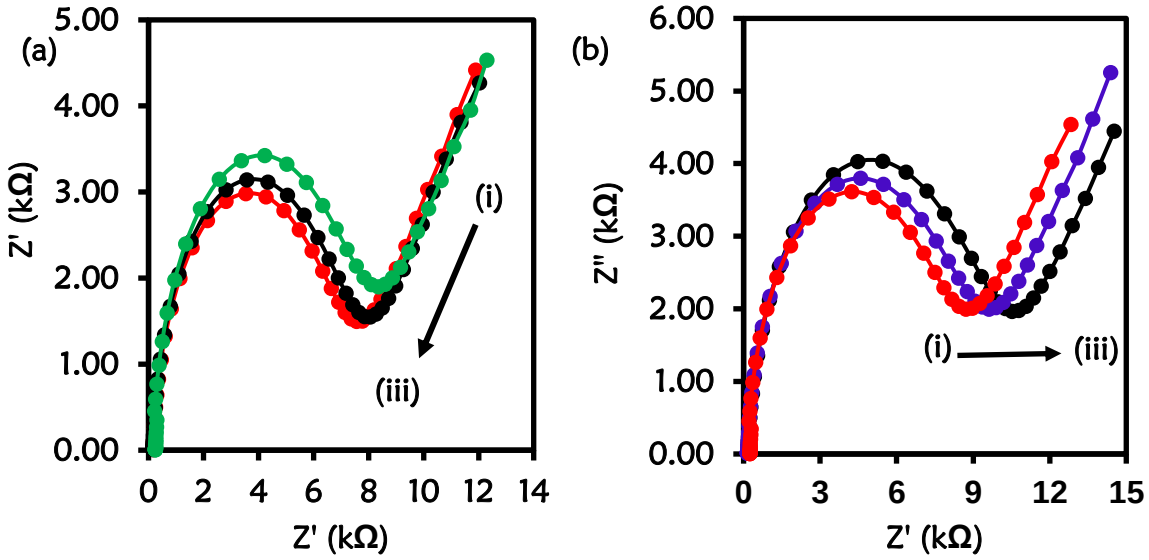

Figure S6.3: Nyquist plot showing (a) the decrease in R_{CT} at higher CRP-antigen concentrations (i –iii) 100 – 400 ng mL^{-1} for the direct immunoassay, (b) a slight increase in R_{CT} signal after (i)-(iii) for 100 – 400 ng mL^{-1} for CRP-antigen observed for sandwich immunoassay

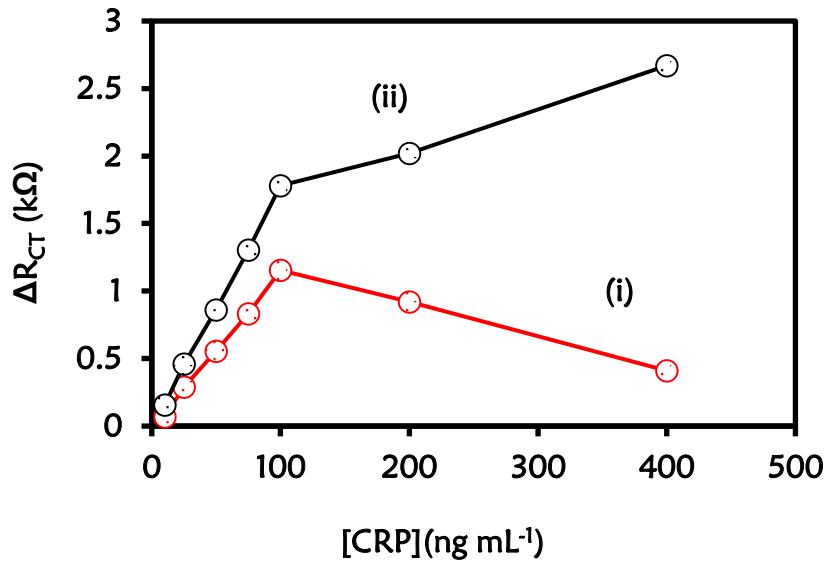

Figure S6.4: Calibration curves (ΔR_{CT} vs [CRP]) showing concentrations from 10 – 400 ng mL^{-1} for (i) direct immunoassay and (ii) sandwich immunoassay

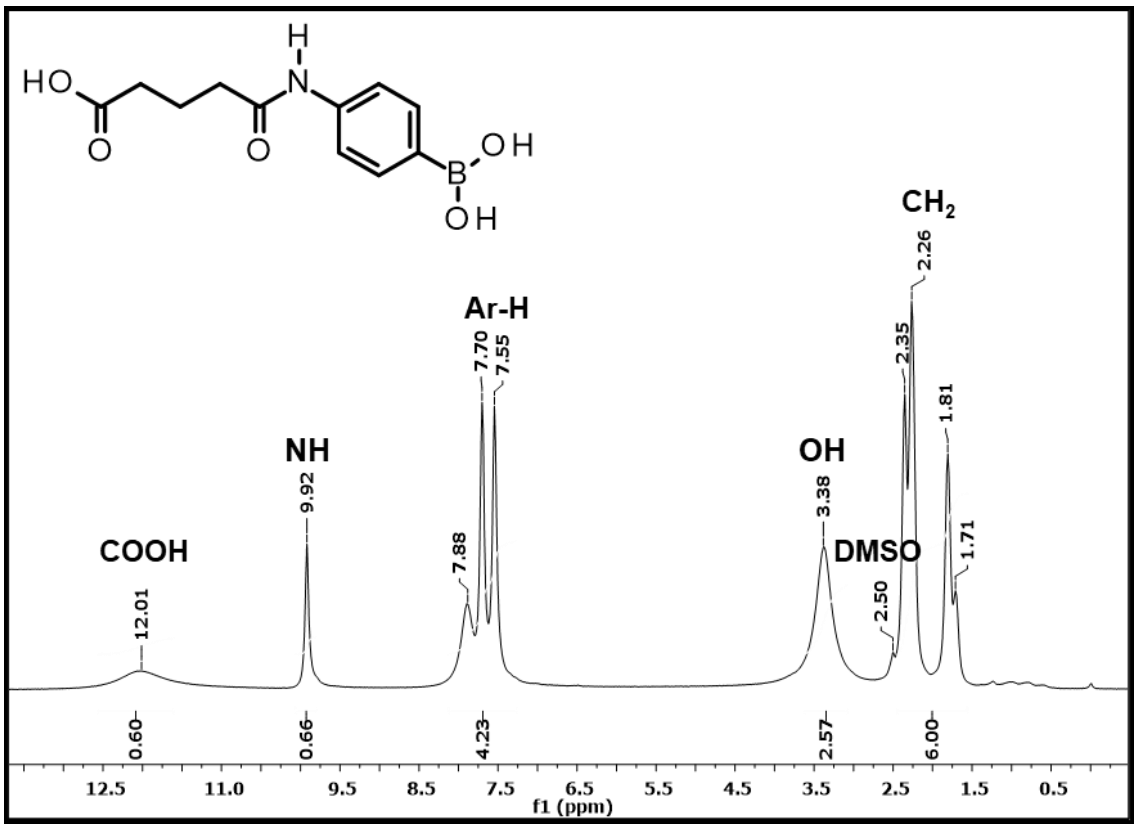

Figure S6.5: NMR spectrum of 5-(4-boronoanilino)-5-oxo-pentanoic acid

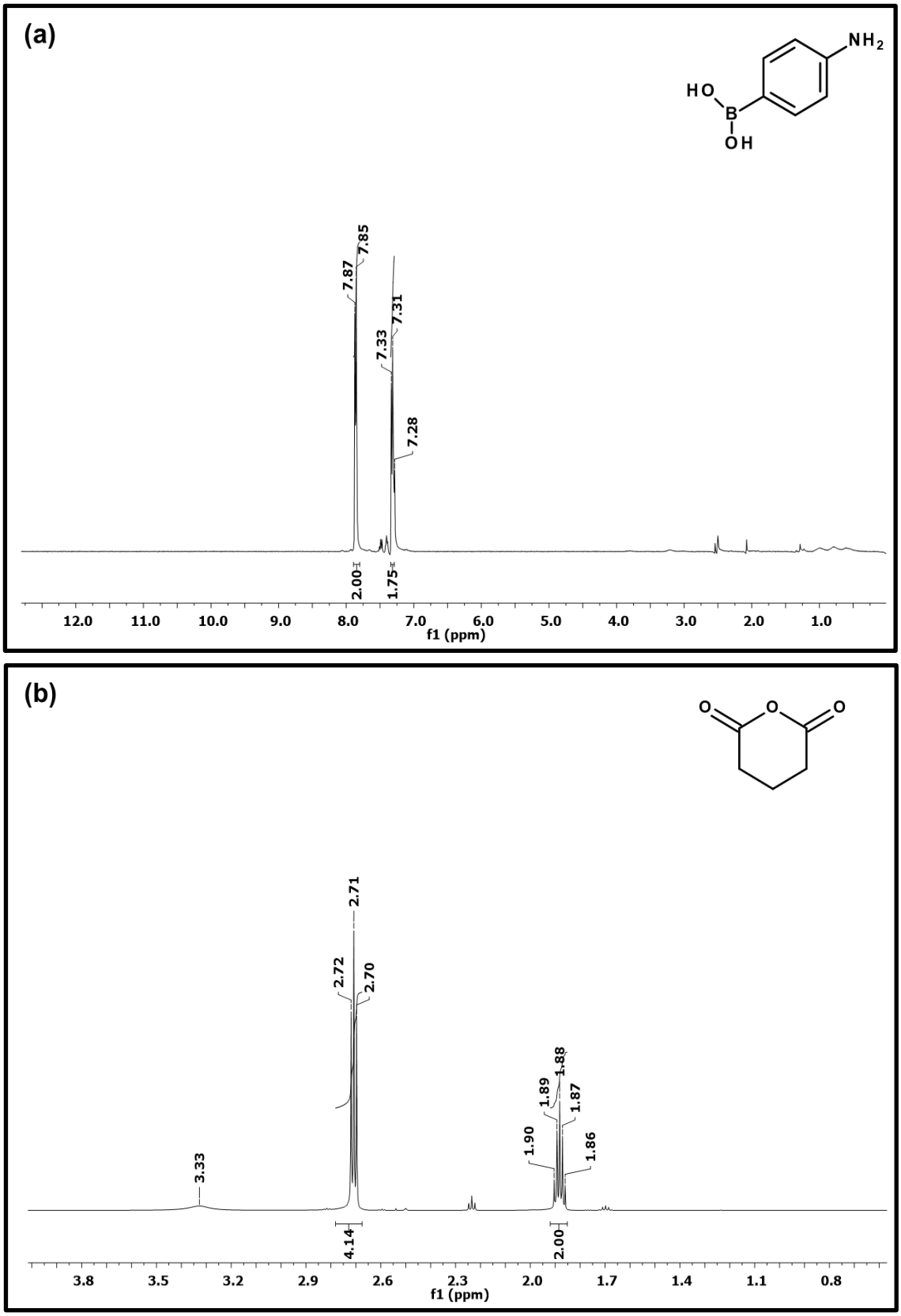

Figure S6.6: NMR spectra of (a) 4-aminophenylboronic acid (b) glutaric anhydride

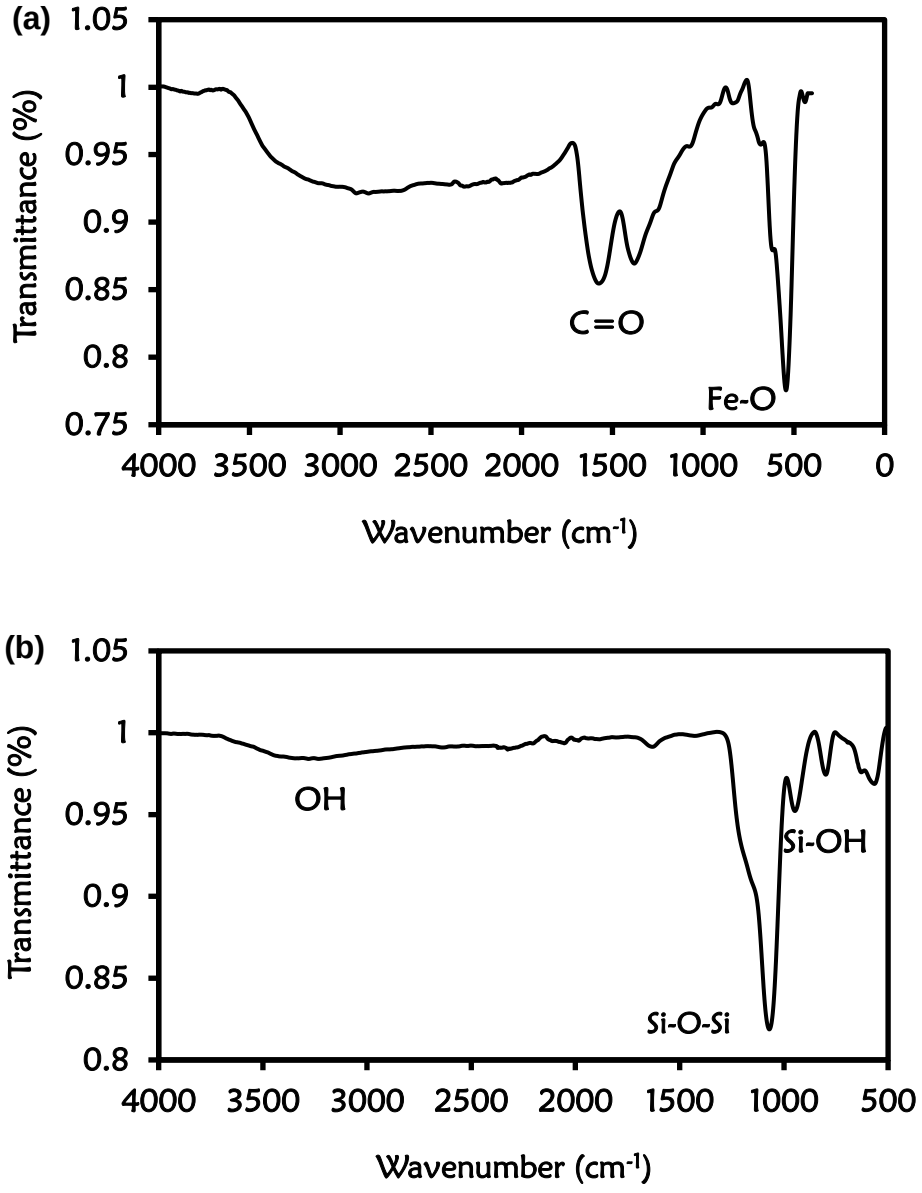

Figure S6.7: FTIR spectra of (a) MNPs (b) MNP-SiOH

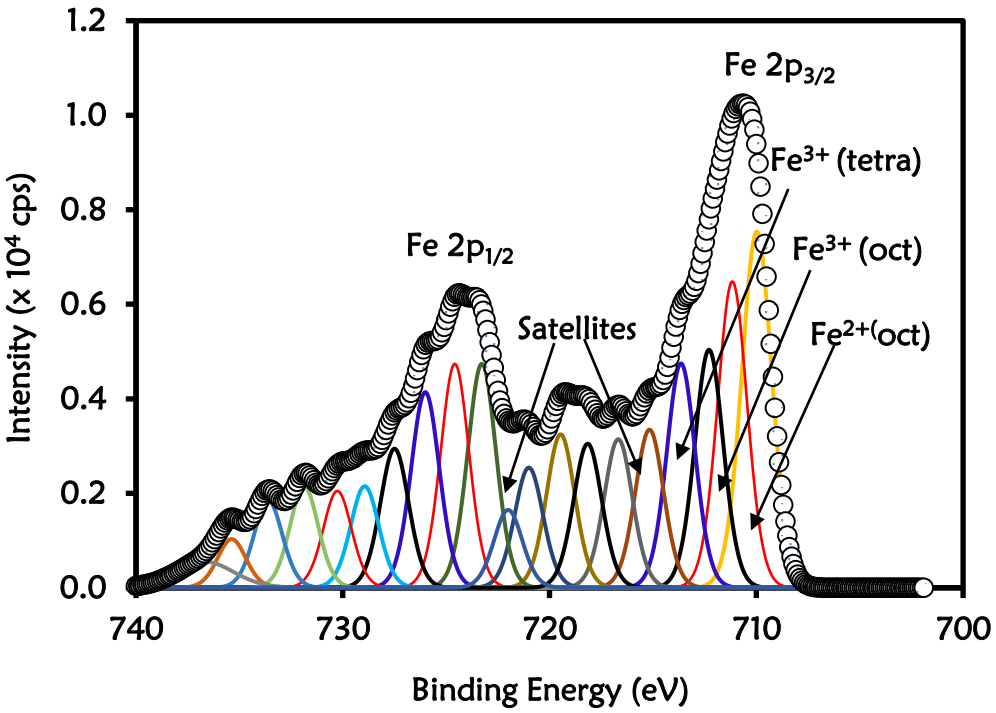

Figure S6.8: The high-resolution spectrum of Fe 2p

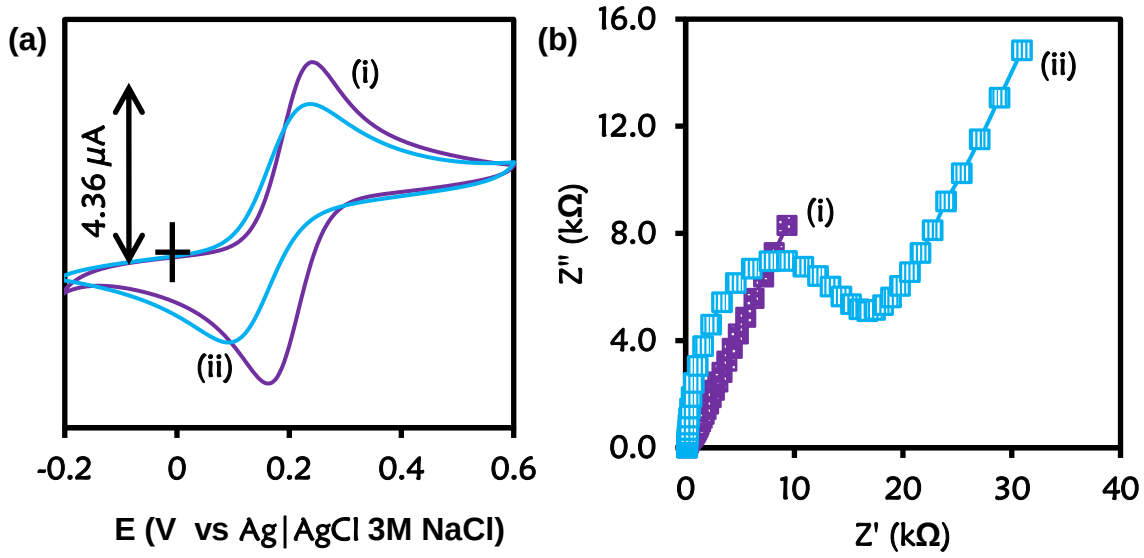

Figure 6.9: (a) CV and (b) EIS of (i) Au-PEA and (ii) Au-PEA-SA-APBA-mAb in (1:1) 2 mM $K_3Fe(CN)_6$:$K_4Fe(CN)_6$ solution containing 0.1 M KCl.

APBA concentration

The concentration of 4-aminophenylboronic acid (APBA) that gave the best antibody capture was optimised. Different concentration of 4-aminophenylboronic acid (10, 25, 50, 75 and 100 mM) were allowed to capture a fixed concentration (30 μg mL^{-1}) of the anti-CRP monoclonal antibody (capture antibody). 25 mM of the 4-aminophenylboronic acid gave the optimum capture with the highest charge transfer resistance. Therefore, 25 mM of 4-aminophenylboronic acid was chosen for the capture antibody.

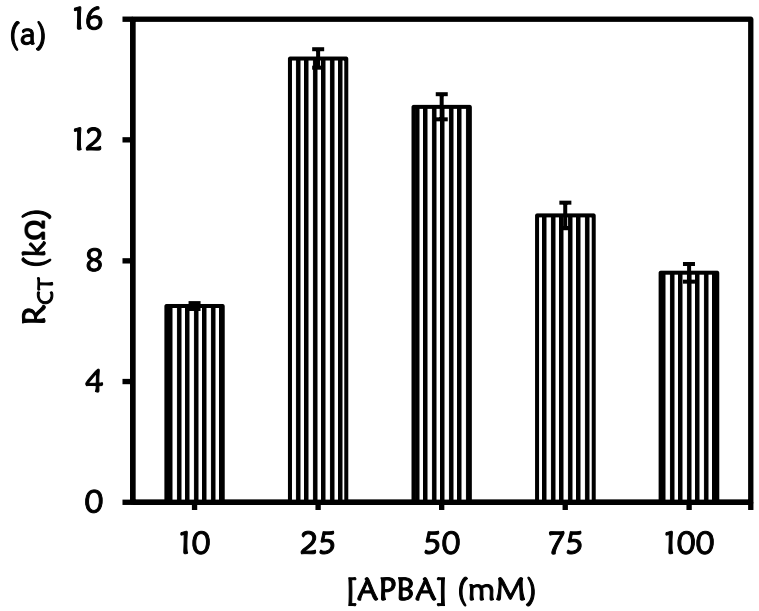

Conc.(mM)	RSD (%)
10	1.47
25	2.06
50	3.19
75	4.46
100	3.84

Figure S6.10(a): Bar chart showing the effect of APBA concentration at 10 mM, 25 mM, 50 mM, 75 mM and 100 mM of APBA and the corresponding table showing the relative standard deviation.

Optimization of the capture antibody concentration

Different concentrations of immobilized anti-CRP monoclonal antibody (anti-CRP MAb) ranging from (10, 20, 30, 40 and 50 μg mL^{-1}) were investigated for the optimization study. All other experimental conditions were kept constant. The charge transfer resistance (R_{CT}) increases with the increase in the concentration of the immobilized CRP antibody. The (R_{CT}) began to decrease at after 30 μg mL^{-1} which could be attributed to the saturation of the electrode surface. Therefore, 30 μg mL^{-1} was chosen as the optimum concentration that was used for the fabrication of the immunosensor.

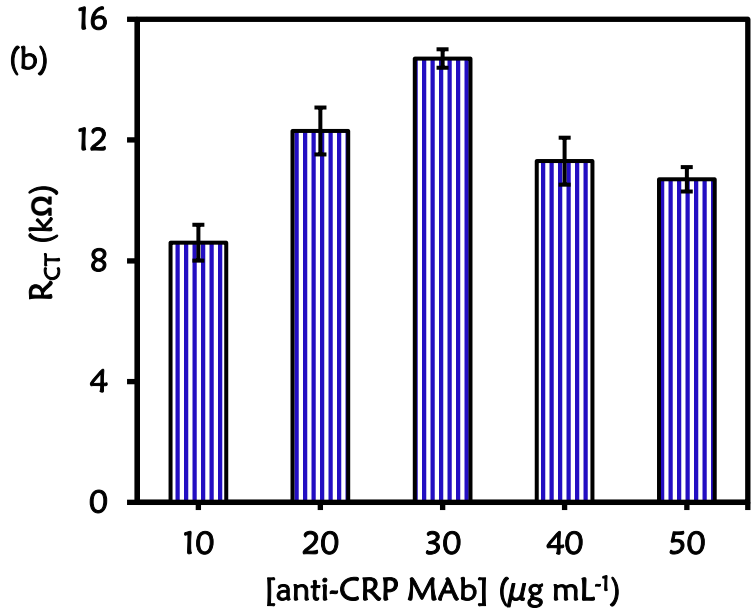

Conc. (μg mL^{-1})	RSD (%)
10	6.87
20	6.33
30	2.06
40	6.91
50	3.76

Figure 6.10(b): Bar chart showing the effect of immobilized antibody concentration at 10 20, 30, 40 and 50 μg mL^{-1} and the corresponding table showing the relative standard deviation.

Blocking reagent

Different concentrations of the blocking reagent (D-glucose) ranging from (0.055, 0.110, 0.167, 0.222 and 0.277 μ mol.L^{-1}) were studied. The R_{CT} increases with increase in the concentration of the blocking reagent up to 0.167 μ mol.L^{-1}). A decrease in R_{CT} was observed from 0.222 μ mol.L^{-1} up to 0.277 μ mol.L^{-1}. Therefore 0.167 μ mol.L^{-1} of the blocking solution gave the optimum result and was used for the fabrication of the immunosensor.

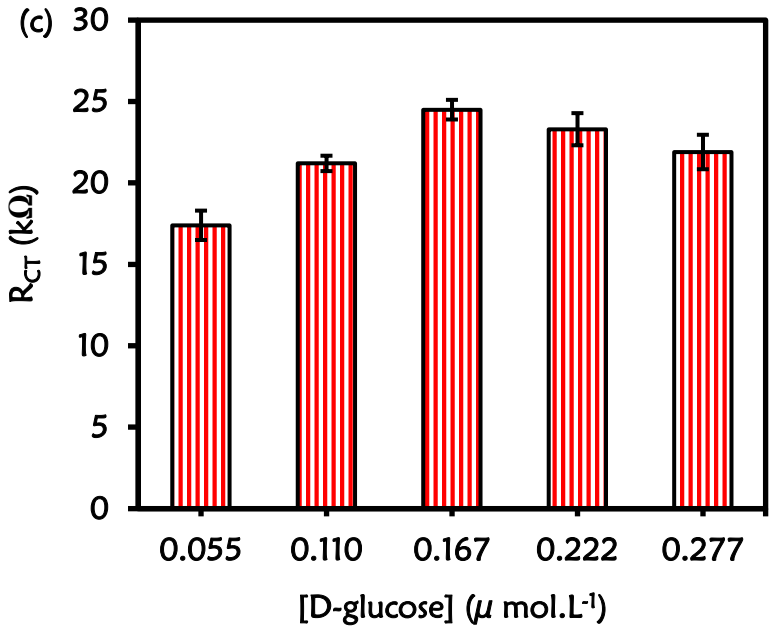

Conc. (μ mol.L^{-1})	RSD (%)
0.055	5.16
0.110	2.22
0.167	2.45
0.222	4.22
0.277	4.83

Figure 6.10(c): Bar chart showing the effect of concentration of the blocking solution at 0.055, 0.110, 0.167, 0.222 and 0.277 μ mol.L^{-1} and the corresponding table showing the relative standard deviation.

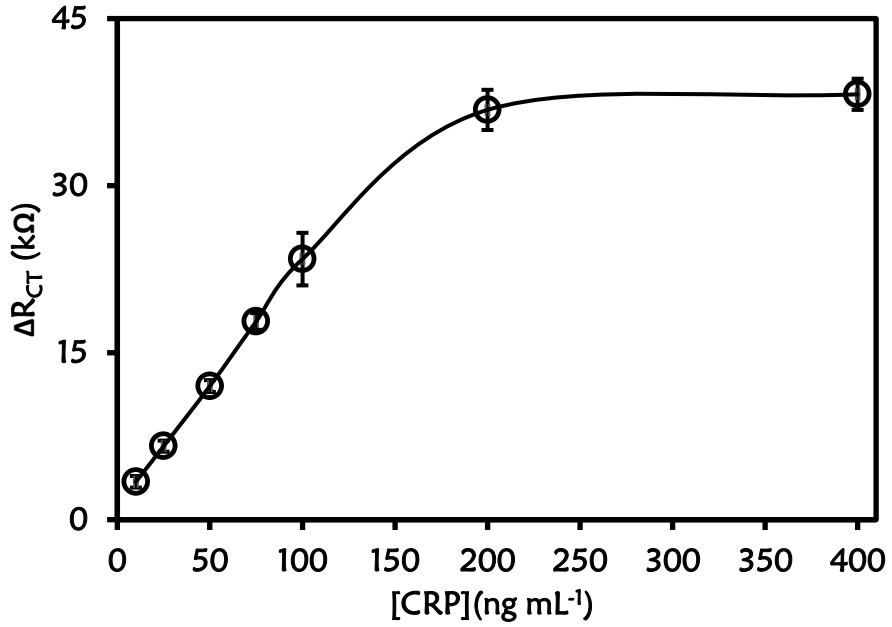

Figure S6.11: Calibration curve for Au-PEA-SA-APBA-mAb/glucose at [CRP] ranging from (1 – 400 ng mL^{-1})

Table S6.1: The relative standard deviation (% RSD, n = 3) obtained from EIS for direct and sandwich immunoassay at different antigen concentrations for Au-MBA-APBA-mAb/glucose.

[CRP-antigen] (ng mL^{-1})	Direct immunoassay (RSD %)	Sandwich immunoassay (RSD %)
10	9.42	6.07
25	7.71	3.14
50	5.84	4.23
75	1.68	0.86
100	4.83	7.21
200	0.84	4.34
400	2.43	0.65